WAVEFORM DESIGN AND PROCESSING TECHNIQUES IN OFDM RADAR

Gabriel Lellouch
MSc ENSEEIHT

Thesis Presented for the Degree of

DOCTOR OF PHILOSOPHY

in the Department of Electrical Engineering

UNIVERSITY OF CAPE TOWN

Rondebosch, September 25, 2015

“It always seems impossible until it’s done.”

-Nelson Rolihlahla Mandela

Declaration

I declare that this thesis is my own, unaided work. It is being submitted for the degree of Doctor of Philosophy in Engineering in the University of Cape Town. It has not been submitted before for any degree or examination in any other university.

Signed by candidate

Signature Removed

Signature of Author .....

Cape Town
Rondebosch, September 25, 2015

Abstract

With the advent of powerful digital hardware, software defined radio and radar have become an active area of research and development. This in turn has given rise to many new research directions in the radar community, which were previously not comprehensible. One such direction is the recently investigated OFDM radar, which uses OFDM waveforms instead of the classic linear frequency modulated waveforms. Being a wideband signal, the OFDM symbol offers spectral efficiency along with improved range resolution, two enticing characteristics for radar. Historically a communication signal, OFDM is a special form of multicarrier modulation, where a single data stream is transmitted over a number of lower rate carriers. The information is conveyed via sets of complex phase codes modulating the phase of the carriers. At the receiver, a demodulation stage estimates the transmitted phase codes and the information in the form of binary words is finally retrieved. In radar, the primary goal is to detect the presence of targets and possibly estimate some of their features through measurable quantities, e.g. range, Doppler, etc.. Yet, being a young waveform in radar, more understanding is required to turn it into a standard radar waveform.

Our goal, with this thesis, is to mature our comprehension of OFDM for radar and contribute to the realm of OFDM radar.

First, we develop two processing alternatives for the case of a train of wideband OFDM pulses. In this, our first so-called *time domain* solution consists in applying a matched filter to compress the received echoes in the fast time before applying a fast Fourier transform in the slow time to form the range Doppler image. We motivate this approach after demonstrating that short OFDM pulses

are Doppler tolerant. The merit of this approach is to conserve existing radar architectures while operating OFDM waveforms. The second so-called *frequency domain* solution that we propose is inspired from communication engineering research since the received echoes are tumbled in the frequency domain. After several manipulations, the range Doppler image is formed. We explain how this approach allows to retrieve an estimate of the unambiguous radial velocity, and propose two methods for that. The first method requires the use of identical sequence (IS) for the phase codes and is, as such, binding, while the other method works irrespective of the phase codes. Like the previous technique, this processing solution accommodates high Doppler frequencies and the degradation in the range Doppler image is negligible provided that the spacing between consecutive subcarriers is sufficient. Unfortunately, it suffers from the issue of intersymbol interference (ISI). After observing that both solutions provide the same processing gain, we clarify the constraints that shall apply to the OFDM signals in either of these solutions. In the first solution, special care has been employed to design OFDM pulses with low peak-to-mean power ratio (PMEPR) and low sidelobe level in the autocorrelation function. In the second solution, on the other hand, only the constraint of low PMEPR applies since the sidelobes of the scatterer characteristic function in the range Doppler image are Fourier based.

Then, we develop a waveform-processing concept for OFDM based stepped frequency waveforms. This approach is intended for high resolution radar with improved low probability of detection (LPD) characteristics, as we propose to employ a frequency hopping scheme from pulse to pulse other than the conventional linear one. In the same way we treated our second alternative earlier, we derive our high range resolution processing in matrix terms and assess the degradation caused by high Doppler on the range profile. We propose using a bank of range migration filters to retrieve the radial velocity of the scatterer and realise that the issue of classical ambiguity in Doppler can be alleviated provided that the relative bandwidth, i.e. the total bandwidth covered by the train of pulses divided by the carrier frequency, is chosen carefully. After discussing a deterministic artefact caused by frequency hopping and the means to reduce it at the waveform design or processing level, we discuss the benefit offered by our

concept in comparison to other standard wideband methods and emphasize on its LPD characteristics at the waveform and pulse level.

In our subsequent analysis, we investigate genetic algorithm (GA) based techniques to finetune OFDM pulses in terms of radar requirements viz., low PMEPR only or low PMEPR and low sidelobe level together, as evoked earlier. To motivate the use of genetic algorithms, we establish that existing techniques are not flexible in terms of the OFDM structure (the assumption that all carriers are present is always made). Besides, the use of advanced objective functions suited to particular configurations (e.g. low sidelobe level in proximity of the main autocorrelation peak) as well as the combination of multiple objective functions can be done elegantly with GA based techniques. To justify that solely phase codes are used for our optimisation(s), we stress that the weights applied to the carriers composing the OFDM signal can be spared to cope with other radar related challenges and we give an example with a case of enhanced detection.

Next, we develop a technique where we exploit the instantaneous wideband transmission to characterise the type of the canonical scatterers that compose a target. Our idea is based on the well-established results from the geometrical theory of diffraction (GTD), where the scattered energy varies with frequency. We present the problem related to ISI, stress the need to design the transmitted pulse so as to reduce this risk and suggest having prior knowledge over the scatterers relative positions. Subsequently, we develop a performance analysis to assess the behaviour of our technique in the presence of additive white Gaussian noise (AWGN). Then, we demonstrate the merit of integrating over several pulses to improve the characterisation rate of the scatterers.

Because the scattering centres of a target resonate variably at different frequencies, frequency diversity is another enticing property which can be used to enhance the sensing performance. Here, we exploit this element of diversity to improve the classification function. We develop a technique where the classification takes place at the waveform design when few targets are present. In our case study, we have three simple targets. Each is composed of perfectly electrically conducting spheres for which we have exact models of the scattered field. We

develop a GA based search to find optimal OFDM symbols that best discriminate one target against any other. Thereafter, the OFDM pulse used for probing the target in the scene is constructed by stacking the resulting symbols in time. After discussing the problem of finding the best frequency window to sense the target, we develop a performance analysis where our figure of merit is the overall probability of correct classification. Again, we prove the merit of integrating over several pulses to reach classification rates above 95%.

In turn, this study opens onto new challenges in the realm of OFDM radar. We leave for future research the demonstration of the practical applicability of our novel concepts and mention manifold research axes, viz., a signal processing axis that would include methods to cope with intersymbol interference, range migration issues, methods to raise the ambiguity in Doppler when several echoes from distinct scatterers overlap in the case of our *frequency domain* processing solutions; an algorithmic axis that would concern the heuristic techniques employed in the design of our OFDM pulses. We foresee that further tuning might help speeding up our GA based algorithms and we expect that constrained multi-objective optimisation GA (MOO-GA) based techniques shall benefit the OFDM pulse design problem in radar. A system design axis that would account for the hardware components' behaviours, when possible, directly at the waveform design stage and would include implementation of the OFDM radar system.

Acknowledgements

I remember precisely the moment when I said to myself "Let's do it!". From this quasi-impulsive thought a countless number of obstacles have piled up. Many doubts have lived in me and with me but my optimistic mindset, my best friend along the way has rubbed them away, slowly.

Clearly, I required academic support to effectively make this mere will real. In that respect, my utmost gratitude goes to Prof. Michael Inggs and Dr. Amit Mishra from the Radar and Remote Sensing Group of the University of Cape Town who kindly acknowledged my request and accepted to move it forward. I am thankful to them for they assigned me the role of teaching assistant in the radar master program starting from my arrival in February 2013 and therefore secured me with financial support to carry on. Needless to say, the long way that lead me to finally writing this section fills me with joy and pride.

Even though writing a PhD dissertation is nothing but an intense individual effort, I wish to acknowledge those people who gave me the tools to mature and grow in this field.

Dr. Mishra, Amit, my supervisor, who provided me with an invaluable guidance. He authorised me no waste of time, e.g. in less than one month I had tamed my worst enemy, Latex. The pain I endured getting started has been by no means comparable to the time saving I experienced thereafter. Prof. Inggs, my co-supervisor, who provided me with helpful input especially in the context of academic procedure.

The authors of the book "Principles of modern radar", Dr. Richards *et al.*,

whose comprehensive material and the various open source codes associated to it, have been a major source of inspiration to catch up with my research. The lecturers from the radar master program who taught in 2013 and 2014 as well as the students. The opportunity to act as a teaching assistant for this program has been very useful to position my work.

The anonymous reviewers who provided valuable comments and suggestions to my academic papers and the various authors of all the free and open source software tools that I made use of during the course of my research.

The technical and administrative staff from the electrical engineering department of the University of Cape Town, in particular Nicole and Carol for providing solutions to the numerous administrative related issues I encountered.

The University of Cape Town upper campus for being such a stunning place to wander and get a break.

I also wish to acknowledge those people who contributed to my living experience on that side of the world.

My office mates who inspired a pleasant working environment with the help of the table mountain, faithfully by my side. Doreen (mummy, *The Cranes*), Leo (proudly Namibian, *The Brave Warriors*), Titus (uncle Scrooge, *The Super Eagles*), Lerato (Ubuntu guru, *The Crocodiles*) and Dominique (*Las Palancas Negras*). Good luck to everyone for the remaining effort. Craig who kindly gave me the template of this thesis and the other members of the Radar and Remote Sensing Group, past and present who provided motivation and company during this work.

The friends I met along the way. Kuba, proud resident of Mowbray for we shared our passion for large and small scale football. My past house mates for the cheerful and literate atmosphere, Tali, Ilana, Liz, Muhammad, Seb, JP (*Oxford scholar*), Lisa. *Mon pote de l'île Maurice*, Vinand for bringing his OSS117 vibes to Cape Town. My teachers from Cordão de Ouro-South Africa, all the way from Brazil, for sharing this ecstasy that is Capoeira. Rodolfo, whose delightful cuisine has nourished my mind while writing this dissertation. My special thanks

go to Emma, my partner of adventure who I owe some wonderful discoveries in the breathtaking Nature of the Western Cape on bicycle or on foot. Together with her *Entertainer Cape Town* books she lead my beetle and I visit some mighty places that our situation could not afford otherwise. She deserves extra thanks here for she took the time to proof read some of my writings and propose valuable improvements.

I would also like to thank my overseas friends for their infallible friendship despite the distance, Yanno *le savoyard hollandais*, Rock *le toulousain strasbourgeois*, Luigi *le normand finlandais*, Pije *le toulousain danois*, Mex *le mexicano californien*, Tonio *le Pat Viera du CoMö*, Peps *la toulousaine des HP*, Paulo *l'indien d'Alesia*, ma Kace *le parisien du centre*, Zaz *la banlieusarde de province*, Astrid *la 3/4 centre*, Ja *le Zlatan de Meknes*, CECICA Capoeira *du 14ème de Paname*, the football collectives "USTR", "CoMö" and "REMO VI" respectively from Limours, Paris and The Hague, my Soestdijksekade family, Floriane, Blanka, Raul, Benoit, Kinga and all the fabulous friends who have come across my path, for all the precious moments of life I have been carrying ever since with me.

My virtual friends from *La chanson du dimanche* and *made in Groland* for the free of charge and incomparable therapeutic impact throughout the years.

Finally, my deepest thanks go to the members of my family. Albeit odd has my journey been, they have always been encouraging and supportive of my endeavours and I am grateful to have had them around me for the past 31 years. My mum Carole for not taking offence when I asked her to call me back outside my unpredictable golden hours' pattern. I shall be grateful for I inherited her optimism and could keep up with my home town during my expatriate years. My dad Michel, for smoothing my relationship with French administration bodies and decorating his garage with my sport equipments. I guess I inherited his sense of travelling and his appreciation for bicycles. Juliette, my sister, for her unrestricted auscultations, her instinct for strategic living locations and her soothing fraternity. My *mamie* Madeleine, for her contagious genuineness, jolly mind and unfailing energy. My aunt Sabine for contributing to my cinematographic plus comic strips culture and for offering me a cosy house at each of

my transits through Paris. My aunt Muriel for being sweet and caring to me. I would also like to acknowledge my cousins Anaïs, Kerim and Shanon for those non-academic times spent feasting on pastries, in preparation for the long academic season. Adolfo, my uncle in law for opening his culinary and artistic talents to our family. I would also like to acknowledge the friendly support I received from Elisabeth and Maël. Last but not least, I would like to thank Noé, my newcomer nephew for creating a diversion and thus leaving me in peace to finish this dissertation. This work is dedicated to them.

Contents

List of Figures

List of Tables

List of Algorithms

List of Abbreviations

1D 1-dimension. 147

2D 2-dimension. xxiv, 2, 70, 82

2D-DFT 2D DFT. xxxvi, 68, 76, 78, 98

3D 3-dimension. 2, 137, 185

ACF Auto-Correlation Function. 115

ADC Analogue to Digital Converter. 26, 39, 89

AF Ambiguity Function. xxx, 44, 48, 52, 82, 102, 105

ATR Automatic Target Recognition. 147, 169, 183

AWGN Additive White Gaussian Noise. v, xlii, 17, 18, 33, 52, 62, 79, 98, 152, 157, 167, 168, 188, 195

BPSK Binary Phase Shift Keying. 50, 86, 126, 129

CFAR Constant False Alarm Rate. 44

CLS Chirp Like Sequence. 128

COCS Consecutive Ordered Cyclic Shifts. 128

COFDM Coded Orthogonal Frequency Division Multiplexing. 44

CP Cyclic Prefix. 36

CPI Coherent Processing Interval. 80, 110, 111, 117, 191, 195

CR Cognitive Radar. 165

CRLB Cramer Rao Lower Bound. 149

DAB Digital Audio Broadcasting. 44

DAC Digital to Analogue Converter. 25, 29, 30, 33, 35

dB deci Bel. xxxviii, 13, 16, 18, 33, 44, 58–60, 62, 71, 72, 76–78, 80–82, 97, 98, 100, 105–107, 110, 111, 114, 128, 134–136, 142, 156, 159, 161, 162, 188

DFT Discrete Fourier Transform. xii, xxiv, xxvi, xxxiii, xxxv, xxxvi, 13, 15, 26, 36, 38–40, 50, 51, 58, 60–62, 69, 70, 72–74, 77–80, 82, 92, 95, 96, 99, 104, 108, 119, 156, 191, 195

DVB-T Digital Video Broadcast - Terrestrial. 27, 30

EA Evolutionary Algorithm. 118

ECCM Electronic Counter Counter Measures. 112

ESD Energy Spectral Ddensity. 166

FDM Frequency Division Multiplexing. 22

FFT Fast Fourier Transform. xxvi, 4, 24, 51

GA Genetic Algorithm. v, vi, xxvii, xxx, xxxi, 9, 15, 16, 18, 21, 119, 128, 129, 131–135, 137, 142–144, 168, 177–179, 191, 193–196

GTD Geometrical Theory of Diffraction. v, 17, 147

HiSL Highest Side Lobe. 105

HRR High Range Resolution. xvi, xix, xxix, xxx, xxxvii–xl, xlii, 15, 21, 84, 85, 88, 89, 92, 95, 98, 99, 101, 110, 115, 116, 201

HRRP High Range Resolution Profile. xviii, 2, 8, 10, 11, 45, 84, 85, 95–97, 101, 103, 114, 116, 146

HYCAM HYperfrequence CAMera. 167

I In phase. 120, 198, 199

ICI Inter Carrier Interference. 35–37, 39, 71

IDFT Inverse DFT. xxxiii, xxxv, xxxvii, 13, 15, 24, 25, 27, 32, 50, 51, 58, 92, 95–98, 103, 104, 111, 130, 132, 148, 150, 172, 179

IF Intermediate Frequency. xx, 111, 197–199

IFFT Inverse FFT. 4, 24, 50, 174

IFT Inverse Fourier Transform. 150

iid independent and identically distributed. xxxix, 149

IS Identical Sequence. iv, xxxvii, 41, 69, 73, 103, 114, 115, 127, 191

ISAR Inverse SAR. 2, 146

ISI Inter Symbol Interference. iv, v, 13, 14, 17, 35–37, 43, 89, 108, 114–117, 120, 121, 153, 162, 192–195

ISLR Integrated Sidelobe Level Ratio. 9, 11, 124–126, 128, 137, 138, 144, 191

LFM Linear Frequency Modulation. 3, 41, 58, 85, 108, 110, 112, 117, 192, 193, 196

LNA Low Noise Amplifier. 196

LoS Line of Site. 36

LPD Low Probability of Detection. iv, v, 8, 14, 108, 113, 117, 192, 193

MCPC Multicarrier Phase Coded. 48

MI Mutual Information. 166, 167

MIMO Multiple Input and Multiple Output. 46

ML Maximum Likelihood. 148

MOO Multiple Objective Optimisation. 128, 193

MOO-GA Multiple Objective Optimisation GA. vi, 119, 129, 137, 142, 144, 196

MSc Master in Science. 43, 44, 46

NSGA Non Dominated Sorting Genetic Algorithm. 119, 135

NSGA-II Non Dominated Sorting Genetic Algorithm II. 16, 17, 119, 131, 132, 135, 136, 142, 193

OFDM Orthogonal Frequency Division Multiplexing. iii–vi, xvi–xix, xxi, xxvii, xxx–xxxii, xli, 2–18, 21–58, 60–63, 65, 71, 81–87, 89, 92, 102, 103, 105, 108, 111–126, 128, 130, 132, 134, 138–142, 146, 147, 149, 150, 152, 154, 155, 162, 163, 165, 167–170, 174, 176, 177, 179, 185, 188, 190–197, 200

OFDM-PCSF OFDM phase-coded stepped frequency. 45

PAPR Peak to Average Power Ratio. 125, 126

PDF Probability Density Function. xix, 159, 160, 173, 174

PEC Perfectly Electrically Conducting. xxxix–xli, 12, 141, 169, 170, 189

PhD Doctor in Philosophy. 43, 45, 46

PMEPR Peak to Mean Envelope Power Ratio. iv, v, xvi, xix, xxxii, 9, 11, 16, 17, 42, 44, 69, 114, 115, 117–119, 125–128, 130, 133–138, 140, 142–144, 189, 191, 193, 196

PRF Pulse Repetition Frequency. 54, 61, 103, 110–112, 114, 191

PRI Pulse Repetition Interval. xxxii, 55, 61, 65, 81, 87–89, 106, 108–111, 113

PSK Phase Shift Keying. 23

PSLR Peak to Sidelobe Level Ratio. xvi, xix, 9, 11, 13, 15–17, 114, 115, 119, 124–128, 135–138, 142, 144, 191, 193

Q Quadrature. 120, 198, 199

QAM Quadrature Amplitude Modulation. 23

QPSK Quadrature Phase Shift Keying. 27, 30, 50, 129, 133–135, 193

RadCom Radar & communication. 5, 6, 45, 46

RCS Radar Cross Section. xvi, xix, xxxviii, 11, 12, 45, 164, 165, 169–173, 181–186

RF Radio Frequency. xx, xxxii, xxxix, xli, xlii, 23, 25, 29, 33, 34, 86, 139, 169, 196–198

SAR Synthetic Aperture Radar. xxvi, 46, 146, 147

SFW Stepped Frequency Waveform. xiii, xxi, xxix, xxxvi, 6, 84, 86–89, 102, 105, 108, 111–114, 116, 117

SGA Simple Genetic Algorithms. 130, 134

SHT Sequential Hypothesis Testing. 167

sinc Sinus Cardinal (=sin(x)/x). 25, 70, 76, 82

SINR Signal to Interference plus Noise Ratio. 166, 167

SNR Signal to Noise Ratio. xxxi, xlii, 13, 18–20, 46, 79, 80, 97, 98, 102, 110, 112–114, 116, 138, 139, 157–164, 166, 167, 180, 188, 192, 194, 201, 203

UCT University of Cape Town (South Africa). 196

List of Symbols

A_m Same as A specifically for Pulse m. 86

A Normalisation factor introduced to normalise OFDM pulses when normalisation is not accounted directly in the frequency weights w_n. xxix, 123

B_p Bandwidth of the OFDM pulse used in the HRR technique, in Hertz. 87, 94

$B_{\mathbf{tot}}$ Total bandwidth covered by the SFW in the HRR technique, in Hertz. 104–107, 112

B Bandwidth in Hertz. 18, 19, 30, 32, 33, 51, 52, 54, 60, 61, 70, 81, 105–107, 109, 110, 115, 120–122, 125, 126, 139, 140, 151, 154, 155, 157, 159, 161, 162, 173, 176, 197

C Number of classes among which the classification takes place. 158

E_f Electric field, in Volts per metre. 147, 149, 150

E Energy of a signal. 54, 112, 157, 182, 186, 187

F_0 Lowest carrier frequency covered in the train with the HRR technique, in Hertz. 87, 94, 95, 100, 101, 104, 105, 113, 203

G Cumulated processing gain. 62, 80, 98

H_f Deterministic target reflectivity spectrum. f stands for frequency domain. This function is similar to ς_s but this notation puts emphasis on the filtering aspect. 149, 150, 171

H Filter transfer function. 138

$ISLR$ Integrated sidelobe level ratio. 124

I_1 Coefficient used in the calculation of the AF of the OFDM pulse. 59

I_2 Coefficient used in the calculation of the AF of the OFDM pulse. 59

J Squared error used to characterise the canonical scatterers. 148, 149

K Number of symbols composing an OFDM pulse. xxx, xxxv, xxxvi, xl, 49, 51, 52, 54, 58–62, 64, 68–70, 74, 75, 79–81, 86, 92, 93, 97, 98, 100–103, 111–115, 123, 124, 126, 128–130, 132, 135, 136, 192, 202, 203

L_T Total number of targets in the scenario. 87–89, 169, 174–176

$L_{\mathbf{mut}}$ Number of offsprings that undergo mutation in the GA based techniques. 131, 133

$L_{\mathbf{pop}}$ Population size as used in the GA based techniques. 129–133, 135

L Function of the four variables N, K, f_D and Δf used in the calculation of the magnitude loss due to Doppler in the HRR processing. 99, 100

$M_{\mathbf{noise}}$ Number of realisations of noisy measurements. 158, 161, 172, 173, 187, 188

M Number of pulses transmitted for coherent processing. 49, 51, 54, 55, 61–63, 68, 70, 76, 78, 80, 81, 86–89, 92, 95–98, 102–114, 192

N_0 Noise power. 140

N_p Number of pulses used for integration in the OFDM phenomenology techniques. 160, 161, 187, 188

$N_{\mathbf{corr}}$ Number of range migration filters in the HRR processing. 104

$N_{\mathbf{int}}$ Number of batches used for coherent integration in the HRR processing. 113

N Number of subcarriers in an OFDM symbol. xxx, 19, 25, 28, 31, 42, 49–52, 54, 60–62, 64–70, 72, 73, 75, 79–82, 86, 87, 89–100, 103–107, 111–115, 119, 122–126, 128–130, 132–136, 140, 141, 154, 155, 157, 161, 162, 176–178, 188, 192, 201–203

$PMEPR$ Peak to mean envelope power ratio. 125

PRF Pulse repetition frequency. xvii, 54–57, 61, 81, 104, 110–112

$PSLR$ Peak to sidelobe level ratio. 124

P Number of point scatterers composing a complex target. xxxviii, 141, 143, 147, 149, 150, 158

Q_g Number of genes per chromosome in GA based techniques. 129, 130

R_0 Range of the direct path between the radar and the target, in metres at time t=0. 63, 67, 72, 77, 97, 109

R_l Range of the direct path between the radar and Target l, in metres. 88

$R_{\mathbf{corr}}$ Autocorrelation function, in the continuous or discrete form. 124

$R_{\mathbf{min}}$ Minimum range without eclipsing, in metres. 70, 122

$R_{\mathbf{ua}}$ Unambiguous range according to pulsed waveform theory, in metres. 70, 89, 110, 151, 152

$R_{\mathbf{win\ start}}$ Starting range of the unambiguous window, in metres. 151, 152

$R_{\mathbf{win\ stop}}$ Stopping range of the unambiguous window, in metres. 151, 152

R Range of the direct path between the radar and the target, in metres. xxxiv, 32, 61, 63, 78, 81, 82, 88, 141, 147, 149, 150, 156, 158

$SNR_{\mathbf{in}}$ SNR at the input of the processing. 110, 111

$SNR_{\mathbf{out}}$ SNR at the output of the processing. 110

S_1 OFDM spectrum after optimising the frequency weights for detection. 142

$S_{\mathbf{b}}$ Spectrum of a signal at baseband. As opposed to S it characterises a signal in the receiver. 149, 156

S_{nn} One-sided noise power spectral density. 139, 140

S_{opt} OFDM spectrum after optimising the frequency weights for detection and the phase codes for minimum PMEPR. 142

S An arbitrary signal in the frequency domain. It can be a continuous or discrete signal at baseband or at RF. xxxii, 138–141, 149, 150, 155, 197–200

T_r PRI, in seconds. 54, 55, 61, 63, 66–68, 70, 72–75, 78, 80–82, 86–89, 91, 94, 104, 105, 108–113

$T_{\mathbf{co}}$ Duration of the comb signal for the sample-and-hold operation, in seconds. 33

V_l Same as V, for Target l. 87, 88, 91

$V_{\mathbf{MF}}$ Output of the matched filter in the frequency domain. 138

V Target range rate as seen from the radar, in metres per second. xxxii, 15, 63, 104, 108, 109

ΔR_t Target range extent, in metres. 121, 151, 152

$\Delta R_{0,l}$ Difference between the range corresponding to time p_0 and R_{l0}, in metres. 96

ΔR Range cell extent, in metres. 89, 96, 97, 111, 112, 115, 121

$\Delta\phi$ Phase excursion resulting from the echoes' migration on the first non zero subcarrier, in radians. 70

$\Delta\tau_0$ $\Delta\tau_m$ for the first echo (convention m=0). xxxii, 66, 202, 203

$\Delta\tau_m$ Time difference in seconds between the first intercepted gate and the beginning of Echo m. xxxii, xxxiii, 67, 72–74, 201–203

$\Delta\tau_{0,l}$ Same as $\Delta\tau_0$ specifically for Target l. 96

$\Delta\tau_{m,l}$ Same as $\Delta\tau_m$ specifically for Target l. 91, 92, 94, 96, 99

$\Delta\theta$ Resolution of an angle between 0 and 2π, in radians. 129

Δf Spacing in Hertz between two consecutive subcarriers in an OFDM symbol. xxx, xxxix, xl, 3, 25, 28, 30–32, 51, 52, 54, 56–60, 64, 67, 69, 70, 72–75, 78, 86, 87, 89, 91, 94–97, 99–101, 103–107, 111–113, 115, 122, 123, 140, 150, 154, 155, 176, 201–203

α_0 Complex coefficient resulting from mixing down the echo . xxxv, 66, 68, 69, 72, 75

α_R Range margin coefficient, in metres. 121

$\alpha_{\mathbf{th}}$ Threshold coefficient used to generate masks $\mathbf{m_l}$. 175

$\alpha_{m,l}$ Complex coefficient resulting from mixing down echo issued by Pulse m and Target l . xxxv, 90–93, 99

α Coefficient of the scattering center, which takes discrete values within $\{-1, -1/2, 0, 1/2, 1\}$. xxxvi, 9, 17, 18, 147–149, 151, 156, 158–162

$\beta_{\mathbf{tol}}$ Coefficient used in the calculation of the ambiguity function of an OFDM pulse (for assessing Doppler tolerance). 59

β n^{th} root of unity used in IDFT and DFT operations. 66, 67

$\check{\mathbf{c}}_{-1}$ Decoding vector extended in size. 94, 95, 104

χ Ambiguity function. xviii, 58–60

δR Range resolution in metres. 32, 33, 61, 70, 81, 97, 103, 105, 109, 110, 173

δV Range rate resolution, in metres per second. 105

δf_D Doppler resolution in Hertz. 61, 70, 81, 82

δt Time resolution in seconds. 32

δv_r Radial velocity resolution, in metres per second. 70, 109, 110

$\boldsymbol{R}$ Vector of ranges R. 148, 149

ϵ Parameter used in the generation of the masks $\mathbf{m_l}$. 175

$\eta_{\mathbf{tol}}$ Coefficient used in the calculation of the ambiguity function of an OFDM pulse (for assessing Doppler tolerance), in seconds. 59

$\eta_{k,m}$ Complex number accounting for the phase shift due to Doppler at the start of Echo m and Symbol k. It is used to derive the received signal closed form expression. 66

$\eta_{m,l}$ Complex number accounting for the phase shift due to Doppler between two consecutive samples at baseband for Echo m and Target l. 91

η Complex number accounting for the phase shift due to Doppler between two consecutive samples at baseband (with critical sampling). 66, 67

γ_m Complex number accounting for the phase shift on Subcarrier n=1 at the time of the first intercepted time gate as compared to the phase at the start of the pulse, for Pulse m . 66, 67, 69, 70

$\gamma_{m,l}$ Complex number accounting for the phase shift on Subcarrier n=1 at the time of the first intercepted time gate as compared to the phase at the start of the pulse, for Pulse m and Target l. 91, 93

κ_0 Complex coefficient accounting for the phase shift inferred by Doppler modulation between the beginning of the first echo and the first intercepted time gate. It is used to derive the received signal closed form expression. xxxv, 66, 68, 69, 72, 75

$\kappa_{m,l}$ Complex coefficient accounting for the phase shift inferred by Doppler modulation between the beginning of the echo, issued by Pulse m and Target l, and the first intercepted time gate. It is used to derive the received signal closed form expression. xxxv, 90–92, 99

λ Wavelength of the propagating electro-magnetic wave, in metres. 12

$\mathbf{A_m}$ Matrix formed by the phase codes. Its column vector k comprises all N phase codes corresponding to Symbol k and Pulse m arranged in descending order from subcarrier N-1 to 0. 68–70, 73, 93

$\mathbf{B_{k,m,l}}$ Output vector resulting from applying a DFT upon $\mathbf{s_{bk,m,l}}$ when the constant phase terms ς_l, $\alpha_{m,l}$ and $\kappa_{m,l}$ are ignored. 99, 201

$\mathbf{B_{k,m}}$ Output vector resulting from applying a DFT upon $\mathbf{s_{bk,m}}$ when the constant phase terms ς, α_0 and κ_0 are ignored. xxxvii, 72–74, 201

$\mathbf{D_{k,m}}$ Diagonal matrix of the phase codes corresponding to all N subcarriers in Pulse m and Symbol k. It is used to derive the received signal closed form expression . 66, 68, 90–92

$\mathbf{F^{-1}}$ IDFT matrix. 66–68, 90, 92, 96

$\mathbf{F}$ DFT matrix. 92

$\mathbf{I}$ The identity matrix. 92

$\mathbf{\Delta_m}$ Matrix resulting from stacking all K column vectors $\delta_{\mathbf{k,m,l}}$. 93

$\mathbf{\Delta_m}$ Simplified version of the diagonal matrix $\mathbf{\Delta_{k,m}}$. It is used to derive the received signal closed form expression . 68

$\mathbf{\Delta_{k,m,l}}$ Same as $\mathbf{\Delta_{k,m}}$ for Target l. 90–92

$\mathbf{\Delta_{k,m}}$ Diagonal matrix of complex numbers to account for the phase shift due to Doppler in Pulse m, Symbol k. xxxv, 66, 68

$\mathbf{\Delta h_{l,ll}}$ Difference reflectivity spectrum using $\mathbf{h_{lnorm}}$ for two different Targets, l and ll . 175

$\mathbf{\Gamma_m}$ Diagonal matrix of complex numbers accounting for the phase shift on each subcarrier at the time of the first intercepted time gate as compared to the phase at the start of the pulse, for Pulse m . 66, 68

$\mathbf{\Gamma_{m,l}}$ Diagonal matrix of complex numbers accounting for the phase shift on each subcarrier at the time of the first intercepted time gate as compared to the phase at the start of the symbol, for Pulse m and Target l . 90–92

$\mathbf{\Lambda}$ Matrix preceding the final 2D-DFT step in our *frequency domain processing*. xxxvi, xl, 68–70, 75, 77, 78, 80

$\mathbf{\Theta_m}$ Matrix composed by the K column vectors $\delta_{\mathbf{k,m}}$. 68, 69, 201

α Vector of coefficients α. 148, 149

$\bar{\mathbf{h}}_\mathbf{l}$ Mean reflectivity spectrum of Target l in vector format . xxxvii, 175

$\breve{\mathbf{d}}_\mathbf{l}$ Vector created after rearranging $\breve{\mathbf{d}}_{\mathbf{m,l}}$ while making use of the new variable ξ. xxxvii, 95–97, 99, 103

$\breve{\mathbf{d}}_{\mathbf{m,l}}$ Vector created after rearranging $\tilde{\mathbf{d}}_{\mathbf{m,l}}$ so that the samples represent carrier frequencies that would follow a linear progression. xxxvi, 94, 95

$\delta_{\mathbf{k,m,l}}$ Output vector resulting from applying a DFT on $\mathbf{s}_{\mathbf{bk,m,l}}$. xxxv, 92, 93

$\delta_{\mathbf{k,m}}$ Output vector resulting from applying a DFT on $\mathbf{s}_{\mathbf{bk,m}}$. xxxvi, xxxvii, 68, 73, 74, 201

$\tilde{\mathbf{d}}_\mathbf{m}$ Vector used to generate matrix $\mathbf{\Lambda}$. xxxvi, 68, 69, 75, 201, 202

$\tilde{\mathbf{d}}_{\mathbf{m,l}}$ Same as $\tilde{\mathbf{d}}_\mathbf{m}$ for Target l . xxxvi, 93, 94

ς Vector of complex scattering coefficients ς. 148, 149

$\mathbf{a}$ Vector of phase codes. 138, 143, 177

$\mathbf{b_m}[n]$ Autocorrelation peak for the sequence of phase codes on Subcarrier n in Pulse m. 68, 69, 93

$\mathbf{c}_{-1}$ Decoding vector directly linked to $\mathbf{c}$. 94, 95, 102

$\mathbf{c}$ Randomisation vector introduced to code the frequency steps of the SFW when other than linear ordering is desired. xxxvi, 87, 94, 102

$\mathbf{d_m}$ Vector created in an intermediate step of the processing. m is the pulse index. xxxvi, 68, 75

$\mathbf{d}_{\mathbf{m,l}}$ Same as $\mathbf{d}_\mathbf{m}$ for Target l. 93

$\mathbf{g_m}$ Vector involved in the calculation of $\mathbf{B_{k,m}}$ in the special case when IS are used for the phase codes. 73–76

$\mathbf{h_f}$ Deterministic target reflectivity spectrum in vector format. f stands for time domain. 150, 172

$\mathbf{h_{lnorm}}$ Normalised $\bar{\mathbf{h}}_\mathbf{l}$. xxxv, 175

$\mathbf{h_t}$ Deterministic target impulse response in vector format. t stands for time domain. 150, 151, 155, 172

$\mathbf{h_{corr}}$ Vector of corrective terms used in the HRR technique to create a bank of range migration filters. 103, 104

$\mathbf{m_{lnorm}}$ Normalised mask corresponding to Target l. 175, 177, 178

$\mathbf{m_l}$ Mask corresponding to Target l. xxxiii, xxxiv, 175

$\mathbf{n}$ Vector of noise samples. 157

$\mathbf{r}$ Vector resulting from applying an IDFT on $\breve{\mathbf{d}}_\mathbf{l}$. 96

$\mathbf{s_m}$ Vector involved in the calculation of $\delta_{\mathbf{k,m}}$ in the case of the complete solution. 74, 75

$\mathbf{s}$ An arbitrary vector. 140, 154–158, 170, 179

$\mathbf{w}$ Vector of frequency weights. It is used to derive the received signal closed form expression. 28, 66, 68, 90–92, 138–140, 177

$\mathbf{z_{nnorm}}$ Normalised vector $\mathbf{z_n}$. 177–179

$\mathbf{z_n}$ Vector of complex numbers z_n for target n. xxxvii, 177

$\mathbf{s_{bk,m,l}}$ Same as $\mathbf{s_{bk,m}}$, specifically for target l. xxxv, xxxvi, 90, 92, 99

$\mathbf{s_{bk,m}}$ Closed form expression for Symbol k of received Echo m. xxxv–xxxvii, 66, 68, 72, 79

$\mu_{k,m,l}$ Complex coefficient accounting for the phase shift due to Doppler on Echo m, Symbol k and Target l. 91

σ_{std} Standard deviation variable . 149, 172, 173, 183, 185–188

σ RCS of an object when observed by the radar, in square metres . 12, 141

τ_0 τ_m, for the first pulse (convention m=0). 64–66, 202, 203

τ_l Same as τ, specifically for target l. 88

τ_m Two ways propagation time delay corresponding to pulse m, in seconds. xxxviii, 67

$\tau_{0,l}$ $\tau_{m,l}$, for the first pulse (convention m=0). 90, 96

$\tau_{m,l}$ Two ways propagation time delay corresponding to Pulse m and Target l, in seconds. xxxviii, 89, 91–94, 96

τ Two ways propagation time delay, in seconds. xviii, xxxviii, 32, 52, 58, 59, 63, 64, 88, 94, 95, 124, 150

$\mathbf{L_{PCdB}}$ Compression loss due to Doppler in dB. This is a positive quantity. xlii, 59

$\mathbf{Pcc}_i$ Probability of correct classification for class i. 158, 160

$\mathbf{Pfa}_i$ Probability of false alarm for class i. 183, 184

$\mathbf{Pmc}_i$ Probability of misclassification for class i. 183, 184

θ_p Model parameter vector used to characterise scattering Centre p. 147

θ Model parameter vector used to characterise P scattering centres. 147–149

$\tilde{v}_{r_{\mathbf{ua}}}$ Partial unambiguous radial velocity in the HRR processing, in metres per second. 104, 113

$\varepsilon_{\mathbf{tol}}$ Coefficient used in the calculation of the ambiguity function of an OFDM pulse (for assessing Doppler tolerance). 59

ε Negligible quantity. 38

ϱ_m Complex number accounting for the phase shift due to Doppler at the start of Echo m. 68, 69

ς_l Same as ς for point Scatterer l. xxxv, 88, 90, 92–96, 99

ς_s Target reflectivity spectrum. It can be a continuous or discrete signal at baseband or at RF. xxix, 138–141

$\varsigma_{\mathbf{norm}}$ Normalised target reflectivity spectrum. It is used in discrete form. 141

ς Complex scattering coefficient of the point scatterer, in square metres. xxxv, xxxvi, xxxix, 63, 66, 68, 69, 72, 75, 97, 141, 147, 149, 156, 158

ξ Variable used in the HRR technique. xxxvi, 95, 96, 99, 104, 202, 203

a_n Phase code applied on Subcarrier n when only one symbol is considered. xlii, 141, 177

a_s Radius in metres of a PEC sphere. 12, 170, 171

$a_{k,m}$ Phase code applied on Symbol k, Pulse m. This notation refers to the case of identical sequences where all N subcarriers in the pulse are attributed the same phase code. 73–75

$a_{n,k,m}$ Phase code applied on Subcarrier n, Symbol k, Pulse m. 64, 69, 73, 86, 93, 114

$a_{n,k}$ Phase code applied on Subcarrier n and Symbol k. xl, 59, 123, 127, 130, 132

a Phase code. 28, 29, 59, 66, 72, 91, 99, 142, 177, 201, 202

c Speed of light, in metres per second. 32, 61, 63, 64, 67, 69, 70, 88, 89, 91, 96, 97, 104, 105, 109–113, 121, 122, 141, 147, 149–151, 154, 155, 173

df Interval of frequencies between two samples in the frequency domain, not to confuse with Δf. 150–152

e_n Complex, zero mean, independent and identically distributed (iid), Gaussian random variables. 149

f_0 Carrier frequency, in Hertz. 19, 25, 28, 31, 33, 50, 63, 64, 66, 67, 70, 110, 138–140, 147, 149, 150, 156, 161, 162, 188, 198, 202, 203

f_D True Doppler shift in monostatic configuration, in Hertz. xviii, xxx, xl, 14, 52, 53, 55, 58–61, 63, 64, 66–68, 71–75, 77, 78, 80–82, 100, 101, 113, 203

f_m Carrier frequency of Pulse m used in the HRR technique, in Hertz. 86–88, 91, 111, 114

f_n Discrete frequency samples, in Hertz. 149

f_s Sample rate in Hertz or samples per second. 25, 39, 51, 70, 89, 90, 110, 120, 125, 126, 157, 198

f Continuous frequency as an independent parameter of a function, in Hertz. 9, 78, 138–142, 147, 149, 150, 155, 156, 171, 197–200

g Unitary processing gain. 62, 79, 80

h_t Deterministic target impulse response. t stands for time domain. 149, 150, 168

h Function of the three variables f_D, K and Δf involved in the derivation of matrix $\mathbf{\Lambda}$. 75

j Imaginary unit. 147, 149, 199

k_w Wave number, in radians per metre. 12

p_0 First time gate intercepted by the received echo, in seconds. xxxii, 65, 67, 69, 70, 89–93, 95, 96

q_g Number of genes used to code one phase code $a_{n,k}$. 129

$q_{\mathbf{peak}}$ Index of the peak in the HRR profile. 96

r_k Window function scaled to the symbol duration t_b. 64, 86, 123

r_s Radius of the PEC sphere, in metres. 172

s_r Received signal at RF before down conversion is applied. 88

s_{b2} Second contribution of the received signal at baseband. 64

s An arbitrary signal in the time domain. It can be a continuous or discrete signal at baseband or at RF. 28, 58, 63, 86, 88, 123–125, 139, 140, 149, 150, 168, 199

t_b Duration of an OFDM symbol or bit, in seconds. xl, 3, 25, 32, 54, 59, 64–67, 70, 72–75, 86, 89, 95, 99, 102, 122–125, 176

t_p OFDM pulse duration, in seconds. 53–55, 61, 70, 110–112, 122, 154

t_s Sampling period, in seconds. 65, 89, 90, 93, 95, 121, 125

t Continuous time as an independent parameter of a function, in seconds. 58, 63, 64, 86, 88, 90, 123, 124, 139, 149, 150, 168, 199

u_m m^{th} transmitted OFDM pulse. 63, 64, 86, 88

v_l Lower bound for the weight value (dimensionless coefficient). 177, 179, 182

v_r Target radial velocity as seen from the radar, in metres per second. 61, 63, 64, 67, 78, 80–82, 89, 100, 104

v_u Upper bound for the weight value (dimensionless coefficient). 177, 179

$v_{r_{\mathbf{ua}}}$ Unambiguous radial velocity according to pulsed waveform theory, in metres per second. 110, 112, 113

w Frequency weight. xxix, xlii, 28, 31, 59, 64, 66, 68, 72, 80, 86, 91, 93, 99, 123, 127, 128, 140, 142, 177, 201, 202

x_s x-axis for the PEC sphere centre, in metres. 170, 172

x Compressed pulse at baseband. 149, 150

y_s y-axis for the PEC sphere centre, in metres. 170, 172

$y_{\mathbf{b}}$ In comparison to y, it is the compound signal in the receiver at baseband. xlii, 150

y Compound signal in the receiver at RF comprising the received pulse and AWGN. xli, 149

z_n Complex number with magnitude w_n and argument a_n. xxxvii, 177

R_{l0} Range of the direct path between the radar and Target l, in metres at time t=0. xxxii, 88, 91, 96

R_{p0} Range corresponding to the first time gate intercepted by the received echo, in metres. 96, 97

SNR_{t0} SNR at the time instant t_0. 139, 140

$\Delta R_{\mathbf{min}}$ Minimum separation in range between two point scatterers, in metres. 151, 152

$\hat{f}_{D\mathbf{coarse}}$ Coarse estimate of Doppler resulting from differentiating between two range estimates, in Hertz. 80, 81

$\mathbf{y_b}$ Compound signal in the receiver at baseband y_b in vector format. 157, 158

$f_{D\mathbf{1dB}}$ Doppler value corresponding to the 1 dB compression loss as calculated by $\mathrm{L_{PCdB}}$, in Hertz. 60, 81

$f_{D\mathbf{amb}}$ Doppler shift folded within the non ambiguous window, in monostatic configuration, in Hertz. 14, 72, 77

$f_{Dm,l}$ True Doppler shift in monostatic configuration corresponding to Pulse m and Target l for use in the HRR technique, in Hertz. 88, 91, 99

f_{sbb} Sample rate of the baseband signal, in Hertz or samples per second. It can be the critical sampling rate or anything higher if oversampling is present. 26

s_{b1m} First contribution of the received signal at baseband for transmitted Pulse m. 63, 64

s_{bm} Received signal at baseband for transmitted Pulse m. 64, 88

Pcc Overall probability of correct classification. 158, 160, 161, 183, 184

Chapter 1

Introduction

As Darwin noted, "it is not the strongest or the most intelligent who will survive but those who can best manage change." Adaptation is a necessity. It is true for bacteria, dolphins, bats, zebras as well as human beings. For the latter, sight, hearing, taste, smell, and touch are the five traditionally recognised senses.

Sight and hearing provide most of the vital information, since they can be effective over long distances as compared to taste, smell and touch. On top, they are similar for they both sense a remote phenomenon by means of propagating waves. This is true up to a certain extent though, since many perturbations may affect the sensing process. For instance, our vision is poor when fog obstructs the line of sight and null in the dark. In these scenarios where our natural sensors fail, supplementary resources are required. Radar, an acronym for RAdio Detection And Ranging, is an example of the mankind's response to this necessity of adaptation. Like sight, radar systems rely on the propagating properties of electromagnetic waves to detect and locate objects.

Since Hülsmeyer's historical experiment in 1904 [1] till now, capabilities of radar systems have constantly evolved from its pioneer use for detection and ranging; historical references are provided in [2, chap. 1.6] and [3] for further reading. Able to operate at night and in difficult environmental conditions, today's radar systems are ubiquitous and on-board all sorts of vehicles (on the ground, in the

air and in space), in typical applications i.e. speed control, air traffic control, airborne and space-borne missions, military applications and remote sensing. Research for medical radar applications is also progressing well for breast cancer detection and tumour localisation.

Scenes increasingly more complex are being monitored and solutions to a wider scope of scenarios are needed. Clearly, only a limited number of outcomes can be generated from the radar raw measurements. Standard outcomes include, information about the presence of a target, its range, position (in the three-dimensional, 3D, space), radial velocity and high range resolution profile (HRRP). More advanced outcomes include but are not limited to the targets' class, identity.

In the early developments, the stakes were to design favourable waveforms and signal processing techniques to detect the presence of a target, measure its range, its radial velocity and localise its position. In turn, further knowledge over the target was obtained through a clever use of this information, viz., position and radial velocity can be used to distinguish a missile from an aircraft. Alternatively, HRRPs can discriminate between a small boat and a big ship. Beyond these considerations relating to the classification function, conventional methods to characterise or even identify the target have been to compare the obtained HRRP with a library of HRRPs and find the best match [4]. Recently, more sophisticated techniques like the inverse synthetic aperture radar (ISAR) have emerged [5], which can produce high resolution two-dimension (2D) images and permit better target characterisation.

When introducing a new type of signal for radar, one is expected to show that either of these standard or advanced outcomes are obtained at a lesser effort than what the current state-of-the art systems afford. Of course, anyone in the field is aware that there, again, is *no free lunch*. Throughout this dissertation we endeavour evoking the trade-offs for each contribution.

In this chapter, we run through the assets of OFDM signals in radar and reflect on the origin of OFDM radar. Next, we elaborate on the scope of our research and present in detail our contributions in this field.

1.1 Motivation for OFDM radar

In radar, "multicarrier" has often been preferred to "orthogonal frequency division multiplexing" (OFDM). We explain it from the fact that in communication, OFDM refers to the method of encoding digital data on multiple carrier frequencies. It does not account for the features of the signal unlike linear frequency modulation (LFM). In this dissertation, we refer interchangeably to OFDM or multicarrier unless mentioned otherwise.

Along with providing improved range resolution [6] and spectral efficiency [7], the OFDM signal has two other enticing properties, viz., multiple phase references and frequency diversity. The multiple frequencies provide phase references that can be exploited to assess the migration in range from one echo to the next, which can in turn yield the target radial velocity. Frequency diversity is attractive for it can be used to classify a target as one knows that target responses strongly depend on the frequency content of the transmitted signal [8].

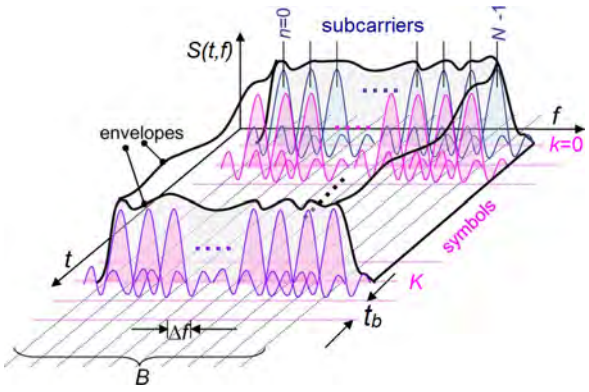

Figure 1.1: Time-Frequency scheme of a multicarrier signal [9]

Fig. 1.1 illustrates the time-frequency scheme of the multicarrier signal. The orthogonality property is of utmost importance in communication as it guarantees that the information conveyed by each subcarrier is recovered. Mathematically, it follows $t_b = k/\Delta f$ where Δf corresponds to the spacing between two consecutive subcarriers, t_b is the time duration of an OFDM symbol or bit and k is a positive integer usually equal to 1. Another way to characterise this property is to realise that the spectrum of each subcarrier has a null at the centre frequencies

of all other subcarriers in the system, as shown in Fig. 1.1. Hence, if one wants to design a 1 μs pulse, the subcarrier spacing will have to be equal or larger than 1 MHz.

As the understanding over OFDM radar is maturing, it is believed to be the way forward for future radar systems [10, 11]. The following motivations are often put forward by researchers in the field:

- simple signal generation (it requires to apply an inverse fast Fourier transform, IFFT algorithm on the "communication" symbols),
- the coded signal can contain information,
- consecutive pulses can be made different,
- compression in time and frequency supports high compression gains,
- all processing is solely digital (can use fast Fourier transform, FFT and IFFT algorithms).

In a nutshell, OFDM not only has appealing radar features but being a communication standard [12], many hardware-software developments may nourish its upgrowth in radar.

1.2 Origin of OFDM radar

Although what marks the beginning of OFDM radar is questionable and subject to the authors's sources, it can be argued that research in the realm of radar network, including those applications for short range surveillance (harbour, border control, traffic monitoring, etc.) and car-to-car collision avoidance have served as catalyst agents to move beyond the pioneer analyses from Levanon et al. [13]. In both cases, the main argument was to realise that the radar signal could convey information, such that both sensing and communication tasks would happen with the same infrastructure. This substantial simplification of the system architecture would in turn benefit and justify the concept of radar network.

In what can be deemed to be a seminal paper, published in 2006 [14], Genderen *et al.*, from the University of Delft, looked into the communication link that would result from transmitting OFDM pulses via directive scanning antennas in terms of the throughput rate and more specifically the feasibility to transfer a decent number of radar detections from one station to the other [14]. Several other papers published by the same research group inspected further the communication aspects [15, 16] while other works approached the waveform design [17] and the radar processing, respectively in the framework of pulsed [18, 19] and continuous[20, 21] OFDM waveforms. A thorough summary of the main contributions from the group both in term of radar and communication have been compiled in [22, 23, 24], published in 2009 and 2010.

Almost in parallel, a group from the Karlsruhe Institute of Technology was working on similar concepts in the background of intelligent transportation applications requiring both communication links to other vehicles and active environment sensing functions. The results were published in a series of papers [25, 26, 27, 28, 29, 30] between 2009 and 2010. A detailed and comprehensive summary of their early contributions was compiled in a paper published in 2011 [9].

Despite the similarities at the conceptual level, it is worth mentioning that both research imply fundamentally distinct underlying assumptions. Essentially, in automotive radar, the largest distance considered for the detection problem may stretch up to few hundred metres, with expected radial velocities limited to the speed of commercial cars. Most critical problems involve the risk of shadowing (i.e. caused by large trucks) and the presence of multipath and interference as a result of the many reflectors and users. In the case of short range radar network, larger distances must be covered. Beside, the variety in terms of targets of interest infer that more heterogeneous radar cross sections and higher radial velocities including those of airplanes and fighters shall be handled.

In summary, most efforts devoted to developing OFDM radar for RadCom applications have focused on utilising continuous OFDM transmissions. This, in turn, implies the use of two antennas, one on transmit and one on receipt.

1.3 Problem Description

Moving away from RadCom dedicated applications, a legitimate thought that follows Levanon *et al.* early ideas [31] would be to employ OFDM signaling in existing pulsed waveform systems, if it can be demonstrated that OFDM effectively adds value. The merit of this approach is to reuse the system architecture and "only" plug in a new signal at baseband. Despite the amount of work realised in the area of OFDM radar in the past 15 years, which we review more thoroughly in Chapter 2, we have identified the lack of comprehensive and consistent studies tackling the main constituents of a pulsed OFDM radar whose first and foremost objective would be to outperform traditional pulse Doppler radar in the acquisition of radar data.

1.3.1 Research Hypothesis

The research hypothesis for this thesis is therefore:
The unique time-frequency structure of the pulses in OFDM radar offers advantageous capabilities over traditional pulsed waveforms.

The research questions associated with this hypothesis relate to the acquisition of the standard and advanced outcomes evoked previously. They are formulated as follows:

- *Can the OFDM structure be exploited to resolve range and Doppler unambiguously in one train of pulses using the model of a moving point scatterer?* If that is the case, OFDM pulses can be used to circumvent the constraint of transmitting multiple trains of pulses with distinct pulse repetition intervals. In addition to reducing the complexity of the waveform scheduling, this solution would contribute to save some of the radar time budget.
- *Can we use the OFDM pulse structure in the concept of a stepped-frequency waveform (SFW) and what are the benefits, if any?* If that is the case, we can exploit existing stepped-frequency systems and plug in OFDM pulses

instead. This approach could improve the low probability of detection of the system if the OFDM pulses in the train are all different. Besides, if needed (i.e. battlefield scenario), the pulses can convey information.

- *How can the OFDM pulse be designed to cope best with the technical constraints of constant envelope and minimum autocorrelation sidelobe level?* The main drawback of OFDM signals is the variation of their envelope, which may turn in saturation the amplifiers and cause distortion of the signal. If we find a simple method to reduce this variation by exploiting the parameters at hand, without affecting radar measurements, then we are clearing off a significant con.

- *Can the OFDM structure be exploited to characterise better targets composed of canonical scatterers?* Thus far, characterisation of canonical scatterers would involve long measurements to cover the wide bandwidth with narrowband transmissions and computationally intensive algorithms. If we can conceive a method with instantaneous wideband transmissions, a significant performance improvement can be obtained .

- *Can the OFDM structure be exploited to enhance the target classification function of the radar?* If one can exploit the frequency diversity to distinguish between targets then clearly, OFDM signalling is the favourite candidate to become the waveform.

1.3.2 Scope of research

Although the concepts of pulse compression and Doppler processing have been extensively tackled for traditional radar waveforms (unmodulated pulses, chirps, etc.) [32], existing analyses regarding appropriate range-Doppler processing for pulsed OFDM waveforms are sketchy and incomplete [33]. Hence, we propose to establish a comprehensive processing framework to estimate the parameters of interest, viz., range and Doppler in the context of a monostatic radar. Two methods are considered. The first method operates on the time domain signal

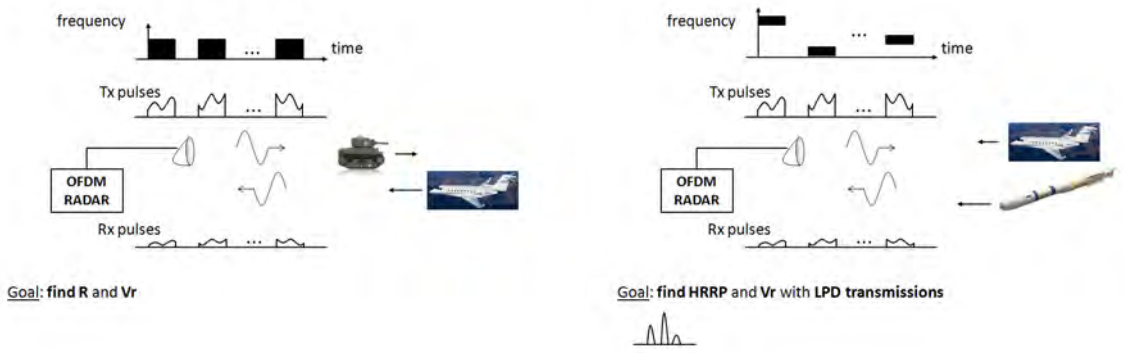

(a) Research question 1

(b) Research question 2

Figure 1.2: Sketches related to research question 1 and 2

while the second one runs in the frequency domain. We explain what precautions need to be accounted for and we stress what consequences the use of one or the other infers on the design of the OFDM signal. Both cases of slow and fast moving targets are inspected. As shown in Fig. 1.2(a) our approach considers a train of OFDM pulses where each pulse covers the same bandwidth.

We develop a comparable analysis for the case of a stepped-frequency waveform that can retrieve HRRPs and radial velocities of point targets. Existing studies are also sketchy and incomplete [34]. Besides, to improve further the low probability of detection (LPD) feature of the waveform, we suggest, as hinted in Fig. 1.2(b), adding an agility pattern other than linear. Ultimately we investigate the benefits of using OFDM pulses.

The prominence of the challenge the fluctuating OFDM time domain envelope creates is evident in the volume of literature and the variety of methods developed to remedy it. In [35] the constant envelope is obtained at the cost of performance degradation and increased complexity in the radar processing chain. In [36], the technique used to reduce the fluctuation relies on the presence of all consecutive subcarriers and a degradation occurs as soon as few subcarriers are

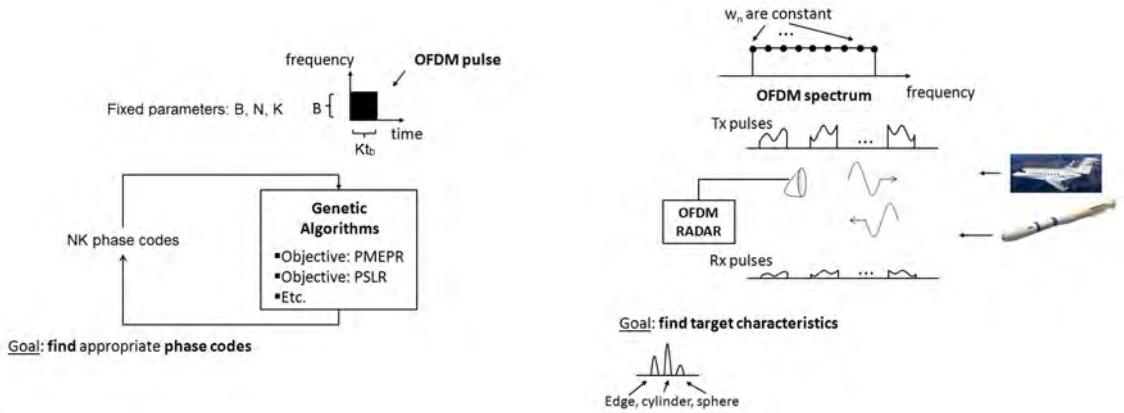

(a) Research question 3 (b) Research question 4

Figure 1.3: Sketches related to research question 3 and 4

missing. Hence, we choose to investigate the possibilities to employ genetic algorithm (GA) based methods to optimise the PMEPR of OFDM pulses without degrading the radar properties. We include a multi-objective approach for designs with multiple constraints. We apply the procedure given in Fig. 1.3(a), viz., after fixing the pulse frame, our optimisation phase consists in finding optimal sets of phase codes for the particular objective(s). Minimum peak-to-sidelobe level ratio (PSLR) and minimum integrated sidelobe level ratio (ISLR) are such objectives.

Except the works from Paichard and Sen [37, 38], little effort has been spent to investigate the benefits of OFDM radar for target characterisation and classification. The concept of matched-illumination to enhance the detection of targets or improve the classification function has been a popular topic in radar since the seminal paper from Bell in 1993 [39]. It has been pointed out in [22, 40] (2010) to be a relevant subject for future research in OFDM radar. In particular nothing has been published concerning the possibility to exploit OFDM signals to appraise the canonical scatterers composing a target. Known to have predictable frequency dependencies in the form f^{α}, (α=-1,-1/2,0,1/2,1) our idea consists in transmitting flat spectra OFDM pulses to characterise those scatterers, viz.,

cylinder, sphere, edge, etc.. Knowledge regarding the scatterer type along with its position on the HRRP can be a valuable information to assess the type of target. As stated in Fig. 1.3(b) the flat spectrum is obtained by assigning the weights composing the pulse with the same value.

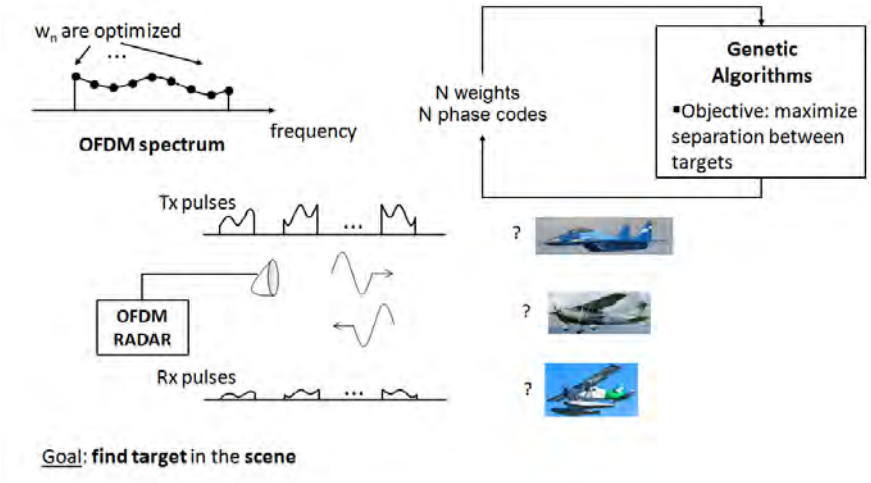

Figure 1.4: Sketch related to research question 5

Like in the above case, nothing was reported in the literature on the use of OFDM radar to improve the radar classification function. However, a number of contributions [41, 42] stressed the benefit of shaping the spectrum of the transmitted pulse for classification. OFDM being by nature generated in the frequency domain it seems to be a suitable candidate to move forward into this research. Not only we propose to use OFDM signals to improve the classification function but we investigate further the technique to simplify the state-of-the art processing. Our approach is summarised in Fig. 1.4. Provided that we come up with an objective function to optimise the separation index between the targets in the scene, the subcarrier weights and the phase codes are optimised accordingly by means of genetic algorithms.

1.3.3 Statement of Originality

The candidate believes that the following parts of this work constitute original contributions to the field of OFDM radar:

- The presentation of two alternative schemes to process a train of OFDM pulses and a performance analysis associated to each solution.
- The presentation of a stepped OFDM waveform-high range resolution processing technique to synthesize HRRPs, resolve the Doppler ambiguity, and a performance analysis associated to this technique.
- The use of genetic algorithm based methods, where the parameters are the phase codes of the OFDM signal, to control the OFDM pulse in terms of PMEPR, PSLR and/or ISLR.
- The use of flat spectra OFDM pulses to characterise canonical scatterers.
- The presentation of a radar technique combining genetic algorithm based pulse design and energy detector for target recognition.

Note that like the aforementioned applications which operate at distinct carrier frequencies (X-band, K band etc.), our concepts developed in the realm of OFDM radar are generic and not restricted to a particular frequency band as long as the underlying assumptions are valid. In the typical example of the perfectly conducting sphere, below a certain value for the wavelength (as compared to the sphere diameter), the sphere will behave like a point target (optical region). On the other hand, for larger values the RCS oscillates (resonance region) or varies linearly with respect to the frequency. A plot of the RCS normalised by the projected area of the sphere is given in Fig. 1.5.

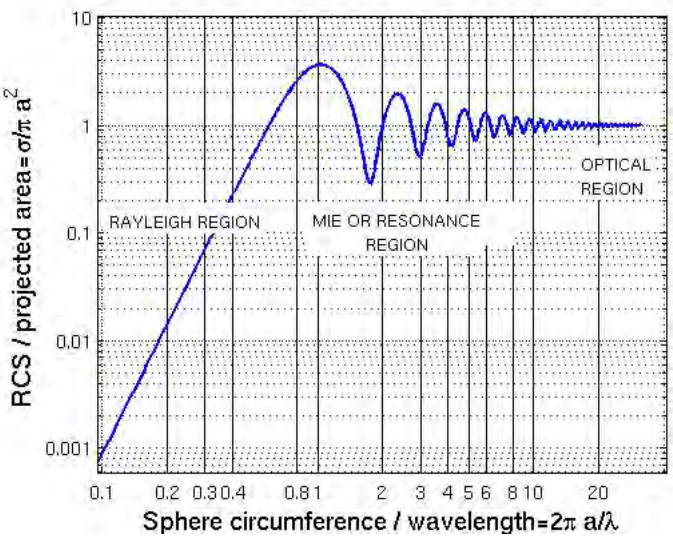

Figure 1.5: Monostatic RCS of a perfectly electrically conducting (PEC) sphere as a function of sphere circumference normalised to wavelength, $k_w a_s = 2\pi a_s/\lambda$ (calculated by Mie theory). In the low frequency Rayleigh scattering region where the circumference is less than the wavelength, the normalised RCS is proportional to ${a_s}^2(k_w a_s)^4$. In the high frequency optical region, $\sigma/(\pi {a_s}^2) \sim 1$.

1.4 Contributions

In this research, we produce a performance analysis on the aspect of target parameters' estimation, pulse design, target characterisation and classification with the intention to show that OFDM radar outperform state-of-the art radar systems on several key aspects. Throughout this work we put forward the versatility of the OFDM structure and exploit it to tailor the waveform to our needs. In the following, we summarise our contributions.

OFDM pulsed radar waveform and alternative processing methods

After discussing our model for the received echoes, we present two processing alternatives applicable to a train of OFDM pulses as from a radar prospective. The first solution operates on the time domain signal while the second solution processes the signal in the frequency domain. As such, the second technique is

subject to the problem of intersymbol interference (ISI), typical of OFDM, and requires prior knowledge upon the target position. In return, we show that it is possible to retrieve an estimate of the unambiguous Doppler frequency even for high radial velocities, far beyond the classic unambiguous Doppler value. We demonstrate that both solutions can be implemented by means of discrete Fourier transforms (DFT) and inverse discrete Fourier transforms (IDFT) operations, which make them efficient in real time. We finally prove that both achieve the same SNR gain. In Fig. 1.6(a) we illustrate the output of the first processing for a single slow moving point scatterer. The range axis is centred around the initial target position. The size of the range cell is inferred from the pulse bandwidth. Most sidelobes being in blue/light blue colour we infer from the plot that they fall below -25 dB. Beside, the Doppler sidelobes are only limited by the well-known Fourier sidelobes and thus can be made lower via the use of windowing. In Fig. 1.6(b), the outcome of the second solution shows that despite the distortion caused by the very high radial velocity, the peak position in the ambiguous window remains close to the true scatterer position (green point). Along with the range profiles available at no extra computational cost and used to derive a rough estimate of the radial velocity as shown in Fig. 1.7, the ambiguity in Doppler can be raised. Eventually, unlike the first solution built on the concept of correlation and thus dependant on the quality of the OFDM phases codes in terms of the low PSLR, the second solution involves a demodulation step such that the sidelobes in the final range Doppler image are Fourier based.

Stepped OFDM radar technique to resolve range and Doppler simultaneously

A novel wideband OFDM based waveform and the corresponding high range resolution processing is derived. We show by means of comparisons with standard wideband waveforms the benefits of this concept. Radial velocities can be retrieved unambiguously and high velocities can be handled at no extra computational effort since the range migration constraint is related to the small pulse

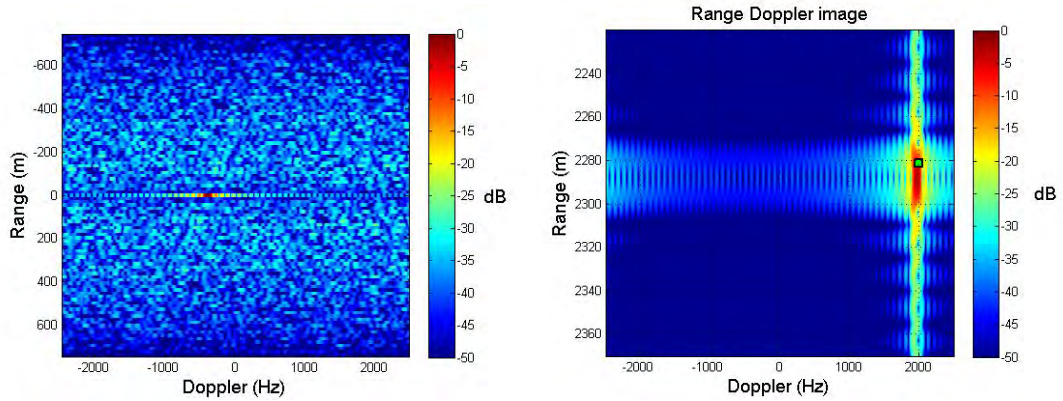

(a) First processing solution (b) Second processing solution

Figure 1.6: Range Doppler images resulting from our two alternative processing solutions in OFDM radar. In a) the target flees the radar and the corresponding Doppler is f_D=-400 Hz. In b) the fast fleeing target has a true Doppler frequency f_D=-73 kHz, which folds back at $f_{D\text{amb}}$=2 kHz. The colour scale corresponds to dB.

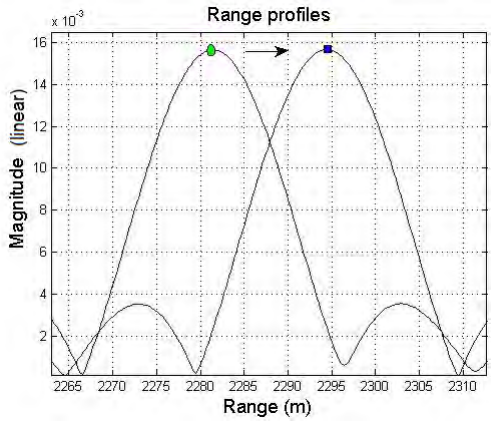

Figure 1.7: The range profiles obtained in the second processing solution enable finding a "rough" estimate of the true radial velocity, which along with the ambiguous estimate from Fig. 1.6(b) results in a refined unambiguous estimate.

bandwidth as opposed to the large synthetic bandwidth. In our analysis, we inspect the impact of Doppler modulation on the processing and give recommendations for improvement in terms of the OFDM parameters. We address the problem caused by a correlation artefact and recall the risk of ISI. Lastly, we show that our concept has inherent low LPD characteristics. In Fig. 1.8(a) an

example of the range-Doppler image resulting from the HRR processing is used to illustrate our contribution. The scatterer is observed repeatedly (6 times as we use 6 batches in the processing) at its true radial velocity, beyond the classical unambiguous radial velocity, ±75 m/s in that particular case. Beside, the use of OFDM pulses to synthesize the wide bandwidth offers an intermediate range resolution which can be exploited when the high resolution is not required. Fig. 1.8(b) shows the autocorrelation function of an OFDM pulse for two sets of phase codes as developed in Chapter 3. Again the use of DFTs and IDFTs make this HRR solution efficient in real time.

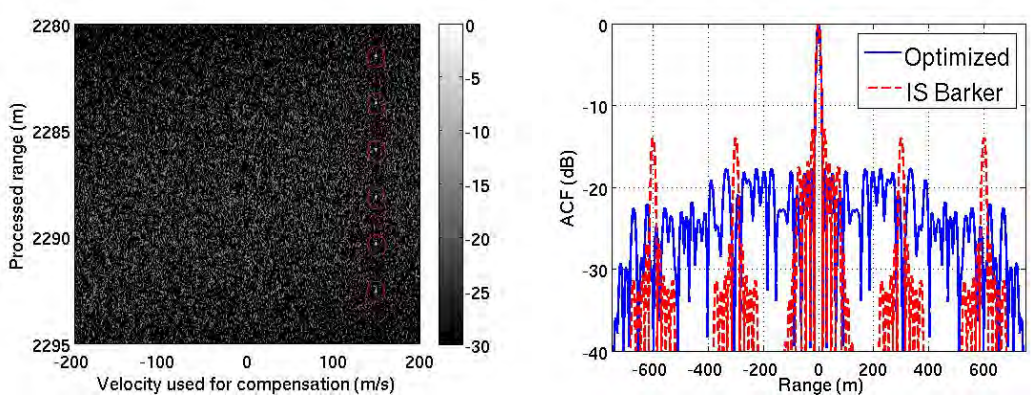

(a) HRR range and radial velocity image (b) OFDM pulse autocorrelation function

Figure 1.8: Outcome of the a) HRR processing with a bank of range migration filters to retrieve the scatterer radial velocity over 6 batches and b) autocorrelation function of an OFDM pulse when using an identical sequence length-5 Barker code or a set of phase codes found to minimise the PSLR. In a) the classical unambiguous velocity is ±75 m/s while the scatterer range rate is V=150 m/s.

Design of OFDM radar pulses using genetic algorithm based techniques

We use a GA optimisation based waveform design framework to improve the features of OFDM radar pulses. Our optimisation techniques focus on finding optimal phase code sequences for the OFDM signal. Several optimality crite-

ria are used since we work with two different radar processing solutions which call either for single or multiple-objective optimisations. When minimisation of the PMEPR single objective is tackled, we compare our findings with existing methods and emphasize on the merit of our approach when the OFDM spectrum is sparse. Figs. 1.9(a)-1.9(b) show how our GA solution equates and even outperforms robust coding methods like Newman, respectively for full or sparse spectrum coverage. Our analysis makes use of pulses with typical dimensions in terms of the number of subcarriers and the bandwidth. In the two-objective optimisation scenario, namely PMEPR and PSLR, we show that our approach based on the non-dominated sorting genetic algorithm-II (NSGA-II) provides design solutions with noticeable improvements as opposed to random sets of phase codes. Improvements as high as 7 dB and 4 dB respectively for the PSLR and PMEPR are observed in Fig. 1.10 when the pulse is composed of 25 subcarriers and 4 symbols. We motivate the sole use of the phase codes as the parameters in our optimisation procedure with a case study, where we show that the subcarrier weights can be saved for other radar related challenges such as enhanced detection.

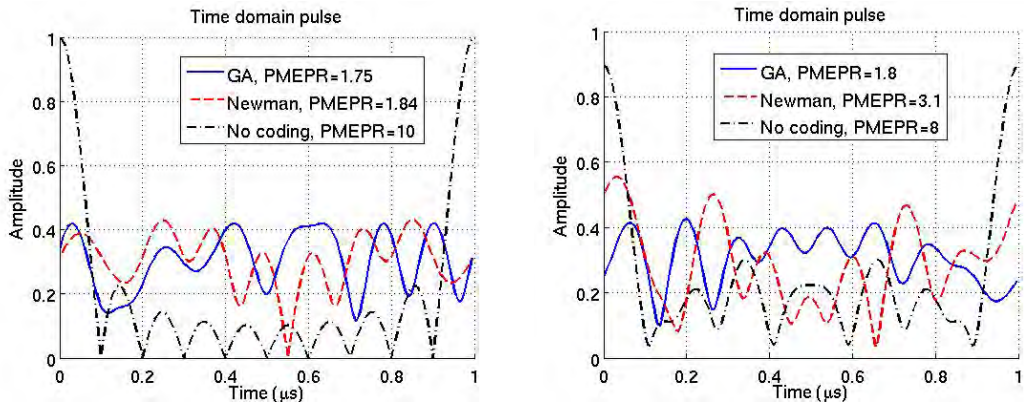

(a) Full band (b) 80% of the band

Figure 1.9: Amplitude of the time domain OFDM symbol for different coding solutions when a) all 10 subcarriers are used and b) only 8 subcarriers are used. In the case of sparsely populated bands, our GA solution outperforms the Newman approach.

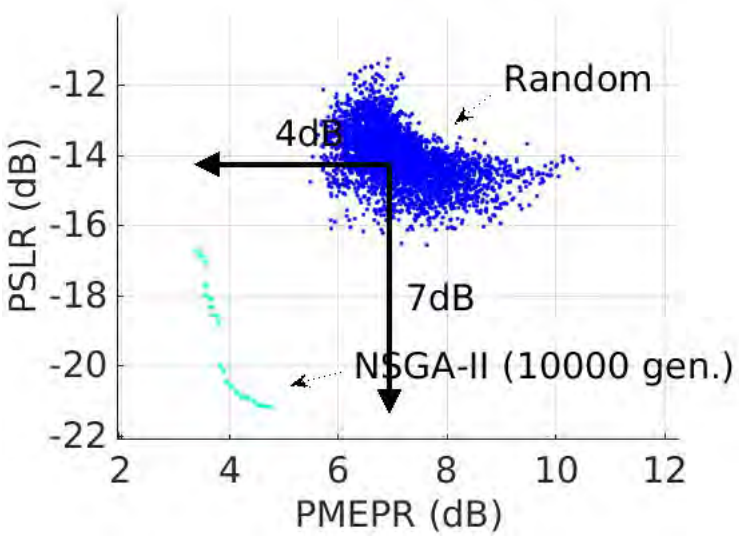

Figure 1.10: Comparison between random phases and phases resulting from the NSGA-II optimisation for PSLR and PMEPR.

OFDM phenomenology: recognition of canonical scatterers using flat spectra OFDM pulses

We present a novel approach to characterising scattering centres from their radar returns using specially designed waveforms. The widely accepted scattering model derived from the geometrical theory of diffraction (GTD) is considered. We show how the use of flat spectrum OFDM pulses can help discriminating between the various scattering mechanisms. The technique runs in two steps. The first step consists of designing pulses of appropriate length to mitigate the ISI when several scatterers compose the target. The second step is the processing itself. The spectrum of the received echo is calculated and the slope of this spectrum is estimated as shown in Figs. 1.11(a)-1.11(b) where either a 300 MHz or 1500 MHz bandwidth pulse is considered. We then relate our estimation to the most adequate value of α (1 in our example). α is a dimensionless coefficient that retains the geometry information. Eventually, we assess the sensibility of this approach with respect to additive white Gaussian noise (AWGN) in terms of the overall probability of correct classification. Our results, presented in Fig. 1.12 are in agreement with a previous study that employed a different estimation

method [43]. Next, we show that an integration procedure can help improving the classification rate even in low SNR conditions.

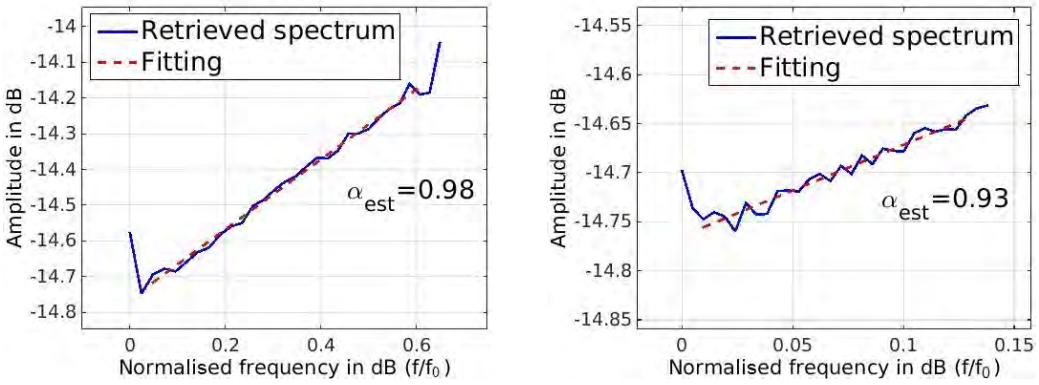

(a) Spectrum when α=1 and B=1500 MHz (b) Spectrum when α=1 and B=300 MHz

Figure 1.11: Spectra of the received echoes when the bandwidth of the transmitted pulse was B=1500 MHz and B=300 MHz, SNR=∞. a) Small target case and b) Extended target case.

OFDM phenomenology: radar technique combining genetic algorithm based pulse design and energy detector for target recognition.

We investigate the potential of OFDM radar to enhance the recognition functionality. We propose a novel phenomenology based framework whereby the pulse is composed of several symbols each matched to a particular target and the recognition function in the receiver reduces to an energy detector. In this approach, we make use of simple target models as in Figs. 1.13(a)-1.13(c) for which we have exact analytical expressions and apply genetic algorithm (GA) based methods to design the symbols. We demonstrate the merit of our technique with simulated results and show how the integration of multiple echoes improves significantly the overall probability of correct classification despite AWGN. In Fig 1.14, we observe that reasonable values of the number of pulses give satisfactory results under low SNR conditions, such as 0 dB or 10 dB, e.g. at 10 dB, 100 pulses provide a probability of correct classification for each target superior to 95 %.

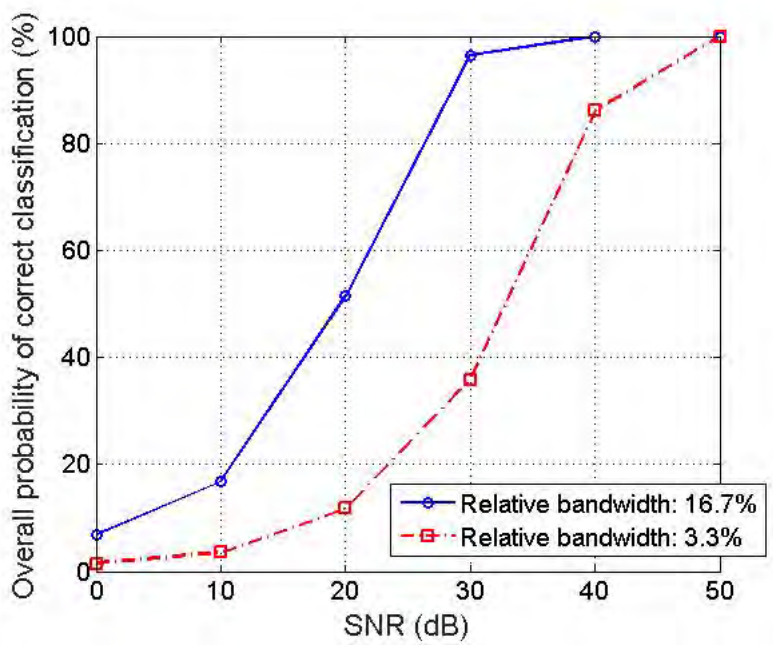

Figure 1.12: Overall probability of correct classification versus SNR using f_0=9 GHz, N=30 subcarriers and two cases for the bandwidth, B=300 MHz and B=1500 MHz.

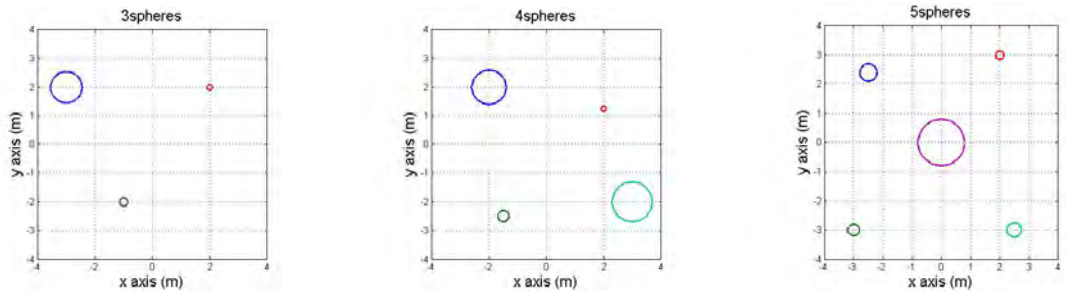

(a) Target 1 (b) Target 2 (c) Target 3

Figure 1.13: Geometrical model for the targets considered in the experiment.

1.5 Publications

The research detailed in this thesis has contributed to the following publications:

G Lellouch, A Mishra, *Multi-carrier based Radar signal optimisation using genetic algorithm*, in Proceedings of the Third International Conference on Soft

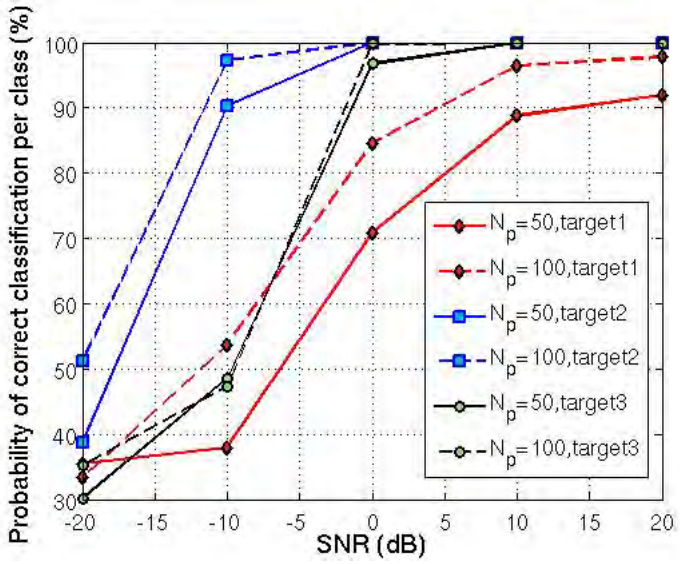

Figure 1.14: Improvement resulting from the integration of several pulses on the probability of correct classification per target class for different values of SNR.

Computing for Problem Solving (pp. 525-534). Springer India (2014, January) [44].

G Lellouch, A Mishra, M Inggs, *Impact of the Doppler modulation on the range and Doppler processing in OFDM radar*, Radar Conference (RADARCON), 2014 IEEE (pp. 0803-0808) [45]

G Lellouch, A Mishra, M Inggs, *Processing alternatives in OFDM radar*, International Conference in Radar, 2014 IEEE (pp. 1-6) [46]

G Lellouch, A Mishra, M Inggs, *Stepped OFDM radar technique to resolve range and Doppler simultaneously*, IEEE Trans. Aerospace and Electronic Systems, vol. 51, no 2, p. 937-950 [47]

G Lellouch, A Mishra, M Inggs, *Design of OFDM radar pulses using genetic algorithm based techniques*, IEEE Trans. Aerospace and Electronic Systems, (accepted in the first review)

G Lellouch, A Mishra, M Inggs, *OFDM phenomenology: recognition of canonical scatterers using flat spectra OFDM pulses*, IET Radar Sonar and Navigation,

(accepted in the first review)

G Lellouch, A Mishra, M Inggs, *OFDM phenomenology: radar technique combining genetic algorithm based pulse design and energy detector for target recognition*, IET Radar Sonar and Navigation, (accepted in the first review)

1.6 Outline of the Dissertation

The rest of the dissertation is organised as follows. We first review the concept of OFDM for communication and touch upon OFDM radar in Chapter 2. In Chapter 3, we present our processing schemes for the case of a train of short OFDM pulses where all pulses have the same bandwidth. Then, in Chapter 4, we present our stepped frequency waveform composed of narrowband OFDM pulses arranged to span a wide bandwidth and derive our HRR processing technique. In Chapter 5 we propose GA based optimisation techniques to tailor the OFDM pulse according to various constraints established in Chapter 3 and 4. Chapter 6 and 7, respectively describe our work on OFDM phenomenology for the characterisation of canonical scatterers and the classification of targets. Finally, in Chapter 8, we summarise our contributions and discuss some possible future work.

1.7 Summary

This chapter provided a brief introduction to radar including the merits of such systems. We elaborated onto the origin of OFDM radar and evoked the potential for further research. This lead to the formulation of our research hypothesis and the characterisation of a set of five research questions that are the socle of our work. We then stressed what we believe to be original contributions to the realm of OFDM radar and evoked our contributions in further details. Lastly, we recalled the outline of this dissertation. In essence, this chapter provides an overview of the dissertation in a comprehensive manner.

Chapter 2

Basics of OFDM for radar

OFDM is a special case of the spread spectrum technique, frequency division multiplexing (FDM). By analogy, a conventional communication technique would be equivalent to water flowing out of a faucet while OFDM would be like a shower. Although the big stream cannot be subdivided, the shower is divided in many little streams. To maintain equivalent flows, the narrow stream from the faucet will feel rougher than the OFDM shower jet, whose individual streams will feel gentle. The consequence of an obstruction on the aperture of the faucet or on one of the apertures of the shower shall also affect the mood of the bather differently. This simple analogy gives a first indication on the merit of OFDM. Another comprehensive analogy where OFDM is compared to the delivery of goods via the use of one big truck or several smaller trucks is given in [48].

Figure 2.1: In a) a whole bunch of water is coming all in one stream while in b) the same amount of water is coming from a lot of small streams.

In OFDM, the multiple frequencies which are also called subcarriers are chosen to be orthogonal to each other. Not only inter-carrier guard bands are not required but the spectra of the multiple carriers can overlap, resulting in an improved spectral efficiency. As evoked in Section 1.1, orthogonality results from the time frequency arrangement of the signal.

Information is conveyed on the subcarriers via the use of modulation symbols that place amplitude weights and phase modulations on the individual subcarriers. As such, the modulation parameters can be determined independently for each subcarrier. Typical constellations employed to transmit communication messages are phase shift keying (PSK) or quadrature amplitude modulation (QAM).

Note that the goal of this chapter is not to give a complete treatment of OFDM as used in the communications. Rather, the objective is to familiarise the reader with the OFDM modulation technique and ground the framework of OFDM radar. For that reason, we endeavour to keep the high-level description since the following chapters will delve in more mathematical representations. To start with, we revisit OFDM via a block diagram and use elementary examples to illustrate the steps, all the way from the binary message at the transmitter, to the binary message at the receiver. We then build upon those examples to approach the limiting factors of OFDM in telecommunication engineering and address the assets and challenges for radar. Thereafter, we review the relevant and/or significant research efforts that have been published relating to the field of OFDM radar.

2.1 The OFDM block diagram

A typical simplex point-to-point OFDM transceiver can be conceived as in Fig. 2.2. Since our focus is at the conceptual level we intentionally ignore those elements (i.e. RF front end, amplifiers) that do not add information to the overall scope. In fact, in this dissertation we ignore all effects of the RF front end. Note however that we relate its impact on the performance of the whole system in Section 2.3.

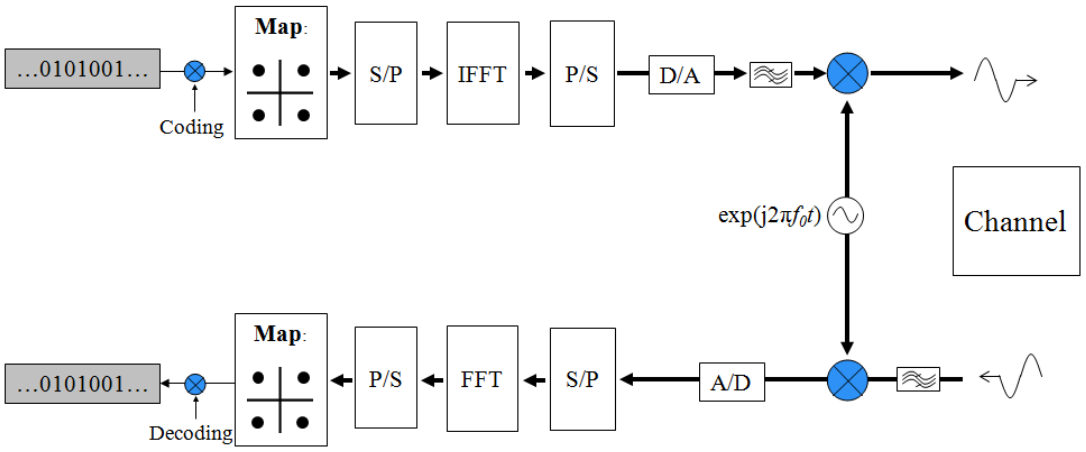

Figure 2.2: Simplex point-to-point OFDM transceiver.

At the transmitter side, the first step consists in mapping the communication message, which takes the form of a binary sequence, onto sets of phase codes. Sometimes, an additional coding step is applied amidst, correspondingly a decoding step is then implemented at the receiver side. Then, the flow of complex symbols is converted from serial to parallel and the phase codes are distributed onto the many subcarriers. Once a phase code is attributed to each subcarrier, an inverse discrete Fourier transform (IDFT) is applied. Following the prior analogy, the fast incoming flow is divided into slower outgoing flows. The inverse fast Fourier transform (IFFT) algorithm is commonly used. The invention of those FFT and IFFT algorithms in the mid 60's inferred a major breakthrough on the system architecture complexity, which in turn triggered the success of OFDM as a communication signal [49]. The discrete signal resulting from the IDFT is then converted from parallel to serial to become the discrete time domain counterpart of the OFDM chip or symbol. In the context of communication, many consecutive OFDM symbols are formed to encompass a larger data package as required by the communication protocols. However, here, the focus is on the single OFDM symbol as we evolve with the background of radar applications. We address later our design for the radar waveform, which typically, will be a train of pulses where the short pulses are composed of one or few OFDM symbols.

In the absence of oversampling in the IDFT, the sampling period of the OFDM symbol is t_b/N, where t_b and N are respectively the symbol (or bit) duration and the number of subcarriers. One talks about critical sampling according to the Nyquist sampling criterion, since it easy to verify that the sampling frequency f_s equates to the signal bandwidth, $f_s{=}N\ \Delta f$. However, in practical systems, it is common to introduce oversampling in the IDFT. The main motivation is to relax the constraint on the filter that follows the digital-to-analog converter (DAC) [50], which is usually designated as *reconstruction filter*. In our simulation, the DAC is modelled as a sample-and-hold operation where we simply increase the sampling frequency further to simulate the continuous signal. In that step, we employ a discrete rectangular window with a sampling rate equivalent to the high sampling rate desired. Note that before carrying the convolution, zero-padding must be implemented onto the baseband signal, where the zeros are padded between consecutive samples to predispose the signal to the high rate.

Convolution in the time domain being equivalent to point-wise multiplication in the frequency domain, the spectrum of the signal resulting from the sample-and-hold step presents spurious spectra at multiples of the baseband sampling frequency, as seen in Fig. 2.3. The later spurious spectra coincide with the replicas of the spectrum of the initial baseband signal. Hence, the smooth "continuous" signal is obtained as a result of filtering this *staircase* signal with the reconstruction filter. Being a low pass filter, ideally, it shall suppress the spurious spectra and correct for the sinc shape over the main band with a 1/sinc response. Being difficult to implement, this correction can be anticipated directly in the signal design though, by setting the weights of the OFDM signal accordingly.

Commonly, real signals are passed through the DAC, nevertheless the correctness of our analysis is not dwindled if we deem complex signals throughout. For completion, we invite the reader to refer to Appendix A, where we expound the steps undergone by the signal spectrum throughout a basic OFDM transceiver chain, with complex baseband and real RF signals.

Using a local oscillator, the "continuous" complex signal is then up-converted to the carrier frequency f_0, which can be few GHz depending on the selected

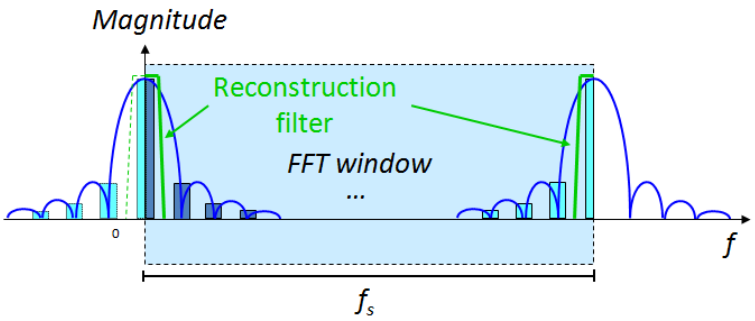

Figure 2.3: The role of the reconstruction filter is to filter out all spurious replicas of the baseband signal positioned at multiples of the baseband sampling frequency f_{sbb}.

transmission band. Although not shown here, the signal is then amplified before it is finally transmitted into the channel via an antenna. Because the channel through which the signal propagates contains scatterers and reflectors, it can be modelled as a filter modifying the incoming signal. Like any filter, it has a finite duration and can be modelled by time taps with corresponding complex coefficients. Hence, the received signal comprises of multiple copies of the transmitted signal with different delays, magnitudes and phase shifts that correspond to the different filter coefficients. We review the fundamental characteristics of the channel and the precautions related to it in Section 2.3.

When entering the receiver, the signal must be filtered to suppress any unwanted signals from the other bands. Next, it shall be down-converted, ideally, with the very same local oscillator that was used in the transmitter. Although this basic approach is that of an homodyne architecture, other more sophisticated heterodyne architectures with intermediate frequencies may be used. Consequence of mismatch between both references is addressed in Section 2.3.3. The baseband signal is then sampled via an ADC before it is finally decimated back to the initial baseband sampling frequency. The OFDM symbol is then parallelised and symmetrically to what happened in the transmitter, a DFT is applied to retrieve the phase codes. After going through a parallel-to-serial conversion step and possibly decoding, the binary message is recovered, hopefully error-free.

During propagation, a wide range of effects will impact the signal and possibly alter the performance of the system, whether it is intended for telecommunication or radar. As a result, the designer must be aware of those artefacts and when possible, compensate for them beforehand.

2.2 Examples of OFDM signals

Having revisited the OFDM block diagram, we now use two simple examples to illustrate some key aspects. In our first example, we present the case of an OFDM signal composed of only one subcarrier, while our second example is a simplified version of the notorious digital video broadcasting-terrestrial (DVB-T) standard used worldwide to broadcast transmissions of digital terrestrial television. In that respect, useful materials for simulation purposes are available in [51, 52].

2.2.1 Single carrier

With this example, our objective is to capitalise on the OFDM modulation-demodulation technique and comprehend the distortion in phase suffered by the subcarriers. To motivate our approach, we argue that, in some cases (i.e. in QPSK all phase codes have the same magnitude), the sole phase of the received symbols could be critical for correct estimation. In our simulation, we consider the parameters as given in Table 2.1. Essentially, they would suit the design of an OFDM signal composed of 10 subcarriers with a large oversampling factor as a result of the 1014 extra subcarriers being considered.

Fig. 2.4(a) confirms the values taken by the phase codes, 1 if they belong to active subcarriers, 0 for the rest. In fact, because we want to use only one subcarrier, we multiply each phase code by a coefficient (or a weight) which is set to 0 for all 9 subcarriers except one, this way we enable the use of a single subcarrier as shown in Fig.2.4(b).

Consequently, the discrete complex signal resulting from applying the IDFT onto

Table 2.1: OFDM parameters for the single carrier example

Symbol	Parameter Name	Parameter Value
Δf	Subcarrier spacing	4.464 kHz
N	Total number of subcarriers	1024
N_{ON}	Number of active subcarriers	10
i_{ON}	index of active subcarriers	1...10
i_{OFF}	index of inactive subcarriers	11...1024
$\mathbf{w}$	weight vector	$[0\ 1\ 0\ 0\ 0\ 0\ 0\ 0\ 0\ 0]^T$
f_0	Carrier frequency	2 GHz

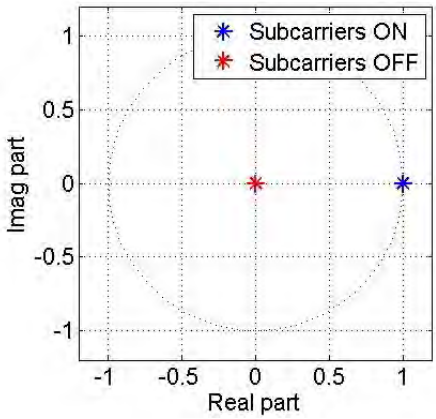

(a) Phase codes before weighting

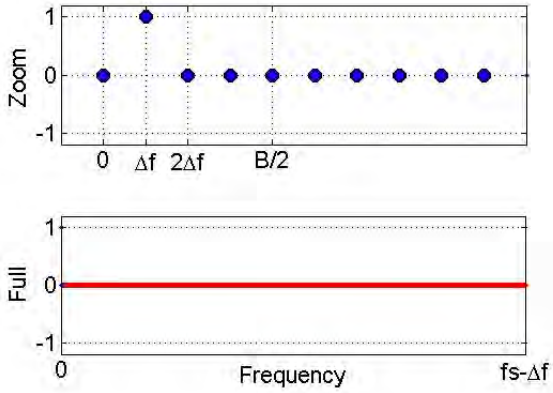

(b) Frequency content of the OFDM symbol after weighting

Figure 2.4: Content of the OFDM spectrum for one symbol. In a) the phase code transmitted, 1, is plotted on the complex plan, and in b) the spectrum of the OFDM symbol shows that amongst the 10 subcarriers active only one is used.

the vector of weighted phase codes is plotted in Fig. 2.5(a). Mathematically it follows Eq. 2.1.

$$s[n] = \sum_{k=0}^{N-1} w_k a_k \exp(j2\pi \frac{nk}{N}), \qquad n = \{0,\ 1,\ 2,\ ...,\ N-1\}.$$
$$a_k = \begin{cases} 0, & k \geq N_{\text{ON}} \\ 1, & k < N_{\text{ON}} \end{cases}, \quad w_k = \begin{cases} 0, & k \neq 1 \\ 1, & k = 1 \end{cases} \tag{2.1}$$

Our choice for the subcarrier corresponds to the first harmonic, such that one period is observed. Owing to the orthogonality principle, exactly one period is covered during the total duration. It is easy to understand that, would the third, fourth, fifth etc. subcarrier be selected, accordingly, the corresponding harmonic would be displayed. The first subcarrier corresponds to the DC component.

Here, the phase code is a_1=1. If we perform an autocorrelation of this signal we obtain a triangular function, the same as if we had used a rectangular pulse. Obviously, the single subcarrier case does not induce any compression gain.

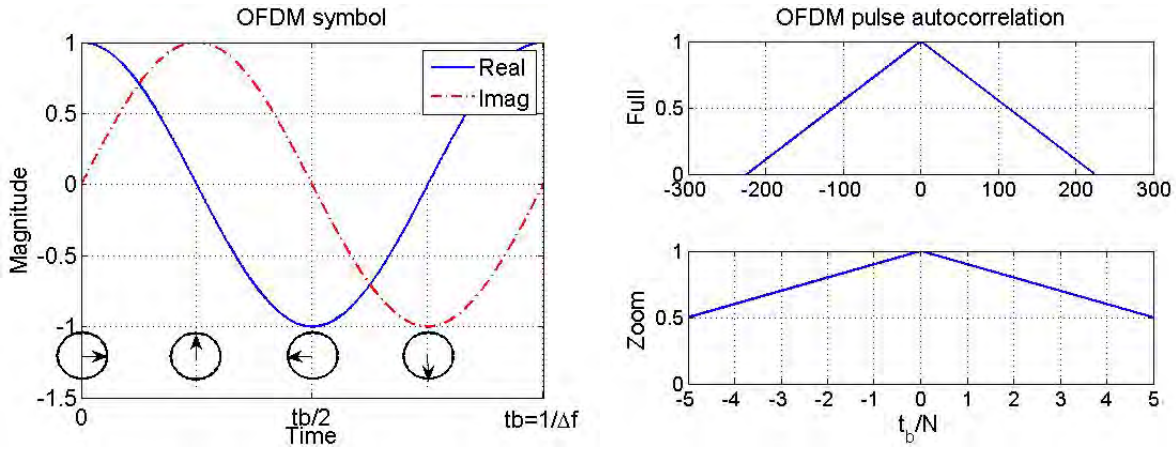

(a) Time domain

(b) Autocorrelation function

Figure 2.5: a) the complex time domain single subcarrier OFDM symbol and b) its autocorrelation function after normalisation.

Proceeding further down the chain, with the DAC and the up-conversion we obtain the spectrum of the RF signal as in Fig. 2.6(a). If we disregard the channel and simply assume a direct path with no delay (this is not realistic but it serves our purpose), ignore the RF filter, do the down-conversion with the exact same local oscillator, decimate the signal and perform the demodulation we retrieve the phase code as in Fig. 2.6(b). We must compare it with the transmitted phase code from Fig. 2.4(a). Essentially we show the case with and without the reconstruction filter. In the latter case, there is no magnitude loss but a phase shift as a result of the down-conversion, caused by the symbol duration not being an integer multiple of the carrier period (0.5 ns) and in the former

case, an additional small phase shift and magnitude loss are present. These observations show how important it is to understand the distortions in amplitude and phase caused by the different elements of the system. But not only, since the major phase shift contribution results in this case from the "simplistic" channel, which, in typical situations, is not under our control. To cope with these issues, communication systems make use of OFDM pilot symbols [7, chap. 5]. Known at the receiver they are used to assess how much compensation, in amplitude and phase, is required.

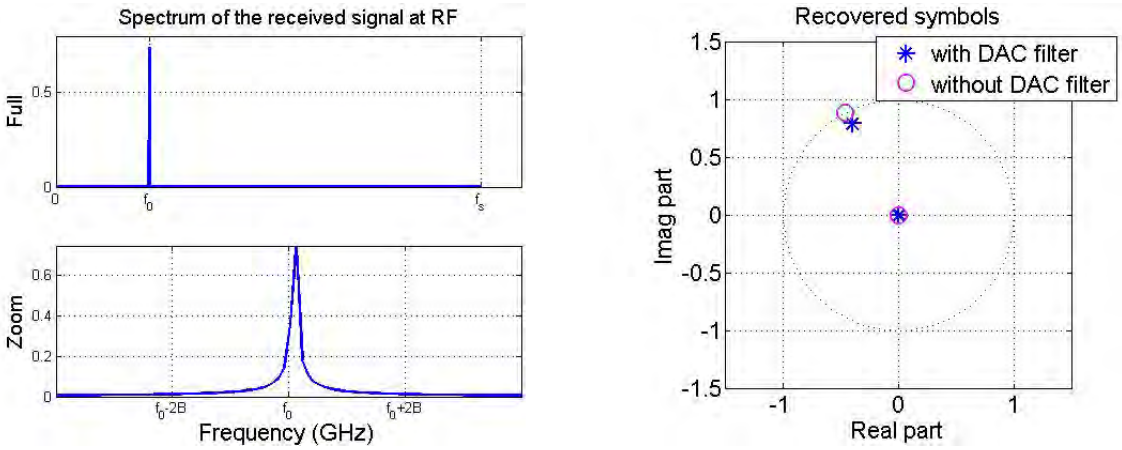

(a) Spectrum at RF

(b) Complex symbol recovered

Figure 2.6: a) the spectrum of the received OFDM symbol at RF and b) symbols recovered with or without the DAC reconstruction filter.

2.2.2 DVB-T simplified

To touch on more realistic OFDM signals, we propose another simulation based on a simplified version of the DVB-T standard, with parameters as given in Table 2.2. The signal comprises of N_{ON}=250 subcarriers and the bandwidth is B=$N_{\text{ON}}\Delta f$=1.116 MHz.

We now suggest using QPSK symbols to convey information data. Hence, we first generate a random binary sequence to account for the communication message as in Fig 2.7(a). Because QPSK is a four point constellation (2^2), each phase

Table 2.2: OFDM parameters for the DVB-T simplified example

Symbol	Parameter Name	Parameter Value
Δf	Subcarrier spacing	4.464 kHz
N	Total number of subcarriers	1024
N_{ON}	Number of active subcarriers	250
i_{ON}	index of active subcarriers	1...125 and 900...1024
i_{OFF}	index of inactive subcarriers	126...899
$[w_1 \cdots w_{N_{\text{ON}}}]^T$	weight vector	$[1 \cdots 1]^T$
f_0	Carrier frequency	2 GHz

code carries two bits. By anticipation, the first two bits will be conveyed by the first subcarrier, the next two bits by the second, etc.. Fig. 2.7(b) illustrates this concept of multicarrier multiplexing whereby a set of 8 bits is transmitted by forming pairs and allocating them to the multiple subcarriers.

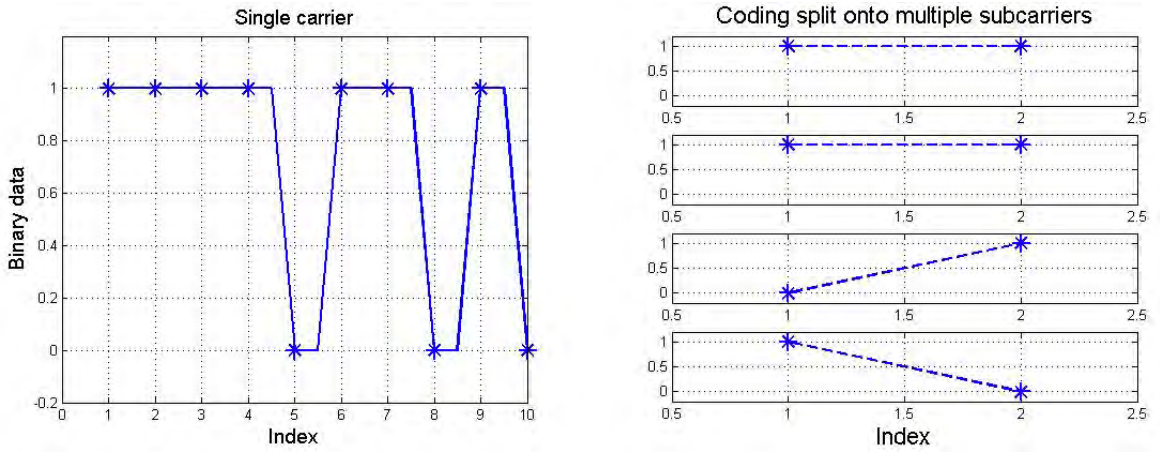

(a) Sequence of incoming data

(b) Data over the first four subcarriers

Figure 2.7: a) incoming sequence of binary data and b) distribution of pairs of bits over the four first subcarriers.

Overall, the phase codes transmitted in this simulation are represented on the complex plane in Fig. 2.8(a), with their corresponding digital code. The vector of phase codes which is equivalent to the OFDM symbol spectrum is shown in Fig. 2.8(b). Following the parametrisation disclosed in Table 2.2, the bunch of active subcarriers is divided in two groups. Due to the repeatability of the spectrum, these two groups are actually adjacent, such that the overall bandwidth

remains $N_{\text{ON}}\Delta f$.

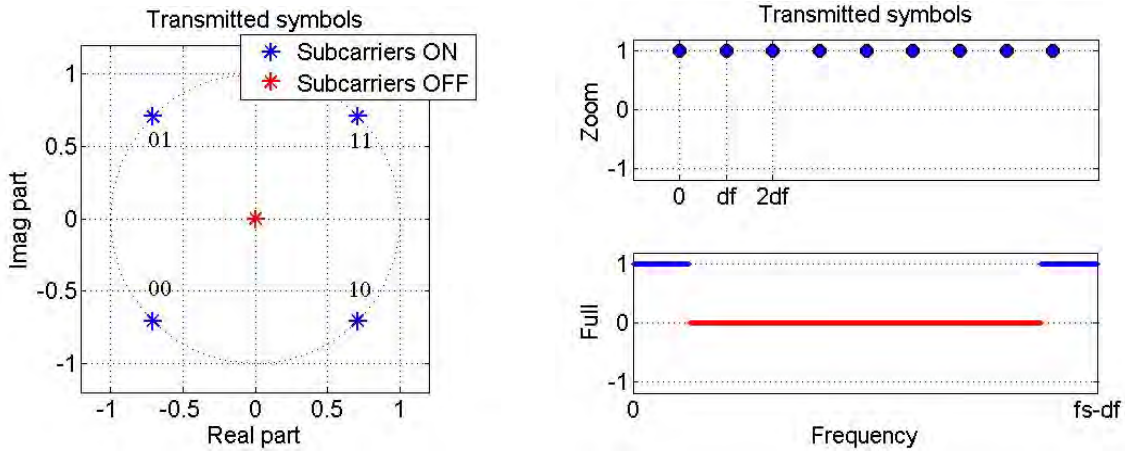

(a) Symbol transmitted

(b) Frequency content of the OFDM symbol

Figure 2.8: Content of the OFDM spectrum for one symbol. a) the phase codes transmitted (QPSK) are plotted on the complex plane, and b) the spectrum of the OFDM symbol shows the arrangement of the subcarriers.

Unlike the previous example, the discrete signal resulting from the IDFT no longer follows a well defined curve, rather, it is noise-like. This aspect ensues the mathematical formulation and the presence of different phase codes on the multiple subcarriers. Although we plotted in Fig. 2.9(a) both real and imaginary parts, we glimpse one of the major challenges of OFDM, viz., the risk of high fluctuations of the signal envelope. The high peaks observed in either domains result from the multiple carriers that combine constructively. In constrast, the autocorrelation function displayed in Fig. 2.9(b) exhibits an enticing narrow peak. According to the Rayleigh criterion [32, chap. 20], the resolution in time equates to the separation between the peak and the first null, that is: $\delta t{=}t_b/N_{\text{ON}}$. Given a monostatic radar, time delay τ and range R are linked by the relation $R{=}c\tau/2$, where c is the speed of light ($\approx 3 \times 10^8$ m/s). Hence, we can verify that the range resolution δR is as in Eq. 2.2.

$$\delta R = c/2B, \tag{2.2}$$

which is a commonly accepted definition of the range resolution in the monostatic radar case. In comparison to the single subcarrier case, the resolution in range has greatly improved[1].

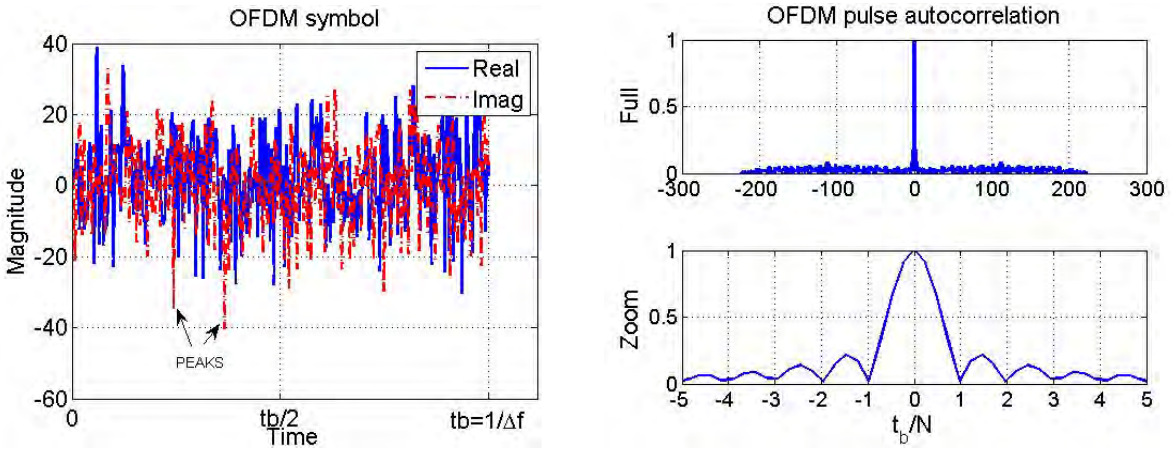

(a) Time domain

(b) Autocorrelation function

Figure 2.9: a) the complex time domain OFDM symbol and b) its autocorrelation function after normalisation.

The next step is to pass the baseband OFDM symbol through the DAC. The signal resulting from the sample-and-hold operation has a "staircase" shaped output as shown in Fig. 2.10(a). In light of Fig. 2.3, unsurprisingly, the spectrum of this signal presents replica at multiples of the baseband sampling frequency, $1/T_{\text{co}}$ where T_{co} is the duration of the comb signal used for the convolution.

Following the up-conversion, we consider the same channel as in the previous case, except that we add two narrowband interfering signals at f_0-$2B$ and f_0+$3B$ as shown in Fig. 2.11(a), such that we must utilise the RF filter to clean the spectrum as in Fig. 2.11(b). We also add additive white Gaussian noise (AWGN) onto the signal to reach a signal-to-noise ratio of 30 dB.

Next, we proceed with the down-conversion, decimate the signal and perform the demodulation to retrieve the phase codes, which we display in Fig. 2.12(b). In

[1] To clarify the terminology used to quantify resolution, the terms *improved* or *enhanced* resolution refer to a decrease of δR, while the terms *degraded* or *reduced* resolution refer to an increase in δR. One talks about fine resolution for small δR values, whereas coarse resolution implies large δR values.

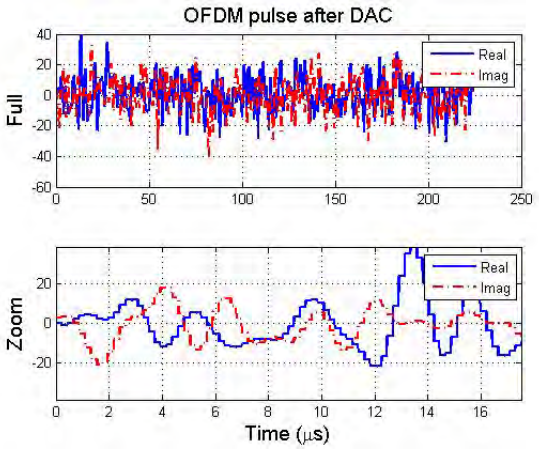

(a) Time domain after sample-and-hold

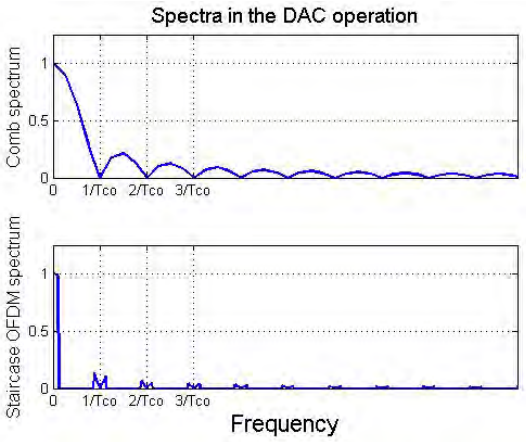

(b) Comb and staircase spectra

Figure 2.10: OFDM symbol in a) the time domain and b) in the frequency domain after the sample-and-hold operation.

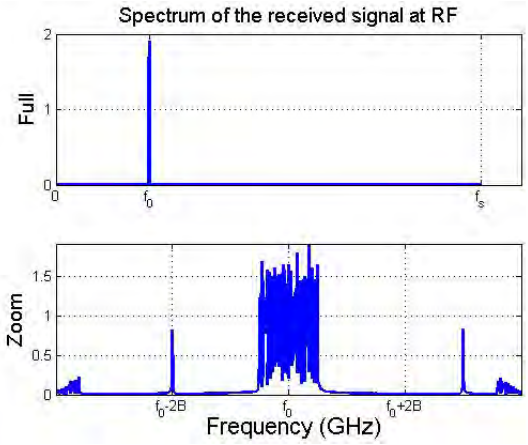

(a) Before RF filtering

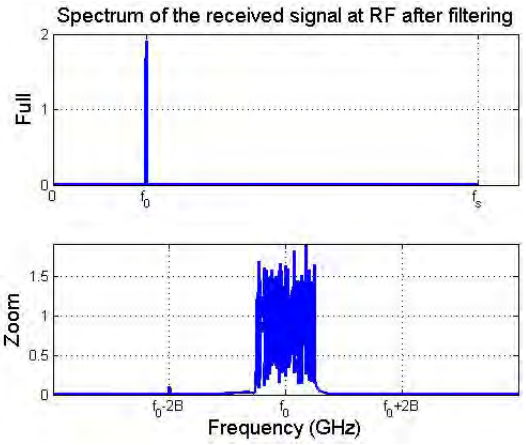

(b) After RF filtering

Figure 2.11: Spectrum of the received RF OFDM signal a) before and b) after filtering with a bandpass filter.

comparison to the first example, we compensate for the phase offset due to the channel and we show the results with and without the reconstruction filter. In the latter case, the clouds of points are centred around the true values, while in the former case, they are scattered around the unit circle such that the original phase codes can no longer be retrieved. Interestingly, we observe that the RF

filter has had little impact on the shift in phase, therefore similar elements (in that case filters) may have dissimilar impacts.

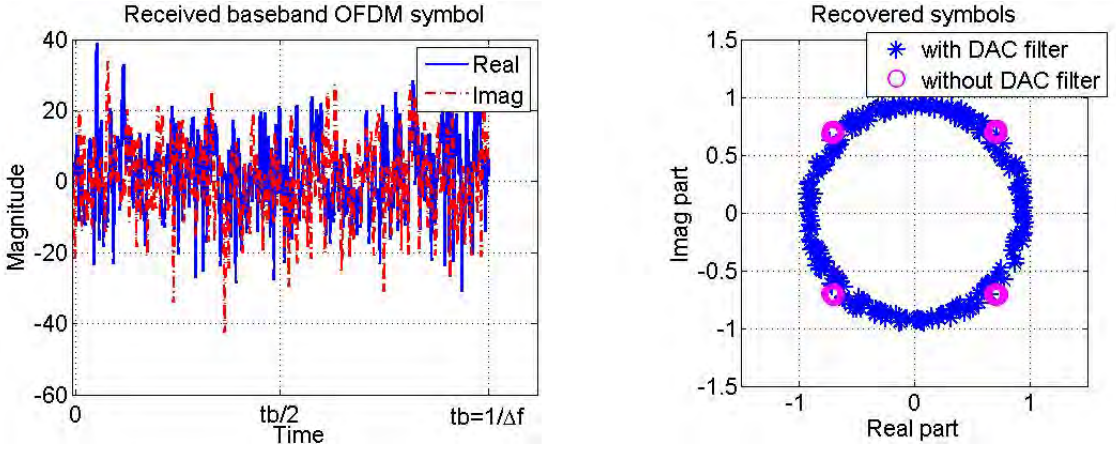

(a) Received time domain symbol at baseband

(b) Complex symbols recovered

Figure 2.12: a) received time domain symbol at baseband and recovered phase codes with or without the DAC reconstruction filter.

2.3 OFDM specific issues

In OFDM based communication systems, the phase codes used at the transmitter must be recovered at the receiver. In the previous examples, we have shown how equipments like filters can be detrimental to the retrievals. Not sketched in our block diagram in Fig. 2.2, amplifiers also have magnitude and phase responses, which may affect the OFDM signal. However, because the characteristics of these components can be assessed precisely, the overall complex distortion can be known and in fact, it shall be possible to compensate for it directly on transmit by adding complex phasors to the original phase codes. In addition to those hardware artefacts, two other effects, viz., intersymbol interference (ISI) and intercarrier interference (ICI), are harmful for communication and must be overcome. In the following subsections, we review them briefly and touch upon their impact in radar.

2.3.1 Intersymbol interference

Realistically, radio channels cannot be modeled as in our examples, except, perhaps, for satellite links. In practice we need to deal with the problem of multipath, consequence of the many scatterers as evoked in Section 2.1 and the problem can be exposed as follows. Considering that we use the echo corresponding to the line-of-sight (LoS) propagation to position at the receiver the DFT window for each symbol, we realise that the delayed echo of the (i-1)th symbol will cause interference onto the LoS echo of the ith symbol as shown in Fig. 2.13(a). The first solution to counteract this issue is to introduce a guard interval between consecutive symbols, at least equal to the largest delay in the channel. Although this approach suppresses the risk of ISI, the sudden change of waveform within the DFT window, as seen in Fig. 2.13(b) engenders higher spectral components and results in ICI. Therefore, the solution to limit ISI and mitigate the risk of ICI consists in the well-established guard interval insertion technique with cyclic prefix CP. Essentially, for each symbol the last portion is copied and replicated upfront. As shown in Fig. 2.13(c), the DFT window now contains a full cycle of the subcarrier for both LoS and delayed echoes. Again, the length of the CP shall be at least equivalent to the maximum delay in the channel.

2.3.2 Intercarrier interference

Intercarrier interference (ICI) is an impairment known to degrade the performance of OFDM systems that can have manifold origins. In the case of a moving point scatterer, the received echo is subject to Doppler modulation such that the spectra of the OFDM symbols are displaced by a small quantity. If this shift is unaccounted for, the DFT will retrieve incorrect values for the phase codes as illustrated in Fig. 2.14. Essentially, for each subcarrier, the sampling of the spectrum no longer occurs at the peak but at a slight offset such that the contribution of the other subcarriers is not null, hence they interfere and alter the recovery of the information.

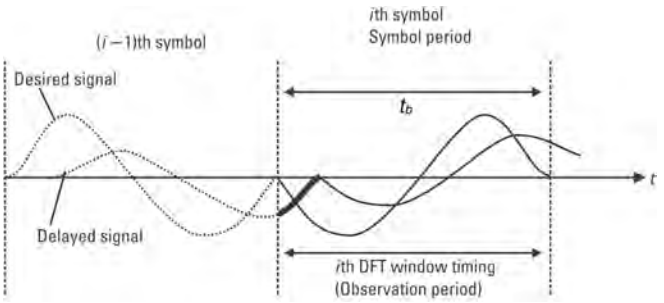

(a) No guard interval insertion

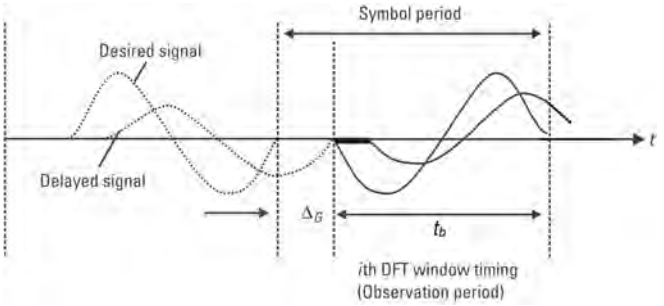

(b) guard interval insertion

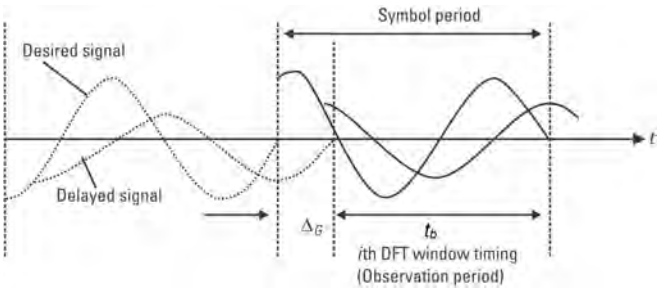

(c) guard interval insertion with cyclic prefix

Figure 2.13: Received OFDM signals in multipath environment for different configurations. In a) no guard interval is considered and the compound received signal suffers from ISI, in b) ISI is suppressed but the sudden change of waveform causes ICI, in c) the guard interval insertion technique with cyclic prefix eliminates ICI [7].

2.3.3 Synchronisation errors

Our block diagram and the examples used to introduce OFDM for communication assume ideal channel behaviour as well as ideal components such that the

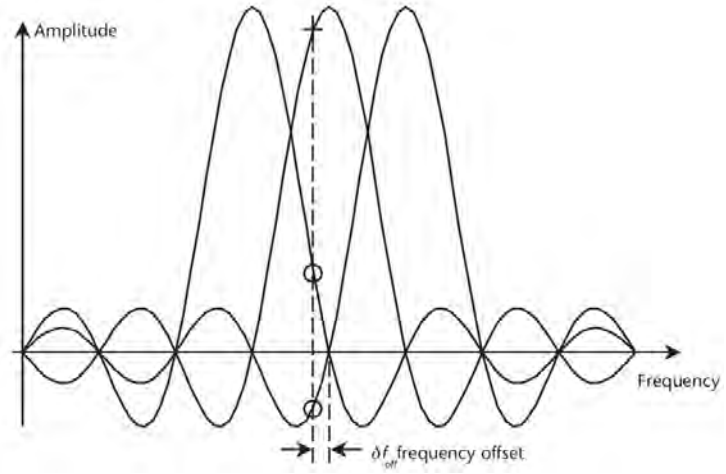

Figure 2.14: Intercarrier interference as a result of mis-sampling the OFDM spectrum [12].

above impairments are not detrimental to the retrieval of the communication message, provided that we compensate for the hardware artefacts and that the noise remains negligible. In particular, synchronisation errors tend to affect the overall performance of the system and the robustness of an OFDM receiver will depend on its ability to cope respectively with time and frequency synchronisation issues.

2.3.3.1 Time synchronisation errors

In OFDM, half of the information being contained in the phase of the subcarriers, it is clear that time synchronisation errors are detrimental. With the same example of Fig. 2.13(c), would the DFT window be slightly shifted to the left for the ith symbol, the phase read for the subcarrier of the desired signal would no longer be 0 but ε assuming that the imaginary part is being displayed.

At this stage, it is important to realise that the paramount function of the guard interval is not the relaxing of the time synchronisation requirement. In fact, with the same example of Fig. 2.13(c), we see that the communication symbol conveyed by the delayed echo cannot be recovered correctly if the delay is not taken into account. However, a common practice in OFDM systems is

to use pilot symbols that are known at the receiver to estimate the delay of the multiple echoes and re-inject this information in the processing of the other unknown symbols. This aspect has been extensively covered in the literature and many techniques have been proposed to detect the start of the communication symbols [53, 54, 55, 56].

2.3.3.2 Frequency synchronisation errors

Besides uncompensated Doppler, other factors introduce intercarrier interference. A compound model for the ICI has been formulated in [57]. Firstly, the frequency offset between the transmitter and the receiver local oscillators will displace the subcarriers of the baseband spectrum in a similar manner. Critical when the transmitter and the receiver are not collocated, like in most communication systems, it shall be harmless for the monostatic radar case, since both transmitter and receiver share the same frequency source, provided that the oscillator does not drift significantly during the round trip propagation. Secondly, the presence of sampling offset in the analog-to-digital converter (ADC) will also cause ICI. In that case, the shorter (respectively longer) sampling period implies that slightly less (respectively slightly more) than an integer number of cycles for the subcarriers are considered before the DFT. To illustrate this effect, in Fig. 2.15, we sample a 1 kHz complex exponential with two sampling frequencies, f_{s1}=10 kHz and f_{s2}=10.5 kHz and store in either case 10 samples. While the period of this complex exponential fits precisely an integer number of the first sampling period $1/f_{s1}$, it is not the case of the second sampling period $1/f_{s2}$. For, behind the DFT lies the assumption of periodicity, it is relevant to think of the discrete signals as a repetition of those samples as shown in Figs. 2.16(a) and 2.16(b). The extension in time asserts the difference between both frequencies and with no surprise the corresponding spectra can be found as in Fig. 2.17. While all the energy is concentrated on the appropriate frequency bin in Fig. 2.17(a), this same energy is spread over many frequency bins in Fig. 2.17(b), leading to interference.

Known to be a paramount impairment for communication systems, the area of frequency synchronisation errors in OFDM has been researched intensely. Again,

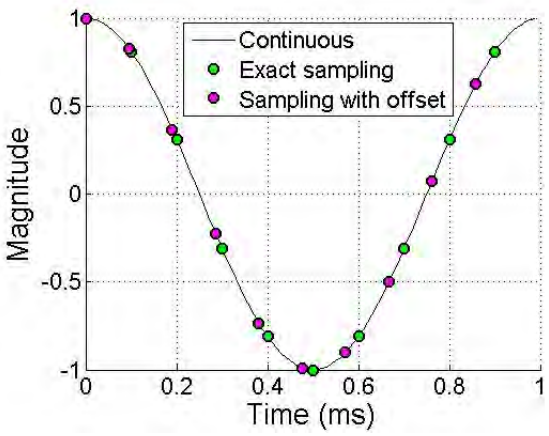

Figure 2.15: Collection of 10 samples to feed the DFT, with and without offset for the sampling frequency.

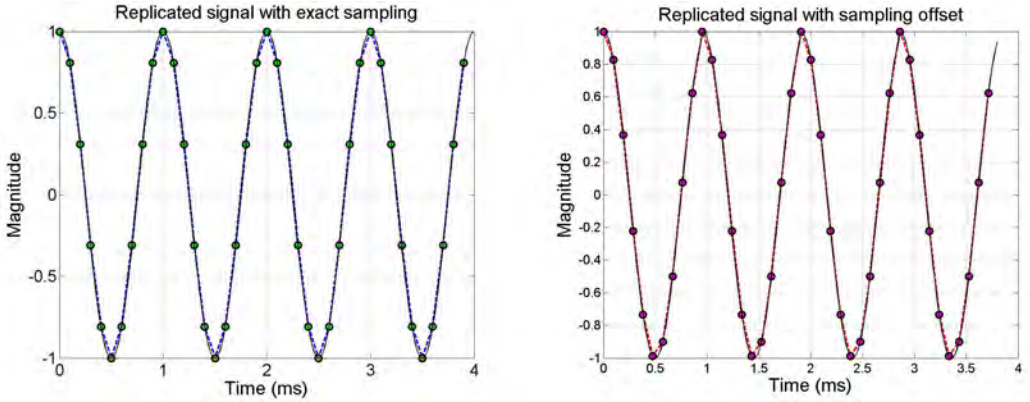

(a) Period signal with exact sampling

(b) Periodic signal with sampling offset

Figure 2.16: Periodic time domain signal seen by the DFT when the sampling frequency is either exact or has a slight offset.

most methods used to combat the degradation rely on the transmission of carrier and/or pilot symbols [58, 59, 60].

2.3.4 Non constant envelope

When all subcarriers of an OFDM symbol are given the same phase code, the resulting signal is a sum of harmonics. It presents a peak equal to, the total

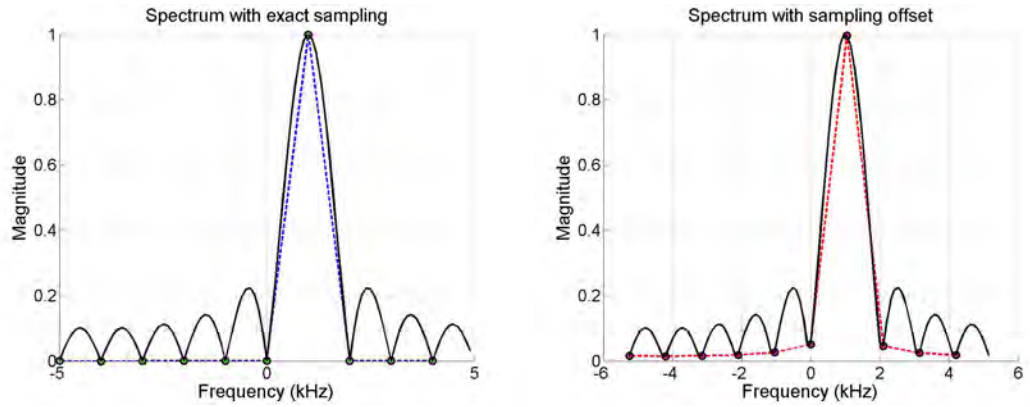

(a) Spectrum with exact sampling

(b) Spectrum with sampling offset

Figure 2.17: Spectra resulting from sampling the complex exponential when the sampling frequency is ideal or presents a slight offset.

sum of the weights, or, if unitary weights have been applied, the number of subcarriers at the time instant when they add up in phase as in Fig. 2.18(a). If several adjacent symbols are generated following this strategy, but with different phase codes from symbol to symbol, one refers to this pulse as an identical sequence (IS) OFDM pulse. For OFDM pulses in radar must be comparable, we usually employ a normalising factor to normalise their energy to unity. In that case, both OFDM symbols presented in Fig. 2.18(a) become as in Fig. 2.18(b).

In communication and radar systems, the intention is to extort as much from the equipment as possible and therefore maximise the overall efficiency. Hence, amplifiers shall be used in saturation and the input signals must have constant amplitude to avoid distortion. In that context, linearly frequency modulated (LFM), or phase-coded pulses work well while OFDM pulses become inconvenient.

Nevertheless, as soon as random phase codes are applied, the envelope is modified and the OFDM signal appears more like random noise. However, this does not prevent from the risk of peaks as observed earlier in Fig. 2.9(a).

In fact, it is the intention of Chapter 5 to analyse how one can regulate the envelope of the OFDM pulse. Because the analysis is taking place in the discrete

domain, it is important to realise that the figure of merit that we refer to as the peak to mean envelope power ratio, PMEPR, may be different for different sampling (oversampling) factors. In a nutshell, it seems admitted that an oversampling of four as compared to the critical sampling frequency shall permit to assess the PMEPR of the continuous signal without failure [61].

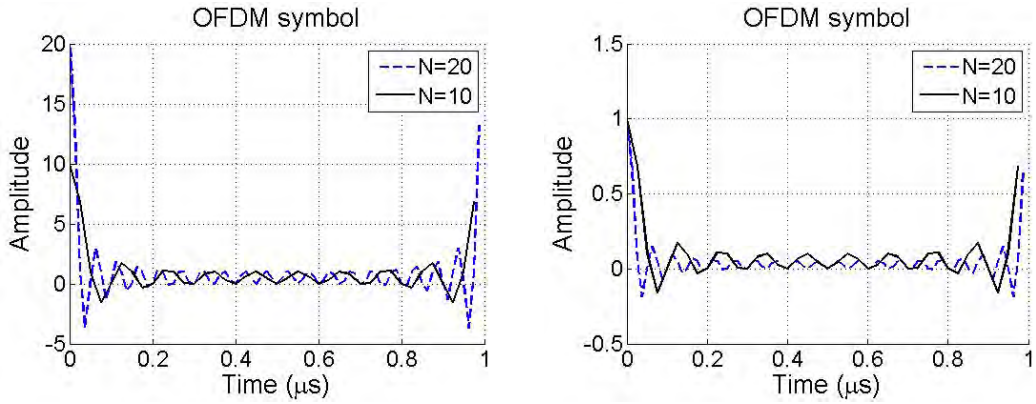

(a) OFDM symbols (b) Normalised OFDM symbols

Figure 2.18: Real part of OFDM symbols for N=20 and 10 subcarriers a) before and b) after normalisation. In either case, the symbol is generated with an oversampling factor of 4.

2.3.5 Impact on radar and framework of our study

Switching from OFDM for communication to OFDM for radar, two aspects must be underlined.

Firstly, the wideband OFDM signal is suited for radar as illustrated by Fig. 2.9(b). Like a linearly frequency modulated signal (or chirp) OFDM can be used as a *pulse compression* signal to enable fine range resolution while maintaining long transmissions with high energy content and low peak power, desirable in radar, to reach remote targets or ensemble of targets.

Secondly, it must be noted that in radar, delays and Doppler shifts of the echoes are both the parameters of interest, unlike in communication where we are trying to compensate for them. In fact, it is common to repeat several transmissions to

improve the accuracy of those estimates. The coherent processing interval (CPI) is the duration of the measurement intended to estimate Doppler.

Although most works on OFDM radar assumed continuous waveforms, our incentive to work within the framework of pulsed waveforms, is twofold: the possibility to re-use existing pulsed systems, and the characterisation of novel properties of the OFDM signal, especially as a result of the short symbol duration or large subcarrier spacing. In particular, we will see how weight and phase code vectors of the OFDM symbols can be used to improve manifold radar capabilities.

Because the concept of guard interval with the insertion of cyclic prefix is not obvious for pulsed radar, our analysis in the following chapters considers pulses where the consecutive symbols are adjacent. Interestingly, we will see in Chapter 3 that more than one method can be used to process the OFDM pulses and extract useful information such as delay and Doppler. In fact, we will show that a similar processing chain as used for telecommunication can be used and in that case, the problem of ISI also applies. In those configurations where ISI is present, a more conventional radar processing can be employed.

In terms of Doppler retrieval, the only problem would be, in the monostatic case, the presence of sampling frequency offset. However, it is not the purpose of this study to evaluate the degradation of the performance under such conditions, hence it is left for future work.

2.4 Literature review

Having presented an overview of the mechanisms of OFDM for communication and touched upon the possibilities for radar, we now review the existing works in the realm of OFDM radar. To gauge the type of effort, we endeavor to refer to the characteristic of the publication whether they are MSc, PhD theses, series of papers or isolated articles. To facilite the reading we sort them chronologically.

- **Ambiguity properties** and **range-Doppler resolution** analyses of the

multicarrier signal have driven the work of Levanon et al. reported in [13, 31] respectively in 2000 and 2002. Throughout their work, the ambiguity function (AF) is used as the main tool. In [62, 36], the authors approached the problem of peak-to-mean envelope power ratio (PMEPR) reduction, typical of multicarrier signals.

- **Improvement in target detection performance** with multicarrier signals as compared with the single carrier signal has been reported in 2004 [63]. In this article, the author argues that the required constant false alarm rate (CFAR) detection threshold for point-target detection based on multicarrier modulation is lower than that required in the case of a single carrier radar system.

- **A detection feasibility study** was lead and reported in 2005 in the context of passive radar[2] [65]. In his article, Poullin analysed specifically the coded orthogonal frequency division multiplex (COFDM) used in digital audio broadcasting (DAB).

- **Doppler tolerance** of **OFDM symbols** is assessed and indications regarding the 1 dB compression loss are given in the MSc work published in 2006 [6].

- **OFDM design choices** and **agility patterns** are investigated in [17]. In his MSc thesis, Tran reports on a conceptual study concerned with the design of a pulsed OFDM radar waveform for optimal behaviour in the context of a radar network. He first investigated various design configurations for the OFDM pulse with respect to few criteria, viz., the **autocorrelation sidelobe level** and the **spectrum occupancy**. Under the assumption of a frequency division multiplexing for the various radar stations, he then examined several agility pattern alternatives, in terms of **ambiguity** and **cross correlation properties**.

[2] The passive or commensal radar [64] uses the transmissions of opportunity from an existing system without degrading in any way the performance of the other system. It can be foreseen to offer solutions for low cost radar systems (e.g. for air traffic control applications in developing countries or small airports).

- **Calculation of the radar cross section (RCS) of time varying targets** [37]. In his PhD thesis reported in 2006, Paichard investigates the capability of a short time wideband OFDM signal to extract the RCS features of time varying targets (e.g. helicopter) subject to global motion and internal fluctuations that induce respectively Doppler and micro-Doppler on the transmitted radar waveform. It is noteworthy that the radar processing is not regarded in this work.

- Preliminary analyses concerning the **processing of pulsed OFDM radar waveforms** to **retrieve Doppler** in the context of, either, **frequency agility** in the waveform [18] or under the **wideband model assumption** for the received signal [19] in the continuity of Tran's work.

- **Studies of less computationally demanding matched filtering** methods for multicarrier signals have been reported by Mohseni et al. [33, 66] in 2008, as well as methods to maintain constant the envelope of the OFDM signal by mapping the OFDM envelope on the phase of a single carrier [33]. At the same time, Sebt et al., also from the university of Tehran, were inspecting the design of OFDM radar signals with **optimised ambiguity function** and **low peak-to-average power ratio** (PAPR) [67].

- **A feasibility study of a RadCom system** relying on OFDM for short range application with high range resolution capabilities in radar [68] was published in 2009. Compiling a series of contributions [69, 70, 71] spanning the period between 2006 and 2009, this work focuses on the design and architectural composition of a radar system built on an OFDM platform.

- **Incorporation of the OFDM signal into the concept of netted radar** [72]. In this article released in 2009, the OFDM signal is evaluated in terms of its peak-to-average power ratio and cross-correlation properties for different codes that would allow the use of orthogonal codes by distinct nodes of the network.

- **Extraction of HRRPs** based on OFDM phase-coded stepped frequency (OFDM-PCSF) [34]. Published in 2010, this paper reports the concerns

of the author to develop a new stepped frequency waveform that would permit to relax the constraints on sampling rates. Initial considerations with respect to motion compensation issues are addressed.

- **Derivation of favourable signal processing algorithms for range and Doppler** when the waveform is a continuous OFDM signal has been reported in [40, 73, 74]. Within the context of a RadCom system, this PhD work presented in 2010 covers a novel technique patented in [75] that aims at recovering range and Doppler unambiguously by means of manipulations in the frequency domain.

- **Design of adaptive OFDM waveforms to detect and track targets**. In his PhD work reported in [38, 76, 77, 78, 79], Sen makes use of multi-objective algorithms to design the waveform in the frame of a cognitive radar where the current measurement is used to design the pulse in the next transmission. The focus of this work is on the development of algorithms to detect and track targets in the presence of multipath.

- **Derivation of signal processing methods for range and Doppler** when the radar signal is a continuous OFDM waveform that includes a systematic cyclic prefix [25, 27, 9]. These results form part of the substantial study on RadCom intended for car-to-car networks.

- **Improving the detection of fluctuating targets**. In this MSc work published in 2012 [80], Kafshgari et al. suggest that the signal-to-noise ratio (SNR) needed to achieve a given probability of detection decreases as the number of subcarriers composing the multicarrier signal increases.

This enumeration attests the growing interest of the radar community to comprehend the benefits offered by the multicarrier waveform in the context of a monostatic radar. Besides, many other works have been published that investigate the use of OFDM signals for synthetic aperture radar (SAR), multiple input multiple output (MIMO) radar, ultra-wideband radar, etc.. Our interest in this dissertation lies in the monostatic radar case.

2.5 Summary

In this chapter, we proposed a comprehensive treatment of the OFDM block diagram for telecommunication engineering. We illustrated with examples the main steps from the communication message to be transmitted to the decoded message on receipt. Next, we inspected some of the typical impairments encountered with continuous OFDM for communication and evoked the concern raised by synchronisation errors. We addressed the impact of those impairments in the framework of a pulsed OFDM radar and finally reviewed the most relevant literature in the field.

Chapter 3

OFDM pulsed radar waveform and alternative processing methods[3]

The allure of OFDM radar to applications aiming to combine communication and radar providing continuous transmission of the waveform has somewhat strayed OFDM radar away from the first milestones erected about a decade ago by Levanon et al. in [13] and [31]. At that time, mainstream ideas were to incorporate the multicarrier phase coded (MCPC) structure in pulsed waveforms to enhance radar functionalities such as reduced sidelobes in the range domain, low range ambiguities and high spectral efficiency. Analyses focused on the features of the ambiguity function (AF) and little attention was paid to questions, viz: what processing can be applied onto the OFDM pulse train to estimate both range and Doppler; how do the scenario and processing constrain the waveform parameters?

[3] Based on Lellouch, G. et al. "Impact of the Doppler modulation on the range and Doppler processing in OFDM radar," in *Radar Conference, 2014 IEEE* (pp. 0803-0808) and Lellouch, G. et al. "Processing alternatives in OFDM radar," in *International Conference on Radar, 2014 IEEE* (pp. 1-6)

3.1 Introduction

From the very first ideas formulated in [18] till now, the continuous counterparts of both questions have been extensively researched and a processing technique that estimates the range and the Doppler of a target at short range has been proposed in [9], in the context of car-to-car radar network. Further analyses regarding the behaviour of the processing under noisy conditions in terms of accuracy of the estimates were reported in [81], and some efforts were spent to address the customisation of the waveform as far as radar and communication are concerned for some particular car-to-car scenarios [29].

In this chapter, we address these questions in the scope of pulsed waveforms. Our contribution aims at bridging the gap that remains between the continuous and pulsed designs as explained above. While Fig. 3.1 represents a typical train of M pulses, Fig. 3.2 illustrates the structure of an OFDM pulse for different ratios of the number of subcarriers N versus the number of symbols K. The main aspect is again the orthogonality property, which we introduced in light of Fig. 1.1.

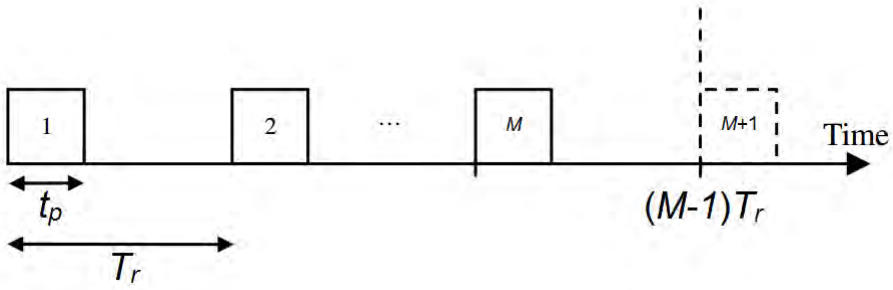

Figure 3.1: Train of OFDM pulses.

3.2 Needs for Doppler processing

Throughout this chapter we build our work assuming point targets such that the received signal is a delayed version of the transmitted signal multiplied by a com-

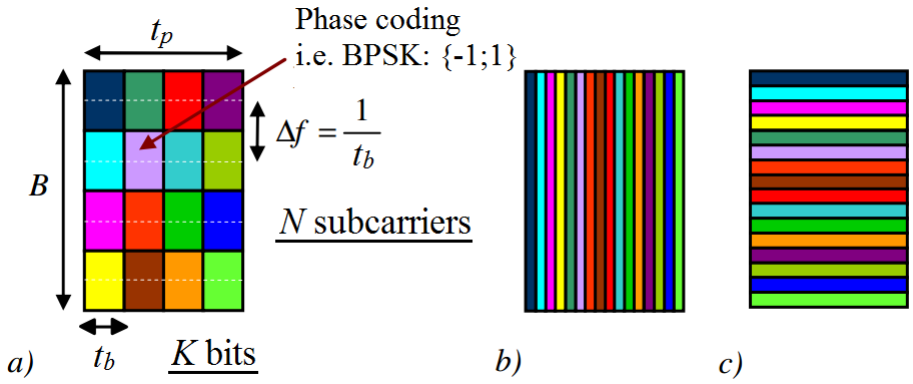

Figure 3.2: Time frequency structure of an OFDM pulse corresponding to a fixed time bandwidth product. a) intermediate, b) one subcarrier c) one symbol

plex exponential that represents the Doppler modulation. In other words we invoke the narrowband assumption for the OFDM pulses. We put this study in the background of a short range radar working at X-band, hence in our simulations, Doppler frequencies are calculated based on the carrier frequency f_0=10 GHz.

3.2.1 Our test bench

The test bench that we use for our simulations is first described.

3.2.1.1 OFDM symbol generation

To generate an OFDM symbol, the simplest technique is to apply an IDFT over a sequence of N phase codes [18]. The IDFT can be performed with the IFFT algorithm, and provided that each phase code has been weighted, the signal results in a weighted sum of N harmonic components with real and imaginary parts. The starting phase of each harmonic equates to the phase code. In communication systems, the information is coded onto these phase codes, which would belong to a particular alphabet, binary phase shift keying, quadrature phase shift keying etc. (BPSK, QPSK) and by means of a DFT, the weighted phase codes and then the information is retrieved at the receiver. Symmetrically,

DFT is usually performed with the FFT algorithm. The weights are primarily used to control the energy content of the signal. They can either be equal or, if we want to put more energy on some of the components, they can be adjusted accordingly.

3.2.1.2 OFDM pulse generation

If the pulse needs to include not one but K symbols, the IDFT can simply be applied over an $N \times K$ matrix of weighted phase codes rather, where each column vector of the matrix corresponds to one symbol and each row corresponds to an harmonic component also called subcarrier. After the IDFT, each column of the resulting matrix[4] contains complex time domain samples of the corresponding symbol. To construct the pulse, the matrix can be reshaped into a longer column vector of length NK.

3.2.1.3 OFDM pulse train generation

A complete waveform composed of M OFDM pulses can be generated by repeating the previous steps for each pulse. Eventually, the waveform is described by a new $NK \times M$ matrix.

3.2.1.4 Synthetic data generation

One way around the problem of memory limitation with simulated radar data is to limit the data model to the received echoes. Hence, we build an echo structure in the same way we constructed a waveform structure on transmit. The echo is also an $NK \times M$ matrix but the values reported in each column now consist of the values of the received pulses as intercepted by the time gates. Because we assume that the received signal is at baseband and sampled at the critical sampling frequency[5], $f_s = N\Delta f = B$, the received pulse will intercept as many as

[4] Assuming that the IDFT operates column-wise like it is the convention in Matlab
[5] The sampling period and the time resolution are equal

NK time gates. Δf is the subcarrier spacing and B is the bandwidth of the OFDM pulse. We assume that the pulses are not received in a blind zone.

3.2.2 Ambiguity function

The ambiguity function as defined by Woodward [36] is a valuable tool in radar engineering. However, despite the concise formulation, caution shall be employed when trying to interpret it. In our case, we want to understand how the features revealed by the ambiguity function affect the design of the radar processing. To stress the relevance of the ambiguity function one must recall that the matched-filter has been shown to be the optimum processing that maximises the signal-to-noise ratio for any signal buried in AWGN [32].

3.2.2.1 Single matched-filter

To start our analysis, let us first consider a Doppler cut, say, at Doppler f_{D_1}. In the general definition, the level of the AF along the Doppler cut essentially indicates the amount of correlation between the signal itself and a time delayed Doppler modulated copy of it. If the level is small or even zero except at one delay τ_1, we can say two things depending on how we interpret this information. On one hand we could be satisfied and say that this high value at τ_1 means that a detection is possible despite the mismatch. On the other hand we will rather say that the pair (τ_1, f_{D_1}) is an ambiguity. The underlying reason why we would give more credit to our second statement is that detection on its own matters less if we are unable to link it to some estimates, which in the end characterise the measurement. In our case, the parameters which we want to estimate are: range and Doppler.

Ambiguity in the sense of the ambiguity function implies that, would the received echo (unknown delay, unknown Doppler) be processed by a single matched-filter, matched to the reference signal, there is an ambiguity on whether the underlying target is at (τ_1, f_{D_1}) or (τ_0, f_{D_0}) where the latter pair of coordinates defines the position of the central point on the ambiguity diagram (f_{D_0}=0).

If we now assume that the Doppler cut at f_{D_1} is zero for all delays (the previous ambiguity has been suppressed), the pessimist way to interpret this information is to say that our processing based on the single matched-filter will not give any detection when the echo returns with a Doppler modulation equal to f_{D_1}.

3.2.2.2 Bank of mismatched-filters

These observations put in light the fact that when we plan to use the concept of matched-filter to improve the signal-to-noise ratio, and are interested in finding the estimates of the corresponding detection, the ideal scenario is twofold. First, the ambiguity function of our reference signal shall exhibit a thumb tack shape with a narrow peak centred around the origin and null values in the rest of the domain of interest. Then, a bank of mismatched filters must be used to insure selectivity in Doppler. All filters would run in parallel, therefore, when one detection is observed, the Doppler associated to that particular filter becomes an estimate of the Doppler for that detection.

This ideal scenario is however hard to achieve in theory and in practice. In theory, it has been demonstrated that the volume of the ambiguity function is constant and independent of the signal. Also the peak of the normalised ambiguity function is achieved at the origin and is equal to 1 [36]. These two properties reveal the limits of the thumb tack ambiguity function. With a central peak value limited to 1, the volume which does not fit within this peak has to reappear somewhere else, at the cost of ambiguities or pedestal. In practice, the use of a bank of Doppler filters may impose a cumbersome computational load.

3.2.2.3 Ambiguity function of the OFDM pulse train

We are now ready to interpret the ambiguity diagram obtained when the reference signal is a train of OFDM pulses. In Fig. 3.3 the ambiguity diagram of a train of non-modulated OFDM pulses is plotted [82]. The narrowband assumption is considered. For the sake of readability, we restricted the domain in time to $\pm t_p$ where t_p is the pulse length. In Doppler, the domain has been limited

to the pulse repetition frequency (PRF) PRF. The symmetry property of the ambiguity function suggests that it is sufficient to study and plot two adjacent quadrants. We therefore look at the quadrants with positive Doppler. Note that oversampling has been used to produce these graphs. We added Fig. 3.4 to provide a better picture of the Doppler cut.

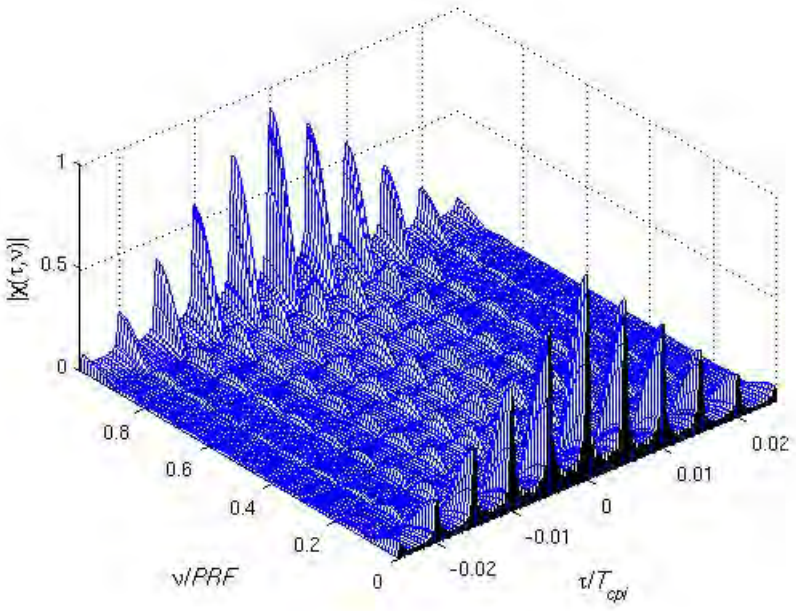

Figure 3.3: Ambiguity function for the train of OFDM pulses. One pulse comprises K=5 symbols and N=10 subcarriers. The phase codes are 1 (no coding) and the weights are equal such that the energy E of the pulse is normalised to unity. The waveform consists of M=10 pulses. The bandwidth is B=10 MHz so that the subcarrier spacing is Δf=1 MHz. Therefore t_b=1 μs and t_p=5 μs. The pulse repetition interval is T_r=20 μs=4t_p.

In delay, we can observe the ambiguities caused by the K non-modulated symbols at kt_b, $k = 1, 2...K$ where t_b is the symbol or bit duration. Random phase coding will bring them closer to zero. In Doppler, we see that the first ambiguity occurs at PRF. Stretching the limits of the Doppler cut to a bit more than Δf, in Fig. 3.5(b) (note that Δf=20PRF in our example) we observe more ambiguities at multiples of PRF. We also observe that instead of ambiguities (peaks), we have nulls at 4PRF, 8PRF etc.. The reason behind this is that, the same as

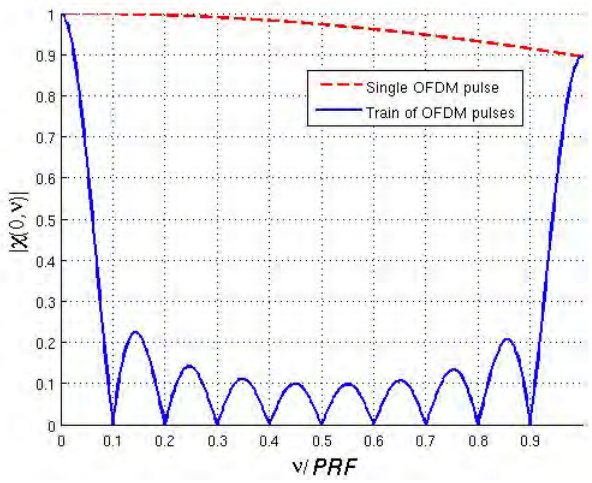

Figure 3.4: Doppler cut before the first ambiguity at PRF.

in the case of a train of identical non-modulated pulses discussed in [36], the resulting Doppler cut is the product of the Doppler cut for a single pulse with the expression $|\sin(M\pi f_D T_r)/M\sin(\pi f_D T_r)|$. The dashed curve is the Doppler cut of the single non-modulated OFDM pulse. We also note in Fig. 3.4 that the first null happens at $f_{D1^{st}\text{null}} = PRF/M$ as compared to $f_{D1^{st}\text{null}} = 4PRF$ for the single OFDM pulse[6]. We can see that the coherent processing of M OFDM pulses has improved drastically the Doppler resolution offered by the single OFDM pulse.

Eventually, Fig. 3.5(a) reveals the many ambiguities at multiples of the pulse repetition interval (PRI) mT_r, $m = 1, 2...M-1$. Again, the use of random phase codes will mitigate those ambiguities too.

Hence, with the very same waveform parameters we apply random phase codes to obtain Fig. 3.6 and Fig. 3.7. In our case, the phase codes do not belong to any alphabet but their modulus is 1. The phases are chosen randomly in $[0, 2\pi[$. That way, all pulses are now different.

In comparison with Fig. 3.3 we observe that most ambiguities in time have been

[6] For these simulations that we have considered T_r=4t_p which implies for the single OFDM pulse a Doppler resolution equal to $1/t_p$ or $4PRF$

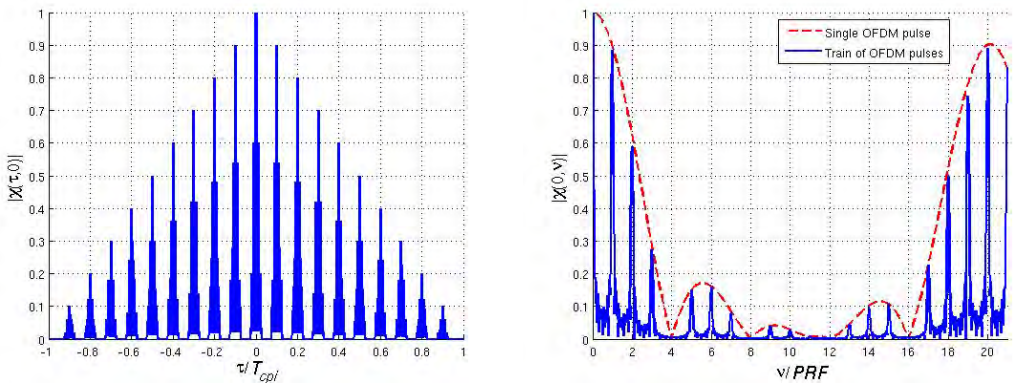

(a) Delay cut extended up to the CPI

(b) Doppler cut

Figure 3.5: Delay and Doppler cuts of the ambiguity function presented in Fig. 3.3.

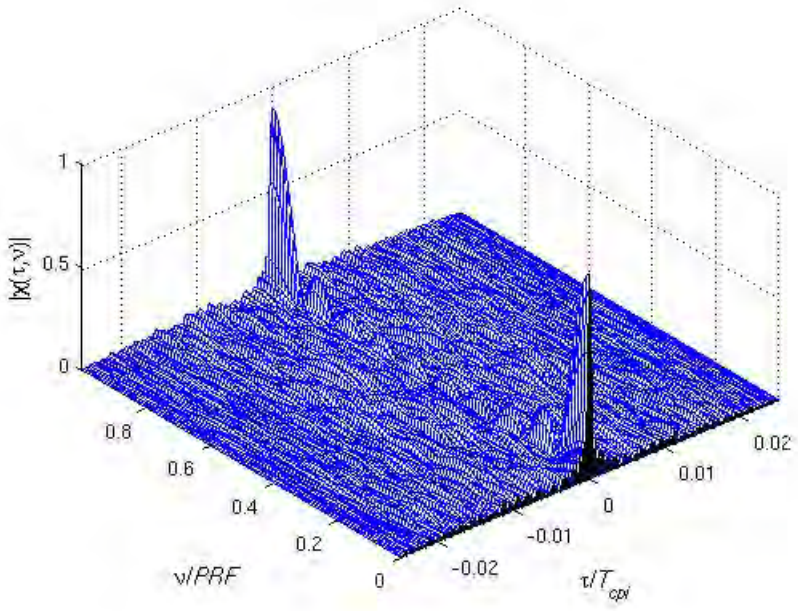

Figure 3.6: Ambiguity function for the train of OFDM pulses. The waveform parameters are unchanged but the phase codes are now random with absolute value unity.

reduced. From Fig. 3.7(b) we see that in Doppler, the subsisting ambiguities are those at multiples of PRF whose value remain lower than $\Delta f/2$ such that the

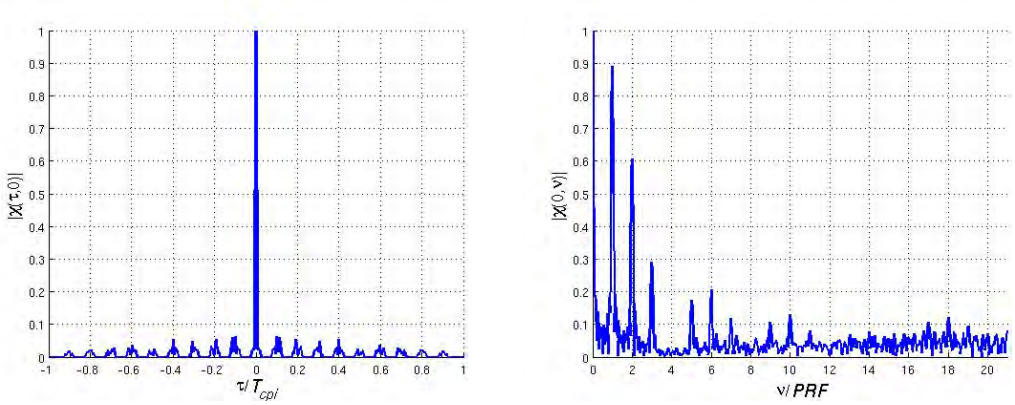

(a) Delay cut extended up to the CPI

(b) Doppler cut

Figure 3.7: Delay and Doppler cuts of the ambiguity function presented in Fig. 3.6.

effect of the random coding on the neighbouring subcarriers is not yet effective. It can thus be expected to have ambiguities as high as $10PRF$, which, with our set of parameters as defined in Fig. 3.3 corresponds to $\Delta f/2$.

However, because ambiguities need to be addressed in light of the processing we will see in Section 3.3 that they are not harmful. We can indeed be satisfied with the ambiguity function as it is now.

3.3 Processing alternatives

After this introductory discussion on the interpretation of the ambiguity function in the case of a train of OFDM pulses, we now present our processing alternatives. We show that they offer equal processing gains under ideal conditions and we elaborate on their respective outcomes, in particular we show that the second approach enables solving the ambiguity in Doppler.

3.3.1 Matched-filter and Doppler processing

The favourite technique used to process pulsed Doppler waveforms, often found in airborne radar applications, consists in applying subsequently a zero-Doppler matched-filter on the individual echoes and Doppler processing on the bunch of compressed samples in every time (or range) cell [36]. We refer to this technique as our *time-domain processing*. The advantage of this technique based on simple operations (especially if the correlation is implemented with DFT and IDFT) is to put in practice the concept of a bank of mismatched filters, without having the burden of the computational load mentioned earlier. The necessary condition is that the individual pulses shall be Doppler tolerant. We aim to show how this technique can be applied onto our train of OFDM pulses.

3.3.1.1 Doppler tolerance of the OFDM pulse

Like the LFM pulse, the OFDM pulse offers good tolerance to Doppler. In [6], an expected value for the compression loss due to Doppler has been calculated. The calculation has been based on one single OFDM symbol. The compression loss indicates the loss at the output of the matched-filter as compared to the zero Doppler case. To maintain the compression loss lower than 1 dB it was shown that the Doppler frequency shall not exceed $\Delta f/4$. Because we are interested in the compression loss for the more general case of an OFDM pulse composed of K symbols, we derive analytically the matched-filter output. And since our echo is assumed to be modulated by a Doppler frequency f_D we use the notation of the ambiguity function $\chi(\tau, f_D)$. The expression becomes:

$$\chi(\tau, f_D) = \int_{-\infty}^{+\infty} s(t)s^*(t-\tau)\exp(j2\pi f_D t)dt, \tag{3.1}$$

where $s(t)$ is our OFDM pulse. The guideline for the calculation is given in Fig. 3.8. The integration domain is split in two domains A and B.

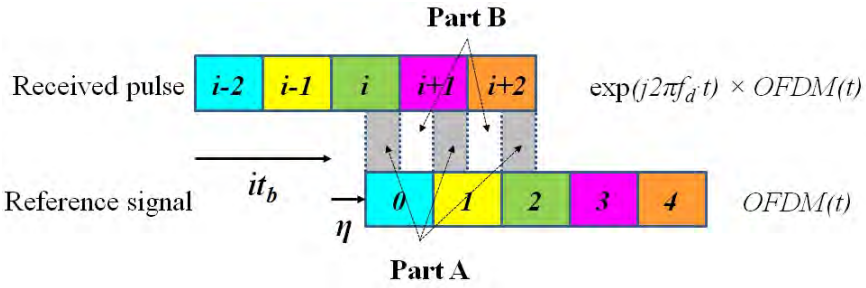

Figure 3.8: Calculation of the output $\chi(\tau, f_D)$.

In the end the output is expressed as:

$$\begin{aligned}\chi(it_b+\eta_{\text{tol}}, f_D) = &\sum_{q=1}^{N} \exp(j2\pi q\frac{\eta_{\text{tol}}}{t_b}) \times \sum_{n=1}^{N} w_n w_q^* \\ &\times \Bigg[I_1 \sum_{k=0}^{K-1} a_{n,k} a_{q,k-i-1}^* \exp(j2\pi f_D k t_b) \\ &+ I_2 \sum_{k=0}^{K-1} a_{n,k} a_{q,k-i}^* \exp(j2\pi f_D k t_b) \Bigg],\end{aligned} \tag{3.2}$$

where $\tau = it_b + \eta_{\text{tol}}$, i is an integer, $0 \leq \eta_{\text{tol}} < t_b$, and where I_1 and I_2 are given by,

$$I_1 = \eta_{\text{tol}} \exp(j\beta_{\text{tol}}) \text{sinc}(\beta_{\text{tol}} + \pi f_D \eta_{\text{tol}}) \exp(j\pi f_D \eta_{\text{tol}}), \tag{3.3}$$

$$\begin{aligned}I_2 = &(t_b \varepsilon_{\text{tol}} - \eta_{\text{tol}}) \exp(j\beta_{\text{tol}}) \text{sinc}(\beta_{\text{tol}} - \pi f_D (t_b - \eta_{\text{tol}})) \\ &\times \exp(j2\pi f_D \eta_{\text{tol}}) \exp(j\pi f_D (t_b - \eta_{\text{tol}})),\end{aligned} \tag{3.4}$$

with $\beta_{\text{tol}} = \pi(n-k)\Delta f \eta_{\text{tol}}$ and $\varepsilon_{\text{tol}} = f_D/(f_D + (n-k)\Delta f)$ and where we define $a_{n,k}$ as zero for "illegal" values of k (i.e., $k > K-1$ or $k < 0$).

To find the compression loss on the main peak at $\tau = 0$ we can analyse the ratio $|\chi(0, f_D)|/|\chi(0,0)|$. We propose to formulate the compression loss in terms of a positive quantity in dB, as:

$$\text{L}_{\text{PCdB}}(f_D) = 20 \log |\chi(0,0)| - 20 \log |\chi(0, f_D)|. \tag{3.5}$$

This function is plotted in Fig. 3.9. In order to cancel the effect of the random phase codes in Eq.(3.2) we ran a fifty run Monte Carlo simulation and considered the mean value of these fifty $[\chi(0, f_D)]_{1...50}$ functions. We observe that the 1 dB compression loss occurs at $|f_{D1\text{dB}}| \simeq \Delta f/4K$. This observation complies with the result given in [6] for the single symbol case. Indeed, an equivalent one symbol pulse would be obtained when the subcarrier spacing is dropped to $\Delta f/K$.

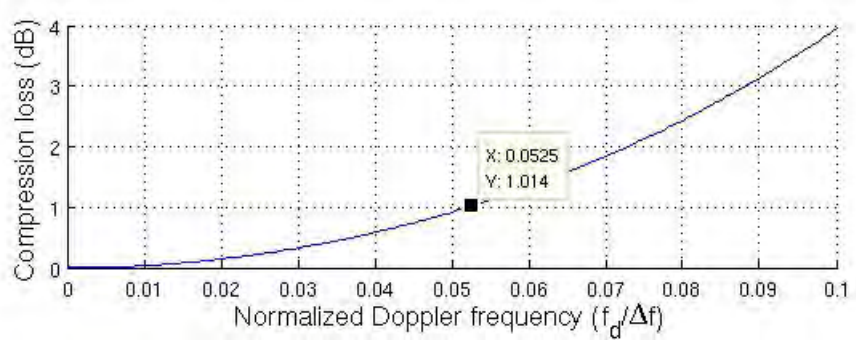

Figure 3.9: Main lobe compression loss as a function of the Doppler frequency for N=10 subcarriers and K=5 symbols. The bandwidth is B=10 MHz.

If a train of OFDM pulses is sent towards a moving point target giving rise to a Doppler frequency lower than $f_{D1\text{dB}}$ we can expect that the peak after Doppler processing would be at worst -1 dB. This statement assumes that the received echoes have their energy normalised to unity, which can be assumed given our synthetic environment. Note that we have not considered the straddling loss due to the misalignment of the point target with respect to the range cells. Eventually, in Fig. 3.10 we show the range Doppler image, obtained as a result of the matched-filter and Doppler processing for a slow moving target.

In this ideal case, the peak is almost at 0 dB and the sidelobes in Doppler at -13.3 dB result from the Doppler DFT. They can be reduced with windowing. We see that in the rest of the domain we are dealing with sidelobes at around -30 dB or less. Note that the scale in range has been adjusted to centre the point target.

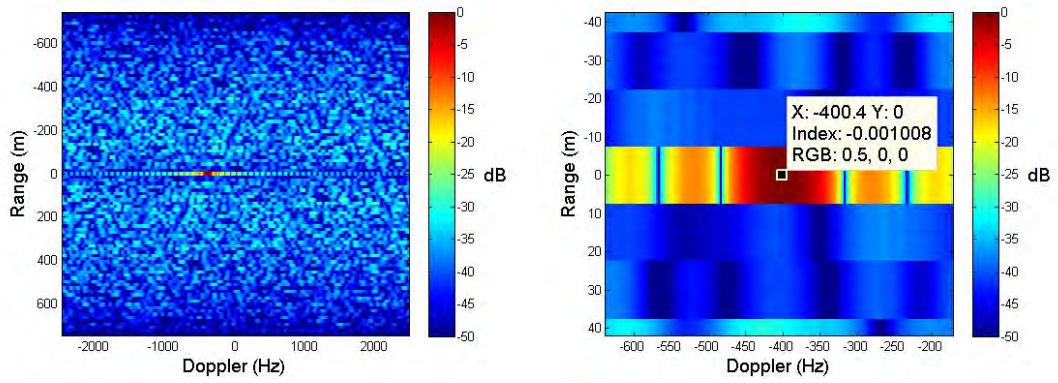

(a) Range Doppler image

(b) Zoom around the peak

Figure 3.10: Range Doppler image resulting from mached-filter and Doppler processing of a train of M=60 diverse OFDM pulses, each composed of N=10 subcarriers, K=5 symbols and with a bandwidth B=10 MHz. All NKM phase codes are randomly selected. PRI is equal to 200 μs. The range resolution is δR=15 m and the Doppler resolution is δf_D=83.3 Hz. The point target is located at R=2294.85 m and it flees the radar with a radial velocity $|v_r|$=6 m/s, so that the Doppler frequency is f_D=-400 Hz.

3.3.1.2 Ambiguities

As expected, the use of random phase codes has reduced all close range ambiguities resulting from the neighbouring symbols. The range domain in Fig. 3.10 is restricted to $\pm ct_p/2 = \pm 750$ m, where c is the speed of light, but we could show that the rest of the ambiguities at multiples of the PRI (equivalently, $\pm mcT_r/2$ in range) have also been reduced. In Doppler, the domain is restricted to $\pm PRF/2$ and there is no point to extend it further. Indeed, it is well-known that the DFT is ambiguous at the sampling frequency. In the case of pulsed Doppler waveforms, the sampling rate of the input data that come into the Doppler DFT is equal to PRF. This unique characteristic supports our earlier statement and demonstrates that the ambiguities observed in the ambiguity function at multiples of the PRF in the Doppler domain are of no harm because the processing is in essence ambiguous with the same ambiguity rate. Therefore, the point target retrieved with f_D=-400 Hz could hide a different Doppler frequency e.g. -5.4 kHz, 4.6 kHz, 9.6 kHz etc.

3.3.1.3 Processing gain

Although we have worked with normalised echoes of unit energy and showed that in the ideal case (no compression loss, no straddling loss), the peak in the range Doppler image is 1 (or 0 in dB scale), the peak value is not a measure of the processing gain. The processing gain tells by how much the coherent integration increases the signal-to-noise ratio and it is a critical figure-of-merit as far as detection and accuracy are concerned. Our two-stage processing results in two contributions. The first processing gain g_1 is called the pulse compression gain and is equal to the time bandwidth product. With the orthogonality property of the OFDM signal, the time bandwidth product is simply expressed in terms of the product KN hence $g_1 = KN$. The second processing gain results from the DFT in the Doppler processing. It is well known that the DFT improves the signal-to-noise ratio by an amount equal to the number of samples [32], when the initial signal has the form of a complex exponential times a constant and the noise is AWGN. With M the number of samples, the corresponding processing gain is g_2=M. The cumulated gain is then:

$$G_1 = KNM. \tag{3.6}$$

3.3.2 Range Doppler processing in the frequency domain

After characterising our first processing solution we now look into our second solution, which has been inspired by communication processing techniques for OFDM. As pointed out in [9], in radar, the waveform and the processing shall withstand the effect of Doppler and at the same time, allow to retrieve the Doppler shift in order to estimate the relative velocity of the target of interest with respect to the radar. In this section, we first assume that the Doppler effect is negligible within the pulse and show how the processing simplifies.

3.3.2.1 Model of the received echo

Moving away from the narrowband assumption to deal with fast targets that infer high Doppler modulations, we introduce a realistic model for the received echo whose main attribute consists in accounting for the migration in range. Note that Fig. 3.10 resulted from using this very same model.

- Continuous model

The transmitted OFDM waveform $s(t)$ can be expressed as:

$$s(t) = \left(\sum_{m=0}^{M-1} u_m(t - mT_r) \right) \exp(j2\pi f_0 t), \tag{3.7}$$

where $u_m(t)$, T_r and f_0 correspond respectively to the m^{th} of the M transmitted OFDM pulses, the pulse repetition interval and the carrier frequency. Subsequently, we suggest to model the received waveform as the product of two expressions in order to distinguish two contributions. In this work we assume a single point scatterer and consider that its position relative to the radar is varying linearly throughout the time-on-target. The kinematic representation of the range is given by $R(t) = R_0 - v_r t$, with R_0 the initial range at t=0 and v_r the constant radial velocity. We use the convention that a closing target has a positive radial velocity and a positive Doppler shift. A closing target has a negative range rate V however. A receding target has the opposite signs.

The first contribution consists in the echo pulses themselves. The returned echo resulting from the m^{th} pulse after it bounces off the scatterer can be expressed as:

$$s_{b1\,m}(t) = \varsigma u_m(t - mT_r - \tau(t)), \tag{3.8}$$

where ς is the complex scattering coefficient of the point scatterer and $\tau(t)$=$2R(t)/c$ is the two-way time delay from the radar to the scatterer versus time with c the speed of light.

The second contribution is the Doppler frequency f_D, which comes as a result of the compression or dilation of the carrier frequency induced by the scatterers'

linear motion towards or away from the radar according to:

$$f_D = \frac{2v_r f_0}{c}. \tag{3.9}$$

This second term appears after down-conversion and is independent of the pulse number. It can be characterised by:

$$s_{b2}(t) = \exp(-j2\pi f_0 \tau_0) \exp(j2\pi f_D(t - \tau_0)), \tag{3.10}$$

where $\tau_0 = \tau(0)$. The resulting signal at baseband for the m^{th} transmitted pulse can therefore be expressed as:

$$s_{bm}(t) = s_{b1m}(t) s_{b2}(t). \tag{3.11}$$

The origin of the time axis coincides with the "raising edge" of the first pulse, would the pulse have a rectangular shape. The expression for $u_m(t)$ is given [44] by:

$$u_m(t) = \sum_{n=0}^{N-1} w_n \left(\sum_{k=0}^{K-1} a_{n,k,m} r_k(t) \right) \exp(j2\pi n \Delta f t), \tag{3.12}$$

where

$$r_k(t) = \begin{cases} 1 & kt_b \leq t \leq (k+1)t_b \\ 0 & \text{elsewhere} \end{cases}$$

is the window function scaled to the symbol duration t_b. In Eq.(3.12) N stands for the number of subcarriers used per pulse and Δf is the subcarrier spacing that is inversely proportional to the symbol duration $\Delta f = 1/t_b$. As explained in Section 1.1, this relation establishes the condition for orthogonality to hold. We will see in Section 3.4 how detrimental it is to deviate from this condition. The terms w_n and $a_{n,k,m}$ are respectively the frequency weight applied on subcarrier n of any symbol and any pulse and the phase code applied on the subcarrier n of symbol k from pulse m. Note that we use the weights to normalise the pulse so that it has unit energy. The complex phase codes considered in our analysis have unit magnitude, $|a_{n,k,m}| = 1$.

- Discrete model

Following this preparation and recalling that in the receiver the same critical sampling rate as used to generate the OFDM pulse shall be employed to retain the benefit of the signal structure, it is now possible to move on towards the discrete model of the received signal.

Importantly, we assume to have prior knowledge of the point target position, since our processing considers snapshots of the received signal on a fix set of time gates where the echo is expected to lie, as shown in Fig. 3.11. These time samples are collected at a rate equal to the pulse bandwidth, hence this dimension is often referred to as fast time. On the other hand, the pulse number dimension is often called slow time because the sampling interval in that dimension, which is the radar PRI, is much greater [32, chap. 14]. Another critical assumption is that throughout the time-on-target range walk by more than one range gate does not occur. Seemingly binding, these assumptions are reasonable if we would consider a tracking radar. In order to derive the signal model we define p_0 as the first time gate intercepted by the received echo at any sweep. It is used as a reference for the assessment of various phase delays and given by:

$$p_0 = [\text{floor}\,(\tau_0/(t_b/N)) + 1]t_s. \tag{3.13}$$

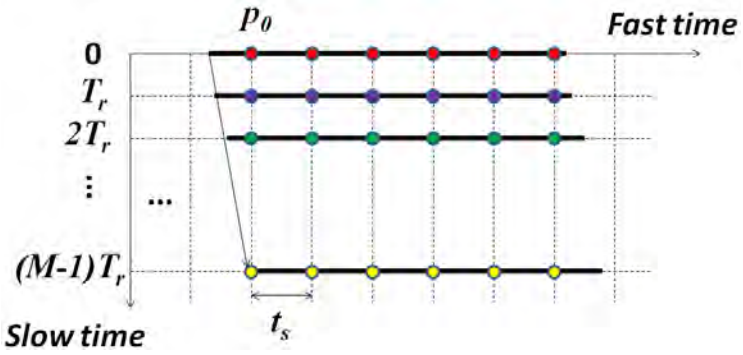

Figure 3.11: Data model of the discrete OFDM pulse for moving scatterers scenarios. Our processing assumes that the echoes received from the point scatterer intercept the very same time gates. The circles represent the samples obtained for all echoes. The red circles stand for the samples of the first echo, the blue for the samples of the second echo, etc..

From this model we can draw a closed form expression for the received signal. The N-element column vector composing the k^{th} symbol of the complex baseband echo resulting from the m^{th} pulse returning from the point scatterer is given in its discrete form by:

$$\mathbf{s_{bk,m}} = \varsigma\alpha_0\kappa_0\mathbf{\Delta_{k,m}}\mathbf{F^{-1}}\mathbf{\Gamma_m}\mathbf{D_{k,m}}\mathbf{w}. \tag{3.14}$$

The derivation of this expression is lengthy but quite intuitive if the data model as presented in Fig. 3.11 is taken into account. The various terms are given hereafter:

$$\alpha_0 = \exp(-j2\pi f_0\tau_0), \tag{3.15}$$

$$\kappa_0 = \exp(j2\pi f_D\Delta\tau_0), \tag{3.16}$$

$$\mathbf{\Delta_{k,m}} = \eta_{k,m}\text{Diag}\{1\ \eta\ \eta^2\ \ldots\eta^{N-1}\}, \tag{3.17}$$

$$\mathbf{F^{-1}} = \begin{bmatrix} 1 & 1 & 1 & \ldots & 1 \\ 1 & \beta & \beta^2 & & \beta^{N-1} \\ 1 & \beta^2 & \beta^4 & & \beta^{2(N-1)} \\ & \vdots & & \ddots & \vdots \\ 1 & \beta^{N-1} & \beta^{2(N-1)} & \ldots & \beta^{(N-1)^2} \end{bmatrix}, \tag{3.18}$$

$$\mathbf{\Gamma_m} = \text{Diag}\{1\ \gamma_m\ {\gamma_m}^2\ \ldots{\gamma_m}^{N-1}\}, \tag{3.19}$$

$$\mathbf{D_{k,m}} = \text{Diag}\{a_{0,k,m}\ a_{1,k,m}\ \ldots\ a_{N-1,k,m}\}, \tag{3.20}$$

$$\mathbf{w} = [w_0 \ldots w_{N-1}]^T, \tag{3.21}$$

where:

$$\eta_{k,m} = \exp(j2\pi f_D(mT_r + kt_b)), \tag{3.22}$$

$$\eta = \exp(j2\pi f_D t_b/N), \tag{3.23}$$

$$\beta = \exp(j2\pi/N), \tag{3.24}$$

$$\gamma_m = \exp(j2\pi\Delta f\Delta\tau_m). \tag{3.25}$$

Eventually the term $\Delta\tau_m$ in Eq.(3.25) is:

$$\Delta\tau_m = p_0 - \tau_m, \tag{3.26}$$

where,

$$\tau_m = 2(R_0 + mT_r v_r)/c, \tag{3.27}$$

and m refers to the pulse number in the train, value comprised between 0 and M-1. It is interesting to note that in Eq.(3.18), $\mathbf{F^{-1}}$ is the IDFT matrix.

3.3.2.2 Simplifications

From the orthogonality relationship recalled earlier, one sees that short symbols and a fortiori short pulses (when few symbols are used to build the pulse) will be generated when the subcarrier spacing is large. Size of this spacing depends on the bandwidth tolerated by the system and the number of subcarriers desired. For example, a 1 MHz spacing will induce a 1 μs symbol. In pulsed radar, we are usually concerned with pulse lengths in the range of few micro seconds. From Eq.(3.9), we can assess the values for Doppler frequencies at X-band (10 GHz) and derive the resulting phase extent within, let's say, a 5 μs pulse duration.

Table 3.1: Doppler modulation over a 5 μs pulse (f_0=10 GHz)

Speed (km/h)	Speed (m/s)	Doppler (kHz)	Phase extent (rad)
50	14	0.93	0.03
500	140	9.3	0.3
5000	1400	93	3

The values presented in Table 3.1 show that for low radial velocities, the phase extension of the Doppler shift within the pulse will be small enough to assume that:

$$\mathbf{\Delta_{k,m}} \approx \mathbf{\Delta_m} \tag{3.28}$$

$$= \exp(j2\pi f_D m T_r)\text{Diag}\{1 \ \dots \ 1\} \tag{3.29}$$

$$= \varrho_m \text{Diag}\{1 \ \dots \ 1\}. \tag{3.30}$$

As a result, the k^{th} symbol of the m^{th} pulse returning from the point scatterer given earlier by Eq.(3.14) reduces to:

$$\mathbf{s_{bk,m}} = \varsigma \alpha_0 \kappa_0 \varrho_m \mathbf{F^{-1}\Gamma_m D_{k,m} w}. \tag{3.31}$$

3.3.2.3 DFT processing

With the expression obtained in Eq.(3.31), the processing applied to retrieve both range and Doppler information follows the algorithm shown in Box 1.

Algorithm 1 Range Doppler processing

1: **for** sweep = 1 to M **do**
2: **for** $k = 1$ to K **do**
3: Apply a DFT of length N on $\mathbf{s_{bk,m}}$ and store the output in $\delta_{\mathbf{k,m}}$.
4: **end for**
5: Stack all K column vectors $\delta_{\mathbf{k,m}}$ in matrix $\mathbf{\Theta_m}$.
6: Multiply $\mathbf{\Theta_m}$ with the conjugate transpose matrix $(\mathbf{A_m})^H$ of the phase codes corresponding to pulse m.
7: Extract the N diagonal elements into the vector $\mathbf{d_m}$.
8: Divide the n^{th} element of $\mathbf{d_m}$ by the term $w_n \mathbf{b_m}[n]$ to create the new vector $\tilde{\mathbf{d}}_\mathbf{m}$
9: **end for**
10: Stack all M $\tilde{\mathbf{d}}_\mathbf{m}$ column vectors in matrix $\mathbf{\Lambda}$.
11: Apply a 2D-DFT with oversampling in both dimension on $\mathbf{\Lambda}$.

The new terms are given by:

$$\delta_{\mathbf{k,m}} = N \varsigma \alpha_0 \kappa_0 \varrho_m \mathbf{\Gamma_m D_{k,m} w}. \tag{3.32}$$

$$\mathbf{\Theta_m} = [\delta_{\mathbf{0,m}}\ \delta_{\mathbf{1,m}} \dots \delta_{\mathbf{K-1,m}}]. \tag{3.33}$$

$$\mathbf{A_m} = \begin{bmatrix} a_{0,0,m} & a_{0,1,m} & \dots & a_{0,K-1,m} \\ \vdots & \vdots & & \vdots \\ a_{N-1,0,m} & a_{N-1,1,m} & \dots & a_{N-1,K-1,m} \end{bmatrix} \tag{3.34}$$

$$\mathbf{b_m}[n] = \sum_{k=0}^{K-1} |a_{n,k,m}|^2. \tag{3.35}$$

$$\tilde{\mathbf{d}}_\mathbf{m}[n] = N\varsigma\alpha_0\kappa_0\varrho_m{\gamma_m}^n. \tag{3.36}$$

$$\mathbf{\Lambda} = [\tilde{\mathbf{d}}_\mathbf{0}\ \tilde{\mathbf{d}}_\mathbf{1} \dots \tilde{\mathbf{d}}_\mathbf{M-1}]. \tag{3.37}$$

3.3.2.4 Simulation results

In this section we present our simulation results conducted with the set of parameters as presented in Table 3.2. The weights have been chosen to normalise the echo energy to 1. The DFTs from step 11 have been normalised so that the peak in the range Doppler image for the stationary case (no distortion) equals to 1.

The first parameter of Table 3.2 denotes the phase code as being equal to a 5-Barker code identical sequence (IS). This implies that the sequence is repeated on each subcarrier. In other words, all subcarriers get the same coding for any symbol. This is harmful from a PMEPR perspective but it offers other interesting benefits as discussed in Section 3.5.

The scenario of a single target has been considered. From the data model described in Section 3.3.2.1, the range profile is meaningful over a portion smaller than the full range extent obtained at the output of the DFT. Essentially, the range extent after the DFT (applied on the columns of $\mathbf{\Lambda}$) is equal to $c/(2\Delta f)$=150 m but the values of interest will lie within the interval $[cp_0/2$-

Table 3.2: OFDM radar parameters

Symbol	Parameter Name	Parameter Value
$\mathbf{A_m}$	Phase codes	IS Barker +1,+1,+1,-1,+1
B	Bandwidth	10 MHz
Δf	Subcarrier spacing	1 MHz
K	Number of symbols per pulse	5
M	Number of pulses	60
T_r	Pulse repetition interval	200 μs
f_0	Carrier frequency	10 GHz
N	Number of subcarriers	10
t_b	Symbol duration	1 μs
f_s	Critical sampling frequency	10 MHz
t_p	Pulse duration	5 μs
δR	Range resolution	15 m
δf_D	Doppler resolution	83.3 Hz
δv_r	Velocity resolution	1.25 m/s
R_{ua}	Classical unambiguous range	30 km
R_{min}	Minimum range without eclipsing	750 m

$c/(2f_s)$;$cp_0/2$[=[2280;2295[m in the example considered. Regarding the Doppler DFT (applied on the rows of $\mathbf{\Lambda}$), the extent is equal to $1/T_r$ but to include positive and negative frequencies we centre the unambiguous window around 0, hence the interval $[-1/(2T_r); 1/(2T_r)[$. Although the term unambiguous window is meaningful when discussing Doppler, it is not applicable to range, since, as stressed in Section 3.3.2.2 the snapshot starts at a known value p_0.

In Fig. 3.12, the 2D sinc shape that results from the two orthogonal complex exponential terms in $\mathbf{\Lambda}$ is clearly identifiable. Both resolutions in range and Doppler comply with the expected values derived in Table 3.2. With the velocity considered in this example, γ_m can be approximated by γ_0. Indeed the extra phase obtained in the last pulse is negligible: $\Delta\phi = 2\pi\Delta f \cdot 2 \cdot 0.225/c = 9.4\times10^{-3}$, where 0.225 m is the range migration throughout the time-on-target.

In Fig. 3.13, the velocity has been increased. One sees that the extra phase $\Delta\phi = 2\pi\Delta f \cdot 2 \cdot 3.24/c \simeq 0.14$ is no longer negligible. Therefore $\mathbf{\Lambda}$ no longer consists of two orthogonal complex exponentials as assumed in [9] and some distortion occurs. The peak is now slightly shifted away from the true Doppler

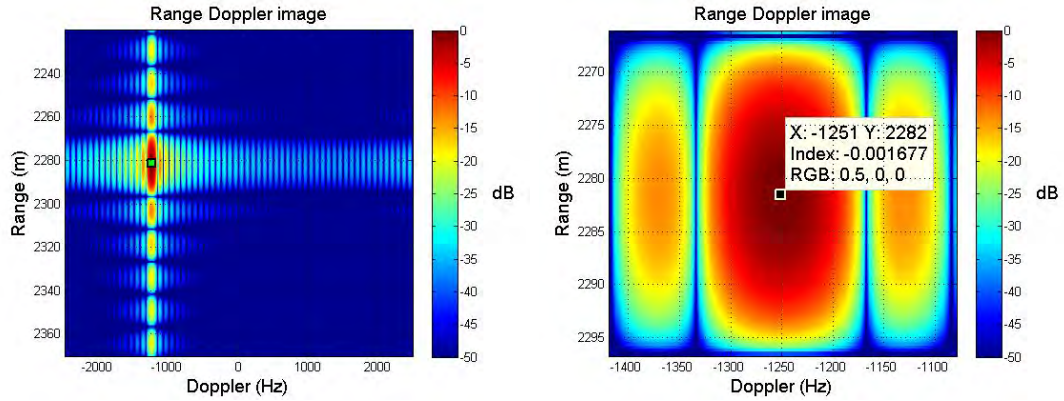

(a) Range Doppler image

(b) Zoom at the peak

Figure 3.12: Result of the range Doppler processing when the point target flees the radar with a velocity of 18.75 m/s. It corresponds to an unambiguous Doppler frequency f_D=-1.25 kHz. Its initial position is $R_0 = 2281.5$ m and the dot at the peak reflects the true position of the scatterer. During the time-on-target the target has travelled 22.5 cm. The value at the peak is equal to -0.002 dB.

(see Fig. 3.13(b)) and the sidelobe level as seen in Fig. 3.13(a) has increased in comparison with Fig. 3.12. The value at the peak has been reduced to -0.18 dB. The reduction results from the loss of orthogonality as developed in Section 3.4.

3.4 Impact of the loss of orthogonality

In this section, we investigate what happens when the assumption formulated in Eq.(3.28) no longer holds. This is equivalent to saying that the OFDM pulse suffers inter carrier interference (ICI), term that is commonly employed by telecommunication engineering related literature [12]. As opposed to [6], where the pulse compression loss of an OFDM symbol is analysed versus the Doppler frequency, we aim to assess the degradation of the range and Doppler estimates, as well as the loss at the peak.

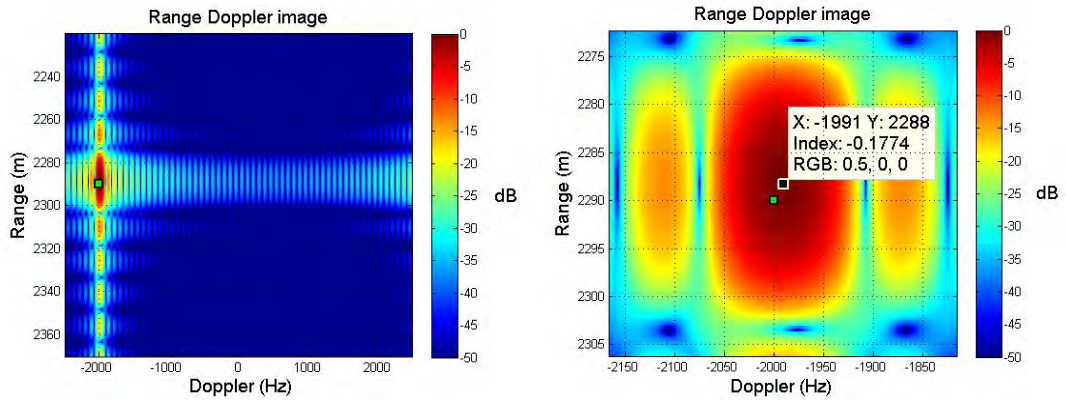

(a) Range Doppler image

(b) Zoom at the peak

Figure 3.13: The point target approaches the radar with a velocity of 270 m/s. It corresponds to a true Doppler frequency f_D=18 kHz, which folds back at $f_{D_{\text{amb}}}$=-2 kHz. Its initial position is R_0=2289.95 m and the dot at the peak reflects the true initial position of the scatterer. During the time-on-target the target has travelled 3.24 m. The value at the peak is equal to -0.18 dB.

3.4.1 Distortion term

Ignoring the constant phase terms, namely, ς, α_0 and κ_0, the result of applying the DFT upon $\mathbf{s_{bk,m}}$, as given by Eq.(3.14) is examined. In particular the value in bin p (p is an integer between 0 and $N-1$), which we write $\mathbf{B_{k,m}}[p]$ can be expanded into:

$$\begin{aligned}\mathbf{B_{k,m}}[p] = &\left(\sum_{q=0}^{N-1} w_q a_{q,k,m} \exp(j2\pi q \Delta f \Delta\tau_m)\right. \\ &\left.\times \left(\sum_{n=0}^{N-1} \exp(j2\pi \frac{(q-p)n}{N}) \exp(j2\pi f_D \frac{nt_b}{N})\right)\right) \\ &\times \exp(j2\pi f_D(mT_r + kt_b)).\end{aligned} \tag{3.38}$$

$\mathbf{B_{k,m}}[p]$ corresponds to a spectrum and p is an index that relates to a frequency. Several observations shall be stated. In the case where the Doppler frequency is small enough so that the second term in the n summation can be ignored, one sees that the geometric sum will equate to N when $q = p$ and 0 otherwise.

$\mathbf{B_{k,m}}[p]$ will therefore be equal to N times the other terms, independent of n, taking systematically $q = p$. When we further neglect the kt_b phase term in the last factor, which is fine when the Doppler effect is negligible within the duration of the pulse, we end up with $\mathbf{B_{k,m}} \propto \delta_{\mathbf{k,m}}$ as given in Eq. 4.21, where the proportionality is used to account for the constant phase terms that were not included in $\mathbf{B_{k,m}}$. When the Doppler frequency is large enough so that the contribution of the Doppler shift within the pulse is no longer negligible, we see that the summation over n when $q \neq p$ will no longer be 0, therefore a distortion term is introduced. Intuitively, this result makes sense since we have calculated the value for the bin p in the output of the DFT, while the frequency of interest has slightly shifted away from $p\Delta f$ to $p\Delta f + f_D$.

3.4.2 Special case of the Identical Sequence

As mentioned before, when identical sequences (IS) are used to build the phase code matrix $\mathbf{A_m}$, one has:

$$\forall n \; \forall k \; \forall m \quad a_{n,k,m} = a_{k,m}. \tag{3.39}$$

Therefore the phase code terms can be left out of the summation in Eq.(3.38) and assuming unitary weights (note that their effect is anyway negligible as long as they are all equal), $\mathbf{B_{k,m}}$ can be expressed in its vector form as:

$$\mathbf{B_{k,m}} = \mathbf{g_m} a_{k,m} \exp(j2\pi f_D(mT_r + kt_b)), \tag{3.40}$$

where $\mathbf{g_m}$ is given by,

$$\begin{aligned} \mathbf{g_m}[p] = \Bigg(& \sum_{n=0}^{N-1} \exp(j2\pi f_D \frac{nt_b}{N}) \exp(-j\pi \frac{n}{N}(2p+1)) \\ & \frac{\sin(\pi N \Delta f \Delta\tau_m)}{\sin(\pi \Delta f \Delta\tau_m + \frac{\pi n}{N})} \Bigg) \\ & \times \exp(j\pi(N-1)\Delta f \Delta\tau_m). \end{aligned} \tag{3.41}$$

Remark that would the delay coincide with one time gate, $\Delta\tau_m$=0, a simpler expression would be obtained,viz.

$$\mathbf{B_{k,m}}[p] = N a_{k,m} \exp(j2\pi f_D(mT_r + kt_b)). \tag{3.42}$$

Thus, in the general case, $\mathbf{g_m}$ introduces a complex distortion that depends not only on the Doppler frequency but also on the time offset $\Delta\tau_m$. From pulse to pulse, the migration implies that the distortion will vary although Doppler remains the same. Interestingly, this distortion term has no dependence on the symbol index k. We show in Fig. 3.14 that it is possible to estimate Doppler, $\hat{f_D}$ with a single pulse. The idea is fairly simple. After step 4 of our processing, at every frequency bin, we track the phase information over the K symbols present in the pulse. After the demodulation, the phase codes $a_{k,m}$ are removed from Eq. 3.42. Although the resolution is coarse, since the DFT integrates over the pulse duration (few μs), an unambiguous estimate of the Doppler frequency is retrieved. With a pulse designed with the parameters as in Table 3.2, the ambiguous Doppler is equal to Δf=1 MHz and will therefore be higher than most Doppler frequencies of interest. An example is given in Section 3.5.

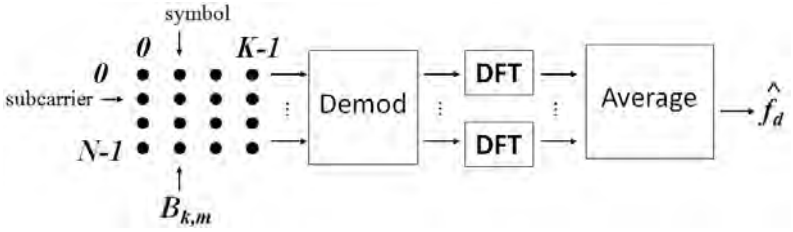

Figure 3.14: Intermediate processing applicable on the individual echo to extract the Doppler frequency unambiguously.

3.4.3 Complete solution of the DFT processing

Following the analysis of the previous section, the new expression for $\delta_{\mathbf{k,m}}$ can be formulated as:

$$\delta_{\mathbf{k,m}} = \mathbf{s_m} a_{k,m} \exp(j2\pi f_D k t_b). \tag{3.43}$$

where $\mathbf{s_m}$ is a N-element vector.

$$\mathbf{s_m} = \varsigma\alpha_0\kappa_0\mathbf{g_m}\exp(j2\pi f_D m T_r). \tag{3.44}$$

Applying steps 5 to 7 of the algorithm introduced in Section 3.3.2.3, one gets for each of the N terms $\mathbf{d_m}[p]$ the following expression:

$$\mathbf{d_m}[p] = \mathbf{s_m}[p]\sum_{k=0}^{K-1}|a_{k,m}|^2\exp(j2\pi f_D k t_b). \tag{3.45}$$

Since we have assumed $|a_{k,m}| = 1$, $\mathbf{d_m}[p]$ simplifies further into:

$$\mathbf{d_m}[p] = \mathbf{s_m}[p]h(f_D, K, \Delta f), \tag{3.46}$$

where the function h that returns a scalar is given by,

$$h(f_D, K, \Delta f) = \exp(j\pi f_D(K-1)/\Delta f)\frac{\sin(\pi f_D K/\Delta f)}{\sin(\pi f_D/\Delta f)}. \tag{3.47}$$

Applying steps 8 to 10 results in the vector $\tilde{\mathbf{d}}_\mathbf{m}$,

$$\tilde{\mathbf{d}}_\mathbf{m}[p] = \mathbf{s_m}[p]h(f_D, K, \Delta f)/K. \tag{3.48}$$

and eventually the matrix $\mathbf{\Lambda}$ can be derived as:

$$\mathbf{\Lambda} = [\tilde{\mathbf{d}}_\mathbf{0}\ \tilde{\mathbf{d}}_\mathbf{1}\ldots\tilde{\mathbf{d}}_\mathbf{M-1}]. \tag{3.49}$$

3.4.4 Simulation results

In the next simulations, we show the effect of the distortion term $\mathbf{g_m}$ on the range Doppler image for the two scenarios presented in Section 3.3.2.4. It is clear from Fig. 3.15(a) that the reconstructed image is accurate for small velocities as expected from the analysis in Section 3.3.2.3, however high speed scenarios suffer a non negligible bias in Doppler as observed in Fig. 3.15(b). The same behaviour was observed at the output of the processing in Fig. 3.13. Note that in this

second scenario the Doppler frequency is anyway ambiguous. The Doppler bias is approximately 7.5 Hz and the range bias is about 1.6 m, which makes sense since the point target has travelled about 3.2 m through the time-on-target.

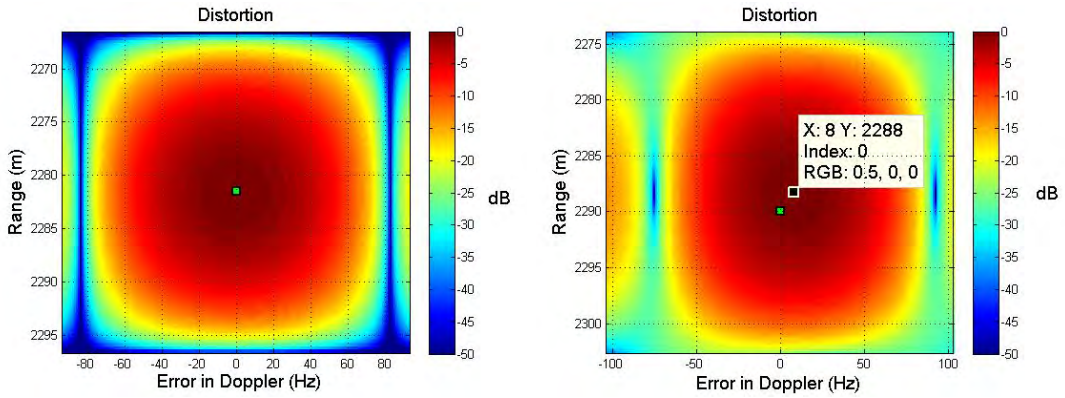

(a) No error (b) Error in Doppler

Figure 3.15: Analysis of the distortion matrix obtained from stacking the M column vectors $\mathbf{g_m}$. The plots show the results of a 2D-DFT for both scenarios as in Section 3.3.2.4. We normalised the outputs, hence the peaks are at 0 dB.

We then run a simulation with a target moving at a much faster radial velocity and observe the range Doppler image. In comparison with Fig. 3.12, the 2D sinc has been modified and a zoom around the peak in Fig. 3.16(b) reveals an offset from the true values (range and Doppler) even larger than in Fig. 3.15(b). Again, the peak falls at a range equal to the target location at about half the time-on-target, roughly 2288 m. In Doppler, the peak lies around 1.97 kHz, 30 Hz lower than the true folded Doppler (equal to 2 kHz) resulting from folding the true Doppler within the unambiguous Doppler window. This value seems consistent with our observation in Fig. 3.13(b). For a velocity about four times faster, the resulting Doppler bias is about four times higher. At X-band this Doppler bias translates into a radial velocity bias equal to 0.45 m/s. The value at the peak has been reduced to -2.95 dB.

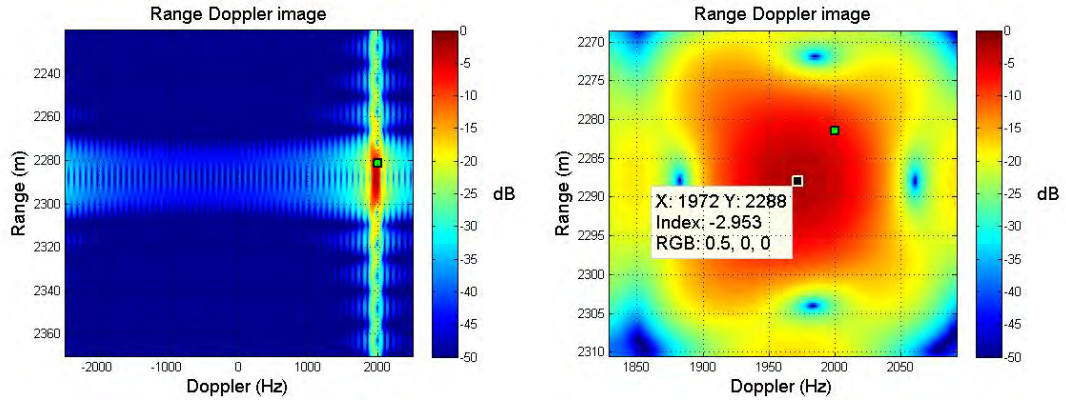

(a) Range Doppler image

(b) Zoom around the peak

Figure 3.16: The point target flees the radar with a velocity of 1095 m/s. It corresponds to a true Doppler frequency f_D=-73 kHz, which folds back at $f_{D_{\text{amb}}}$=2 kHz. Its initial position is R_0=2281.5 m and the dot at the peak reflects the true initial position of the scatterer. During the time-on-target the target has travelled 13.14 m. The value at the peak is equal to -2.95 dB.

3.5 Discussion

Our analyses demonstrate that the algorithm derived in Section 3.3.2.3 is suited to retrieve both range and Doppler estimates of the point target provided the bias in Doppler is negligible in comparison to the accuracy required. The position in range of the peak refers to the target position at half the time-on-target and is not considered to be a bias. With high Doppler frequencies, a complex distortion term causes a drop of the peak value, the ambiguous Doppler estimate becomes biased and the sidelobe pattern is modified. These unwanted effects can be mitigated by arranging the phase codes according to identical sequences. The main results for the three scenarios that we looked at are summarised in Table 3.3. Since our Doppler estimate retrieved from the range Doppler image is ambiguous, we have proposed two methods to estimate the unambiguous value. The first solution exposed in Section 3.4.2 works when the phase codes are arranged following identical sequences as shown in Fig. 3.17(a). The second solution consists in calculating the target radial velocity from the range profiles, which are obtained by taking DFTs on the columns of the output matrix $\mathbf{\Lambda}$. Oversampling

Table 3.3: Summary of the results

	v_r (m/s)	Peak loss (dB)	Ambiguous Doppler bias (Hz)
Case 1	18.75	0.002	0
Case 2	270	0.18	8
Case 3	1095	2.95	30

the output signal can improve the accuracy of the range estimates, thereby, the estimate of the radial velocity. In the example given in Fig. 3.17(b), an estimate of the radial velocity can be calculated as the difference between the last measurement and the first, knowing that there are M=60 sweeps apart. As a result, $\hat{v_r} = -\frac{\hat{R}_{\text{end}} - \hat{R}_{\text{start}}}{(M-1)T_r} = -1095$ m/s, where the minus sign results from our convention for the radial velocity. Note that the resolution obtained in our range profiles is inferred from the transmitted signal bandwidth (see Table 3.2).

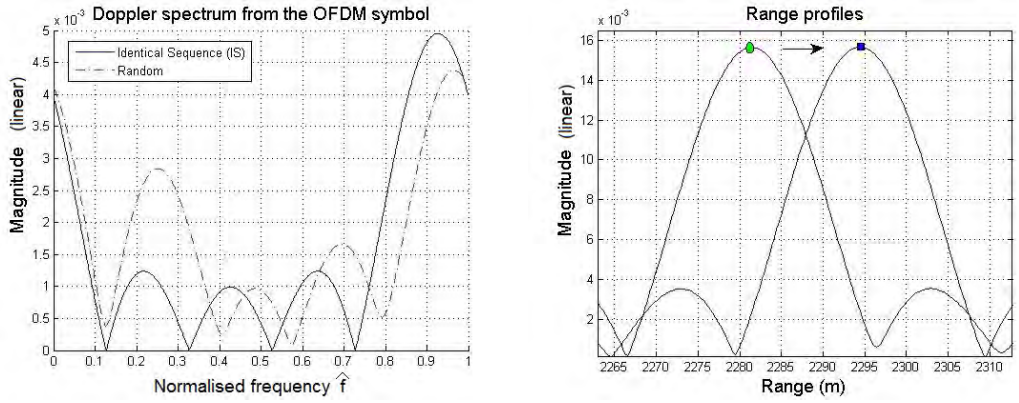

(a) Method 1 (b) Method 2

Figure 3.17: The scenario considered is the same scenario as used to build Fig. 3.16. In Fig. 3.17(a) the output of the processing presented in Fig. 3.14 is given when the phase codes follow either a IS or random coding. The estimate for Doppler is $\hat{f_D}$=$\Delta f(\hat{f} - 1)$ where $\hat{f}$=0.927. Hence $\hat{f_D}$=-73 kHz and $\hat{v_r}$=-1095 m/s. This applies when one uses a DFT while dealing with negative Doppler.

In the above method, we showed that it is possible to derive the processing steps with matrix and vector formulations such that the outcome itself can be compiled into a matrix $\mathbf{\Lambda}$, which, when processed by a 2D-DFT, also produces a range Doppler image. We also discussed how Doppler modulation impacts the range

Doppler image when its effect is no longer negligible within the pulse length. In this section, we wish to elaborate on the gain offered by that processing and show how it compares to the gain of the previous one. We first assume a low Doppler frequency so that the simplified formulation as given in [44] applies. The processing is characterised by the block diagram in Fig. 3.18. $\mathbf{s_{bk,m}}$ represents the N-long time domain vector of the k^{th} symbol from the echo corresponding to the m^{th} pulse, as introduced in Section 3.2.1.

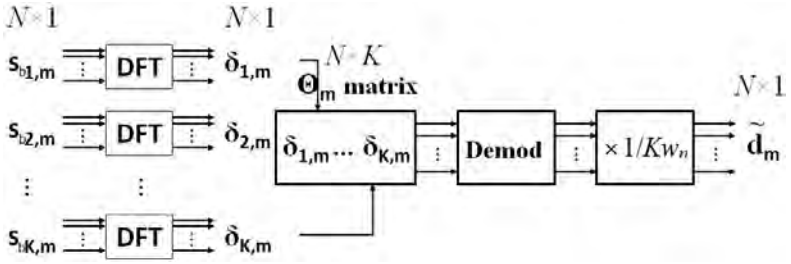

(a) 1st part of the processing: over the pulse

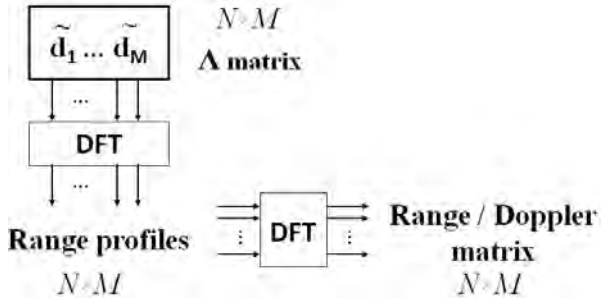

(b) 2nd part of the processing: over the waveform

Figure 3.18: Block diagram for our range-Doppler processing in the frequency domain.

3.5.1 Processing gain

When AWGN adds up onto the echo, the processing gain can be calculated as follows. The first sets of DFTs are used to topple in the frequency domain. Because our wideband signal is present as all frequency bins (assuming all N subcarriers are used), there is no SNR gain at that stage. Then, the demodulation block can be seen as a coherent integration and the gain is $g'_1 = K$. The normalisation

block that follows does neither contribute to any SNR gain nor any loss since both noise and signal are divided by Kw_n. Once the matrix $\mathbf{\Lambda}$ is formed, the first DFT generates a processing gain equal to $g_2' = N$ and the second DFT gives rise to a processing gain equal to $g_3' = M$. Therefore, we retrieve the same cumulated processing gain:

$$G_2 = KNM = G_1. \tag{3.50}$$

3.5.2 Range and Doppler estimates

In comparison to the first processing solution, our second technique enables to retrieve a finer estimate of the range when oversampling is used in the last DFTs. Provided that Doppler modulation is not detrimental on the individual pulses and that the range migration is negligible within the coherent processing interval (CPI), the range Doppler image localises the peak at the true point target range and ambiguous Doppler frequency. The merit of this technique is to resolve Doppler in one CPI while relying on standard Fourier transformations. The first set of DFTs applied on the columns of $\mathbf{\Lambda}$ generate as many range profiles as M where M is the number of pulses in the train. Differentiating further between two range profiles gives an estimate of the radial velocity. In Fig. 3.19, the scenario involves a point target moving with a radial velocity slightly higher than the unambiguous velocity. At first sight, the range Doppler image seems undistorted, which suggests a low and non ambiguous radial velocity. A coarse differentiation allows a first opinion. The target seems to be fleeing the radar at a radial speed of $|\hat{v_r}| \simeq \frac{7510.45-7509.98}{(M-1)T_r} \simeq 79.7$ m/s which translates into a Doppler frequency of $\hat{f}_{D\text{coarse}} \simeq -5.3$ kHz, whose value lies outside the unambiguous window bounded by $\pm$ 5 kHz. A more accurate value is obtained by unfolding the Doppler given by the range Doppler image into the first negative ambiguous window. We find $\hat{f_D} \simeq -5.254$ kHz and the error on the estimate is 4 Hz. Note that the loss at the peak is found to be about 1.02 dB.

In Fig. 3.20, we have considered a point target moving with a faster radial velocity but, as compared to Fig. 3.19, we increased the subcarrier spacing from

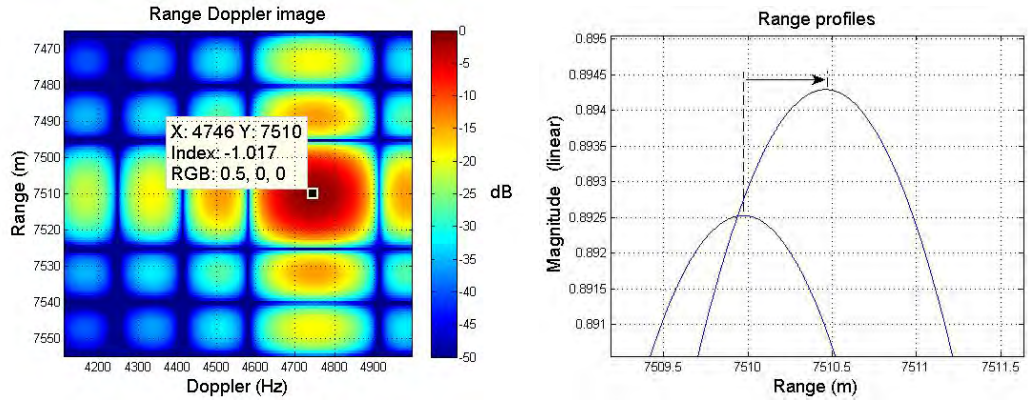

(a) Range Doppler image

(b) First and last range profiles

Figure 3.19: Range Doppler image when our processing in the frequency domain is applied onto a train of M=60 diverse OFDM pulses, each composed of N=100 subcarriers, K=5 symbols and with a bandwidth B=10 MHz. The NKM phase codes are all randomly selected. The PRI is equal to 100 μs. The range resolution is δR=15 m and the Doppler resolution is δf_D=166.7 Hz. The point target is located at R=7510 m and flees the radar with a velocity $|v_r|$=78.75 m/s, so that the Doppler frequency is f_D=-5250 Hz.

100 kHz to 1 MHz so that the Doppler frequency $|f_{D\,1\text{dB}}|$ is supposedly relaxed from 5 kHz to 50 kHz. Note that we observe a loss at the peak of about 1 dB although the Doppler frequency involved is lower than $|f_{D\,1\text{dB}}|$. Note also that the use of random phase codes has little effect on the distortion which is mostly caused by the high Doppler frequency. The image appears distorted but it remains easy to identify the peak position. If we look at the range profiles we obtain a new coarse value for the radial velocity, $\hat{v_r} \simeq -\frac{2292.8-2285}{(M-1)T_r} \simeq -661$ m/s and $\hat{f}_{D\text{coarse}} \simeq -44.067$ kHz, with the negative sign to account for the target direction, away from the radar. Because PRF=5 kHz, we can find out that the true Doppler belongs to the 9^{th} negative ambiguous window ranging between [-47.5 kHz,-42.5 kHz]. Using the value read on the image and unfolding it into this ambiguous window, we find $\hat{f_D} \simeq -44.020$ kHz. The error on this new estimate is 20 Hz.

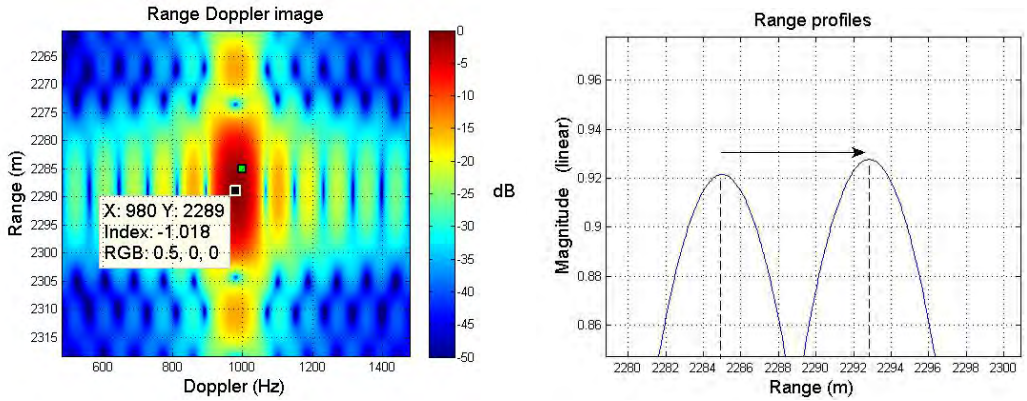

(a) Range Doppler image

(b) First and last range profiles

Figure 3.20: The same waveform parameters as in Fig. 3.19 have been used except for N=10 and T_r= 200 μs. The Doppler resolution is δf_D=83.3 Hz. The point target is located at R=2285 m and flees the radar with a radial velocity $|v_r|$=660 m/s, so that the Doppler frequency is f_D=-44 kHz.

3.6 Summary

We have developed two techniques that can be used to process a train of diverse OFDM pulses and proved that both offer equal processing gains. Based on zero-Doppler matched filters and DFTs, the first technique provides an estimate of the range limited to the size of the range cell and an estimate of the ambiguous Doppler. It suffers possible straddling loss but provided that the subcarrier spacing is chosen to accommodate the maximum Doppler frequency that we can expect, the peak of the scatterer in the range Doppler image will suffer at worst 1 dB loss. Because of the correlation process, the sidelobes of the scatterer's characteristic function in the range Doppler image follow the sidelobes of the ambiguity function, hence, one must look for OFDM pulses with optimal AF characteristics. Next, we showed that our second technique offers more accurate estimates. In particular it can resolve Doppler. In comparison to the first approach, the demodulation process implies that the scatterer characteristic function is nothing but a 2D sinc. Hence, the sidelobes are based on the Fourier sidelobes irrespective of the OFDM pulse design. Because it requires prior knowledge of the target range, we believe that this technique could suit

tracking tasks while the former would be appropriate for search. Also note that in either cases the phase codes shall be adjusted so that the complex envelope of the OFDM pulse remains close to constant. Although pulsed random signals could be chosen in place of OFDM signals with similar behaviour of the ambiguity function, we believe that understanding OFDM radar and its corresponding processing alternatives is relevant for one can build upon existing communication infrastructure to perform radar.

Chapter 4

Stepped OFDM radar technique to resolve range and Doppler simultaneously[7]

In [83], SFW composed of OFDM pulses were used to produce HRRP. The analysis assumed stationary point targets and the processing applied a modified stretch processing, whereby the individual pulses are first compressed with a matched-filter before HRR processing is applied in slow time. The waveform would consist of pulses built from few subcarriers to provide, at first, a coarse range resolution, and later, the wide bandwidth is synthesized out of the many pulses. Since then, the idea has been extended by Huo *et al.*. In [34, 84] the authors proposed to apply a processing that demodulates the received echoes. In principle, it is the same idea as evoked by Sturm *et al.* adapted to the stepped frequency case.

[7] Based on Lellouch, G. et al. "Stepped OFDM radar technique to resolve range and Doppler simultaneously," in *IEEE Transactions on Aerospace and Electronic Systems* vol. 51, no 2, p. 937-950.

4.1 Introduction

In this chapter, we develop the idea from Huo *et al.* further with the intention to provide a new framework for stepped frequency waveforms based on OFDM pulses. Our principal achievement is to demonstrate that when lumping the intra-pulse OFDM structure with inter-pulse Costas frequency coding to synthesize a wide bandwidth, Doppler can be retrieved unambiguously.

Although the term stretch processing first characterised the technique, which in short, implements a local oscillator sweeping over the frequencies with the same slope as used to generate the pulses, typically LFM pulses [85], Levanon extended the technique's name to the concept of creating HRRP from a stepped-frequency train of unmodulated pulses [86].

There are three major novelties in this work. Firstly, the data model of the received OFDM pulses is derived in a closed matrix form and a novel radar processing is derived. Importantly, the data model accounts for range migration of the pulses as well as Doppler modulation. Secondly, we introduce our new waveform-processing concept, where the individual pulses are stepped according to Costas sequences. The selectivity in radial velocity is achieved by means of a bank of range migration filters. The main merit of this technique is to retrieve, unambiguously, the radial velocity of the scatterers. Thirdly, we demonstrate the benefits of this technique in regard of other classical wideband methods following a system design approach.

4.2 Synthesizing the HRR profile with the OFDM SFW radar signal

In this part we define our discrete model for the received signal and detail the steps of our technique to synthesize the HRRP. We use a similar approach as in Section 3.3.2.1. We also report our analysis on the influence of Doppler modulation on the HRR samples. The technique is then applied on a scenario with

stationary point targets.

4.2.1 The proposed OFDM SFW radar signal for transmit

An OFDM pulse is expressed as the concatenation of K symbols (also called chip or bit) in the time domain. The frequency structure of one symbol retains the key principle of orthogonality [12]. The m^{th} baseband pulse can be expressed as:

$$u_m(t) = A_m \sum_{n=0}^{N-1} w_n \left(\sum_{k=0}^{K-1} a_{n,k,m} r_k(t) \right) \exp(j2\pi n \Delta f t), \tag{4.1}$$

where

$$r_k(t) = \begin{cases} 1 & kt_b \leq t < (k+1)t_b \\ 0 & \text{elsewhere} \end{cases}$$

is the window function scaled to the symbol duration t_b. In Eq.(4.1) N stands for the number of subcarriers used per pulse and Δf is the subcarrier spacing that is inversely proportional to the symbol duration Δf=$1/t_b$. An illustration of the OFDM structure is given in Fig. 4.2. The terms w_n and $a_{n,k,m}$ are respectively, the frequency weight applied on the n^{th} subcarrier of any symbol and any pulse and the phase code applied on the n^{th} subcarrier of the k^{th} symbol from the m^{th} pulse. w_n is a real positive number and $a_{n,k,m}$ is a complex number. Although communications systems require to select the phase codes from specific alphabets (e.g. BPSK) our radar application does not need this constraint. A_m is introduced to normalise the pulses so that they all have unit energy. Its general expression is:

$$A_m = \frac{1}{\sqrt{\sum_{k=0}^{K-1} \sum_{n=0}^{N-1} w_n^2 |a_{n,k,m}|^2 t_b}}. \tag{4.2}$$

We can verify that when w_n and $|a_{n,k,m}|$ both equate to 1, then $A_m = 1/\sqrt{NKt_b}$. The OFDM stepped-frequency transmitted signal can then be expressed in terms of the individual pulses. In its analytical form the RF signal is:

$$s(t) = \sum_{m=0}^{M-1} u_m(t - mT_r) \exp(j2\pi f_m t), \tag{4.3}$$

where f_m is the carrier frequency of the m^{th} pulse, M is the number of pulses in the train and T_r is the pulse repetition interval (PRI). While in [34] f_m is defined to follow a linear pattern, we introduce the randomisation vector $\mathbf{c}$ so that f_m can be expressed as:

$$f_m = F_0 + \mathbf{c}[m]B_p. \tag{4.4}$$

F_0 is the lowest carrier frequency covered in the train and $B_p{=}N\Delta f$ is the total bandwidth of each pulse. The randomisation factor $\mathbf{c}$ is introduced to code the frequency steps of the SFW when other than linear ordering is desired. The emergence of digital synthesizing techniques fosters the use of frequency steps other than linear. We will see in Section 4.3 that non linear steps can improve the radar capabilities, at the cost of additional complexity in the processing. In the case of a linearly SFW, $\mathbf{c}{=}[0 : M\text{-}1]$. We use the convention that the first element in vector $\mathbf{c}$ is given by $\mathbf{c}[0]$.

4.2.2 Model of the received OFDM SFW echoes

Modelling the received echoes is a critical step towards the design of any processing technique. With pulsed OFDM radar, the multicarrier nature of the OFDM structure eggs on accurate modelling of the range migration because of the sensitivity of the subcarriers with respect to variations in the phase. The target model assumed in this work is the isotropic point scatterer model [32]. The general setup of the simulation assumes L_T point targets, each moving with a radial velocity towards or away from the radar. We use the convention that a closing target has a positive radial velocity and a positive Doppler shift. A closing target has a negative range rate V_l however. A receding target has the opposite signs.

4.2.2.1 Continuous model

The range from the radar to the l^{th} scatterer can be expressed as $R_l(t) = R_{l0}+V_l t$, where R_{l0} is the initial range at t=0. The received signal is given by,

$$s_r(t) = \sum_{l=1}^{L_T} \varsigma_l s(t - \tau_l(t)), \tag{4.5}$$

where ς_l is the complex reflectivity coefficient of the l^{th} scatterer and $\tau_l(t)$=2 $R_l(t)/c$ is the two-ways time delay for the l^{th} scatterer with c the speed of light. To model the mixing process in the receiver we multiply the received echoes from the m^{th} pulse by the expression $\exp(-j2\pi f_m t)$. Our model assumes targets which are non ambiguous in range. In practice, the HRR technique is commonly applied with some prior knowledge about the target of interest, hence the PRI can be adjusted accordingly to keep the target in the non ambiguous ranges. The baseband received signal $s_{bm}(t)$ in its continuous form is expressed as:

$$\begin{aligned} s_{bm}(t) = &\sum_{l=1}^{L_T} \sum_{m=0}^{M-1} \varsigma_l \exp(-j2\pi f_m \tau_l) \exp(j2\pi f_{Dm,l}(t - \tau_l)) \\ &u_m(t - mT_r - \tau_l), \end{aligned} \tag{4.6}$$

where $f_{Dm,l} = -2V_l f_m/c$ is the Doppler frequency resulting from the target motion. In the context of a SFW signal, the Doppler frequency associated to a target may differ from one pulse to the next. Later, in Section 4.2.3.4 we discuss the influence of this Doppler modulation on our processing.

4.2.2.2 Discrete model

To derive the discrete form of the received signal, one must define the sampling instants in the fast time. Another word for sampling instant is time gate and the time span between two consecutive time gates is called the time cell extent. The same terminology applies to the range, observing that range R and time delay τ are tied since R=$c\tau/2$. The range cell as defined for the pulse is also named the coarse resolution cell. As we are dealing with complex signals, the sampling fre-

quency f_s follows naturally from the OFDM property. Having been mixed down to baseband all echoes have the same bandwidth as the initial baseband pulses. The critical sampling frequency of the OFDM symbol equals the bandwidth of the symbol itself, hence $f_s{=}N\Delta f$. It could be larger in the case of oversampling but for now we assume the critical sampling rate. This assumption complies with the idea of using SFW to reduce the constraints on analog-to-digital converters (ADCs). Hence, the sampling period is $t_s{=}t_b/N$.

Because our OFDM frequency domain HRR processing, as we derive it in Section 4.2.3, is subject to ISI, our simulations prevent from this effect by assuming that all L_T echoes from the m^{th} pulse are received between the same time gates. ISI happens when the subcarriers from symbol k interfere with the subcarriers from symbol $k+1$. In communication systems, a technique based on the insertion of a guard interval with cyclic prefix is used to solve this problem [7]. Next, to prevent from any detrimental migration, we consider that all $L_T M$ echoes throughout the time-on-target will be received between the very same time gates modulo the PRI T_r. These assumptions are summarised in Fig. 4.1.

Fig. 4.1(a) and 4.1(c) show the grid of time gates that intercept our received echoes respectively in the case of a stationary or a moving scatterer. Each circle characterises one sample of our OFDM echo, symbolically represented by the thick black line. Fig. 4.1(b) and 4.1(d) zoom around the first intercepted time gate, whose value is given by p_0 and show how it relates to the time delay $\tau_{m,l}$, for pulse m and scatterer l. The scenarios that we consider in our simulations follow this approach. In Section 4.4 we discuss the philosophy of this processing, in particular the risk of ISI and a methodology to deal with it.

To put this concept into perspective and show that it can apply to a real radar scenario, we illustrate with an example. With $\Delta f{=}1$ MHz and $N{=}10$ we find $t_s{=}0.1$ μs. The corresponding range extent is $\Delta R{=}ct_s/2{=}15$ m, more than the size of a car for instance. Considering the following pulse repetition period $T_r{=}200$ μs (gives an unambiguous range, $R_{\text{ua}}{=}30$ km) and $M{=}100$ pulses to provide a high range resolution of 15 cm, a radial velocity $v_r{=}50$ m/s will infer a range migration of 1 m throughout the time-on-target, well below the range

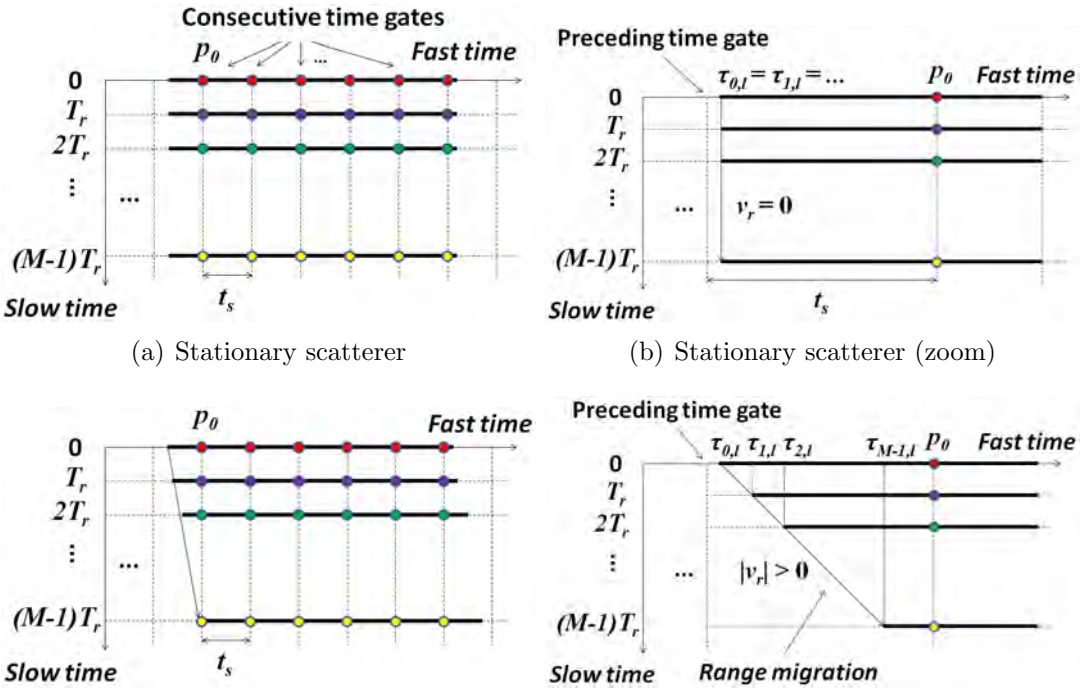

(a) Stationary scatterer (b) Stationary scatterer (zoom)

(c) Receding scatterer (d) Receding scatterer (zoom)

Figure 4.1: Sketches that illustrate the generation of the received echoes. We assume that all echoes received from any scatterer at any sweep intercept the very same time gates.

extent.

Assuming that we start sampling in the fast time domain from t=0 at the critical rate f_s=1/t_s, the value for p_0 as introduced earlier is given by:

$$p_0 = [\text{floor}\,(\tau_{0,l}/t_s) + 1]t_s, \;\; \forall l. \tag{4.7}$$

The N-element vector composing the k^{th} symbol of the complex baseband echo resulting from the m^{th} pulse returning from the l^{th} scatterer is given in its discrete form by Eq. 4.8. Again, similar to Eq. 3.14 in Chapter 3, the derivation of this expression is lengthy but quite intuitive if the data model as presented in Fig. 4.1 is taken into account.

$$\mathbf{s_{bk,m,l}} = \varsigma_l \alpha_{m,l} \kappa_{m,l} \mathbf{\Delta_{k,m,l}} \mathbf{F^{-1}} \mathbf{\Gamma_{m,l}} \mathbf{D_{k,m}} \mathbf{w}, \tag{4.8}$$

The various terms can be expressed as follows.

$$\alpha_{m,l} = \exp(-j2\pi f_m \tau_{m,l}), \tag{4.9}$$

$$\kappa_{m,l} = \exp(j2\pi f_{D_{m,l}} \Delta\tau_{m,l}), \tag{4.10}$$

$$\mathbf{\Delta_{k,m,l}} = \mu_{k,m,l}\text{Diag}\{1 \ \eta_{m,l} \ {\eta_{m,l}}^2 \ \dots {\eta_{m,l}}^{N-1}\}, \tag{4.11}$$

$$\mathbf{\Gamma_{m,l}} = \text{Diag}\{1 \ \gamma_{m,l} \ {\gamma_{m,l}}^2 \ \dots {\gamma_{m,l}}^{N-1}\}. \tag{4.12}$$

$$\mathbf{D_{k,m}} = \text{Diag}\{a_{0,k,m} \ a_{1,k,m} \ \dots \ a_{N-1,k,m}\}, \tag{4.13}$$

$$\mathbf{w} = [w_0 \dots w_{N-1}]^T. \tag{4.14}$$

Note that Diag$\{\cdot\}$ is a diagonal matrix formed by the components of vector argument. From Fig. 4.1, $\mathbf{s_{b0,m,l}}[0]$ corresponds to the sample collected at p_0 (first time gate). The Doppler related terms $\mu_{k,m,l}$ and $\eta_{m,l}$ are given by:

$$\mu_{k,m,l} = \exp(j2\pi k \frac{f_{D_{m,l}}}{\Delta f}), \tag{4.15}$$

$$\eta_{m,l} = \exp(j2\pi \frac{f_{D_{m,l}}}{N\Delta f}). \tag{4.16}$$

The other terms $\tau_{m,l}$ and $\gamma_{m,l}$ introduced respectively in Eq.(4.9) and (4.12) are given by:

$$\tau_{m,l} = 2(R_{l0} + mT_r V_l)/c, \tag{4.17}$$

$$\gamma_{m,l} = \exp(j2\pi\Delta f \Delta\tau_{m,l}), \tag{4.18}$$

Eventually, $\Delta\tau_{m,l}$ in Eq.(4.18) is:

$$\Delta\tau_{m,l} = p_0 - \tau_{m,l}. \tag{4.19}$$

4.2.3 Derivation of the OFDM frequency domain HRR processing

Assuming that we have collected the MNK samples corresponding to our received echoes' discrete model as formulated in Eq.(4.8) we can derive our frequency domain HRR processing. We carefully stress our assumptions as in [44]. For a reason that will soon become obvious, we would like to see the diagonal matrix $\mathbf{\Delta_{k,m,l}}$ reduced to the identity matrix $\mathbf{I}$. In fact, it is the case when the Doppler effect is negligible in the duration of the pulse.

4.2.3.1 Assumption of a negligible Doppler

Our motivation to reduce $\mathbf{\Delta_{k,m,l}}$ into $\mathbf{I}$ results from the fact that the IDFT matrix is positioned next to it on the right hand side. Indeed, multiplying both sides of Eq.(4.8) with the discrete Fourier transform (DFT) matrix $\mathbf{F}$ simplifies the expression. Since the product of the DFT and IDFT matrices is given by:

$$\mathbf{F}\mathbf{F^{-1}} = N\mathbf{I}, \tag{4.20}$$

$\mathbf{s_{bk,m,l}}$ is modified into $\delta_{\mathbf{k,m,l}}$ according to:

$$\delta_{\mathbf{k,m,l}} = N\varsigma_l\alpha_{m,l}\mathbf{\Gamma_{m,l}}\mathbf{D_{k,m}}\mathbf{w}, \tag{4.21}$$

where we assumed $\kappa_{m,l} \approx 1$. Since we multiplied by the DFT matrix and thus toggled in the frequency domain, we refer to this processing as *frequency domain HRR processing*. OFDM based communication systems apply the very same approach but their parameters of interest are the phase codes since they contain the information being conveyed. Therefore, they must employ target or channel models to compensate for the unwanted terms. Conversely, in radar applications,

we aim at finding the coordinates (range and radial velocity) of the scatterers and we know the sequence of phase codes that were transmitted (this assumption is certainly valid in monostatic configurations). Having a closer look at Eq.(4.21), the parameters that capture our attention are essentially the time delays $\tau_{m,l}$.

To remove the phase codes from our signal, we first stack the K column vectors $\delta_{\mathbf{k,m,l}}$ into a matrix:

$$\mathbf{\Delta_m} = [\delta_{\mathbf{0,m,l}}\ \delta_{\mathbf{1,m,l}} \dots \delta_{\mathbf{K-1,m,l}}], \tag{4.22}$$

and multiply it with the matrix $\mathbf{A_m}$ that contains the complex conjugates of these phase codes.

$$\mathbf{A_m} = \begin{bmatrix} a^*_{0,0,m} & a^*_{1,0,m} & \dots & a^*_{N-1,0,m} \\ a^*_{0,1,m} & a^*_{1,1,m} & \dots & a^*_{N-1,1,m} \\ \vdots & \vdots & & \vdots \\ a^*_{0,K-1,m} & a^*_{1,K-1,m} & \dots & a^*_{N-1,K-1,m} \end{bmatrix}. \tag{4.23}$$

We then extract the N diagonal elements of the product matrix $\mathbf{\Delta_m A_m}$ to construct the vector $\mathbf{d_{m,l}}$ that contains the high range resolution information of interest: the delays $\tau_{m,l}$. Note once again that we assume our delays to fall between the time gate preceding p_0, in other words, $p_0 - t_s$ and p_0 itself. If we call $\mathbf{b_m}[n]$ the autocorrelation peak for the sequence of phase codes on subcarrier n in pulse m,

$$\mathbf{b_m}[n] = \sum_{k=0}^{K-1} |a_{n,k,m}|^2, \tag{4.24}$$

the diagonal elements $\mathbf{d_{m,l}}$ may be rearranged so that the impact from the phase codes is fully removed, as shown in:

$$\frac{1}{w_n \mathbf{b_m}[n]} \mathbf{d_{m,l}}[n] = N\varsigma_l \alpha_{m,l} {\gamma_{m,l}}^n. \tag{4.25}$$

At that stage of the processing, we can note that from the NK samples collected at each sweep, we are now left with N samples. The next step requires to plug Eq.(4.4) into Eq.(4.25) and see how we can proceed further. Calling $\tilde{\mathbf{d}}_{\mathbf{m,l}}[n]$ the

new sample, we get:

$$\tilde{\mathbf{d}}_{\mathbf{m,l}}[n] = N\varsigma_l \exp(-j2\pi(F_0 + \mathbf{c}[m]B_p)\tau_{m,l}) \exp(j2\pi n\Delta f\Delta\tau_{m,l}). \tag{4.26}$$

We now introduce the decoding vector $\mathbf{c}_{-1}$, which will be useful to describe our next data set. Fig. 4.2 illustrates the decoding principle that gives $\mathbf{c}_{-1}$. With the objective to reorder the samples and have a linear progression of the carrier frequencies $F_0 + mB_p$, we must use the decoding vector to relate to the appropriate time delays. In particular, the delay corresponding to the echo that was received for carrier frequency $F_0 + mB_p$ is given by $\tau_{\mathbf{c}_{-1}[m],l}$. With this

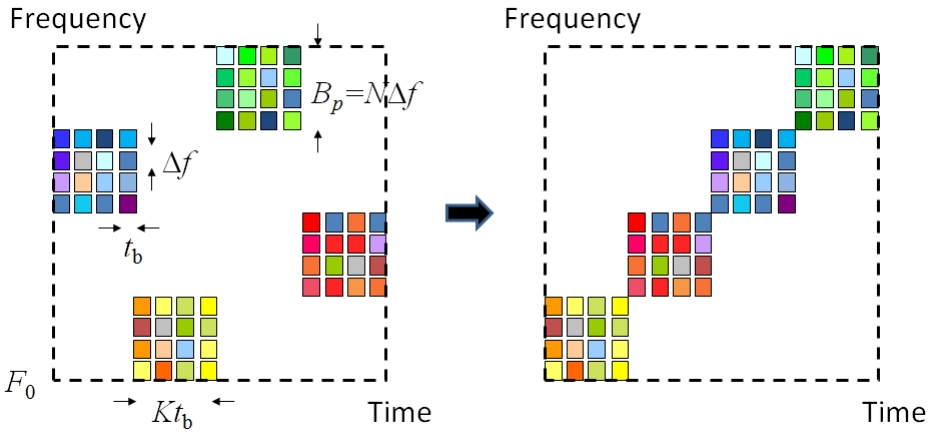

Figure 4.2: Frequency coding $\mathbf{c}$=[2 0 3 1] and inverse coding $\mathbf{c}_{-1}$=[1 3 0 2]. Each colour stands for a phase code that can be unique in case of random phase codes. $\breve{\mathbf{c}}_{-1}$=[$1\cdot\mathbf{I}_{1,4}$ $3\cdot\mathbf{I}_{1,4}$ $0\cdot\mathbf{I}_{1,4}$ $2\cdot\mathbf{I}_{1,4}$], where $\mathbf{I}_{1,4}$=[1 1 1 1]. Note that two consecutive pulses are one pulse repetition interval (T_r) apart.

preparation, the rearranged vectors $\breve{\mathbf{d}}_{\mathbf{m,l}}$ are given by:

$$\breve{\mathbf{d}}_{\mathbf{m,l}}[n] = N\varsigma_l \exp(-j2\pi(F_0 + mB_p)\tau_{\mathbf{c}_{-1}[m],l}) \exp(j2\pi n\Delta f\Delta\tau_{\mathbf{c}_{-1}[m],l}). \tag{4.27}$$

With Eq.(4.19), we can modify Eq.(4.27) further:

$$\begin{aligned}\breve{\mathbf{d}}_{\mathbf{m,l}}[n] =& N\varsigma_l \exp(-j2\pi(F_0 + (mN+n)\Delta f)\tau_{\mathbf{c}_{-1}[m],l}) \\ & \exp(j2\pi n\Delta f p_0).\end{aligned} \tag{4.28}$$

It is clear from Eq.(4.28) that an appropriate variable change of the form $\xi = mN + n$ would enable the phase of the first term to follow a linear progression throughout the MN samples. If the variable change could apply on the second term without extra burden the whole expression could be simplified.

We saw earlier in Eq.(4.7) that p_0 can be expressed as $p_0{=}qt_s$ where q is an integer whose value lies in the interval $[1 : Q]$ meant to represent the possible values of p_0 within the sweep. We must show that irrespective of q the following relation holds:

$$\xi\Delta f q t_b/N \equiv k^{'}\Delta f q t_b/N \qquad \text{mod } 1, \tag{4.29}$$

where $\xi = [N : MN-1]$ and $k^{'} = [0 : N-1]$. Again, the orthogonality relation simplifies the expression and it is then easy to see that:

$$\xi\Delta f q t_b/N = (mN+n)q/N \tag{4.30}$$

$$= mq + nq\cdot 1/N \tag{4.31}$$

$$\equiv nq\cdot 1/N \qquad \text{mod } 1. \tag{4.32}$$

As a matter of fact, we can drop the index m in $\breve{\mathbf{d}}_{\mathbf{m,l}}$ and rewrite it as:

$$\begin{aligned}\breve{\mathbf{d}}_{\mathbf{l}}[\xi] =& N\varsigma_l \exp(-j2\pi F_0\tau_{\breve{\mathbf{c}}_{-1}[\xi],l}) \\ & \exp(j2\pi\xi\Delta f\Delta\tau_{\breve{\mathbf{c}}_{-1}[\xi],l}).\end{aligned} \tag{4.33}$$

Remark that the pulse dependency is now fully contained in the new index ξ. As shown in the caption of Fig. 4.2, $\breve{\mathbf{c}}_{-1}$ is a MN-long dummy vector, which we generate to comply with the new index ξ.

The final step of the HRR processing is now trivial and consists in applying an IDFT (it could either be a DFT) on the vector $\breve{\mathbf{d}}_{\mathbf{l}}$ to reveal the positions and scattering coefficients of the scatterers in the HRRP. The latter that we denote

$\mathbf{r}$ can be expressed by means of the IDFT matrix $\mathbf{F^{-1}}$. Essentially, we have:

$$\mathbf{r}[q] = \sum_{\xi=0}^{MN-1} \breve{\mathbf{d}}_{\mathbf{l}}[\xi] \exp(j2\pi \frac{q\xi}{MN}). \tag{4.34}$$

When the scatterers are stationary or assuming that the migration compensation has been applied such that $\tau_{m,l} = \tau_{0,l}$ and $\Delta\tau_{m,l} = \Delta\tau_{0,l}$, we can easily develop Eq.(4.34) and introduce a geometric series of the form $\sum[\exp(j2\pi a)]^{\xi}$, where $a = \Delta f \Delta\tau_{0,l} + q/MN$. The peak of this function is obtained when a is an integer. If q_{peak} stands for the index of the peak then the relative range of our scatterer is found to be:

$$\Delta R_{0,l} = \frac{c}{2\Delta f}(1 - q_{\text{peak}}), \tag{4.35}$$

where $\Delta R_{0,l}$=R_{p_0}-R_{l0} and R_{p_0}=$cp_0/2$. Because in Eq.(4.34), q can take values between 0 and MN-1, Eq.(4.35) indicates that the range extent of the HRRP is $c/2\Delta f$. However, it is important to recall that we have based our analysis (Fig. 4.1) on the assumption that $\Delta R_{0,l} < \Delta R = c/(2N\Delta f)$. Using Eq.(4.35) we can define the possible values for q_{peak} as:

$$M(N-1) < q_{\text{peak}} \leq MN - 1. \tag{4.36}$$

It turns out that only a small portion ($1/N\%$) of the HRRP is of real interest. We refer to it as the processed window. When we apply an IDFT, it corresponds to the last portion. Would we apply a DFT, it would correspond to the first portion. As a result, we could limit our calculation to the last M terms, in order to save processing power.

Following our theoretical derivations the magnitude at the peak is found to be $\mathbf{r}[q_{\text{peak}}] = \varsigma_l MN^2$, nevertheless, had we normalised our DFT/IDFT operations, the value would be different. In principle, what matters is not the value at the peak but the relative values. The figure of merit that we use is the integration gain, which we discuss later on.

4.2.3.2 Scenario with stationary targets

In light of the above preparation we present some initial results for the case of stationary targets. The scenario used in Fig. 4.3(a) involves a stationary target positioned at R_0=2281.5 m. To express the x-axis in terms of the absolute range we referred to Eq.(4.35). Each pulse being composed of N=10 subcarriers, the spacing being Δf=1 MHz, the range cell extent as defined earlier is ΔR=15 m. With our definition of R_{p0}, we find that R_{p0}=2295 m. Hence the absolute range of the HRRP extends from $R_{p0} - c/2\Delta f$ = 2145 m to 2295 m. In Fig. 4.3(b) we restrict the range extent to the processed window.

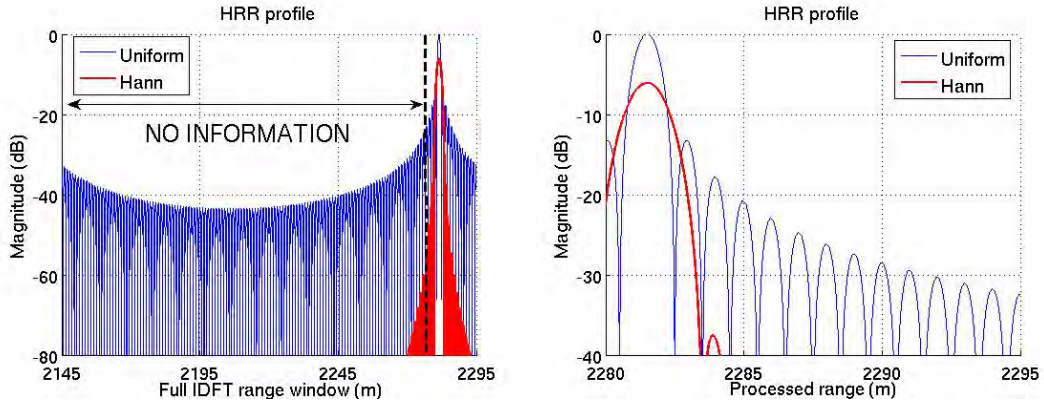

(a) Full HRR window

(b) Processed HRR window

Figure 4.3: High range resolution profile with one stationary scatterer. Uniform and Hann windowing. M=15 pulses, K=5 symbols, N=10 subcarriers, Δf=1 MHz, scatterer at range R_0=2281.5 m, reflection coefficient ς=1 and range resolution δR=1 m.

Note that Figs. 4.3(a) and 4.3(b) were obtained using zero-padding in the IDFT so as to increase the sampling resolution of the HRRP. We show the HRRP when tapering was applied on the column vector $\breve{\mathbf{d}}_\mathbf{l}$ with either a rectangular window or a Hann window. The use of a Hann window lowers the sidelobes from -13.2 dB down to -31.5 dB at the expense of widening the main lobe (resolution loss) and decreasing the main lobe power (SNR loss).

4.2.3.3 Processing block and integration gain

The entire processing can be summarised by means of the block diagram in Fig. 4.4.

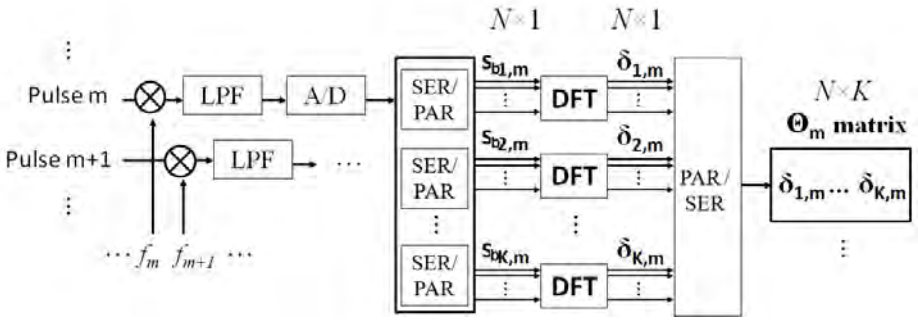

(a) 1st part: carrier demodulation and conversion into the frequency domain. SER/PAR refers to serial to parallel and PAR/SER refers to parallel to serial.

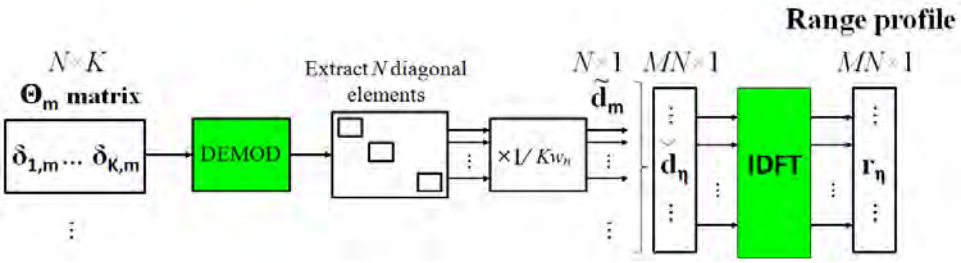

(b) 2nd part: phase codes demodulation and creation of the range profile

Figure 4.4: Block diagram of our frequency domain HRR processing. We colour in green those blocks that present some integration gain.

The steps that achieve integration gain are highlighted in green. The first gain is due to the demodulation process and is equal to K. The rest of the integration gain results from the last IDFT and is equal to the number of samples considered, MN. This gives a total integration gain of: $G{=}NKM$. This value tallies with what we found when we derived our range / Doppler processing in [45]. Here, the 2D-DFT ($N \times M$) is replaced by a longer IDFT ($MN \times 1$). The interpretation of this result is straightforward. Assuming that AWGN adds up onto the received echoes such that the SNR is 0 dB, the SNR at the output of the frequency domain HRR processing will be $10\log(NKM)$ dB.

We now analyse the impact of Doppler modulation when the initial assumption cannot be guaranteed and propose a method to characterise the distortion at the end of the processing.

4.2.3.4 Impact of Doppler modulation

The same analysis as presented in [45] can be applied to our frequency agile pulses with the difference that the Doppler frequency differs from pulse to pulse. Hence we have indexed it as $f_{D_{m,l}}$, where l is the scatterer index. Also, here, we are concerned with the distortion caused by this intra-pulse Doppler on the HRR, as opposed to our analysis in Section 3.4.1 where we looked at the distortion on the range Doppler image. Calling $\mathbf{B_{k,m,l}}$ the outcome of the DFT applied on $\mathbf{s_{bk,m,l}}$ as given by Eq.(4.8), we see that when we ignore the constant phase terms (to simplify the expression), namely, ς_l, $\alpha_{m,l}$ and $\kappa_{m,l}$, the value in bin p (p is an integer between 0 and $N-1$), which we write $\mathbf{B_{k,m,l}}[p]$ can be expanded into:

$$\begin{aligned}\mathbf{B_{k,m,l}}[p] = &\left(\sum_{q=0}^{N-1} w_q a_{q,k,m} \exp(j2\pi q \Delta f \Delta\tau_{m,l})\right. \\ &\left.\times \left(\sum_{n=0}^{N-1} \exp(j2\pi \frac{(q-p)n}{N}) \exp(j2\pi \frac{f_{D_{m,l}}}{\Delta f}\frac{n}{N})\right)\right) \\ &\times \exp(j2\pi f_{D_{m,l}} k t_b).\end{aligned} \tag{4.37}$$

If $|f_{D_{m,l}}|$ is negligible, the sum over n reduces to N when $q{=}p$ and 0 otherwise. In that case there is no interference coming from adjacent subcarriers and the complex value retrieved in $\mathbf{B_{k,m,l}}[p]$ is simply N times the weight w_p multiplied by the phase code $a_{p,k,m}$ and the phase shift term $\exp(j2\pi q \Delta f \Delta\tau_{m,l})$. This result is also intuitive. In the other case where $|f_{D_{m,l}}|$ is not negligible, this expression indicates the amount of interference coming from the neighbour subcarriers as well as the magnitude loss on the subcarrier p.

Making use of the expected value $E\{\breve{\mathbf{d}}_\mathbf{l}[\xi]\}$ to average out the effect of the phase codes, we can express the magnitude loss L (negative value) due to the Doppler

frequency f_D:

$$L(N, K, \frac{f_D}{\Delta f}) = \frac{\sin(\pi \frac{f_D}{\Delta f})}{\sin(\pi \frac{f_D}{N\Delta f})} \times \frac{\sin(\pi \frac{f_D K}{\Delta f})}{\sin(\pi \frac{f_D}{\Delta f})} \times \frac{1}{K}. \tag{4.38}$$

To derive this expression we have assumed the same Doppler frequency for each pulse, $f_{Dm} \simeq f_D$. This assumption is reasonable with short pulses (e.g. few μs at X-band). We show the details of our derivation in Appendix B. Once K and N are fixed, we can thus work out a threshold $|f_D/\Delta f|_{\max}$ to insure that the loss remains bounded.

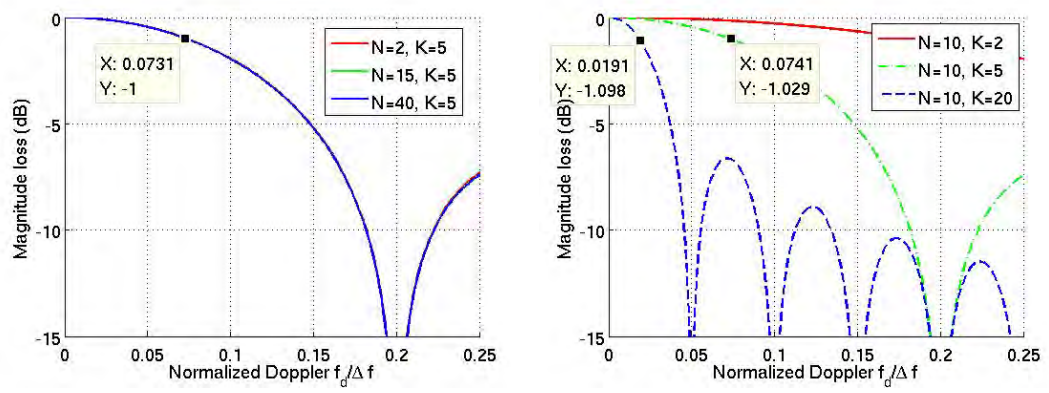

(a) Magnitude loss versus N

(b) Magnitude loss versus K

Figure 4.5: Expected value of the magnitude loss. In 4.5(a), we plot L_{dB} for different number of subcarriers N, while in 4.5(b) we vary the number of symbols K.

Considering a carrier frequency F_0 at X-band, reasonable radial velocities ($v_{r\max} \approx \pm 500$ m/s) and high enough subcarrier spacing Δf (e.g. 1 MHz), then $|f_D/\Delta f|$ will always be smaller or much smaller than 1. Thus, we limited the normalised Doppler in Fig. 4.5 to 0.25. Mark that this approach can perfectly accommodate other frequency bands and scenarios where this condition holds. Fig. 4.5(a) indicates that when we fix K and consider a maximum loss of, say 1 dB, the threshold for $|f_D/\Delta f|$ will not vary when we vary N. This happens because N is in the denominator in $f_D/N\Delta f$, in Eq. 4.38. The opposite happens when we fix N and vary K as observed in Fig. 4.5(b). To limit the magnitude loss to 1 dB,

the rule of thumb obtained from our observations is $|f_D/\Delta f| < 1/(2.5K)$. In practice, an additional margin for $|f_D/\Delta f|$ shall be accounted for if one wants the loss to be strictly limited.

Effects other than magnitude loss are also observed in the HRRP when Doppler modulation becomes too high in comparison to the subcarrier spacing. The latter were commented in [34] and participate to the slipping of the peak (at least when the frequency steps are ordered in a linear fashion) and the presence of phase noise. As shown later in Section 4.3, provided that our waveform parameters comply with the above rule, the use of a range migration compensation technique permits to retrieve effectively the HRRP.

4.3 Costas frequency hopping and range migration compensation processing

In this part we introduce our waveform concept where we use Costas schemes to order the pulses in the frequency domain. We motivate this choice in light of the previous work and show what consequences this design infers on the processing presented in Section 4.2. In particular, we emphasize that this method can reduce conventional Doppler ambiguities when the synthetic bandwidth is sufficiently large compared to the carrier frequency F_0. Like always in radar, one benefit comes at some cost. We observe a high correlation artefact which needs to be reduced. The relationship between the level of this artefact and the waveform parameters is discussed in Section 4.3.5 and we show that integrating the output over several batches can improve the contrast with the scatterers.

4.3.1 Motivation for Costas hopping

The use of a linear law for the frequency steps has already been proposed in [84]. With this approach, the output of the HRR processing reveals the presence of the scatterer despite Doppler mismatch. Depending on the severity of this mismatch,

the position in range of the scatterer is more or less erroneous and the peak suffers some SNR loss. However when the velocities of interest are low enough to give an acceptable error in range this solution becomes suitable since the processing as presented in Section 4.2 applies. In that case $\mathbf{c} = \mathbf{c}_{-1} = [0 : M\text{-}1]$.

However, this approach fails to retrieve the scatterer radial velocity. Levanon *et al.* showed in [86] that the use of non linear steps and in particular Costas hopping schemes offers a solution to this problem. Although in principle other hopping schemes than Costas can be applied, we choose this solution for two reasons. Costas frequency hopping has been studied extensively in radar [87] and there exist Costas sequences for almost any relevant number of pulses[8].

4.3.2 Ambiguity function analysis

The traditional tool that radar designers employ to assess the characteristic of their waveform is the AF. Clearly, the signal processing solution proposed in Section 4.2 does not apply a cross-correlation, nevertheless, because our processing relies on linear operations, the ambiguity function remains a valid tool to apprehend the outcome. As compared to the graph presented in [34] the AF of a Costas coded OFDM based SFW, as shown in Fig. 4.6 indicates no range-Doppler coupling but a narrow peak at the origin. In this example we have used identical sequences (IS) for the phase codes with length 5 Barker codes (K=5); hence we observe 2 sidelobes on both sides of the main lobe, at $\pm 2t_b$ and $\pm 4t_b$, typical with Barker codes. Note that, had we used random phase codes, these sidelobes would not appear as seen later in Fig. 4.9(b). Another important information is the presence of high sidelobes in the zero-delay cut and in general, in the rest of the non-zero Doppler domain. This is the main drawback of the Costas hopping solution as we will discuss in Section 4.3.5.

Hence, the lessons learnt from the ambiguity function are twofold. Firstly the sharp peak suggests the use of a bank of Doppler filters in the processing when the radial velocity is unknown. Secondly, if possible, the level of the sidelobe pedestal,

[8] Levanon provides in [36] a *Matlab* code to generate Costas sequences

which we refer to as correlation artefact, shall be reduced. As mentioned in [86], in practice, the higher the number of scatterers, the higher the pedestal level in the range Doppler image (see Fig. 4.8). Lastly, note the presence of an ambiguity in Doppler at the PRF.

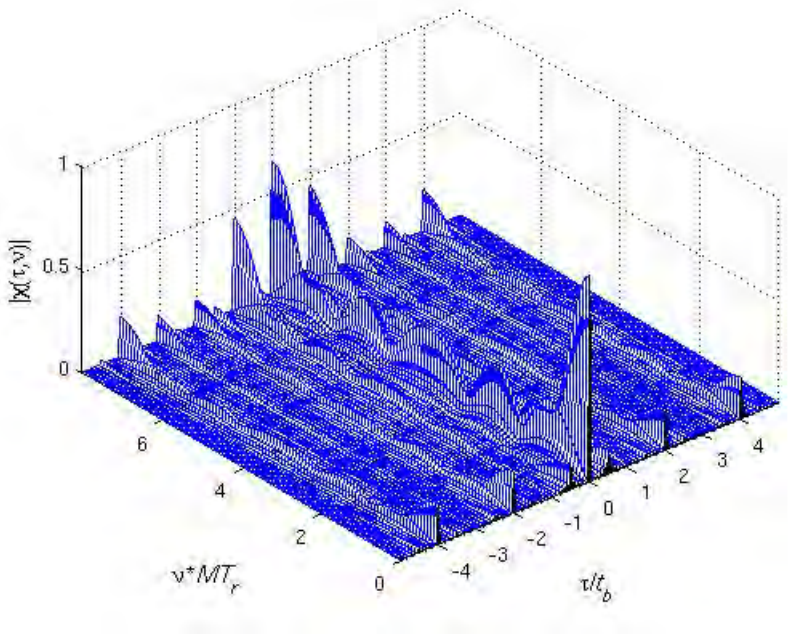

Figure 4.6: Ambiguity function of the Costas coded OFDM based SFW. Time and Doppler axes are limited to the pulse duration and the PRF respectively. Δf=1 MHz, N=10 subcarriers, K=5 symbols, M=8 pulses, Costas hopping sequence with frequency order: 1 5 2 7 6 4 0 3. IS based on 5-element Barker codes are used for the phase codes. The range resolution is δR=1.875 m.

4.3.3 Bank of range migration filters

We showed in Section 4.2.3.1 that when Doppler modulation has a negligible impact during the pulse duration, the vector which we feed into the IDFT to generate the HRRP is $\breve{\mathbf{d}}_l$, as given by Eq.(4.33). If we isolate in this expression the constant terms and the velocity dependant terms we realise that the bank of filters can be constructed by applying the following corrective term $\mathbf{h}_{\text{corr}}$ in each

filter:

$$\begin{aligned}\mathbf{h}_{\text{corr}}[\xi] = &\exp(j2\pi F_0 2\check{\mathbf{c}}_{-1}[\xi]VT_r/c) \\ &\exp(j2\pi\xi\Delta f 2\check{\mathbf{c}}_{-1}[\xi]VT_r/c),\end{aligned} \tag{4.39}$$

where V stands for the range rate which we compensate for. Recall from Section 4.2.2 that by convention, V is opposite of v_r, the radial velocity. Like in [86], the bank of range migration filters can be plugged in Fig. 4.4(b) so that if there are N_{corr} filters the IDFT block is repeated N_{corr} times. The output is no longer a vector which we use to plot a range profile as in Fig. 4.3 but a matrix, which we exploit to construct a range-range rate image.

4.3.4 Analysis of the ambiguity in radial velocity

A careful inspection of the phase progression of both complex exponentials in $\mathbf{h}_{\text{corr}}$ discloses how ambiguities in radial velocity occur when our processing applies range migration compensation. Because of the presence of the carrier frequency F_0 as opposed to $\xi\Delta f$, Doppler ambiguities result from the first term and are found at $\pm k\tilde{v}_{r_{\text{ua}}}$, where:

$$\tilde{v}_{r_{\text{ua}}} = \frac{c}{F_0}\frac{PRF}{2}, \tag{4.40}$$

and k is a non-zero integer. Note that this expression is consistent with the conventional definition of ambiguities in the case of a train of unmodulated pulses where Doppler processing is achieved by means of DFTs. The ambiguous peak discussed in Fig. 4.6 corresponds to the case k=1. We introduce the notation of partial ambiguity $\tilde{v}_{r_{\text{ua}}}$ because these ambiguities are not total. Indeed it is easy to realise that the corrective term at $V_1 \pm \tilde{v}_{r_{\text{ua}}}$ differs from the one at V_1. In fact, the smaller the relative bandwidth B_{tot}/F_0, where B_{tot}=$MN\Delta f$ is the total synthetic bandwidth, the more similar the two corrective vectors $\mathbf{h}_{\text{corr}}$ will be and thus the stronger the partial ambiguities. This observation is a very interesting result when we aim at retrieving an unambiguous estimate of the radial velocity. We can design the waveform to reduce the effect of these partial ambiguities.

This can bring a major improvement as compared to classical SFW techniques based on linear steps. However, note that this characteristic is not inherent to the OFDM based SFW as it is applicable to unmodulated SFWs relying on random coding. For the same bandwidth, say 500 MHz, the range velocity image will exhibit clearer ambiguities in Ka-band than in X-band.

4.3.5 Reducing the correlation sidelobes

Making use of a high relative bandwidth to reduce the Doppler ambiguities, the range-velocity image formed amid the bank of filters localises accurately the scatterer in the processed window, at the correct range and the exact velocity. Note that we use the term velocity for range rate in the rest of this Chapter, e.g. the label in Fig. 4.8. It is easily verified from Fig. 4.8(b) that the resolutions in range and range rate both follow the conventional expressions, $\delta R = c/(2B_{\text{tot}})$ and $\delta V = c/(2F_0 M T_r)$.

The presence of a sidelobe pedestal expected from the AF analysis in Section 4.3.2 is confirmed by Fig. 4.8(a) and Fig. 4.8(b). High sidelobes are observed in those filters that do not match the scatterer's velocity. Special care must be taken to ensure that these sidelobes do not harm the system.

4.3.5.1 Influence of waveform parameters

This sidelobe pedestal being a deterministic effect, we analysed the influence of the number of subcarriers N and the number of pulses M on the sidelobe level. We considered two experiments. In the first experiment, we fixed the pulse bandwidth B and varied N and M, such that the subcarrier spacing is $\Delta f{=}B/N$. We present our results in Fig. 4.7(a). The behaviour of the distribution function of the sidelobe level is very similar irrespective of N. On the other hand, for higher M the distribution shifts to the left which implies that the sidelobes are globally lower. For example, with $M{=}71$, the value of the highest sidelobe (HiSL) is -11 dB while with $M{=}250$ it is -14.5 dB. Hence when the coarse range cell extent is fixed, a longer waveform or a longer Costas sequence ensures lower

sidelobes. In return, the waveform is longer and the total bandwidth is larger. In the second experiment, we fixed the total bandwidth B_{tot}=600 MHz as well as the subcarrier spacing Δf=1 MHz and varied B and M. Both are tied by $B_{\text{tot}}=MN\Delta f$. We present our results in Fig. 4.7(b). Again, the longer the Costas sequence the lower the sideboles. With N=6 and M=100 the value of the highest sidelobes is -12 dB while with N=20 and M=30 it is -8 dB. Our results for both experiments are summarised in Table 4.1. In our last row, *peak* corresponds the value in dB of the sidelobe level at the peak of the distribution.

In both of the experiments the setup is similar. We assumed a stationary scatterer and chose a PRI of 200 μs. The value of the sample where the scatterer is present in the range velocity image is 1, or 0 dB as shown in Fig. 4.8(b). We then generated the range-velocity matrix and selected only those data within the processed window in range and considered only those filters further than the radial velocity resolution in order to exclude any pixel corresponding to the scatterer. We only regarded the velocities within the principal window ±37.5 m/s. We maintained a fine grid for the sampling in range and velocity of the range-velocity matrix to maximise the number of samples and produce an accurate distribution. With this approach the correlation sidelobes belong to the appropriate range domain, as discussed in Fig. 4.3(a). In the end, we characterised the distribution of the correlation sidelobes by squaring the absolute value and converting it in decibel.

Table 4.1: Characteristics of the correlation sidelobes' distributions for two configurations: 1) fixed pulse bandwidth and 2) fixed total bandwidth and subcarrier spacing

	Fixed B			**Fixed B_{tot} and Δf**		
M	71	147	250	30	60	100
B_{tot} (GHz)	0.71	1.47	2.5	0.6	0.6	0.6
B (MHz)	10	10	10	20	10	6
HiSL (dB)	-11	-12	-14.5	-8	-10	-12
Peak (dB)	-20.5	-24	-27	-17.5	-19.5	-22

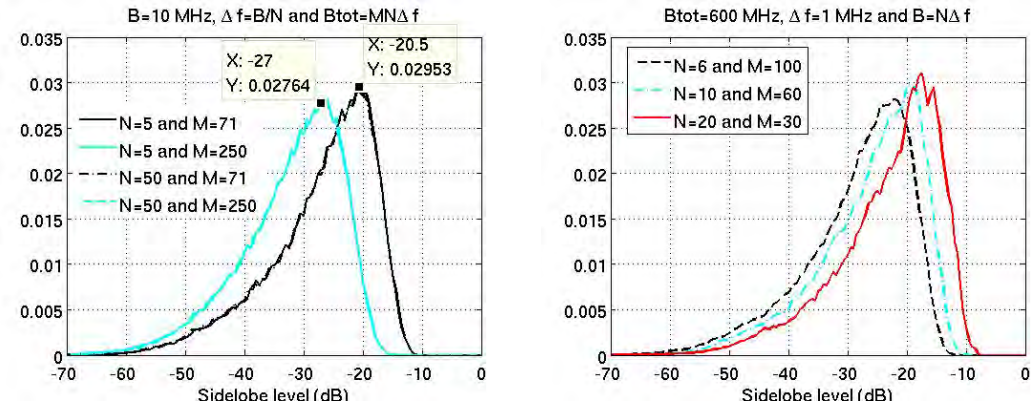

(a) Exp.1: B is fixed

(b) Exp.2: B_{tot} and Δf are fixed

Figure 4.7: Distributions of the correlation sidelobes in the range-velocity image for different values of N and M. Different Costas sequences were used for different length M. The pixels considered are within the processed window in range and exclude the scatterer. The values used to build the histograms are the magnitude squared of the complex samples converted in dB.

4.3.5.2 Contrast improvement via integration

Despite its deterministic nature, the correlation sidelobes are very sensitive to the setup (target position, Costas sequence). We thus propose to improve the contrast of the scatterer over the background by means of coherent integration of several range velocity images. To meet our objective of an improved contrast, thresholding must be applied and only those samples whose magnitude is above this threshold are selected for integration, otherwise the sidelobes saturate the final image. The choice of the threshold value may depend on the detection process that follows. In Fig. 4.8(c) we used the characteristics of the distributions as given in Table 4.1. With M=147, we set the threshold at -18 dB, half way between the highest sidelobe level and the sidelobe level at the peak of the distribution.

In this method, we must make sure that the scatterer remains within the same coarse resolution cell throughout the time span of the several batches as explained in Fig. 4.1. Different Costas sequences can be used for the different batches, although for high velocities, the change in the scene will modify the be-

haviour of the correlation sidelobes anyway. Fig. 4.8(c) shows the range velocity image resulting from this concept with six batches. We considered a fast moving scatterer, V=150 m/s, hence from batch to batch its position shifts significantly. With our choice of PRI (T_r=100 μs) the range migration is 2.2 m from one batch to the next, as expected from the calculation: VMT_r. The scatterer is spotted clearly as it moves within the window. Note that the range of the scatterer in the range velocity image corresponds to the initial range when the first pulse of the train is transmitted.

4.4 Benefits of the technique

In this part, we elaborate on the merits of our concept in light of two standard radar techniques and wrap up with a qualitative analysis related to the OFDM specific issue of ISI.

4.4.1 Comparison with standard wideband techniques

We choose to compare our technique with two classic wideband methods based on the set of requirements presented in Table 4.2. In Section 4.4.2, we consider the design of a train of wideband LFM pulses that would be processed with matched-filters and DFTs to extract both range and Doppler information. In Section 4.4.3 we consider the design of a SFW of unmodulated pulses as proposed in [86, 88]. We present our solution in Section 4.4.4. A thorough comparison is beyond the scope of this study for the obvious reason that the design of radar modes includes many subtleties. Our intention is to demonstrate the capabilities of our solution to cope with the problem of range Doppler ambiguities in the context of a LPD radar.

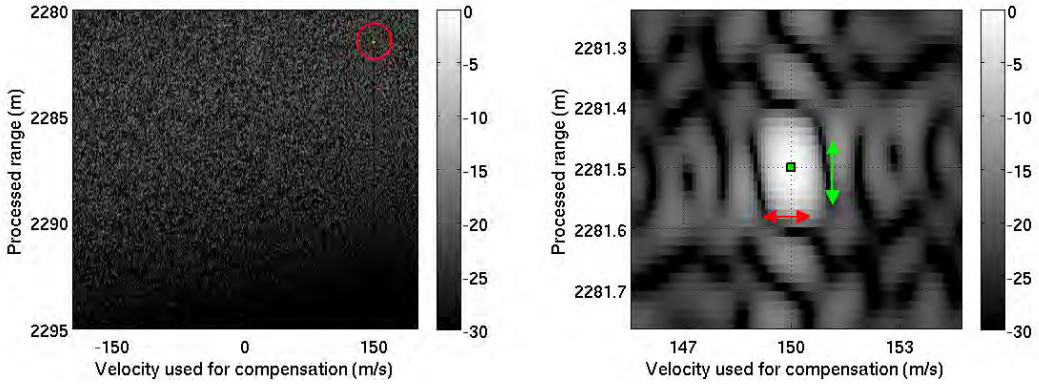

(a) Processing one batch

(b) Zoom around the scatterer

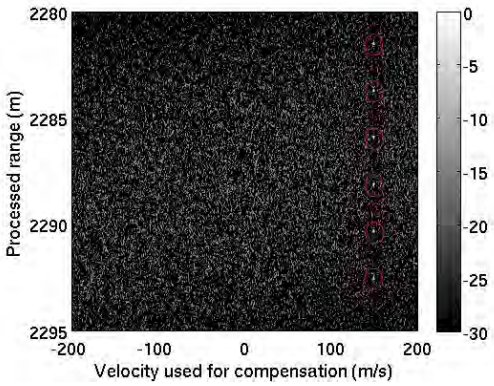

(c) Integrating over 6 batches

Figure 4.8: Range-velocity images showing the scatterer and the correlation side-lobes. The true location is shown with the green dot in 4.8(b). The waveform is composed of M=147 pulses, each with a bandwidth of 10 MHz and the PRI is T_r=100 μs. The range resolution is δR=0.1 m and the radial velocity resolution is δv_r=1 m/s. The conventional ambiguous velocity is $\pm$75 m/s. The scatterer initial range is R_0=2281.5 m and its range rate is V=150 m/s. In 4.8(c) coherent integration over 6 batches has been performed.

4.4.2 Coherent Train of wideband LFM pulses

Although this waveform is commonly used for detection purposes, with pulses covering few Megahertz in bandwidth, here, we inspect the case of wideband transmissions. To cope with Req.1, each pulse shall have a bandwidth equal to B=c/2δR=500 MHz. Req.2 then suggests that the waveform shall be of a *high*

Table 4.2: List of requirements sorted by order of importance from (1) to (5)

	Description of the requirements
Req.1	the range resolution shall be δR=30 cm
Req.2	the unambiguous radial velocity shall be $v_{r_{\text{ua}}}$= ±250 m/s.
Req.3	the unambiguous range shall be: R_{ua}=30 km.
Req.4	the migration in range shall not exceed the size of one coarse range cell during the CPI.
Req.5	for a fixed range, the SNR at the output of the HRR processing shall be greater than 3500 ($\sim$ 35.4 dB) and the energy transmitted per pulse shall be as small as possible.

PRF system, PRF_{min} $\simeq$34 kHz. This choice removes all Doppler ambiguities for the radial velocities of interest. In return, it creates numerous range ambiguities since the equivalent unambiguous range is, R_{ua} $\simeq$4.4 km as opposed to 30 km in Req.3. The high bandwidth of each individual pulse calls for a high sampling rate in the fast time. Assuming complex signals, the sampling frequency is f_s=$1/B$ and the range cell extent which is also the coarse range cell extent is δR=30 cm. To comply with Req.4, a limited number of pulses M can be used: $M_{\text{max}} = \delta R/(T_r v_{r_{\text{ua}}})$ $\simeq$40. Not listed in Table 4.2, the resolution in radial velocity is thus at the rather low value $\delta v_r = c/(2 f_0 M_{\text{max}} T_{r\,\text{max}})$=15 m/s.

Clearly, this technique suffers from two main flaws that require to: 1) solve for the range ambiguities; 2) apply a processing able to cope with higher migration in range (over many range cells) of the received echoes in order to increase the CPI and improve the Doppler resolution. Solutions to problem 1) include the use of multiple transmissions with different PRIs however it involves more complex architectures. Solutions to problem 2) include the use of techniques as proposed in [89] but it implies increased computational load.

For completeness, assuming each echo is received with SNR_{in}=0 dB, Req.5 suggests that the time-bandwidth product Bt_p be at least SNR_{out}/M since the integration gain for a processing based on matched-filtering and Doppler filtering is equal to Bt_pM [32]. The pulse length shall verify $t_p \geq SNR_{\text{out}}/MB$=0.18 μs. A higher bound would follow a constraint on the maximum blind range. Besides, one unfavourable aspect of wideband LFM pulses is that, in some radar systems,

some components cannot operate properly over the entire bandwidth [36].

4.4.3 Stepped frequency Train of unmodulated pulses

As opposed to the previous waveform, traditionally used for detection tasks, SFW of unmodulated pulses are commonly used for target classification tasks. The concept of synthetic range-profile generation reduces the requirement on the sampling frequency and the coarse range cell extent is $\Delta R{=}ct_p/2$. Following the method in [90] one burst of M narrowband pulses is transmitted, where each pulse has a frequency $f_m{=}m\Delta f$. In the receiver, complex samples are collected on the baseband mixer output at a rate $1/t_p$. One synthetic range profile is then formed by applying an IDFT on the M complex samples collected at a particular range gate. When no additional matched-filter is applied on the received pulses, the integration gain is equal to the number of samples M used in the IDFT.

By principle, the PRI shall be chosen such that the furthest target of interest fall within the non ambiguous range as explained in Section 4.2.2.1, otherwise, the corresponding received echo may be filtered in the IF filter.

While Req.1 implies that the synthetic bandwidth be 500 MHz, the above comment implies that Req.3 shall be used to choose the PRI, $T_{r\,\mathrm{min}}{=}200$ μs that is, $PRF_{\mathrm{max}}{=}5$ kHz, which is of a *low PRF system*.

The difference between the unmodulated pulse and the OFDM pulse solution requires the examination of Req.5. Essentially, without the aforementioned additional matched-filter the standard stretch processing offers an integration gain of M while our OFDM based solution has an integration gain of NKM. Hence, would our echoes be received as in Section 4.4.2 with $SNR_{\mathrm{in}}{=}0$ dB, $M{=}3500$ pulses shall be transmitted. This is not acceptable with our low PRF, thus Req.5 will be satisfied provided that a smaller number of more energetic pulses are transmitted. Because Req.4 attributes a maximum value to the number of pulses M_{max} based on the coarse range cell extent, we see a trade-off to choose t_p and M. In summary, longer pulses can accommodate higher values for M under Req.4 at the expense of larger blind ranges and longer CPI.

We can see that the following values comply with Req.4 and Req.5: t_p=0.1 μs, (coarse range resolution) ΔR=ct_p/2=15 m and $M_{\max}$=$\Delta R/(T_r v_{r_{\text{ua}}})$=250; the CPI is 50 ms and the minimum energy for each received echo to achieve the output SNR in Req.5 must be $E_{\min}$=3500/250=14.

This technique suffers from two major flaws that require to: 1) raise the uncertainty in range and Doppler resulting from the range-Doppler coupling; 2) increase the integration gain to permit the transmission of less energetic pulses. Solutions to problem 1) were discussed in [86] and include the combination of several batches with different slopes (up, down and zero). Alternatively, Costas hopping schemes can be used. In both cases, a Doppler filter bank is required. Another solution relies on the transmission of a series of stepped frequency bursts. Doppler processing is then applied on the pulses with the same frequency. However the PRF used for the unambiguous Doppler calculation equals PRF/M, which in our example will cause many ambiguities within the domain of interest. Solutions to problem 2) include the use of matched-filters in the receiver [88]. Alternatively, the rectangular pulses could be replaced by LFM pulses. As such, these solutions are less binding than those in the previous concept. In particular, our OFDM based solution will be equivalent to the LFM based SFW when Costas hopping schemes and matched-filters are used. The main merit of the OFDM based solution is to permit the transmission of diverse and noise-like pulses.

4.4.4 Our OFDM based SFW solution

We propose a set of parameters for our waveform-processing solution and show that Reqs.1-5 are compliant. Essentially, we are able to operate over large unambiguous ranges while retrieving unambiguously high Doppler shifts with low energy pulses. The merit of these characteristics in regard of electronic counter counter measures (ECCM) aspects was pointed out by other authors [89].

Again, Req.1 and Req.3 are used to fix respectively B_{tot}=500 MHz and T_r=200 μs. Then Req.1, Req.2, Req.4 and Req.5 translate into a set of constraints for the four waveform parameters N, M, K and Δf. We also consider the Doppler

based SNR degradation constraint derived in Section 4.2.3.4 which we refer to as Req.6 and add the subsequent parameter N_{int} that defines the number of batches used for coherent integration.

- Req.1 implies: $MN\Delta f$=500 MHz.
- Req.2 and Req.6 imply: $\Delta f/K \geq 5v_{r_{\text{ua}}}F_0/c$
- Req.4 implies: $MN\Delta f N_{\text{int}} \leq c/2v_{r_{\text{ua}}}T_r$
- Req.5 implies: $NKM \geq 3500$

Table 4.3 presents a set of parameters that fulfils the requirements. Unlike Req.1, Req.3 and Req.5 which can be assessed easily, we comment on the other three. For Req.4, it is clear that the maximum migration in range $v_{r_{\text{ua}}}MN_{\text{int}}T_r$=30 m is not larger than the coarse resolution cell $c/2N\Delta f$. For Req.6 we compute the maximum value of $|f_D/\Delta f|$ which we compare to the threshold $1/2.5K$=0.057. With the maximum radial velocity $v_{r_{\text{ua}}}$=250 m/s, we find $|f_{D\max}/\Delta f|$=0.017<0.057. Lastly, for Req.2, the use of a bank of range migration filters covering $\pm v_{r_{\text{ua}}}$ ensures the retrieval of the target radial velocity within that interval. The ambiguities at $\pm k\tilde{v}_{r_{\text{ua}}}$=$\pm k$75 m/s in the range velocity image are reduced as a result of the large relative bandwidth.

Table 4.3: Waveform parameters used in our OFDM based SFW solution to comply with the requirements from table 4.2

Parameter Name	**Symbol**	**Parameter Value**
Number of pulses	M	100
Number of subcarriers/pulse	N	5
Number of symbols/pulse	K	7
Subcarrier spacing	Δf	1 MHz
Number of batches	N_{int}	6

4.4.5 Low probability of detection properties

An aspect that can motivate the use of this OFDM based SFW is its LPD characteristics. Firstly, the processing can tolerate long PRIs despite the high

radial velocities of interest, the duty cycle can thus be far below what high PRF systems would employ (usually between 10 kHz and 100 kHz [32]). We demonstrated this property with our 5 kHz PRF as compared to the high PRF (40 kHz) obtained in Section 4.4.2. Secondly, the energy of each pulse is reduced for the same output SNR. Indeed, we showed that our waveform-processing solution offers an integration gain equal to NKM. As a result, for the same number of pulses transmitted and the same output SNR in the HRRP, the standard SFW of unmodulated pulses will have to transmit pulses with an energy NK higher. Thirdly, the individual pulses can appear noise-like in the time domain and their power spectral density is spread and lower as shown in Fig 4.9(c). Lastly, the random-Costas hopping scheme reduces further the risk of narrowband jamming.

Fig. 4.9(a) shows in the time domain, the magnitude of a pulse relying on a 5-element Barker code IS as opposed to a pulse with phase codes set to minimise the PMEPR of the OFDM pulse. Known to be a severe constraint in OFDM radar, we developed search strategies to come up with optimal phase codes that result in low PMEPR as well as low PSLR [46]. Clearly, the pulse based on the IS barker code offers bad PMEPR properties. Remark that while Costas coding concerns the choice of the carrier frequencies f_m, coding for PMEPR reduction is applied on the phase codes $a_{n,k,m}$. As such, they are independent and compatible. The autocorrelation functions of both pulses are displayed in Fig. 4.9(b). We see that the highest sidelobes have dropped by about 5 dB. Note that we did not add any tapering to reduce further the sidelobes.

4.4.6 Philosophy of the processing

Like OFDM in communication, our frequency domain processing is subject to ISI. That is why we specified so strictly our discrete model to be as in Fig. 4.1. As such it is a harsh constraint since we cannot tolerate other scatterers that would create overlapping echoes shifted in range by more than the size of a coarse range cell. Indeed these interferences would deteriorate our retrieved HRRP. Fig. 4.10 illustrates the "ISI free region". In fact we observe that we can have overlapping echoes without harm as long as two symbols fully overlap. One way

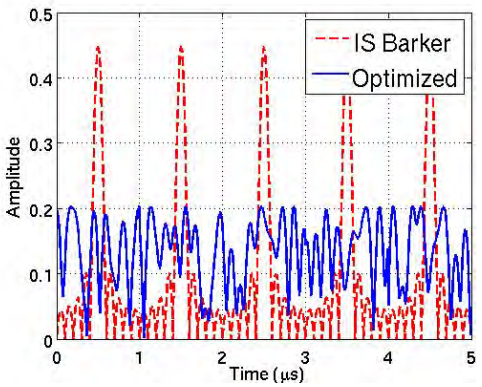

(a) Time domain

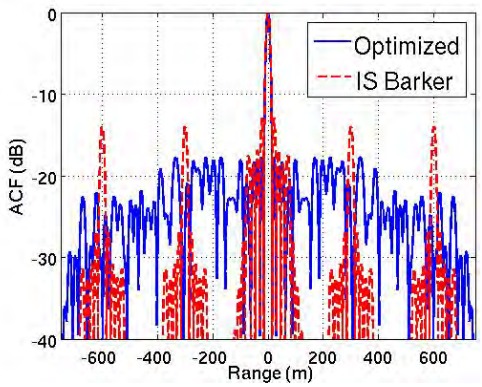

(b) Autocorrelation function

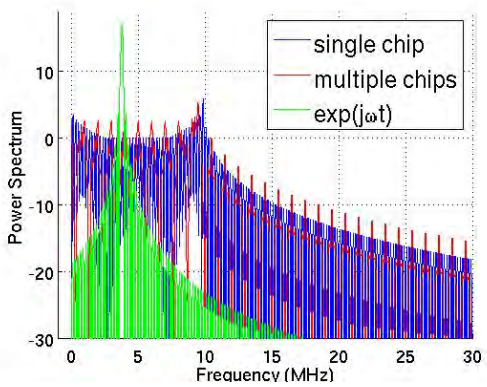

(c) Spectrum

Figure 4.9: An OFDM pulse in the a) time domain and b) its ACF. The pulse is composed of K=5 symbols, N=10 subcarriers and has unit energy. The subcarrier spacing is Δf=1 MHz so that the coarse range resolution is ΔR=15 m. We compare two cases for the phase codes. In one case, the phase codes are based on a 5-element Barker IS while in the second case we used a set of phase codes optimised both for low PMEPR and low PSLR. c) Power spectrum of an OFDM pulse when B=10 MHz for two cases: one symbol and N=50 subcarriers and K=5 symbols and N=10 subcarriers. For comparison we included the spectrum of a single complex exponential. All three signals have unit energy.

around the limited size of this ISI free window is to apply matched-filtering on the individual pulses to produce a coarse range profile. If peaks are present in the ISI free region as indicated in Fig. 4.10, we can then apply our frequency domain HRR technique to zoom in the particular cell of interest and see the

contribution of the various scatterers.

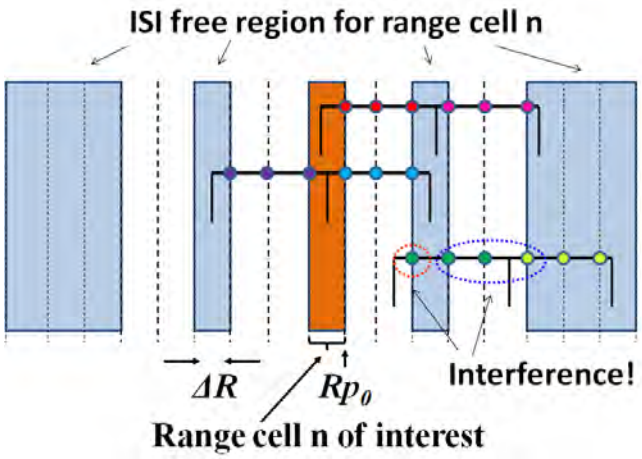

Figure 4.10: ISI free region.

4.5 Summary

A technique to reconstruct a high range resolution profile using an OFDM based SFW with Costas hopping schemes has been proposed. The technique exploits the phase relationships of the OFDM signal to generate the HRRP. Our contributions are as follows: 1) we derived the data model of the received signal in a compact vector format and formulated the frequency domain HRR processing by means of matrix manipulations. The HRRP is only limited by Fourier sidelobes since the OFDM phase codes are suppressed in the processing; 2) we evaluated the integration gain; 3) we inspected how Doppler modulation impacts the HRRP and we derived an expression which can be used as a rule of thumb at the waveform design since it relates the SNR loss and the normalised Doppler frequency; 4) we introduced a new waveform-processing concept, where we apply frequency hopping schemes based on Costas sequences to step the individual OFDM pulses. The processing requires an additional range migration compensation block since unlike linear frequency steps the range migration destroys the HRRP. The merit of this technique is to retrieve unambiguously the radial velocity of the scatterers whilst the flaw was shown to be the high level of the correlation sidelobes. Note

that other methods than blunt thresholding may be applied to decrease these correlation sidelobes. Besides, processing techniques that would realign the scatterers throughout the multiple CPIs could offer more effective integration; 5) we compared our concept with two wideband alternatives: a train of wideband LFM pulses and a SFW of unmodulated pulses. We stressed that our waveform contains favourable properties in terms of low probability of detection (LPD); 6) we then discussed the risk of ISI as a result of the frequency domain processing. In the end, note that unlike other classic wideband radar waveforms, the OFDM structure makes it possible to convey information via the phase codes. In this case, other methods than those employed in this chapter to reduce the PMEPR of the individual pulses are required.

Chapter 5

Design of OFDM radar pulses using genetic algorithm based techniques[9]

It can quickly be verified that non-coded OFDM pulses will not be suitable in radar systems that operate with the conventional matched filter processing, since they will give rise to high sidelobes. Another drawback of non-coded OFDM pulses is their varying time domain signal. Strong variations are detrimental since they can cause distortions in power amplifiers. Therefore, the OFDM pulse needs to be tailored before it becomes a suitable radar waveform.

5.1 Introduction

We argue that the emerging evolutionary algorithms (EA) are particularly adapted to solve the pulse design problem when the pulse is an OFDM signal. Although a number of techniques have been proposed to mitigate the PMEPR and the

[9] Based on Lellouch, G. et al. "Design of OFDM radar pulses using genetic algorithm based techniques," accepted in the first review to *IEEE Transactions on Aerospace and Electronic Systems*

PSLR [36], their flexibility is somewhat limited. For example, the Newman phasing technique gives very low PMEPR for the single OFDM symbol case, and this for most numbers of subcarriers N. However, as soon as some subcarriers are suppressed the PMEPR deteriorates.

Here we aim to show how we can integrate some simple and easy-to-implement mimetic computing techniques in the design of OFDM radar waveforms. Firstly, we focus on the single objective GA optimisation technique. Then we look at the multiple-objective optimisation genetic algorithm (MOO-GA) technique. Although the former method offers a single and straightforward implementation [91], more than one option are found in the case of the MOO-GA. In this work, we use the well known NSGA-II. It has proven to work much faster than the earlier version, NSGA, while providing diversity in the solutions [92]. Few other radar related studies implemented the same algorithm [93, 94].

5.2 Waveform design

In this section, we present the successive steps that form our design strategy for fixing some of the pulse parameters. We show how they are inferred from, on the one hand, the processing and on the other hand, the scenario. This analysis fixes the frame of our pulses. We will show in the following section how we optimise the rest of our free parameters to compose pulses with improved radar features.

5.2.1 Processing related constraints

In the scope of a pulsed OFDM radar waveform, we proposed in Chapter 3 two processing alternatives. The first alternative is based on the combination of matched filtering and Doppler processing while the second alternative transforms the received signal in the frequency domain in the same way OFDM communication systems operate. After a demodulation stage that suppresses the phase codes, two orthogonal DFT processing are applied to form a range Doppler image. The key characteristics of both processing are recalled in Table 5.1. In the

rest of this Chapter we refer to the former as the *time domain processing* while we name the latter our *frequency domain processing*.

Table 5.1: Characteristics of our processing alternatives

	Time Domain Processing	**Frequency Domain Processing**
Pros	Immune to intersymbol interference Doppler sidelobes are phase code independent	Range and Doppler sidelobes are phase codes independent
Cons	Range sidelobes are phase code dependent	Subject to intersymbol interference

Because our frequency domain processing is subject to ISI, we use it for tracking. In tracking configurations we can assume to have some prior knowledge of the illuminated scene and in particular, the target extent. The rule of thumb is that the return echo from the closest point scatterer and the return echo from the furthest point scatterer of the target fall within the same time cell. When satisfied, this condition insures that the orthogonality between the subcarriers is maintained. This issue has been of utmost interest in the early years of OFDM signalling for communication to cope with the multipath effect. To that end the concept of cyclic prefix has been introduced [7]. In our current analysis, rather than inserting a cyclic prefix, we choose to match the size of the time cell according to the target extent. Since the time domain processing does not come up with a severe design constraint we choose to use the constraint of the frequency domain processing as the main guideline.

5.2.1.1 Sampling frequency

In our analysis, the received signal, which we feed into either of these processing, is the complex signal formed from the real and imaginary components, respectively, in the *in-phase* I and *quadrature* Q channels of the receiver. If the transmitted OFDM pulse has a bandwidth B, the received complex signal has the same bandwidth. Because the signal is complex, the Nyquist theorem states that the sampling frequency can be taken as low as $f_s = B$ and the time cell size

is thus inversely proportional to the bandwidth, $t_s = 1/B$. The size of the range cell is then given by $c/2B$, where c is the speed of light.

5.2.1.2 Bandwidth

As a result, if we want to design the size of the time cells such that, despite the superposition of all echoes returning from the different point scatterers of the target, the orthogonality property of the subcarriers is maintained, we shall adjust the bandwidth to comply with: $c/2B \geq \Delta R_t$ where ΔR_t is the target range extent. Practically we can add a margin to account for the target radial velocity and the uncertainty on the target extent and position. Not only the received echoes shall remain in the same time cell as a result of the first pulse but also throughout the coherent processing interval. In the end the bandwidth can be obtained from:

$$B = \frac{c}{2(\Delta R + \alpha_R)} \tag{5.1}$$

where α_R is the margin in range.

Therefore, if there is no need for high range resolution (assuming that the target is known) we suggest to select the bandwidth based on these ISI considerations.

5.2.2 Scenarios related constraints

Other parameters need to be fixed. The pulse length and the number of subcarriers that will compose the OFDM signal.

5.2.2.1 Pulse length

Pulse compression waveforms rely on low peak power transmissions to provide the same maximum detection range and the same range resolution as would be obtained from a short pulse with a high peak power. But as the radar receiver is switched off while transmitting, the pulse length is limited. We commonly refer to as the eclipsed zone, the window that lies between the radar and the

minimum detection range. Even though we could choose one value for each target, for simplicity we choose only one for all. If, say, we expect targets from $R_{\min} = 1.5$ km, an upper bound for the pulse length is found to be [32], $t_p = 2R_{\min}/c = 10$ μs.

5.2.2.2 Number of subcarriers

The orthogonality property is another example of the unique OFDM structure. It states that the bit duration t_b is inversely proportional to the subcarrier spacing Δf, $t_b = 1/\Delta f$. In the extreme case where the pulse is composed of one symbol the maximum number of subcarriers $N_{\max}$ used in the pulse can be derived from:

$$N_{\max} = \frac{2BR_{\min}}{c} \tag{5.2}$$

For the same pulse bandwidth and pulse duration a smaller number of subcarriers can be used if we construct the pulse from several symbols. For example, we can decide to use 250 subcarriers with 4 symbols in the pulse to maintain the same duration. The subcarrier spacing is then increased from 100 kHz to 400 kHz. Information related to the target maximum speed shall also be considered to ensure negligible distortion effects in either processing [45, 46].

In light of the above analysis, the fixed parameters for our pulses are summarised in Table 5.2.

Table 5.2: Scenarios' characteristics for the waveform design

	Case 1 (walker)	Case 2 (truck)
Range extent (m)	2	10
Margin (m)	1	5
Bandwidth (MHz)	**50**	**10**
Maximum number of subcarriers	**500**	**100**

5.3 Optimising the pulse for radar

Having fixed the frame of our pulses, literally the bandwidth and the maximum number of subcarriers, we are now ready to concentrate our analysis on the optimisation of the OFDM pulse for radar. Firstly, we need to define our objective functions and secondly, we need to identify the OFDM parameters/variables upon which we can run our optimisation procedure.

5.3.1 Objective functions

An OFDM symbol is built as a sum of weighted complex sinusoids, where every sinusoid has a given starting phase. When the OFDM pulse is composed of several symbols it can be expressed as:

$$s(t) = A \sum_{n=1}^{N} w_n \left(\sum_{k=1}^{K} a_{n,k} r_k(t) \right) \exp(j2\pi n \Delta f t). \tag{5.3}$$

N is the total number of subcarriers in the pulse, w_n denotes the weight applied on subcarrier n and $a_{n,k}$ is the phase code attributed to subcarrier n in symbol k. K is the total number of symbols in the pulse. The function $r_k(t)$ refers to the rectangular window for every symbol:

$$r_k(t) = \begin{cases} 1 & kt_b \leq t < (k+1)t_b \\ 0 & \text{elsewhere.} \end{cases}$$

Like in [47], the normalisation factor A is given by:

$$A = \frac{1}{\sqrt{\sum_{k=0}^{K-1} \sum_{n=0}^{N-1} {w_n}^2 |a_{n,k}|^2 t_b}}. \tag{5.4}$$

When using OFDM for radar two important aspects must be considered.

5.3.1.1 Sidelobe level

Firstly, would the processing be based on a correlation function like in our time domain processing where matched filtering is applied in range, the sidelobes at the output shall be maintained as low as possible. This consideration is true for any signal and a fortiori for our OFDM signal. When both signals used in the correlation are equal, the correlation function becomes the autocorrelation function. The output of $R_{\text{corr}}(\tau)$ is then given by:

$$R_{\text{corr}}(\tau) = \int_{-\infty}^{\infty} s(t)s^*(t-\tau)dt. \tag{5.5}$$

In our analysis, we rather use the discrete form $R_{\text{corr}}[m]$:

$$R_{\text{corr}}[m] = \sum_{p=0}^{NK-1} s[p]s^*[p-m], \tag{5.6}$$

where m takes integer values between $-NK+1$ and $NK-1$. $s[p]$ represent the discrete values of the OFDM pulse taken at the discrete instants pt_b/N, where p takes integer values from 0 to $NK-1$. If the pulse is composed of only one symbol, then p takes values from 0 to $N-1$, just like n the subcarrier index. In the end, $s[p] = s(pt_b/N)$. In Eq. 5.6, we assume that $s[p] = 0$ for all forbidden values of p, that is $p < 0$ and $p > NK-1$.

To cope with practical applications we commonly distinguish two objective functions. The first function is the PSLR. It returns the ratio between the highest sidelobe and the peak.

$$PSLR = \frac{\max_m |R_{\text{corr}}[m]|}{|R_{\text{corr}}[0]|}, m \neq 0 \tag{5.7}$$

The second function is the ISLR. It returns the ratio between the cumulation of the sidelobes and the peak.

$$ISLR = \frac{\sum_m |R_{\text{corr}}[m]|}{|R_{\text{corr}}[0]|}, m \neq 0 \tag{5.8}$$

The weight attributed to both figure-of-merits depends on the application as well as the environment. For example, if the radar operates in the presence of distributed clutter, it will be important to work with low ISLR in order to keep the weak targets visible. In that case, high ISLR can be interpreted as an increase of the noise floor. Conversely if the application requires detection of targets in the presence of strong discrete clutter, the PSLR is more critical and must be kept low to prevent from deceptively considering one sidelobe as another small target.

5.3.1.2 Peak-to-mean envelope power ratio

This second aspect is specific to OFDM signals and was introduced in Section 2.3.4. It characterises the variations in time of the signal envelope. Because they are generally used in saturation to maximise the transmitted power, devices like power amplifiers can distort the output signal. The distortion caused by amplitude clipping can be viewed as another source of noise that can fall both in-band and out-of-band. In-band distortion cannot be reduced by filtering and results in performance degradation, while out-of-band radiation reduces spectral efficiency. As a result, radar waveform designers shall cleave to mitigate those variations of the signal amplitude. While the PAPR, defined as the ratio of the peak power to the average power of the real-valued multicarrier signal, is usually of interest, we consider the peak-to-mean envelope power ratio (PMEPR) because we work with complex baseband signals. By definition, the PAPR will be smaller than the PMEPR [36] whose expression is given by [95]:

$$PMEPR = \frac{\max_n |s[n]|^2}{\frac{1}{N}\sum |s[n]|^2}, \tag{5.9}$$

In Eq. 5.7, Eq. 5.8 and Eq. 5.9, we have assumed to work at the critical sampling rate $f_s = B$ such that the sampling period is $t_s = t_b/N$, as a result of the relationships that govern the OFDM structure. In Fig. 5.1 we emphasize on the need for oversampling. Because of the quick temporal variations of the OFDM signal, the PMEPR of the critically sampled signal will differ from the PMEPR

of the continuous signal. An important question is how large the oversampling factor should be in order for the approximation to be accurate. In [61], the difference between the continuous-time and discrete-time PAPR is evaluated and the conclusion is that an oversampling factor of 4 is accurate for an OFDM signal with BPSK coding. An exhaustive search through the literature ascertains that this oversampling factor can be admitted as the rule-of-thumb [96, 97]. Despite this pledge for the PMEPR, in this work, we oversample the OFDM signal with a factor of 20 before evaluating our objective functions. This value ensures that both discrete time domain OFDM pulse and autocorrelation functions are representative of their continuous counterpart. Smaller values may be considered to reduce the simulation time. In Fig. 5.1(b), we show how both PSLR and ISLR calculations exclude the values around the main peak. The total peak extent is equal to twice the Rayleigh resolution, which in time is $2/B$ [44].

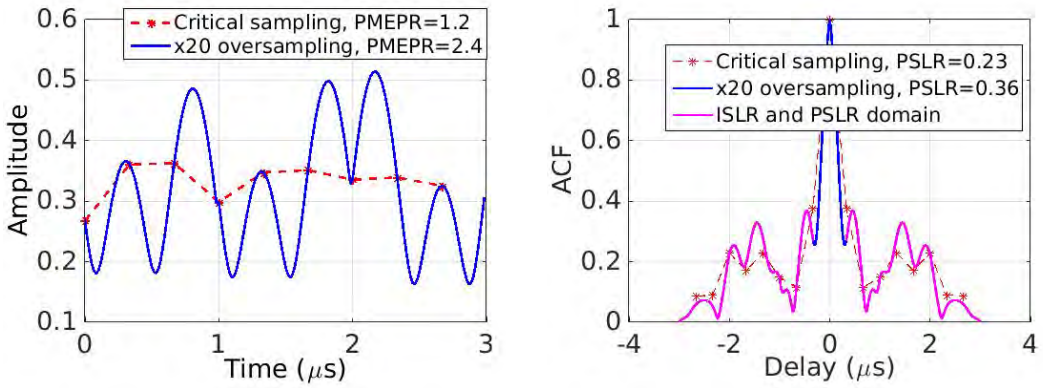

(a) Time domain OFDM pulse

(b) Autocorrelation output

Figure 5.1: a) Amplitude versus time of an OFDM pulse and b) its autocorrelation function versus range when N=3 and K=3 in the case of critical sampling f_s=B and oversampling f_s=20B. The values obtained for the PMEPR and the PSLR are given.

5.3.1.3 Optimisation strategy

Thus, in the process of designing an OFDM pulse, extra care shall be employed so that the signal results in tolerable PMEPR as well as reasonable sidelobe

level. Note however that in this statement we have assumed that the processing is based on a correlation function. In our case, this is valid when we intend to use our time domain processing. However, if rather, we decide to use our frequency domain processing, we have recalled in Table 5.1 that both the range and Doppler sidelobes were phase code independent. In that case, the optimisation can focus on the PMEPR only. In a nutshell, this analysis indicates that with our time domain processing, we are interested in optimising 3 objectives, while with our frequency domain processing, we would have a single objective. We thus have to come up with two solutions, a multi-objective solution and a single objective one.

5.3.1.4 Variables for optimisation

We have seen in Eq. 5.3 that the parameters still available after our initial design in Section 5.2 were the weights w_n and the phase codes $a_{n,k}$. We decide to leave the weights and focus primarily on the phase codes. To justify this approach, we point out that the scattering centres of a target resonate variably at different frequencies [38], therefore it may be desirable to leave the weights for an optimisation that would account for the target model as we will see in Section 5.6. For now, we assume equal weights such that the pulse has normalised energy. The phase codes are also assumed to have constant modulus. Each $a_{n,k}$ is thus a number on the unit complex circle.

5.3.1.5 Existing optimisation methods

The problem of minimising the PSLR and the PMEPR has been researched extensively since the emergence of the multicarrier concept. Levanon et al. [36] have reported the major contributions in that field. Two strategies have stood out. The first strategy considers IS, such that all subcarriers are assigned the same phase code. Optimising the PMEPR of the pulse results in optimising the PMEPR of a single symbol. Newman, Schroeder and Narahashi have suggested different phasing methods to decrease the PMEPR. In their concept the weights

w_n are complex values with quadratic dependence on n. PMEPR as low as 2 (3 dB) can be obtained for any relevant value of N (up to 65,000). The second design strategy is based on modulating all N subcarriers with consecutive ordered cyclic shifts (COCS) of an ideal chirplike sequence (CLS) of length K. For example, an OFDM pulse based on COCS of P4 codes can give PMEPRs below 2 and PSLR below -15 dB for a large range of N (between 0 and 70). A handful of methods to reduce the PMEPR of OFDM symbols for communication are summarised in [98], although their constraint to cope with the transmission of information is out of our scope as it adds an unnecessary level of complexity.

5.3.1.6 Motivation for genetic algorithm optimisation methods

Although the aforementioned techniques produce excellent results in terms of PMEPR alone or PMEPR and PSLR combined, we suggest to introduce GA based methods in this field for three main reasons. Firstly, it will diversify the solutions and increase the potential number of good codes: not necessarily the best but those good enough for the application. Secondly, we can deviate from the conventional objective functions. Assume we want very low sidelobes close to the main peak of the autocorrelation function and can tolerate higher levels further away, the new objective function can be implemented easily in the GA. Also, we can add constraints on the spectrum to ban the use of some subcarriers as in [99]. In that case, if we rely on any of the previous strategies, the loss of one or more subcarriers may affect the PMEPR, the PSLR or both. In both cases, GA based optimisation can come up with optimal sets of phase codes to satisfy our updated objective functions. Thirdly, we can also optimise the ISLR which is not in the focus of the other methods. Not only we can optimise it solely but we can optimise it together with the PSLR and the PMEPR by means of multi-objective optimisation (MOO) techniques. Until now just a few authors have considered the use of GA and MOO techniques for radar however an increasing number of papers have recently established the potential of these optimisation methods [100, 78, 101, 102].

5.4 Optimisation techniques

In this section, we present our GA based optimisation techniques.

5.4.1 Problem encoding

The first step in the implementation of any genetic algorithm is to generate an initial population. Following the canonical genetic algorithm guideline [91], this implies encoding each element of the population into a binary string. Note however that techniques based on real numbers have also been developed [103, 104]. The MOO-GA that we discuss in Section 5.4.4 applies one of them. For now, we simply encode one phase code (value between 0 and 2π) into a string of q_g genes. When we are dealing with a pulse composed of N subcarriers and K symbols, we end up with NK strings of q_g genes each. Stacking these strings together we create one element of the population, which is then formed from $Q_g{=}NKq_g$ genes. This element is called a chromosome. If we require to use for example BPSK, then $q_g = 1$, QPSK, then $q_g = 2$. In the more general case where we have no restriction we can consider the largest value authorised by our system. In our case we use $q_g = 18$. The resolution in angle is then $\Delta\theta = 2\pi/2^{q_g} \simeq 0.024$ mrad. Note that the larger q_g the slower the algorithm. This is caused by the increase of the search space as discussed hereafter. With the values of N and K that we consider in this study, the chromosome length can be as large as 9000, ($N = 500$ and $K = 1$). The search space $\mathcal{S}$ "reduces" to the binary strings of length Q_g.

5.4.2 Population size

To understand what the population size L_{pop} shall be, we followed the guideline given in [105]. The starting point is to say that every point in the search space shall be reachable from the initial population by crossover only. This can happen only if there is at least one instance of every gene at each locus in the entire population. On the assumption that every gene is generated with random

probability (Proba(1)=1/2 and Proba(0)=1/2) the probability that at least one gene is present at each locus is given by [105]:

$$\text{Proba} = (1 - (1/2)^{L_{\text{pop}}})^{Q_g}. \tag{5.10}$$

With $Q_g = 9000$ we see that $L_{\text{pop}} \simeq 23$ when we take Proba $= 99.9\%$ and $L_{\text{pop}} \simeq 26$ when we take Proba $= 99.99\%$.

5.4.3 Genetic algorithm

The genetic algorithm implemented in this work is a two-stage process. Goldberg defined this class of genetic algorithms as simple genetic algorithms (SGA) [91]. It starts with the current population. Then, selection is applied to form the intermediate population. Next, recombination and mutation are applied to form the next population. The process of going from the current population to the next population represents one generation of the execution of the genetic algorithm. We mentioned earlier that we make use of this algorithm for the single objective optimisation, where the objective is the PMEPR. The steps are:

1. Initialise the current population by generating L_{pop} chromosomes. Each chromosome has its Q_g genes set to 0 or 1 with equal probability.
2. For each chromosome, convert the NK binary sequences into real numbers and create a set of NK phase codes: $\exp(ja_{n,k})$.
3. For any of the L_{pop} sets, compute the oversampled complex OFDM signal, obtained as a result of applying an IDFT[10] on the phase codes [18].
4. Evaluate the PMEPR according to Eq. 5.9 and attach this number to the corresponding chromosome.
5. Form the intermediate population by discarding the weakest element (highest PMEPR) and duplicating the strongest element (lowest PMEPR).

[10] If there are several symbols in the pulse the IDFT is applied on each vector of phase codes corresponding to one symbol and so on. At the end the outputs are stacked together to form the pulse

6. Prepare for recombination by associating chromosomes by pair. Each pair shall be composed of two distinct chromosomes.

7. For each pair, apply a one point crossover [91]. This process results in the generation of L_{pop} offspring.

8. Apply mutation every two generations. When the generation number is odd, select at random L_{mut} offspring and for each of them apply mutation on one of their gene, again, selected at random.

9. Feed the intermediate population into the current population.

Steps 2 to 9 are carried out until the stopping criteria is met. The latter is characterised by two elements. A threshold on the population mean fitness that guarantees satisfactory solutions in the current population as well as a threshold on the standard deviation which assesses the convergence of the entire population towards a minimum solution.

5.4.4 Multi-objective genetic algorithm

Our multi-objective problem could be solved as a single optimisation problem by formulating an objective function in the form $s_{\text{obj}} = \alpha PMEPR + \beta PSLR + \gamma ISLR$ and then optimising with respect to s_{obj} with our GA. The drawback of that solution is judicious selection of the weights. If multiple solutions are required, the problem has to be run repeatedly for different sets of weights. To overcome this difficulty, many multi-objective evolutionary optimisation algorithms have been developed, which produce a set of non dominated solutions in a single run. A solution is called nondominated or Pareto optimal, if none of the objective functions can be improved in value without degrading some of the other objective values. Without additional subjective preference information, all Pareto optimal solutions are considered equally good. In this work, we make use of the well-known non dominated sorting genetic algorithm NSGA-II [92]. The principal breakthrough of this algorithm is the convergence towards the Pareto-optimal set with a good spread or diversity of the solutions [106]. When selecting

the best elements not only the respective fitness functions are evaluated but also the crowding distance, which tells whether this element is in a high density zone or conversely in an low density zone. At equal fronts, we select the isolated element in order to maintain diversity in the solutions. In light of this preparation we describe the steps of this algorithm, which we use with either two or three of our objective functions. In comparison to our GA, the NSGA-II uses real numbers throughout. Genetic operations such as cross-over and mutation employ a method that simulates the equivalent binary processes. A thorough review of this technique is available in [103].

1. Initialise the population with L_{pop} sets of NK phases, all real numbers between 0 and 2π and calculate the phase codes $\exp(ja_{n,k})$.
2. For any of the L_{pop} sets, compute the oversampled complex OFDM signal, obtained as a result of applying an IDFT on the phase codes and calculate the autocorrelation function.
3. Evaluate the objective functions following Eq. 5.7, Eq. 5.8 and Eq. 5.9.
4. Sort the chromosomes according to non dominated sort and form the fronts ($\equiv$ rank).
5. Evaluate the crowding distance of each chromosome.
6. Select the parent chromosomes using binary tournament selection. In binary tournaments, two chromosomes are randomly chosen and the strongest in terms of rank is selected to be in the parent population. If individuals with the same rank are encountered, their crowding distance is compared. A lower rank and higher crowding distance is the selection criteria. The parent population has a size of $L_{\text{pop}}/2$.
7. Apply genetic operations such as cross-over and mutation on the selected chromosomes to produce the off-springs.
8. Combine the off-spring population with the parent population and select the best L_{pop} chromosomes for the next generation, again based on the rank and if needed on the crowding distance.

Steps 2 to 8 are carried out until the stopping criteria is met, which occurs in this case when the total number of generations has been covered.

5.5 Simulation results

In this section we present our simulation results. We start with the results obtained with our single objective GA.

5.5.1 Single objective: PMEPR

In our simulations, we considered a population of $L_{\text{pop}} = 22$ chromosomes, and the number of chromosomes selected for mutation every two generations was $L_{\text{mut}} = 5$. Despite the simplicity of our genetic algorithm, we are able to retrieve phase code sequences with optimal PMEPR properties. In Figs. 5.2(a)-5.2(b), we compare the PMEPR of three sets of phase codes for two different configurations. In the first configuration, all subcarriers are enabled. We see in Fig. 5.2(a) that our GA solution with 10 subcarriers outperforms the Newman solution. We also show the relative gain as compared to the non-coded case. The latter results in the highest PMEPR. Possibly not harmful with 10 subcarriers it is certainly not acceptable with 500 subcarriers. In Fig. 5.2(b) we present our GA solution when we disabled two subcarriers and compare now the PMEPR of this solution with the Newman and non-coded cases when the same subcarriers have been disabled. Our GA solution outperforms the Newman solution.

In Table 5.3, we evaluated the PMEPR for higher numbers of subcarriers. We chose to use $N = 500$ and $N = 100$ to comply with our design parameters given in Table 5.2. We observe that in the case of a sparse spectrum our GA based solutions outperform the Newman solution. The results given in the last column were produced while using only two genes per phase, as with QPSK. This aspect is attractive in particular if we were to use a communication system for radar with a predefined alphabet, such as QPSK, etc.

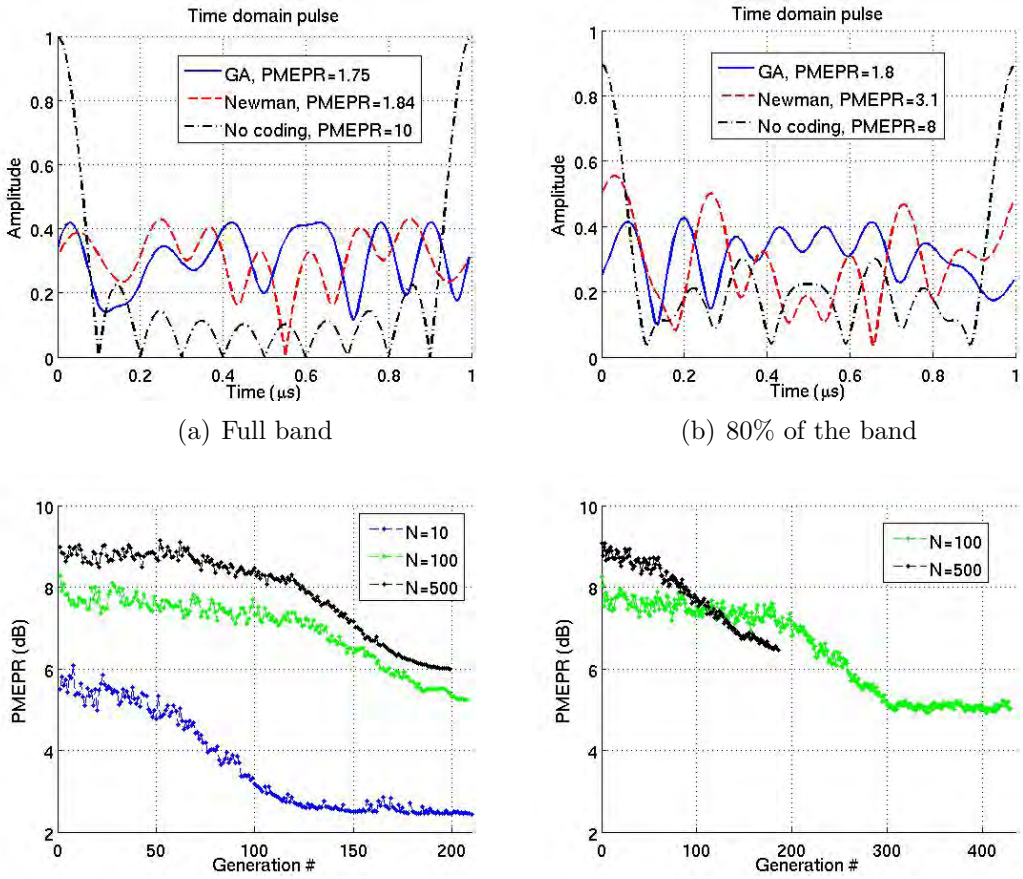

(a) Full band

(b) 80% of the band

(c) No modulation (18 genes)

(d) QPSK (2 genes)

Figure 5.2: Amplitude of the time domain OFDM symbol for different coding solutions when a) all subcarriers are used and b) only 80% of the subcarriers are used, N=10. In the case of sparsely populated bands, our GA solution outperforms the Newman approach. Convergence of the SGA while encoding one phase with either c) 18 or d) 2 genes. A PMEPR improvement of 3 dB is achieved in all cases considered.

In Figs. 5.2(c)-5.2(d), we show the convergence of our GA for both cases of "no modulation" and QPSK modulation. We observe what we could intuitively guess. Because of the shorter chromosome size, the QPSK tends to converge in a more chaotic manner than our "no modulation" case. In the latter, each phase code is represented by a binary string composed of 18 bits. As a result, from one generation to the next, the genetic operations will transform the phase code set

Table 5.3: Simulation results for the PMEPR (in linear unit) with different levels of sparsity. We compare our GA based PMEPR values with existing results: non-coded and Newman phases

		No Coding	**Newman**	**GA**	**GA (QPSK)**
N=100	Full	100	1.8	3.3	3.4
	70%	70	4.2	2.9	3.1
	50%	50	4.1	3.2	3.3
N=500	Full	500	1.8	3.9	4.6
	70%	350	4.9	3.9	4.6
	50%	250	5.0	4.5	4.5

(equivalent chromosome) in a less radical fashion than with QPSK. Hence, the convergence is smoother. This effect is observed when we compare the behaviour of the curve for the case N=100 in Fig. 5.2(c) and Fig. 5.2(d). In addition, the smaller N the longer it takes to converge for the QPSK and other short code length. Overall, we observe that we are able to improve the PMEPR by 3 dB.

5.5.2 Multiple obectives: PMEPR and PSLR

One benefit of the NSGA-II as compared to the prior version, NSGA is its fast computing time as a result of the selection strategy based on chromosome rank and crowding distance. On top, the use of binary simulated crossover and mutation improves the algorithm complexity. The large chromosome sizes from our GA are simply suppressed as we work throughout the algorithm with sets of real numbers for the phase codes. In Figs. 5.3(a)-5.3(b), we show how the NSGA-II can improve both PMEPR and PSLR. Our pulse parameters are as given in Table 5.2. In both cases, we have taken a smaller number of subcarriers, but the time bandwidth product remains the same, $NK = 100$ and $NK = 500$ respectively. For comparison, we plotted 100 realisations of the initial random population. With a population size $L_{\text{pop}} = 40$, each of our clouds comprises 4000 points. After 10000 generations our set of optimal solutions is considerably improved. The Pareto-front is visible and different sets of phase codes can be selected whether the emphasis in on a low PMEPR or low PSLR. In light of

Fig. 5.3(a) we see that improvements as high as 7 dB and 4 dB can be achieved in terms of PSLR and PMEPR for the case of N=25. Likewise, Fig. 5.3(b) shows that improvements as high as 9 dB and 3 dB can be achieved in terms of PSLR and PMEPR for the case of N=125. The improvements reported here refer to the characteristics of the mean point in the random distributions.

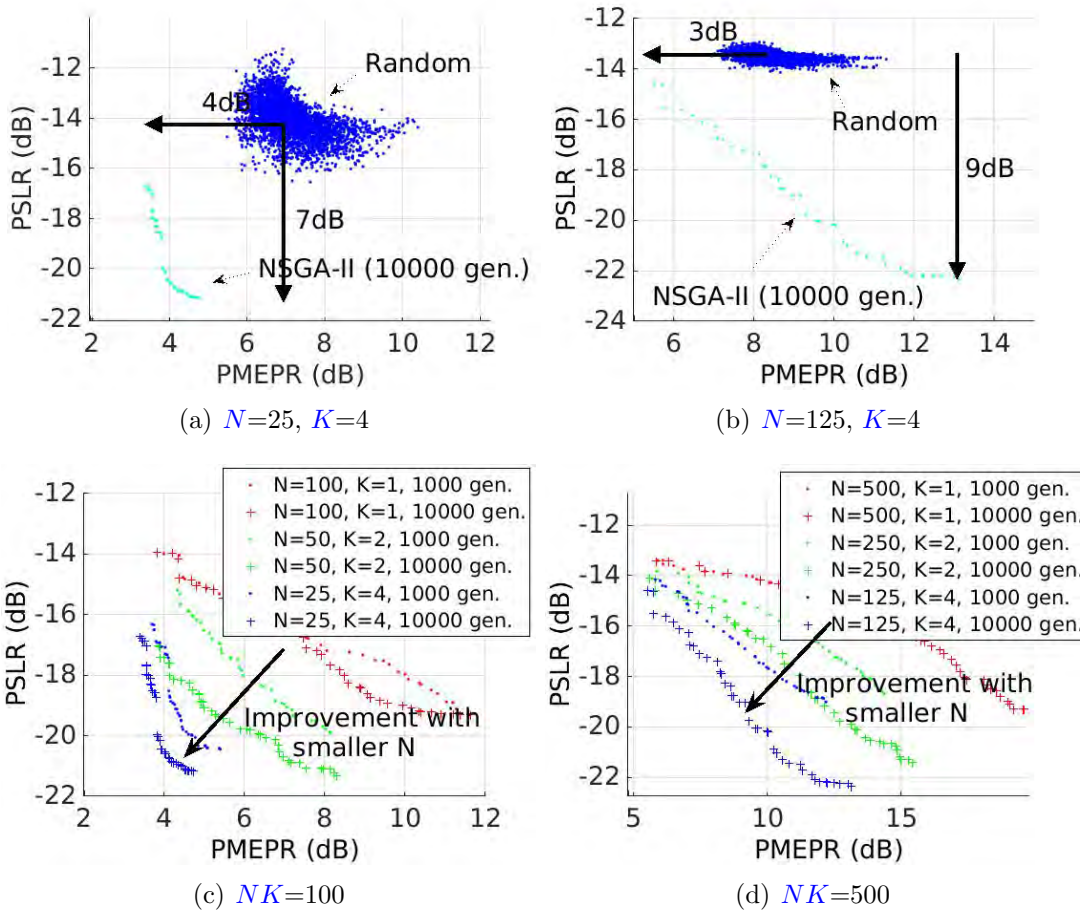

(a) N=25, K=4 (b) N=125, K=4

(c) NK=100 (d) NK=500

Figure 5.3: Comparison between random phases and phases resulting from the NSGA-II optimisation for PSLR and PMEPR in a) and b). Convergence of the NSGA-II optimisation in c) and d).

In Figs. 5.3(c)-5.3(d), the impact of N, the number of subcarriers in the pulse, is assessed. Thus, we compare three cases with equal time bandwidth product, as in Table 5.2. We observe the evolution of the Pareto-front as a function of the generation index and see that design with the smallest N will provide the best

Pareto-front. Again, this results confirms an intuitive guess.

5.5.3 Multiple objectives: PMEPR, PSLR and ISLR

As opposed to our single objective approach [44], where PSLR and ISLR where treated separately, we can now feed all three objective functions into our MOO-GA. The Pareto-front is now a 3-dimension (3D) set of points with coordinates (PMEPR, PSLR, ISLR). The most suitable Pareto-optimal solution can be selected based on the design constraints. Fig. 5.4 shows the two Pareto-fronts of the same design cases evaluated in [44].

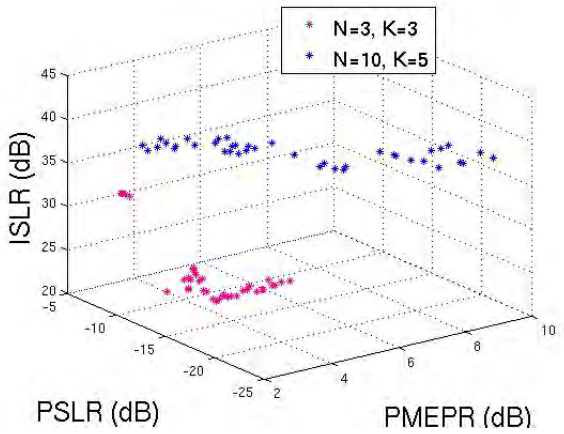

Figure 5.4: Pareto-front after 10000 generations for the same design options as in [44].

5.6 Case study: GA for PMEPR optimisation in a target detection enhancement procedure

In this section we show how our single objective GA based optimisation can be incorporated in a procedure intended to enhance target detection. We use a

two-step approach that addresses both problems of detection enhancement and PMEPR optimisation sequentially. As such, this problem does not require having a multi-objective approach. The first step consists in finding an optimal weight vector $\mathbf{w}$ to enhance the detection characteristics. In other words, it finds the power spectrum of the radar pulse. This vector is then passed on to our single objective GA based optimisation to find a vector of phase codes $\mathbf{a}$ such that the resulting OFDM symbol has optimal PMEPR properties. Our procedure is presented in Fig. 5.5. The complex vector resulting from the element-wise multiplication $\mathbf{w} \cdot \mathbf{a}$ represents the discrete spectrum of our optimal OFDM pulse, which we defined as $S_{\text{opt}}(f)$ in Fig. 5.5.

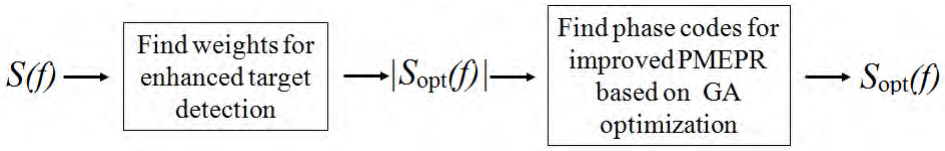

Figure 5.5: OFDM pulse optimisation in two steps.

5.6.1 SNR as the design metric

Unlike traditional notions that consider imaging-based metrics for target detection and classification, another approach has introduced the SNR metric [39]. In that case, there is no need to have low PSLR and ISLR anymore.

5.6.2 Transmitted signal receiver-filter pair

In [107] the authors expressed $V_{\text{MF}}(f)$ the signal at the output of the matched filter as the product of the target reflectivity spectrum $\varsigma_s(f)$, the waveform spectrum $S(f)$ and the filter transfer function $H(f)$:

$$V_{\text{MF}}(f) = \varsigma_s(f + f_0)S(f)H(f). \tag{5.11}$$

In the frequency domain, the signal goes through the steps as indicated in

Fig. 5.6. Both convolution symbols characterise the up and down conversions. In the time domain, we can express the RF analytical signal as $s_{tx}(t)$:

$$s_{tx}(t) = s(t)\exp(j2\pi f_0 t), \tag{5.12}$$

where f_0 is the carrier frequency and $s(t)$ is the OFDM pulse as given in Eq. 5.3. In this analysis, we consider that the pulse is composed of a single OFDM symbol.

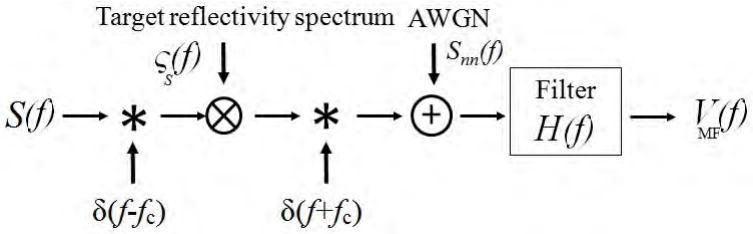

Figure 5.6: Model of the received signal in the frequency domain.

5.6.2.1 Optimum receiver-filter pair

In the case of an extended target, unlike the standard matched filtering problem applicable when the target is modelled as a point scatterer, the optimal receiver filter shall be matched to the waveform scattered by the target, not the transmitted signal itself. When this is the case, the maximum SNR at time t_0 is given by the following equation [39]:

$$SNR_{t0} = \int_{-\infty}^{\infty} \frac{|\varsigma_s(f+f_0)S(f)|^2}{S_{nn}(f)} df. \tag{5.13}$$

While previous works have researched solutions to this SNR optimisation problem in the time domain, in terms of $s(t)$, we propose to run the search in the frequency domain and look for $|S(f)|$ instead. This amount to searching for an optimal weight vector $\mathbf{w}$. If we assume that the spectrum of our OFDM pulse is zero outside the bandwidth[11], and consider that the stationary additive Gaussian

[11] The spectrum of the baseband OFDM pulse is considered to spread from 0 to B rather -B/2 to B/2

noise is white, with one-sided power spectral density $S_{nn}(f) = N_0$, we can modify Eq. 5.13 into:

$$SNR_{t0} = \frac{1}{N_0}\int_0^B |S(f)\varsigma_s(f+f_0)|^2 df. \tag{5.14}$$

Assuming that we have a deterministic expression for the target reflectivity spectrum, we can rewrite Eq. 5.14 in discrete terms:

$$SNR_{t0} = \frac{1}{N_0}\sum_{n=0}^{N-1} |S[n]\varsigma_s[n]|^2, \tag{5.15}$$

where $S[n] = S(n\Delta f)$ is the OFDM spectrum formulated in discrete terms, and n takes values from 0 to $N-1$. Reciprocally, we use $s[n]$ for the time domain pulse as in Eq. 5.6. Assuming that we transmit at all subcarriers, our optimisation problem reduces in finding the weights w_n such that:

$$\arg\max_{w_n} \sum_{n=0}^{N-1} |S[n]\varsigma_s[n]|^2, \text{ s.t. } \begin{cases} w_n > 0 \\ \mathbf{s}^T\mathbf{s} = 1 \end{cases} \tag{5.16}$$

At this stage we propose to simply use a scaled version of the target reflectivity spectrum for $\mathbf{w}$. Our aim is to show that we can decouple the detection enhancement problem with the PMEPR optimisation problem.

5.6.3 Simulation setup and results

In our analysis we assume to work at X-band and consider a 2 GHz bandwidth B centred around 10 GHz, f_0=9 GHz. Our OFDM pulse is composed of N=100 subcarriers and the subcarrier spacing is Δf=20 MHz. To make relevant comparisons we first normalise $\varsigma_s[n]$.

5.6.3.1 Target reflectivity spectrum normalisation

We normalise the discrete target reflectivity spectrum following the strategy presented in [108, chap. 14]. The later states that when a flat spectrum OFDM

pulse of unit energy interacts with the normalised reflectivity spectrum $\varsigma_{\text{norm}}[n]$, the frequency-domain reflected signal shall have unit average power,

$$1/N \cdot \sum_{n=0}^{N-1} |\varsigma_{\text{norm}}[n]S[n]|^2 = 1. \tag{5.17}$$

The discrete elements of our flat spectrum OFDM pulse of unit energy are given by $S[n] = a_n/\sqrt{N}$, where $|a_n|$=1. Hence, we find:

$$\varsigma_{\text{norm}}[n] = \frac{N}{\sqrt{\sum_{n=0}^{N-1} |\varsigma_s[n]|^2}} \cdot \varsigma_s[n], \tag{5.18}$$

5.6.3.2 Complex target model

In our simulation we construct a synthetic target from $P = 50$ point scatterers, each with the same reflectivity $\varsigma_i = \sqrt{\sigma_i} = 1$ and located at range R_i from the radar. The individual point scatterers are assumed to be perfectly electrically conducting PEC spheres, large enough to have a reflectivity constant within the band of interest. It can be shown [32] that the compound target reflectivity spectrum $\varsigma_s(f)$ is equal to:

$$\varsigma_s(f) = \sum_{i=1}^{P} \sqrt{\sigma_i} \exp(-j4\pi f \frac{R_i}{c}). \tag{5.19}$$

The point scatterers are randomly distributed within a rectangle, 5 m wide and 10 m long, whose centre is 10 km away from the radar along the x axis. In this simple model, the reflectivity spectrum depends strongly on the wavelength as well as the relative positions of the scatterers however it would hold true in the case of a controlled environment. Fig. 5.7(a) gives the target reflectivity power spectrum when the interval between two frequencies is equal to the subcarrier spacing. As expected, we observe strong variations of the power spectrum within the frequency band.

5.6.3.3 SNR and PMEPR improvements

Following the above methodology, we first generate an optimal weight vector w_{opt} as a scaled version of the normalised target reflectivity spectrum. The behaviour of our optimal weight vector in Fig. 5.7(b) can be compared to the power spectrum in Fig. 5.7(a). We make sure that the unit energy pulse constraint is respected. This leads to the intermediate OFDM spectrum $S_1(f)$. We present the gain achieved with this optimal weight vector in terms of the average power in table 5.4. The average power is improved by 2.4 dB. In the second step, we feed $S_1(f)$ into our GA based optimisation in search of an optimal set of phase codes a_{opt} with respect to the PMEPR. In Fig. 5.7(c), we observe that the PMEPR has improved by 3 dB after 100 generations, in agreement with our results from Section 5.5.1. In the end, as shown in Fig 5.5 our pulse $S_{opt}(f)$ has enhanced detection capabilities for the target of interest and optimal PMEPR.

Table 5.4: Result for the detection enhancement

	Flat spectrum	**Optimal weights**
Average power (dB)	0	2.4

5.7 Summary

In this chapter, we showed that GA based techniques are suitable to optimise or improve several features of the OFDM pulses. We inspected the possibility to incorporate these optimisation techniques in a waveform design framework in regard of two processing solutions, specific to OFDM radar. The first time domain processing solution requires optimal PSLR and PMEPR properties. While the need for low PSLR applies to any waveform, the need for low PMEPR is specific to the OFDM structure as the amplitude is no longer constant. We showed that it is possible to apply the MOO-GA, so-called NSGA-II to search for optimal sets of phase codes. We observed that substantial improvement is achieved in comparison to random coding. The Pareto-optimal solutions obtained with this technique allow various options for different design preferences. We observed

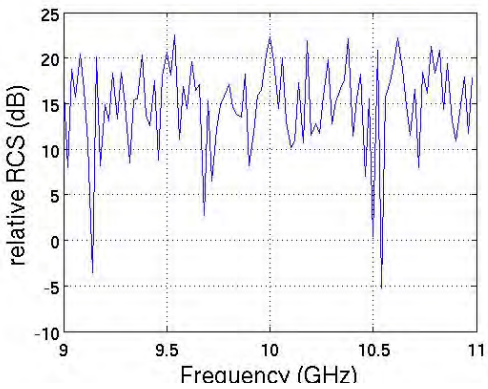

(a) Reflectivity power spectrum

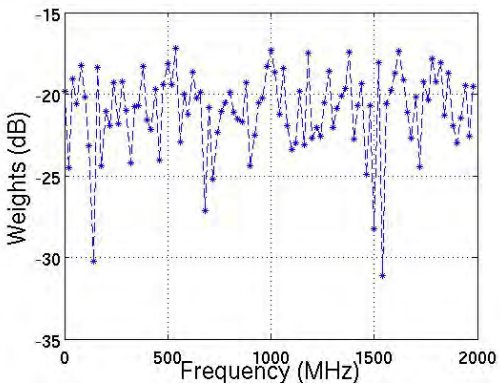

(b) Weights

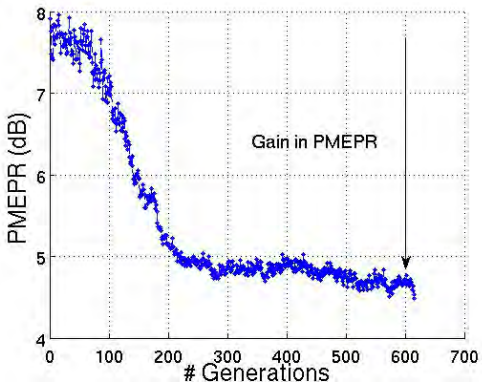

(c) PMEPR improvement

Figure 5.7: a) Reflectivity spectrum of a complex target made of P= 50 point scatterers and b) optimal weight vector in terms of detection respecting the unit energy pulse constraint. The single objective GA based optimisation searches for optimal sets of phase codes **a** to improve the PMEPR.

that for a fixed time-frequency product, the case with the smallest number of subcarriers produces the best Pareto-front.

When dealing with the second processing solution, so-called "frequency domain processing" solution, we stressed that the aim shall be, minimisation of the PMEPR. Hence, the single objective GA can be used. We showed that this evolutionary technique can produce solutions that outperform some of the most robust methods. We motivated further the use of GA based techniques to accommodate complex objective functions or additional constraints. For example,

we addressed the case of sparse spectrum, banning some of the subcarriers and showed that our GA solution gives notable results.

Ultimately, we presented a case study where we introduce the PMEPR optimisation technique into a design framework for optimised detection. We showed that both optimisation problems can be decoupled, as we suggest, for the detection part, to make use of the weights while the phase codes are saved for the PMEPR part. For completeness, when the goal is to minimise both PSLR and ISLR, we suggest to run a MOO-GA with two objectives instead of three, with a constraint on the PMEPR.

Chapter 6

OFDM phenomenology: recognition of canonical scatterers using flat spectra OFDM pulses[12]

A big part of the early developments in radar up till now has been to come up with favourable waveform designs and signal processing techniques to detect the presence of a target, measure its range and radial velocity, localise its position [86, 109]. Ultimately, the goal of radar is to identify the target, especially in military applications.

6.1 Introduction

The common procedure to identify targets consists of collecting features of the target and later comparing them with a database to find the best match. In this,

[12] Based on Lellouch, G. et al. "OFDM phenomenology: recognition of canonical scatterers using flat spectra OFDM pulses," accepted in the first review to *IET Radar and Sonar Navigation*

both HRRPs [110] and SAR images [111] have been used.

Such classic techniques suffer the same paradigm which was noted by Huynen in [112]: "*It may seem strange to say that the behaviour of a radar target as an object is treated with utmost indifference in most radar systems applications; however, a search through the literature soon convinces us that this is indeed the case. The single object is usually considered as a "point source" of scattering and an extended target as a distribution of point sources.*" Indeed, techniques as recent as ISAR have built their theoretical framework upon the point target model. Although this approach reduces many difficulties related to the modelling of extended targets, its pertinence in the achievement of the final goal remains questionable. Hence, the realisation of this "negligence" has urged Huynen to propose a "phenomenological approach" instead. He exposed in [113] how the latter differs from the conventional approach which he calls the "data processing oriented" approach. From a strictly data processing point of view any data relating to the signal scattered off a target of interest is considered as potentially useful information regarding that target. He summarises the data processing people's philosophy as: "the more data one can accumulate from a target, the more accurate the final identification is bound to be". This simplistic approach engenders problems as the vast number of parameters that can characterise a set of targets soon overloads the data processing and procedures to discriminate between targets become cumbersome. Besides, the transient properties of the radar measurement phenomenon implies that for any new measurements involving new targets, new environments, new frequencies, the whole procedure shall be repeated again. In contrast, the proposed approach was called phenomenological because it aims at keeping the primary phenomenon in continual focus of the observer's attention. When the data processor welcomes any new piece of information to work towards the achievement of its objectives the phenomenologist tries to filter out only those data which relate to distinctive target behaviour. The benefice of this approach is twofold: more accurate discrimination capabilities obtained with less complex data processing.

Here, we apply the phenomenological approach to OFDM radar. While Huynen inspected the target polarimetric properties, we focus on the frequency response.

In this Chapter, we analyse the case of canonical scattering objects and show how we can benefit from the OFDM structure to identify the scatterer type.

6.2 Canonical scattering model

In recent years, several authors approached the problem of scattering centre characterisation for use in automatic target recognition (ATR), mostly in synthetic aperture radar (SAR) applications [114, 115]. They grounded their research on the observation that radar measurements of man-made targets are dominated by returns from isolated scattering centres, such as spheres, cylinders, corner reflectors. Indeed, from the geometrical theory of diffraction (GTD) [116, 117], if the wavelength of the excitation is small relative to the object extent, then the backscattered electromagnetic field from an object consists of contributions from electrically isolated scattering centres and the resulting electric field is given by:

$$E_f(f;\theta) = \sum_{p=1}^{P} E_{f_p}(f;\theta_p), \tag{6.1}$$

where $\theta^T = [\theta_1^T, ..., \theta_P^T]$.

When the object lies in the far field, the GTD predicts that the scattering phenomenon follows a $(jf)^\alpha$ dependence, where α is a multiple of $1/2$, [118, 119, 120]. In our 1-dimensional approach (1D), the model is the same as used in [43], viz.

$$E_{f_p}(f) = \varsigma_p \left(j\frac{f}{f_0} \right)^{\alpha_p} \exp\left(\frac{-j4\pi f}{c} R_p \right). \tag{6.2}$$

The model parameter vector $\theta = \{\varsigma_p, R_p, \alpha_p\}_{p=1}^P$ characterises the P individual scattering centres. For each scatterer, ς_p is a complex scalar that provides its magnitude and phase, R_p corresponds to its distance from the radar and α_p is a dimensionless coefficient that retains the geometry information.

The scattering mechanisms are of two types: diffraction or reflection. The values

for α in each of the five cases considered are summarised in Table 6.1.

Table 6.1: Parameter α and characteristic of the scattering centre.

Scattering geometry	α
Flat plate at normal incidence	1
Singly curved surface (e.g. cylinder at broad side)	0.5
Doubly curved surface (point scatterer)	0
Edge	-0.5
Corner	-1

This model generalises the conventional point scattering model obtained when α=0.

6.3 Methodology

Before discussing our contribution, we stress the problem at stake and evoke some of the relevant prior work. We then discuss our simulation setup and describe our target model.

Assuming that the target in the scene is composed of multiple scattering centres, our objective is to retrieve the characteristics of the scatterers. In other words, we expect to evaluate the vector of parameters θ.

So far, authors have taken two different approaches to tackle the problem of scattering centre extraction. The first technique has been to compute the IDFT of the scattered signal to produce an impulse response of the target. The scatterers are then identified by localising the peaks of the estimated range profile [121]. The other technique has been to make use of a parametric model to describe the measured scattering behaviour [43]. The parameters describing the model are then estimated from the data. The second approach has a major advantage in that the range resolution is not bandwidth limited, rather, it is constrained by the parameter estimation error and the characteristics of the scatterers can be estimated. In [43], the authors present an approximate maximum likelihood (ML) algorithm that aims at minimising the squared error $J(\varsigma, R, \alpha)$ defined by:

$$J_n(\varsigma, R, \alpha) = \left| E_n - \sum_{p=1}^{P} \varsigma_p \left(j\frac{f_n}{f_0} \right)^{\alpha_p} \exp\left(\frac{-j4\pi f_n}{c} R_p \right) \right|, \tag{6.3}$$

where E_n=$E_f(f_n;\theta) + e_n$; f_n are the frequency samples within the bandwidth of interest and e_n are complex, zero mean, independent and identically distributed (iid), Gaussian random variables with variance ${\sigma_{std}}^2$. Besides, $\varsigma = [\varsigma_1 \cdots \varsigma_P]^T$, $R = [R_1 \cdots R_P]^T$ and $\alpha = [\alpha_1 \cdots \alpha_P]^T$

The problem of parametric scattering centre information extraction is greatly simplified by our proposed work where we exploit OFDM signal used with a phenomenological intent. In essence, we apply conventional radar signal processing to estimate the range and the amplitude of the scatterers. Our contribution lies in the combination of flat spectrum OFDM pulses on transmit with an algorithm that estimates the slope of the received echo spectrum. Hence, our statistical analysis, presented in Section 6.4.4 concerns the sole scatterer type parameter. Note that a thorough analysis concerning the Cramer-Rao lower bound (CRLB) for the variance achievable by any unbiased estimator for either three parameters has been performed in [43]. It is not the aim here to repeat it.

6.3.1 Simulation setup

In our approach, the successive steps undergone by the radar signal are summarised as follows. The transmitted signal $s_{\text{tx}}(t)$ propagates away from the radar antenna and interacts with the scatterer whose deterministic reflectivity function is given by $h_{tp}(t)$. The scattered signal $s_{\text{rx}p}(t)$ is then received at the radar antenna. Additive white Gaussian noise adds onto the signal and results in the compound signal $y_p(t)$. If the conventional matched filtering process is applied, we eventually obtain the compressed signal $x_p(t)$. In this analysis, we work with analytic signals. The spectrum of the received baseband signal is given as in [107] by:

$$S_{\text{b}p}(f) = H_{f_p}(f + f_0)S(f), \tag{6.4}$$

where $S(f)$ is the spectrum of the OFDM pulse. If $y_{\mathrm{b}_p}(t)$ and $s(t)$ are respectively the baseband compound signal and the baseband transmitted pulse, the output of the matched-filter $x_p(t)$ is given by:

$$x_p(t) = y_{\mathrm{b}_p}(t) * s^*(t). \tag{6.5}$$

We use a simple energy detector to detect the scatterers. An estimate of the range $\hat{R}_p$ is found by the peak position on the range axis and an estimate of the scattering coefficient is given by the value $x(\hat{\tau}_p)$, where $\hat{\tau}_p = 2\hat{R}_p/c$.

6.3.2 Target modelling

In light of Eq. 6.2, we simulate the target in the frequency domain. The target impulse response is then obtained after applying an inverse Fourier transform (IFT) as in Eq. 6.6 and the Dirac-delta at the scatterers' positions are extracted. Note that the reflectivity spectrum H_f can be used interchangeably with the backscattered electromagnetic field E_f as defined in Eq. 6.1. When P scatterers compose the target, $H_f = \sum_{p=1}^{P} H_{f_p}$

$$h_t(t)\exp(-j2\pi f_0 t) = \mathrm{IFT}(H_f(f + f_0)). \tag{6.6}$$

In the discrete-time formulation, the reflectivity spectrum is sampled at a rate such that the scatterers appear at their true position in the target impulse response, so as to avoid aliasing. The interval between two frequency samples is referred to as df, not to be confused with Δf which we introduce later to characterise the OFDM subcarrier spacing. In vector format, the reflectivity spectrum is $\mathbf{h_f}$ and the target impulse response resulting from applying an inverse discrete Fourier transform (IDFT) on $\mathbf{h_f}$ is $\mathbf{h_t}$. Since we work on the reflectivity spectrum at RF, $\mathbf{h_t}$ absorbs the complex exponential from Eq. 6.6. Note that in principle the impulse response can be infinite due to the effects of multiple reflections of the radar energy from different segments of the extended target.

However, such effects of multiple reflections become vanishingly small after some time duration on the order of the waveform transit time across the target, hence an approximation of $\mathbf{h_t}$ based upon a finite size vector is sufficient for numerical simulations.

In this analysis, we consider two cases: a point and an extended target. The minimum distance between any two consecutive scatterers in the first case is smaller than in the second case. Consequences on the pulse design are given in section 6.4.1. Both targets consist of five scatterers. In the small target case, the scatterers are positioned at ranges: 4997 m, 5000 m, 5006 m, 5010 m and 5021 m, hence the minimum distance between two consecutive scatterers is ΔR_{min}=3 m and the target extent is ΔR_t=24 m. In the extended target case, the scatterers are positioned at the ranges: 5000 m, 5030 m, 5052 m, 5090 m and 5120 m, hence the minimum distance between two consecutive scatterers is 22 m and the target extent is 120 m. In both cases, the first and closest scatterer has the type α=1, the second scatterer has the type α=0.5, the third scatterer has the type α=0, the fourth scatterer has the type α=-0.5 and the fifth and furthest scatterer has the type α=-1.

The relationship between time and frequency imposed by the Fourier transform implies an unambiguous range $R_{\text{ua}}=c/2df$. Thus, df must be chosen to comply with the target extent. Fig. 6.1 illustrates the principle whereby oversampling in the frequency domain increases the length of the unambiguous time window. In our simulations we choose for the small target case, df=5.56 MHz which results in R_{ua}=27 m while in the extended target case, df=1.11 MHz and R_{ua}=135 m. These values are summarised in Table 6.2. We observe that the unambiguous window characterised by its boundaries $R_{\text{win start}}$ and $R_{\text{win stop}}$ includes all the scatterers.

For reasons that will become clear in Section 6.4.1, we considered two values for the bandwidth as shown in Fig. 6.2. In the extended target case, we used B=300 MHz and in the small target case we used B=1500 MHz.

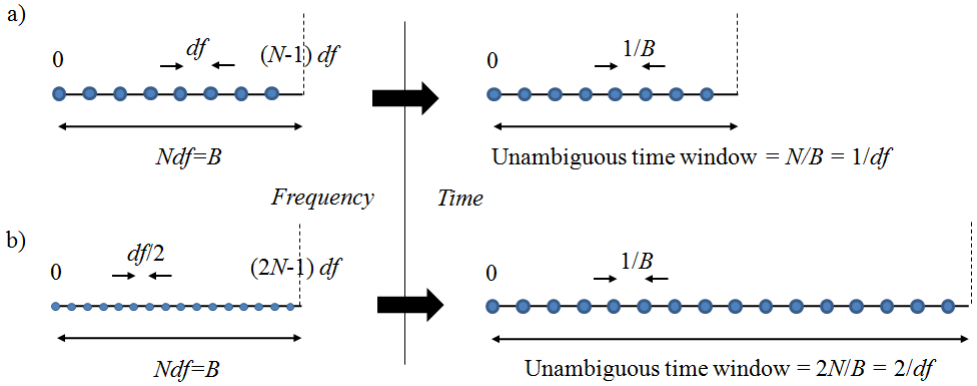

Figure 6.1: Effect of oversampling in the frequency domain. In b) we use twice more samples in the frequency domain than in a) while maintaining the same bandwidth. The consequence in the time domain is a vector twice as long. The sampling period is not modified.

Table 6.2: Parameters considered in the experiment.

	Small target	**Extended target**
ΔR_{min}	3 m	22 m
ΔR_t	24 m	120 m
df	5.56 MHz	1.11 MHz
R_{ua}	27 m	135 m
$R_{\text{win start}}$	4995 m	4995 m
$R_{\text{win stop}}$	5022 m	5130 m

6.4 Estimation technique

In this section we motivate the use of flat spectrum OFDM pulses to estimate the scatterers types. We explain the pulses' design, address the synthetic data generation and present our algorithm. We conclude with a statistical analysis to assess the behaviour of our technique under AWGN conditions.

6.4.1 Pulse design

Our approach assumes to have some prior information on the relative distance between the scatterers. Therefore, we recommend applying it in controlled en-

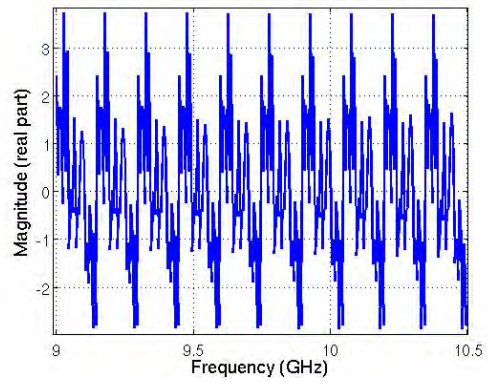

(a) Reflectivity spectrum, small target

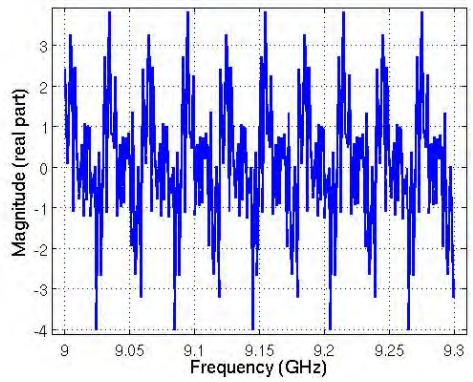

(b) Reflectivity spectrum, long target

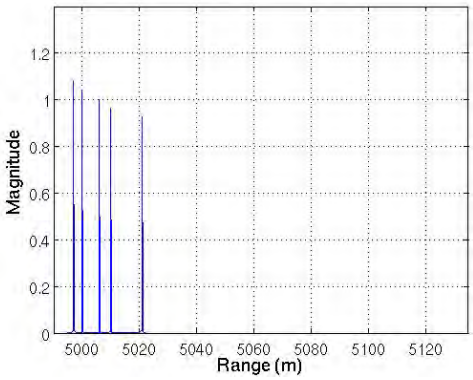

(c) Impulse response, small target

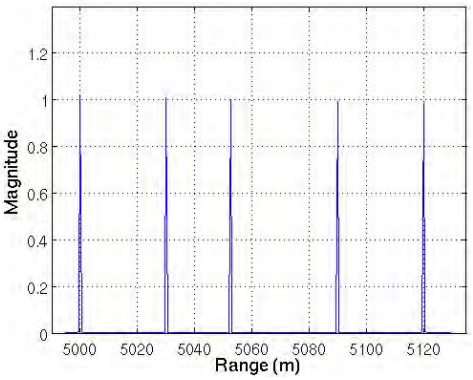

(d) Impulse response, long target

Figure 6.2: Target modelling. In a) and b) we display the reflectivity spectra of the small and long targets, over 1500 MHz and 300 MHz respectively. In c) and d) we show the corresponding impulse responses.

vironment, for example in civilian applications. Our pulse is designed to be no longer than the minimum distance between two consecutive scatterers. This consideration reduces the risk of ISI when we apply our algorithm.

6.4.1.1 Subcarrier spacing

Figures 6.3(a) and 6.3(d) show two different designs intended for two different target configurations.

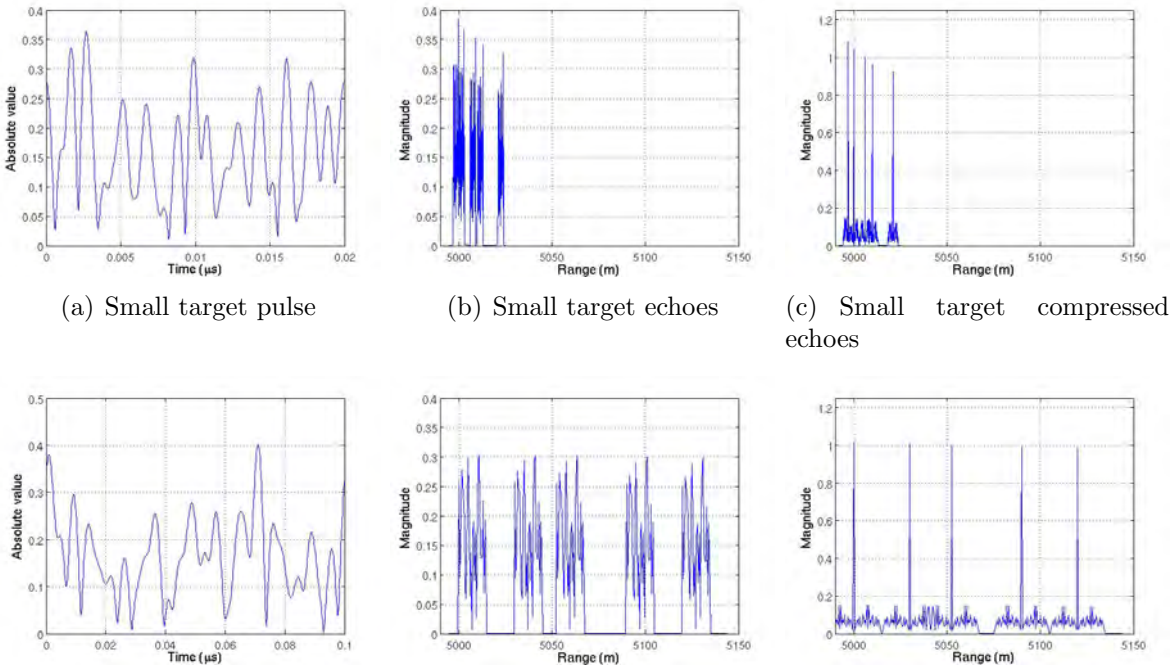

(a) Small target pulse

(b) Small target echoes

(c) Small target compressed echoes

(d) Extended target pulse

(e) Extended target echoes

(f) Extended target compressed echoes

Figure 6.3: Pulse design, received echoes and compressed echoes for a),b),c) small and e),f),g) extended targets. In a) t_p=0.02 μs and in d) t_p=0.1 μs. In both cases the pulse length is no longer than the minimum distance between two consecutive scatterers. The sampling rate of $\mathbf{s_b}$ in range is $c/2B$, that is in b) 0.1 m and in e) 0.5 m.

In the first case the pulse length shall be less than 3 m, equivalently 0.02 μs in time, while in the second case it shall be less than 22 m, equivalently 0.15 μs. The orthogonality property of the OFDM structure implies that the subcarrier spacing shall be at least 50 MHz and 6.8 MHz respectively. To keep things simple we use Δf=10 MHz in the second case and we consider the same number of subcarriers N=30 for both, so that we use the same number of samples to estimate the slope of the spectrum as exposed in section 6.4.3. Inevitably, the bandwidth is impacted and the pulse bandwidth in the small target case will be 5 times larger than in the extended target case. These choices are summarised in Table 6.3. The pulse extent in range is found to be $c/2\Delta f$. For obvious reasons, only one symbol is used to compose the OFDM pulse.

Table 6.3: Parameters considered to design the OFDM pulse.

	Small target	**Extended target**
N	30	30
B	1500 MHz	300 MHz
Δf	50 MHz	10 MHz
$c/2\Delta f$	3 m	15 m

6.4.1.2 Weights

The subcarriers composing the pulse have the same weight. Hence, the spectrum of the transmitted pulse $S(f)$ in Eq. 6.4 is flat. The reflectivity spectrum of the scatterer thus reflects directly on the spectrum of the received echo. It is this property of the signal that we exploit to retrieve the type of scattering as mentioned in section 6.4.3.

6.4.2 Synthetic data generation

To generate our set of synthetic data we make use of the convolution theorem and Eq. 6.4. As a result, the received echo $\mathbf{s_b}$ can be expressed as:

$$\mathbf{s_b} = \mathbf{h_t} * \mathbf{s}. \tag{6.7}$$

In Figs. 6.3(b)-6.3(e), the absolute value of the received signal at baseband is presented for the small and extended target cases. As expected from the prior design, pulses in the small target case are five times shorter than in the extended target case. In either case, the impulse response and the pulse vectors have the same bandwidth B, hence, the sampling rate of the resulting vector is also B.

6.4.3 Algorithm

The subsequent algorithm that we employ to characterise the scatterer is intuitive and follows the mathematical modelling of the received signal. Firstly, we aim at

retrieving the spectra of the received echoes $\mathbf{s}_{\mathbf{b}p}$, secondly, we work on assessing the behaviour of the spectrum with respect to frequency. Ultimately we refer to the cases established in table 6.1 to link the parameter α to the scatterer type. We summarise our algorithm in Box 2.

Algorithm 2 Retrieving the scatterer type

1: Apply a matched filter on the vector of received echoes $\mathbf{s}_{\mathbf{b}}$
2: Find the peaks / detections
3: Verify that the spacing between two consecutive detections is more than the pulse length
4: **for** Each detection p **do**
5: Read the position of the peak and its value to estimate the scatterer range $\hat{R}_p$ and amplitude $|\hat{\varsigma}_p|$
6: Extract the received echo vector $\mathbf{s}_{\mathbf{b}p}$
7: Apply a DFT on $\mathbf{s}_{\mathbf{b}p}$
8: Convert the spectrum from linear to dB, in the form $10 \times \log(\text{Magnitude})$ versus $10 \times \log(f/f_0)$
9: Run a curve fitting of order one on the spectrum and estimate the slope of the line.
10: Deduce the type of scattering with the help of table 6.1
11: **end for**

Importantly, the magnitude of the spectrum shall be expressed in dB, as well as the frequency axis to reveal a linear expression of the form $|S_{\mathrm{b}p}|_{\mathrm{dB}} \propto \alpha_p (f/f_0)_{\mathrm{dB}}$. The curve fitting is done with a first order polynomial. To mitigate the magnitude glitch, we restrict the fitting to the inner samples and excludes both the samples on the edges of the spectra, as shown in Figs 6.4(a)-6.4(b). For the last step, we suggest the following basic decision rule. We suppose five ± 0.24 windows centred around the five values of α respectively. Having assessed the slope of the spectrum, we simply attribute to our scatterer the value of α corresponding to the window, which contains the estimate of the slope.

6.4.4 Statistical analysis

To assess the performance of our technique we employ a statistical approach. The idea is to characterise the slope estimate when additive white Gaussian

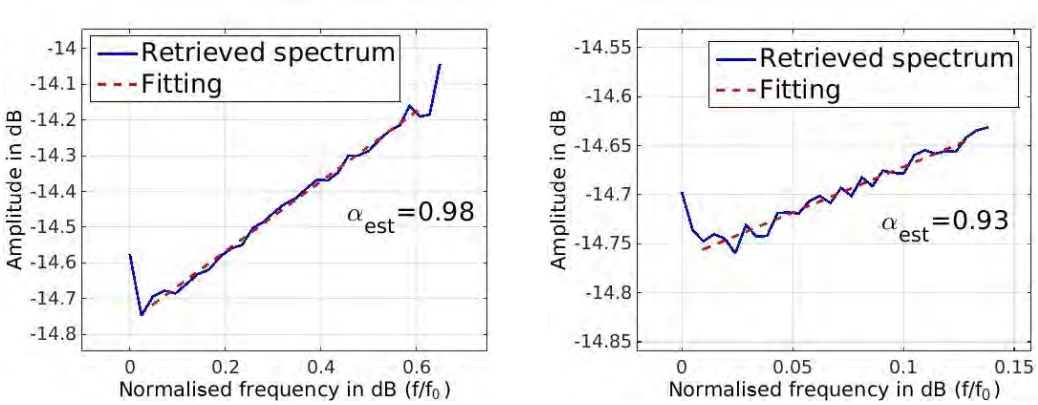

(a) Scatterer 1, α_1=1, B=1500 MHz (b) Scatterer 1, α_1=1, B=300 MHz

Figure 6.4: Spectra of the received echoes when the bandwidth of the transmitted pulse was B=1500 MHz and B=300 MHz. a) Small target case and b) Extended target case.

noise (AWGN) adds up onto our received echoes. We define our signal model as follows: first, we assess the energy of the individual echoes $E = \mathbf{s_b}_p^H \mathbf{s_b}_p$, which we assume to be equivalent to the energy of the pulse[13] $\mathbf{s_b}$ since the impulse response of each scatterer is approximately a discrete Dirac with amplitude 1 as seen in Figs. 6.2(c) and 6.2(d). Because we work with energy-normalised pulses, E=1; $.^H$ denotes the hermitian transposition and we use the convention of column vectors. Then, we calculate the energy that shall have the noise vector of equal length, for a specific SNR, viz. $n_p = E/SNR$ where SNR is in linear scale and we generate the vector of complex AWGN as in Eq. 6.8.

$$\begin{aligned} \mathbf{n} &= \sqrt{\frac{n_p}{2N}}(\mathbf{n}_I + \mathrm{j}\mathbf{n}_Q), \\ \mathbf{y}_\mathrm{b} &= \mathbf{s_b} + \mathbf{n}. \end{aligned} \tag{6.8}$$

$\mathbf{n}_I$ and $\mathbf{n}_Q$ are vectors of equal length as $\mathbf{y}_\mathrm{b}$ whose elements are drawn from a normal distribution with mean 0 and variance 1. The compound signal $\mathbf{y}_\mathrm{b}$ corresponds to the vector of noisy echoes and $\mathbf{y}_{\mathrm{b}p}$ is the noisy echo associated to scatterer p subject to the specified SNR; j=$\sqrt{-1}$.

[13] to calculate the energy of the pulse we consider the critical sampling rate without oversampling, hence the sampling frequency is f_s=B

We now present our results when $\mathbf{y}_{\mathrm{b}}$ replaces $\mathbf{s_b}$ in the algorithm Box 2. We first present our results for very low noise levels before moving towards higher noise levels. The output of the matched filter process, presented in Figs. 6.3(c)-6.3(f) for both the small and extended target cases is used to retrieve the number of scatterers P and estimate both $|\hat{\varsigma}_p|$ and $\hat{R}_p$. As evoked earlier our emphasis is on the classification of the type of scatterer. Hence, our subsequent analyses are dedicated to the solely slope estimation and scatterer type retrieval.

6.4.4.1 Overall probability of correct classification

For every SNR level considered, we generate M_{noise}=5000 realisations of noisy measurements. Hence, as we iterate the previous algorithm, we retrieve 5000 slope values for each scatterer. Our intention is to inspect the degradation of the canonical scatterer classification, which we formulate in terms of the overall probability of correct classification Pcc, as the SNR decreases. In particular, for every realisation and for a given scatterer we declare a correct classification when the estimated slope falls within the appropriate interval, as described earlier. For the overall probability of correct classification we use the same notation as in [122] and express it in terms of the probability of correct classification for a given scatterer type i as:

$$\mathrm{Pcc} = \frac{1}{C}\sum_{i=1}^{C}\mathrm{Pcc}_i, \tag{6.9}$$

where C is the number of classes considered for the canonical scatterer. The index i links to the possible discrete values for α, {-1,-0.5,0,0.5,1}. For low SNR values, we will see that the integration of many noisy spectra from the same scatterer can enhance drastically the classification.

6.4.4.2 Low noise level, SNR=50 dB

For high SNR values, the probability density function (PDF) of the slope for each scatterer is well represented by a Gaussian distribution centred around the true value, as seen in Fig. 6.5(a), for the case B=300 MHz. In the other case, B=1500 MHz, the peak happens to be slightly shifted for α=-1, -0.5, 0.5 and 1 as observed in Fig. 6.5(b). The mean and standard deviation values for all distributions are summarised in Table 6.4. Comparing the results for both bandwidths, we foresee that the standard deviation is inversely proportional to the relative bandwidth. Indeed, we can find that the standard deviation in the case B=1500 MHz is about five times smaller than in the case B=300 MHz.

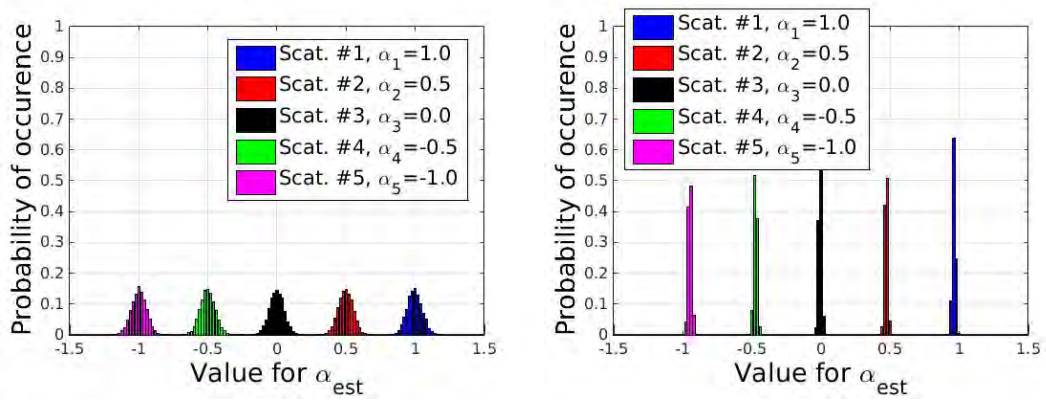

(a) B=300 MHz (b) B=1500 MHz

Figure 6.5: Histograms of the slope estimates for both cases, a) B=300 MHz and b) B=1500 MHz when the SNR is 50 dB. The values in the individual histograms have been normalised so that the total sum adds up to 1.

Table 6.4: Mean value and standard deviation of the slope distribution for all five scatterer types in both cases, B=300 MHz and B= 1500 MHz.

B		Scat.1	Scat.2	Scat.3	Scat.4	Scat.5
300	Mean	0.996	0.497	-0.002	-0.501	-0.999
	Std	0.054	0.053	0.053	0.054	0.054
1500	Mean	0.962	0.471	-0.007	-0.473	-0.949
	Std	0.011	0.011	0.011	0.012	0.012

Because we are interested in retrieving correctly the parameter α, rather than

finding the exact slope value, the small bias (0.05 for α=-1 represents a shift by 10%) is not detrimental with the choice of interval considered $\pm$0.24. Since all slope estimates fall within the appropriate window, we see that in either cases Pcc_i=100% for all scatterer types. With the prior definition for the overall probability of correct classification, we find that Pcc=100%.

6.4.4.3 Overall probability of correct classification versus SNR

As the noise level increases with respect to the energy in the received echo, the PDFs for the slopes flatten and widen. Consequently, the number of slope values falling within the appropriate window decreases, so do the probabilities of correct classification for a given scatterer type. Hence, the overall probability of classification drops accordingly. In Fig. 6.6, we plotted Pcc as a function of SNR. Our findings seem to agree with the results presented in [43]. As we are dealing with smaller relative bandwidth, the curve shifts to the right.

6.4.4.4 Integration of several pulses to improve the classification

One technique commonly used in radar when the probability of detection is poor with a single pulse is to integrate over several pulses. The randomness of the noise averages out, hence the higher the number of pulses used in the integration, the more significant the contrast between the target and the noise floor and the detection is improved. In the present case, we suggest a similar technique to improve the individual and then the overall probability of correct classification. Conversely to the aforementioned method, we do not integrate over the individual echoes but over the spectra of those echoes. Naturally, we use echoes that correspond to the same scatterer in the integration. We then apply our fitting function on that compound echo and calculate the slope of the line. We assess the behaviour of that approach with Monte Carlo simulations where we employ the same set of data used in Section 6.4.4.3 to generate Fig. 6.6. For every number of pulses N_p, we select at random N_p noisy echoes. Then we perform sequentially, integration, curve fitting and slope estimation. We

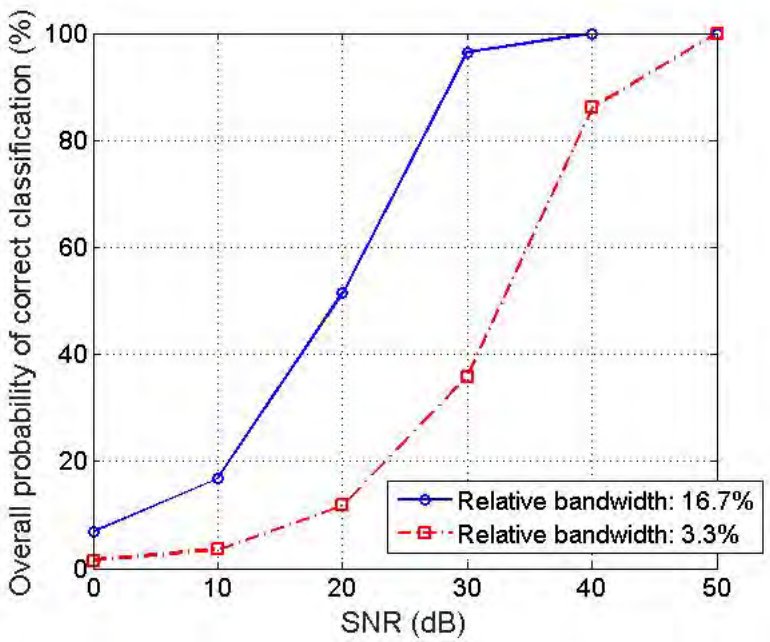

Figure 6.6: Overall probability of correct classification versus SNR using f_0=9 GHz, N=30 subcarriers and two cases for the bandwidth, B=300 MHz and B=1500 MHz. The window extent considered to compute the probability of correct classification for a given scatterer type i is $\alpha\pm0.24$ where α={-1,-0.5,0,0.5,1}.

repeat this procedure M_{noise}=5000 times and visualise the results in histograms as in Fig. 6.5. Contrary to the single pulse case, the histograms do not produce clear Gaussian-like distributions and can happen to be quite heckled for low SNR values. In Fig. 6.7, we display only those relevant results to attest the merit of our technique and the improvement in comparison to the single pulse case from Fig. 6.6. We observe that satisfactory values of Pcc are achieved with reasonable integration factors, for instance Pcc=98% for N_p=50 is achieved with SNR=5 dB for the low relative bandwidth case. For the high relative bandwidth case, satisfactory results are obtained from SNR=-10 dB: Pcc=99% for N_p=100 for example. Hence, in both cases, a gain of about 40 dB is obtained in comparison to the single pulse case for the same performance.

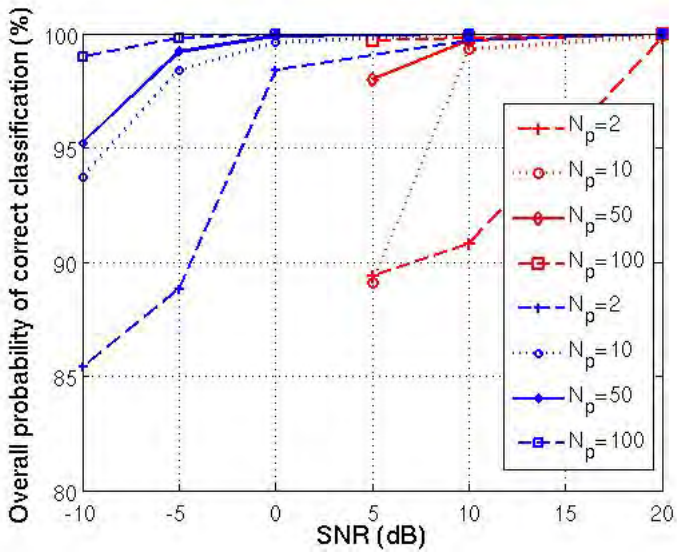

Figure 6.7: Overall probability of correct classification versus SNR using f_0=9 GHz, N=30 subcarriers and two cases for the bandwidth, B=300 MHz (relative bandwidth 3.3%) and B=1500 MHz (relative bandwidth 16.7%) resulting from the integration of several spectra. The window extent considered to compute the probability of correct classification for a given scatterer type i is $\alpha \pm 0.24$ where α={-1,-0.5,0,0.5,1}. For both cases we report only those relevant results. In the low relative bandwidth case, performance improvement is happening from SNR=5 dB while it happens from SNR=-10 dB in the high relative bandwidth case.

6.5 Summary

We have presented a technique for scattering centres extraction using flat spectrum OFDM pulses. Our emphasis was put on retrieving the scatterer type. The underlying principle of our method relies on estimating the slope of the OFDM echoes' spectra. We stressed the need to have separable echoes in order to prevent from any ISI to occur. We showed how prior information over the scatterers' relative distance enabled the design of OFDM pulses to cope with that requirement. Eventually, we performed a statistical analysis to characterise the slope estimates for different SNR levels for two different bandwidth cases. We demonstrated the merit of integrating over several echo spectra to improve the slope estimate in low SNR conditions which in turn improves the scatterer

type characterisation. Lastly, for a given number of subcarriers, the larger the bandwidth of the OFDM pulse, the better the performance of the classification with low SNR levels.

Chapter 7

OFDM phenomenology: radar technique combining genetic algorithm based pulse design and energy detector for target recognition[14]

It is well known that when illuminated by an electromagnetic wave the targets' RCS fluctuates with frequency and aspect angle [32]. This property and its consequences on the performance of the subsequent signal processing have been apprehended by Swerling. He summarised his findings in the form of five Swerling models [123] where each model forms a pair composed by a distribution function of the RCS fluctuation and an information concerning the rapidity of this fluctuation. The merit of these models is to provide analytical expressions for the probability of detection as a function of the average SNR, which can be used by engineers to appraise the design of a radar in front of customers.

[14] Based on Lellouch, G. et al. "OFDM phenomenology: radar technique combining genetic algorithm based pulse design and energy detector for target recognition," accepted in the first review to *IET Radar and Sonar Navigation*

7.1 Introduction

Although RCS fluctuations with respect to frequency make the performance analysis more complex, we propose a radar technique where we avail from the frequency signatures of targets to enhance the classification function directly in the measurement process. We bolster our approach with the following comments.

- Reflectivity spectra with respect to frequency are invariant over small aspect angle windows and the size of this window is a measure of the decorrelation [32].
- The scattering mechanism can be modelled as a convolution of the transmitted signal with the target reflectivity impulse response.
- OFDM signals are generated in the frequency domain and their spectra can be tailored despite bandwidth and energy constraints.

In this second chapter dedicated to OFDM phenomenology, we suggest exploiting the targets' frequency signatures to improve the classification function of our radar system.

7.2 Background

The appeal to the broad scope of waveform diversity in the last years has emanated for a big part from researchers involved in cognitive radar (CR) [124, 108]. The goal of CR is to provide the sensing system with the information about the propagation environment, input from external knowledge sources, system objectives and priorities so that the radar can be self evolving. Hayking [125] materialised this close-loop process with a feedback running from the receiver to the transmitter. Thereby, the intelligent system shall be able to find the best waveform for the next illumination [125].

In that regard, several authors have considered the problem of finding the signal that optimises a particular task. Bell [39] developed a theoretical framework to find a waveform/receiver-filter pair for the optimal detection of extended targets in additive noise. He introduced two different metrics (SNR or mutual information, MI) whether a deterministic impulse response or a random target impulse response are used. Pillai et al. [126] expanded the first part of this work (SNR metric) for the case where the target competes with signal-dependent interference. The authors developed an iterative algorithm to search for the transmit signal-receiver impulse response pair that converges satisfactorily for most values of input signal to interference plus noise ratio (SINR). Among other, they stressed that chirp-like pulses are most probably unacceptable solutions. Garren et al. [42] adapted later this algorithm to finite-dimensional vector spaces in order to facilitate a discrete-time implementation. Kay [127] proposed another extension of [39] to include the case of a Gaussian point target in Gaussian clutter. The merit of his approach is a simple analytical result which is guaranteed to be optimal. Lately, Romero [128] expanded Bell's initial work to include the case where the target competes with signal-dependant interference with both metrics. Eventually, in [129], the authors proposed to design the transmit waveform as a weighted sum of basis sequences for the case of Gaussian point target in signal-dependent clutter and noise. Their idea is to maximise the detection performance with respect to the corresponding weighting factors so that the desired waveform is obtained immediately, while the aforementioned works arrive at the energy spectral density (ESD), which in turn infers a degradation loss as the time series is synthesized.

Besides the use of these so-called "matched illumination-reception" techniques for optimising the target detection, various authors searched to apply the same concept to the problem of target classification. Garren et al. [42] built up over Guerci's work [130] to develop a theoretical framework that finds the optimal waveform for target identification discrimination when the scenario includes coloured noise and non-zero coloured clutter. Extensions for the identification problem are developed via a maximisation of the Mahalanobis distance between

the echoes of the target classes, two in this case. As opposed to the first problem (target detection optimisation) there is no receiver filter involved. Another work [131] investigated further the problem while including aspect angle uncertainties for both cases of SINR maximisation and identification. In [124] both SNR and MI were used to adaptively modify the transmit waveforms for recognition of known targets when the additive noise is AWGN. It was shown that the integration of these waveform design techniques with sequential hypothesis testing (SHT) could reduce the energy required for identification. In [132] the authors analysed further the recognition problem in the presence of clutter. They also demonstrated how their closed-loop framework and waveform design techniques could be applied to a multi-band transmission system where the system must adaptively select which band to use for any single transmission. More recently, Wei et al. investigated in [133] the design of phase-coded waveform for maximum recognition performance under detection constraints.

Ultimately, Paichard *et al.* investigated in [37] the benefit to transmit OFDM pulses to acquire the reflectivity spectra of time-varying targets. The relevance of this study shall become clear as we discuss target modelling in Section 7.3.3. In particular, the use of similar systems like their proposed HYperfrequence CAMera (HYCAM) may permit to acquire reflectivity spectra from target of interest on the fly.

7.3 Technique

Our matched-filterless technique seeks to propose a simple yet reliable framework to support the recognition task when the radar has to choose among several targets characterised by their deterministic impulse responses, respectively their reflectivity spectra. We follow the phenomenological approach first introduced by Huynen [112] whereby most of the focus shall be on the phenomenon under interest. Although it is not our goal to develop a bio-inspired radar mechanism, it must be noted that our approach can serve studies within that scope [134].

7.3.1 Contribution

As opposed to any of the aforementioned works, our technique relies on the OFDM structure for the transmitted pulse. The nature of OFDM and in particular the fact that the time domain pulse is efficiently synthesized from the spectrum motivates the use of this technology. To our best knowledge, the concept whereby the recognition task is solely based on the use of a single pulse (possibly transmitted multiple times) coupled with an energy detector is novel. Besides, we are not trying to find an analytical expression for the optimal radar signal used for recognition, as we make use of an iterative search method based on GAs. This search procedure is fast and permits to generate an infinite number of signals. On top, additional constraints can easily be included.

7.3.2 Simulation setup

Our concept is better described by the block diagram given in Fig. 7.1. In the case where we must recognise between three different targets, our transmitted signal $s(t)$ is composed of three sub-pulses s_1, s_2 and s_3 which we refer to as OFDM symbol one, two and three. The pulse interacts with one of the three targets in the scene, characterised by its impulse response h_{tl}, where l=1, 2 or 3. AWGN adds onto the echo and the energy detector then simply evaluates the amount of energy on each of the sub-echoes. Classification of the target is done upon that information.

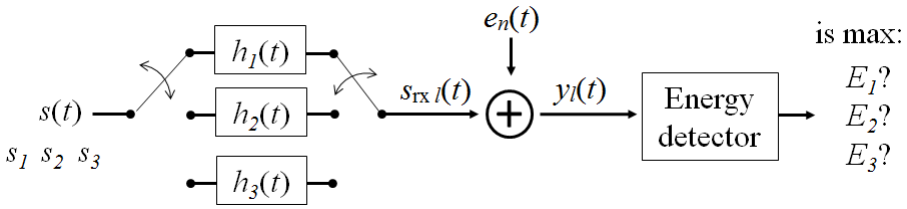

Figure 7.1: Simulation setup of the matched-filterless recognition concept

In Chapter 5 and 6, we showed how scattering can be modelled as a filtering process with the baseband transmitted pulse at the input and the baseband

received pulse at the output, as long as the target reflectivity spectrum considered consists of the portion at RF whose extent equates to the pulse bandwidth.

The whole process employed to generate the OFDM symbols is summarised as follows.

1. Characterise L_T target models
2. Calculate L_T reflectivity spectra
3. Generate L_T masks
4. Design L_T symbols
5. Combine all L_T symbols to compose the pulse

The content of each unitary process is expounded in the next sections.

7.3.3 Target modelling

In our experiment, we use target models constructed from several perfectly electrically conducting (PEC) spheres such that we can apply the Mie theory. In fact, spheres are the sole objects for which there exists a closed-form expression for the backscattered electrical field for all frequencies and polarisations. Together with the superposition principle, we obtain analytical expressions for the RCS as a function of frequency. A similar experimental setup was proposed in [135], where several automatic target recognition (ATR) algorithms are tested on synthetic radar data for recognition purposes. In this work, the emphasis was on the processing side.

7.3.3.1 Mie scattering

The Mie scattering is the Mie solution to the Maxwell's equations named after Gustav Mie that describes the scattering of electromagnetic radiation by a sphere. The solution takes the form of an infinite series [8].

In our experiment, we consider perfectly electrically conducting (PEC) spheres with a size comparable to the wavelength for the range of frequencies of interest so that the RCS varies in the resonance or Mie region. It is this fluctuating behaviour that we intend to use to distinguish between the multiple targets.

7.3.3.2 Models

Our simulation environment assumes that the radar is located 10 km away from the target hence its coordinates are (-10 km,0) and the centre of the reference system lies in the vicinity of the target. Each sphere is characterised by its centre coordinates (x_s, y_s) and radius a_s.

The target models used in our experiment are presented in Figs. 7.2(a)-7.2(c). To simulate different targets, we vary the number of spheres, their sizes and positions. Different setups may consider other models. Our intention here is to generate a preliminary set of synthetic targets upon which we can test our technique.

Arbitrarily, we consider a bandwidth of 30 MHz between 1 GHz and 1.03 GHz. The objective is to have a bandwidth large enough so that the RCS of all three targets behave differently over the band. Figs. 7.2(d)-. 7.2(f) show the RCS over an extended band between 0.9 GHz and 1.1 GHz. The part within the red rectangle corresponds to the 30 MHz bandwidth.

7.3.3.3 RCS normalisation

Before manipulating further the RCS data, we must normalise them. The normalisation is actually done on the reflectivity spectra following the method proposed in Section 5.6.3.1, whereby the frequency domain reflected signal resulting from a flat spectrum OFDM pulse of unit energy $\mathbf{s}$ shall have unit average power. As a result, the RCS values become comparable as observed in Fig. 7.3(a).

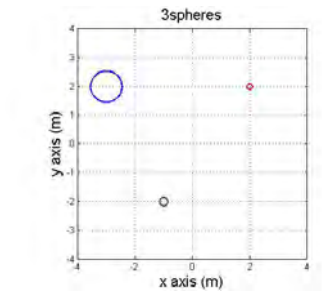

(a) Target 1

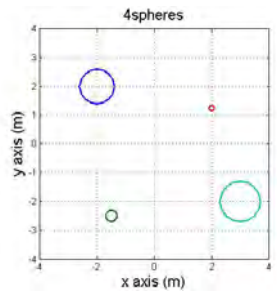

(b) Target 2

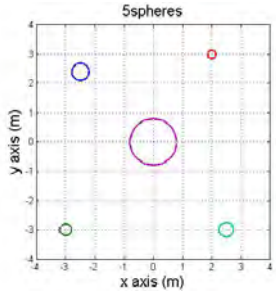

(c) Target 3

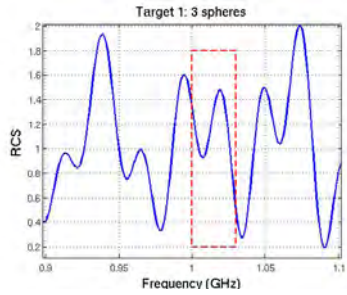

(d) RCS $|H_{f_1}(f)|^2$

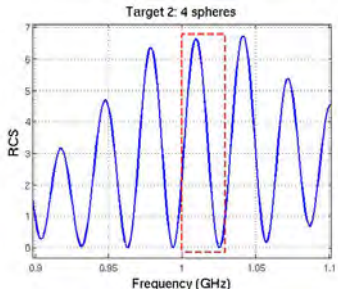

(e) RCS $|H_{f_2}(f)|^2$

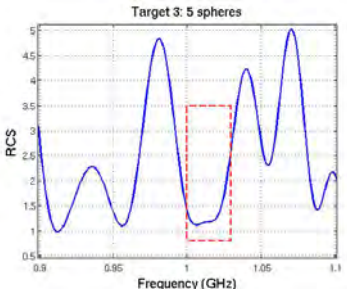

(f) RCS $|H_{f_3}(f)|^2$

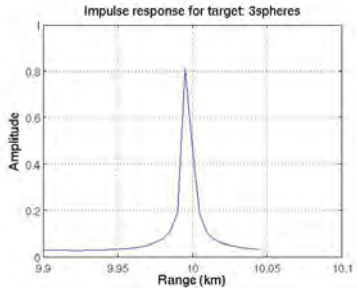

(g) Impulse response for Target 1

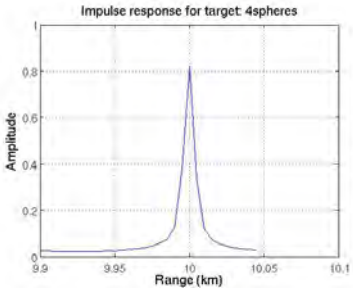

(h) Impulse response for Target 2

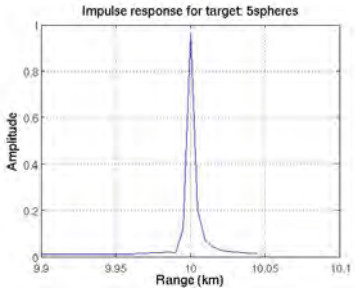

(i) Impulse response for Target 3

Figure 7.2: Geometrical model for the targets considered in the experiment. The coordinates of the centres and the radii a_s are as follows, a) (-3,2), (-1,-2), (2,2) and a_s=0.55 m, a_s=0.15 m, a_s=0.1 m respectively, b) (-2,2), (-1.5,-2.5), (2,1.25), (3,-2) and a_s=0.6 m, a_s=0.2 m, a_s=0.1 m, a_s=0.7 m respectively and c) (-2.5,2.4), (-3,-3), (2,3), (2.5,-3), (0,0) and a_s=0.3 m, a_s=0.2 m, a_s=0.15 m, a_s=0.25 m, a_s=0.8 m respectively. d), e) and f) RCS of the 3 targets considered in the experiment over a frequency band comprised between 0.9 GHz and 1.1 GHz. g), h) and i) Impulse responses for all three targets.

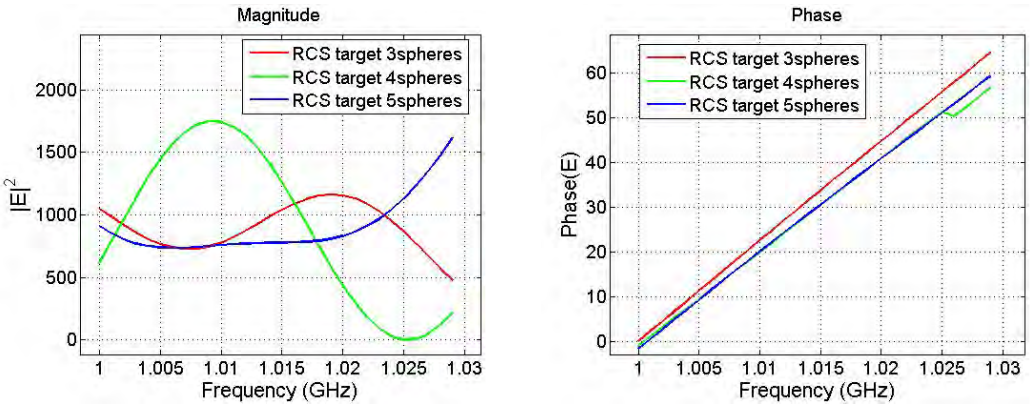

(a) Normalised RCS of all three targets

(b) Phase of the reflectivity spectra of all three targets

Figure 7.3: Normalised RCS and phase of the reflectivity spectra of all three targets within the 30 MHz bandwidth of interest.

7.3.3.4 Target impulse response

For each target model, the impulse response vector $\mathbf{h_t}$ is given by $\mathbf{h_t}$=IDFT($\mathbf{h_f}$). To maintain reasonable values, we normalise them so that they have unit energy and use these normalised vectors to generate the received echoes. In fact, the relative energy level does not matter. The normalised impulse responses are given in Figs. 7.2(g)-7.2(i). While the peak appears at 10 km for both Target 2 and 3, its position is shifted by one sample at 9995 m in the case of Target 1, as justified from the geometrical model in Fig. 7.2(a).

7.3.4 Randomisation

In order to establish a proof of concept, we suggest to use a Monte Carlo approach on a large data set. Essentially, we generate M_{noise} reflectivity spectra from M_{noise} realisations of the target when a slight change on the spheres' coordinates and radii is applied. For each realisation of the target, any of these three characteristics x_{sm}, y_{sm} and r_{sm} are generated from normal distributions with means x_s, y_s and r_s respectively and standard deviation σ_{std}=0.01 m. We illustrate this approach with Figs. 7.4(a)-7.4(c) that show the location of the

centres of the spheres. We used M_{noise}=5000. With σ_{std}=0.01 m, 99.8% of the points are comprised within $6\sigma_{std} \simeq 1\% \cdot \delta R$, where $\delta R = c/2B$=5 m is the range resolution. In practice, these stochastic models render the uncertainty one has on the reflectivity spectrum for a particular target due to the target motion and aspect angle variations.

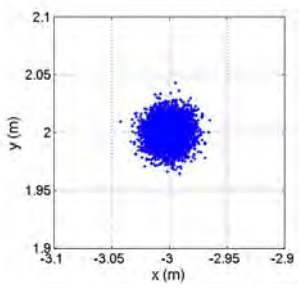

(a) Centres for sphere 1

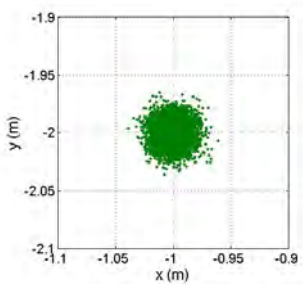

(b) Centres for sphere 2

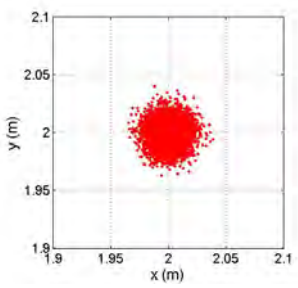

(c) Centres for sphere 3

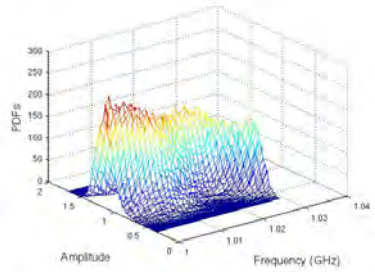

(d) Set of PDFs for Target 1

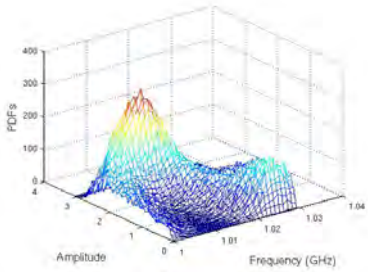

(e) Set of PDFs for Target 2

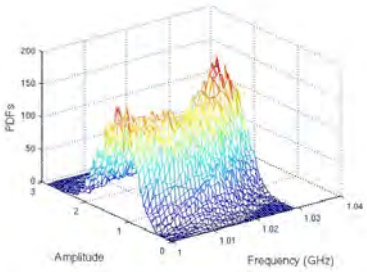

(f) Set of PDFs for Target 3

Figure 7.4: a), b) and c) Effect of the randomisation on the position of the centre of the three spheres for the first target model. We use a normal distribution centred on the original values with a standard deviation of 0.01 m. d), e) and f) Set of PDFs of the reflectivity spectrum for the three target models as a result of the randomisation.

The result is a set of reflectivity spectra, which we can exploit to build a set of histograms for the frequencies of interest. Each histogram is a measure of the reflectivity spectrum for a particular frequency. When normalised, we can interchangeably refer to these histograms as PDFs. The PDFs for the three target models are shown in Figs. 7.4(d)-7.4(f). For each target, we are able to retrieve the trend of the RCS plot given in Fig. 7.3(a). These plots give an indication of the amount of correlation or decorrelation present in the set of targets. In fact,

the sharper the PDF, the stronger the correlation. Hence, from the variations of the allure of the PDFs, we can conclude that the correlation level is not equal along the frequency axis. For example, in Fig. 7.4(e), the level of correlation is strong in the first 10 MHz from 1 GHz to 1.01 GHz and it decreases in the next 20 MHz of the bandwidth. In contrast, the level of correlation of the third target remains high throughout the band as shown in Fig. 7.4(f).

7.3.5 Pulse design

As explained in section 7.3.1, our concept avails from the OFDM technology. The motivation to use OFDM is twofold. Firstly, the signal is fully defined by its discrete spectrum vector. Secondly, the discrete time domain signal is easily synthesized when applying an IFFT algorithm on the discrete spectrum vector. Hence, provided that we find optimal spectra, the time domain signals are generated at no loss. In this section we first discuss the generation of masks which we use later to search for optimal discrete time domain signals.

7.3.5.1 Generation of the masks

The elaboration of the masks is an important step in the design of the pulse as exposed earlier. Intuitively, the mask used for a given target shall compose with those parts of its reflectivity spectrum that exceed the reflectivity spectra of any other targets. If we were to design the OFDM symbol to match the mask, we would excite the target of interest while refraining from exciting the other. Repeating the same procedure for each of the L_T targets under consideration would result in L_T OFDM symbols, each one being matched to only one target. If the pulse is formed out of these L_T symbols, we expect that the signal, received after the pulse has bounced off any of the L_T targets, will present the highest energy level within the corresponding sub-echo. It is this principle introduced in Fig. 7.1 which we develop in greater details now. The mechanism employed to generate the mask is presented in the next algorithm in Box 3.

Figs. 7.5(a)-7.5(f) are used to illustrate the procedure for the case where the

Algorithm 3 Generation of the masks

1: **for** Target model l=1 to L_T **do**
2: Calculate the mean magnitude and phase of the reflectivity spectrum from Target l, $\bar{\mathbf{h}}_{\mathbf{l}}$.
3: Normalise the reflectivity spectrum $\mathbf{h}_{\mathbf{l}_{\text{norm}}}$.
4: **for** all other L_T-1 Target models ll **do**
5: Calculate the mean magnitude and phase of the reflectivity spectrum from Target ll, $\bar{\mathbf{h}}_{\mathbf{ll}}$.
6: Normalise the reflectivity spectrum $\mathbf{h}_{\mathbf{ll}_{\text{norm}}}$.
7: Generate the difference reflectivity spectrum $|\mathbf{\Delta h}_{\mathbf{l,ll}}|=|\mathbf{h}_{\mathbf{l}_{\text{norm}}}|-|\mathbf{h}_{\mathbf{ll}_{\text{norm}}}|$ and $\arg(\mathbf{\Delta h}_{\mathbf{l,ll}})=\arg(\mathbf{h}_{\mathbf{l}_{\text{norm}}})-\arg(\mathbf{h}_{\mathbf{ll}_{\text{norm}}})$.
8: **end for**
9: Calculate the mean magnitude of the difference reflectivity spectra $|\bar{\mathbf{\Delta}}\mathbf{h}_{\mathbf{l}}|=1/(L_T\text{-}1)\sum_{ll=1}^{L_T-1}|\mathbf{\Delta h}_{\mathbf{l,ll}}|$.
10: Calculate the mean phase of the difference reflectivity spectra $\arg(\bar{\mathbf{\Delta}}\mathbf{h}_{\mathbf{l}})=1/(L_T\text{-}1)\sum_{ll=1}^{L_T-1}\arg(\mathbf{\Delta h}_{\mathbf{l,ll}})$.
11: Fix a threshold α_{th}
12: Find the indices k_i where $|\bar{\mathbf{\Delta}}\mathbf{h}_{\mathbf{l}}| > \alpha_{\text{th}}$.
13: Set the mask corresponding to Target model n equal to a default value ϵ: $\mathbf{m}_{\mathbf{l}}=\epsilon[1\ldots1]$.
14: For the indices k_i set the magnitude of the mask equal to the mean magnitude of the difference reflectivity spectra:$|\mathbf{m}_{\mathbf{l}}[k_i]|=|\bar{\mathbf{\Delta}}\mathbf{h}_{\mathbf{l}}[k_i]|$.
15: For the indices k_i set the phase of the mask equal to the mean phase of the difference reflectivity spectra:$\arg(\mathbf{m}_{\mathbf{l}}[k_i])=\arg(\bar{\mathbf{\Delta}}\mathbf{h}_{\mathbf{l}}[k_i])$.
16: Normalise the mask $\mathbf{m}_{\mathbf{l}_{\text{norm}}}$.
17: **end for**

three targets from Fig. 7.2 are considered. For each target, the difference reflectivity spectra with respect to the other two targets and the resulting mean are given. Then, the resulting mask is plotted. As expected, the non constant parts coincide with the frequency segments when the mean magnitude of the difference reflectivity spectra is higher than the threshold α_{th}. In our procedure we chose α_{th}=5 to guarantee that the mask reflects the peaks of this mean profile and the default value is chosen as ϵ=1. This last value is arbirtrary. We reckon that it shall be small enough in comparison to α_{th} to enhance the peak. We observe in Fig. 7.5(b) that the difference reflectivity spectra between Target 2 and 1 and between Target 2 and 3 are strong over the same portion of the spectrum. This is the ideal case as we will see in section 7.4.

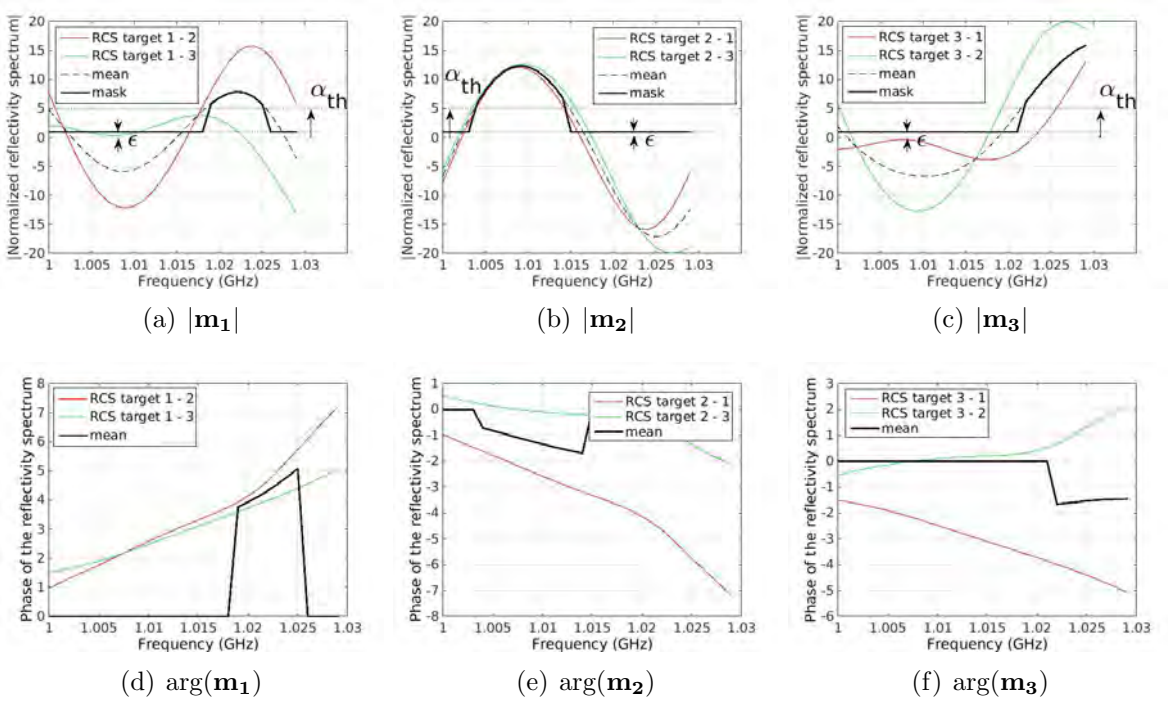

(a) $|\mathbf{m_1}|$ (b) $|\mathbf{m_2}|$ (c) $|\mathbf{m_3}|$

(d) $\arg(\mathbf{m_1})$ (e) $\arg(\mathbf{m_2})$ (f) $\arg(\mathbf{m_3})$

Figure 7.5: Generation of the masks for the 3-target case. Magnitude a), b), c) and phase d), e), f).

7.3.5.2 Sub-pulses optimisation

As indicated in Section 7.3.2, the next step is to design the pulse. More precisely, our task is to search for the L_T optimal OFDM symbols (also called sub-pulses). We define our optimality criterion as follows: the optimal OFDM symbol shall, after normalisation, produce an echo of maximum energy when bouncing off an hypothetical target itself characterised by the normalised mask generated earlier.

We now discuss the parameters at hand for this optimisation. The orthogonality principle [7] ruling the OFDM structure infers that subcarrier spacing Δf and symbol (or bit) duration t_b are linked according to: $\Delta f = 1/t_b$. Hence fixing the symbol duration fixes the subcarrier spacing and then fixing the bandwidth B fixes the number of subcarriers N. In the present case, we use B=30 MHz and t_b=1 μs so that Δf=1 MHz and N=30 subcarriers. In that

context, the OFDM symbol is fully defined by the weight and phase code vectors, $\mathbf{w_n}=[w_1 \dots w_N]^T$ and $\mathbf{a_n}=[a_1 \dots a_N]^T$, respectively. We define the complex number $z_n=w_n a_n$ such that $|z_n|=w_n$, $\arg(z_n)=\arg(a_n)$ and the vector of complex numbers $\mathbf{z_n} = [z_1 \dots z_N]^T$. The question of optimal OFDM symbol reduces to the following optimisation problem,

$$\arg\max_{z_n} \quad |\mathbf{z_{n}}_{\text{norm}}{}^T \cdot \mathbf{m_{l}}_{\text{norm}}|^2, \text{ s.t. } \begin{cases} w_n \geq v_l \\ w_n \leq v_u \end{cases} \tag{7.1}$$

where $\mathbf{m_{l}}_{\text{norm}}$ is the mask vector after normalisation and $\mathbf{z_{n}}_{\text{norm}}$ is the normalised complex spectrum of the OFDM symbol resulting from Eq. 7.2:

$$\mathbf{z_{n}}_{\text{norm}} = 1/\sqrt{N \sum w_n^2} \cdot \mathbf{z_n}. \tag{7.2}$$

Note that our constraints in Eq. 7.1, namely v_l and v_u are introduced to limit the dynamic range of the weights. In the case we would impose a wideband transmission the dynamic range shall be small. Otherwise I can be high. In the following, we present simulation results obtained for different values of v_l when v_u is fixed.

Our experience with genetic algorithms for optimisation problems like this one suggests that similar techniques as used in [44] could be used. In fact, we propose to use a continuous genetic algorithm as proposed in [104]. As opposed to its binary counterpart, the continuous version is adapted to the case where variables are not naturally quantised, like it is the case here. A consequence of this choice is a much faster processing time.

A vast amount of literature is available on the topic [104, 91], hence we restrict our discussion to the specificities of our application.

- Cost function

  The cost function which we use in our GA is the same scalar product as in Eq. 7.1 to the difference that we introduce a minus sign in order to work

out a minimisation rather than a maximisation.

$$cost = f(chromosome) = -|\mathbf{z_n}_{\text{norm}}{}^T \cdot \mathbf{m_l}_{\text{norm}}|^2. \tag{7.3}$$

- Variables

  As indicated in the cost function, the variables are the N pairs of weights and phase codes resulting in $2N$ variables.

- GA parameters

  Multiple parameters must be defined. Firstly, the search space needs to be addressed. The constraints defined in Eq. 7.1 establish the possible values for the weights and the phase codes can take any value around the unit complex circle. Secondly, some more typical parameters for GAs such as the stopping criteria, the population size, the mutation rate and the selection ratio must be assessed. We base our stopping criteria on the number of iterations which we take equal to 1000, we use a population of 20 "chromosomes", take a mutation rate of 0.2 and a selection rate of 0.5. These parameters are used to ensure that the search space is efficiently covered to converge towards a global minimum solution. Of course, different sets of parameters are possible but the overall good behaviour of the algorithm is a first indication of their relevance.

- Initial population

  The initial population is generated at random. In other words 20 vectors with size $2N$ each are generated. The law governing the weights follows a uniform distribution within the bounds given in Eq. 7.1. Likewise, the phases of the phase codes follow a uniform distribution within $[0,2\pi]$. In terms of GAs, each element of the population is a chromosome.

- Convergence check

  The convergence check is based on the stopping criteria defined earlier. Hence, we stop once the number of iterations has reached the end.

- Final population

The final population has the same size as the initial population. We select the element with the best cost and use it to generate our optimal OFDM symbol.

In practice, we include in the initial population a chromosome whose weight and phase vectors are identical to the mask, provided some scaling factor for the weight vector so that its values remain within the bounds given in Eq. 7.1. Intuitively, we expect from vectors whose behaviour is similar to the mask to have favourite characteristics as far as the energy of the received echo is concerned. In Figs. 7.6(a)-7.6(c) we tracked the cost function of the best chromosome in the population versus the generation index. The decreasing trend of the curve attests the gain produced by our GA. We considered three cases, for three different values of v_l, while v_u=10. Namely, we used v_l=0.01, 1 and 5. Some optimal solutions after 1000 iterations for the first target mask are presented in Figs. 7.6(d)-7.6(f). When the dynamic range reduces as in Fig. 7.6(f) the optimal weight vector spreads its energy over the entire peak.

Ultimately, the time domain sub-pulses $\mathbf{s_n}$ are formed after applying an IDFT on the complex vectors $\mathbf{z_{n}}_{\text{norm}}$ and the pulse is composed by associating the three optimal sub-pulses.

7.4 Statistical analysis

The last step of our experiment consists in going through the full process presented in Fig. 7.1. We first report on our preliminary results where each target is modelled by a single deterministic impulse response. We then introduce the results obtained from Monte Carlo simulations. For each realisation, the target has a slightly different geometrical model, which results in a slightly different reflectivity spectrum as explained in Fig 7.4. This approach enables us to generate statistical results for the recognition problem. We then propose to introduce a search technique that relies on an optimality criterion of our choice to position the bandwidth in the most attractive region of the spectrum in terms of the recog-

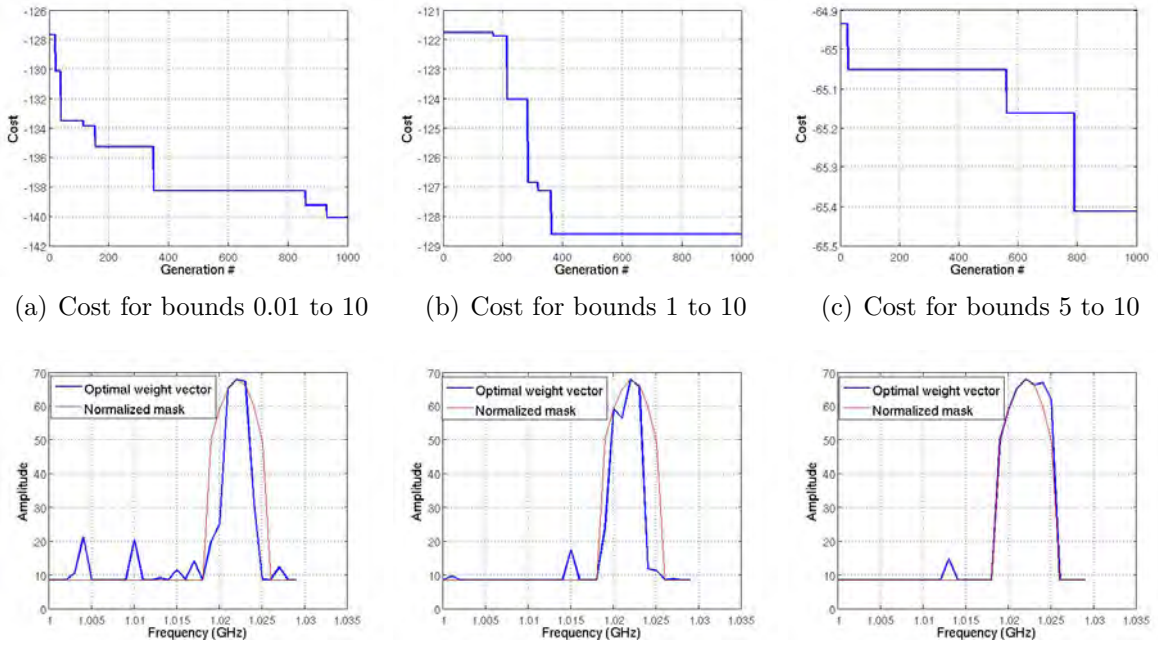

(a) Cost for bounds 0.01 to 10 (b) Cost for bounds 1 to 10 (c) Cost for bounds 5 to 10

(d) Lower bound: 0.01 (e) Lower bound: 1 (f) Lower bound: 5

Figure 7.6: a), b) and c) Cost value as a function of the generation index for the mask from Target 1 and different values of the lower bound constraint used to design the weight vector. d), e) and f) Mask and corresponding weight vector for different values of the lower bound constraint used to design the weight vector. Note that we used a scaled and shifted version of the weight vector to plot both quantities on the same graph. Our interest lies in the overall allure of the weight vector in comparison to the mask.

nition capabilities. We compare the results obtained for both cases and discuss the trade-offs. Ultimately, we inspect the benefit of integrating several pulses before assessing the energy content of the various sub-echoes. We show that this technique brings tremendous improvements even when low SNR conditions are considered.

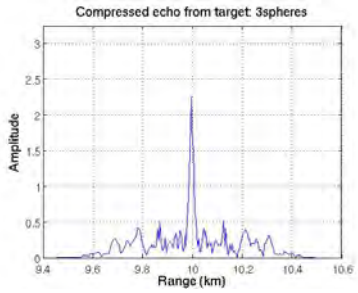

(a) Compressed echo from Target1

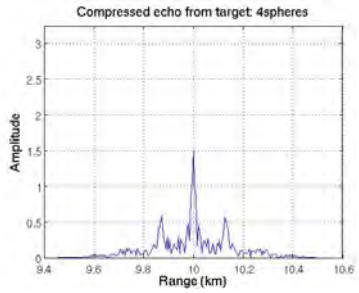

(b) Compressed echo from Target2

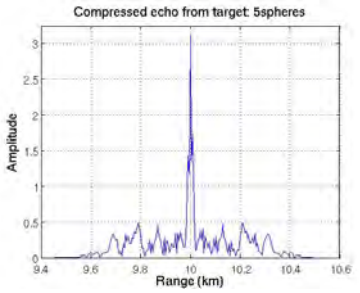

(c) Compressed echo from Target3

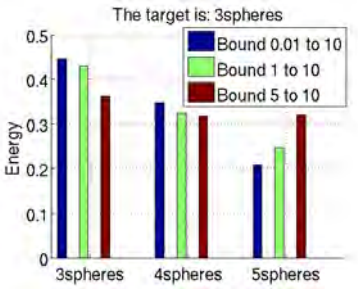

(d) When Target 1 is present

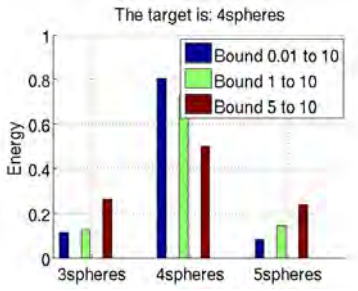

(e) When Target 2 is present

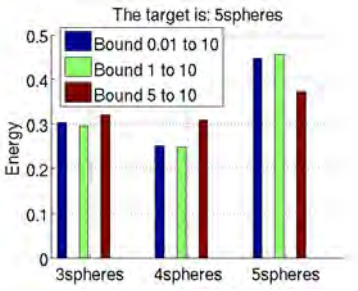

(f) When Target 3 is present

Figure 7.7: a), b) and c) Compressed echoes for either Target 1, 2 or 3. The asymetric allure of the curve results from the extended target behaviour, and as such is different from the simple autocorrelation function of the transmitted pulse. d), e) and f) Energy content in the received sub-echoes for different values of the lower bound used in the design of the pulse.

7.4.1 Preliminary results

7.4.1.1 Unitary test

In fact, prior to the energy detector presented in Fig. 7.1, one needs to localise the beginning of the pulse. To that end we suggest making use of a matched-filter. Hence, we filter the received echo with a replica of the transmitted pulse and the peak in the output is used as an indicator of the first pulse sample. Figs. 7.7(a)-7.7(c) illustrate the compressed echoes for all three targets. The difference in the peak amplitude results from the different values of the three target RCSs despite the normalisation method presented in Section 7.3.3.3. In particular, we observe that the peak is positioned at 10 km for both Targets 2 and 3, while it appears

on the previous sample, 9.995 km for Target 1. This is perfectly in line with the geometric target models where Target 1 presents its main contributor at a range 9.997 km from the radar, which clearly, is closer from the 9.995 km range bin than the 10 km one.

Following our prior preparation, we repeat the experiment for each of the three pulses that we generated with different values of v_l. The energy values E_1, E_2 and E_3 are assessed and our results are given in Figs. 7.7(d)-7.7(f). For the sake of clarity, prior to summing the samples, we normalise the received echo so that its energy is 1. Hence, 100% of the energy is distributed over all three sub-echoes. A fortiori, we expect to get the highest energy content in the symbol corresponding to the target in the scene. This intuition is verified for all three pulses designed with v_l=$\{0.01, 1, 5\}$. However, we observe that the smaller v_l the better the discrimination. As a matter of fact, from a recognition point of view it is optimal to transmit most of the energy on the few subcarriers where the magnitude of the mask is strong as illustrated in Fig. 7.6(e).

The discrepancy in the allure of the histogram for Target 1 and 3 as opposed to Target 2 is to be expected as the amplitude of the mask in Fig. 7.5(b) is analysed in light of the three target RCSs shown in Fig. 7.3(a). In the case of Target 2, it is clear that the mask puts most of the energy on those frequencies where the RCS from Target 2 exceeds significantly the RCS from both Targets 1 and 3. Hence, we can anticipate the result whereby the second symbol will excite Target 2 very effectively. Although Symbols 1 and 3 are exciting Targets 1 and 3 sufficiently to give rise to higher values for E_1 and E_3 respectively, the other values are not significantly lower. Obviously, the case from Target 2 reveals the ideal configuration as it infers an optimal recognition pattern. As a matter of fact we discuss later the possibility to select an optimal bandwidth that could maximise the recognition pattern in all three cases, not only one as it is presently the case.

7.4.1.2 Monte Carlo simulation

To characterise statistically our concept, we run a Monte Carlo simulation where we make use of the stochastic RCS models as generated in Section 7.3.4. For each realisation, the target is described by a slightly different RCS curve. In the end, we observe the distribution of the energy level in all three symbols, but more importantly we check whether the appropriate sub-echo is the most energetic, in which case we declare that the recognition has been successful. This approach enables us to build a confusion matrix which we present in Table 7.1.

The confusion matrix is one of the most adapted ways of representing the results from an ATR exercise. Details concerning the confusion matrix derivation can be found in a paper by Mishra et al. [122]. For the configuration under consideration (stochastic target models with standard deviation σ_{std}=0.01 m for both the sphere positions and radii), Table 7.1 confirms the outstanding performance (94.2%) as far as the recognition of Target 2 when Target 2 is present in the scene is concerned. For the other two cases, our conclusion is mitigated since high probabilities of misclassification Pmc_i are observed. The latter are calculated following the equations in [122]. Likewise, the probabilities of false alarm Pfa_i for a given Target i are calculated as well as the overall probability of correct classification Pcc. These information, extracted from the confusion matrix, are summarised in Table 7.2.

Table 7.1: Confusion matrix resulting from the stochastic target models with σ_{std}=0.01 m

		Predicted Target		
		Target 1	Target 2	Target 3
Actual target	Target 1	63.3%	36.2%	0.5%
	Target 2	5.3%	94.2%	0.5%
	Target 3	9.3%	30.1%	60.6%

In a nutshell, these preliminary results demonstrate the capacity of our technique to classify between several targets, when their RCSs are known, although, clearly, improvements to reduce the false alarm probabilities and increase the overall probability of correct classification are needed. These results also stress the role

Table 7.2: Information extracted from the confusion matrix in Table 7.1

Target i	Pmc_i	Pfa_i	Pcc
1	36.7%	7.3%	**72.7**%
2	5.8%	33.2%	
3	39.4%	0.5%	

of the frequency window in the generation of optimal masks. In that respect, we suggest to consider an additional step where we first search for an optimal frequency window before applying our concept.

7.4.2 Optimal frequency band search

Here, the idea is to see whether a more judicious choice of the frequency window could improve the recognition performance. Note that the bandwidth remains the same, 30 MHz. In the present case, we suggest arbitrarily to run our search within the interval [1 GHz-2 GHz]. From our prior preliminary results we understand that the best configuration would be achieved as the RCSs follow the pattern given in Fig. 7.8(a).

Even though this ideal configuration may not happen within the band of interest, our intention is to converge towards the best solution. We summarised our search technique in the algorithm in Box 4.

Fig. 7.8(b) and Fig. 7.8(c) are used to illustrate the behaviour of the algorithm. In our configuration where the threshold is defined as the mean of all three RCSs, the first window does not get ticked because two peaks are present in the first interval. The vertical lines depict the frequency grid. Conversely, Fig. 7.8(c) shows the RCSs corresponding to one of the optimal solutions. We see that the peaks are well separated so that the maximum for one target RCS will certainly coincide with very low values for the other target RCSs. Besides, the peak values are not perfectly equivalent however the spread remains acceptable based on the threshold that we selected. In the next section, we compare the results obtained as we work with the *default* [1 GHz-1.03 GHz] or this *optimal* frequency window [1.45 GHz-1.48 GHz]. In other configurations (different target models

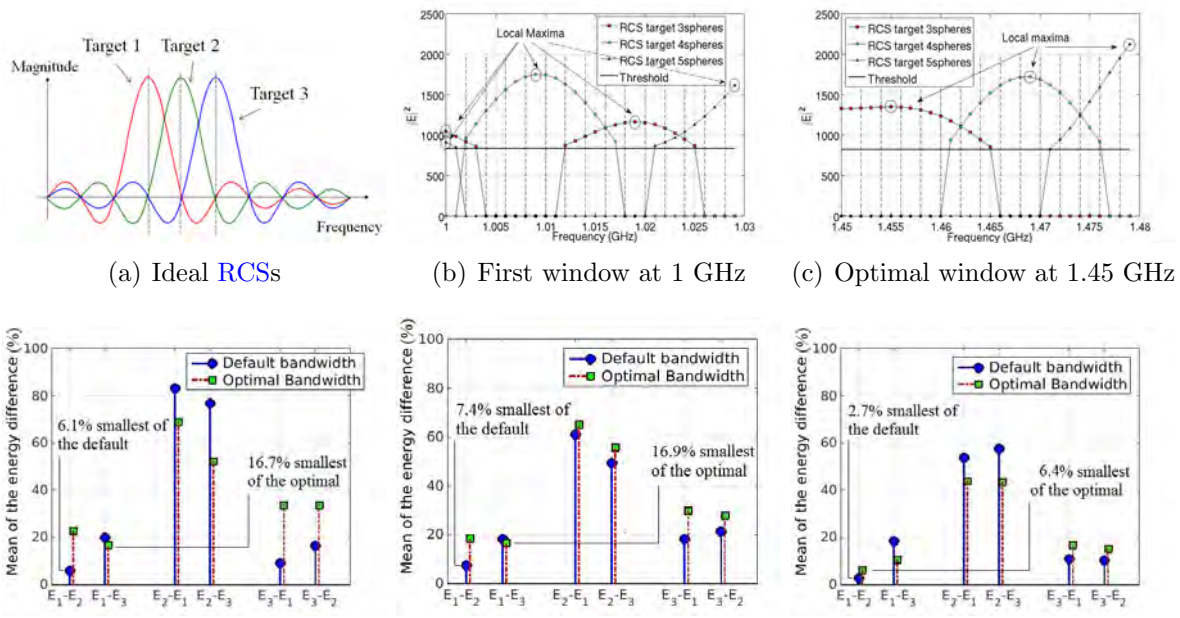

(a) Ideal RCSs (b) First window at 1 GHz (c) Optimal window at 1.45 GHz

(d) σ_{std}=0.001 m (e) σ_{std}=0.005 m (f) σ_{std}=0.01 m

Figure 7.8: a) Ideal situation for the targets' RCSs to provide optimal recognition characteristics. Just like the OFDM structure, we want that the peak for one RCS coincides with low values for the other. b) and c) RCS curves illustrate the behaviour of this algorithm for two different frequency windows, b) the first window starting at 1 GHz and c) one of the optimal windows resulting from the search and starting at 1.45 GHz. d), e) and f) compare the energy differences for the two bandwidth cases.

and different values for the number of targets) this mechanism shall be adapted.

7.4.3 Results and comparisons with one pulse

To understand the "benefit" of the optimal window we generate RCS data from the stochastic geometrical models as in Fig. 7.4 for different values of the standard deviation σ_{std}. We consider the next three values, 0.001 m, 0.005 m and 0.01 m; essentially, the smaller σ_{std}, the less decorrelation throughout the 30 MHz band. In fact, as we generate 3D plots for the optimal window case at 1.45 GHz as in Figs. 7.4(d)-7.4(f) we observe a stronger decorrelation at σ_{std}=0.01 m, which we

Algorithm 4 Searching for the optimal frequency window

```
Initial frequency band = [1 GHz,1.03 GHz]
for each frequency band within [1 GHz,2 GHz] do
    Define a frequency grid within that band (e.g. 1 GHz, 1.002 GHz, 1.004 GHz etc.)
    for each target do
        Identify the portion(s) of RCS above a certain threshold (e.g. it can be the mean value of all RCSs)
        For every portion, identify the frequency corresponding to the peak
        Identify the interval of the frequency grid where the peak occurs
        Store the peak value (if several peaks, store the maximum value)
    end for
    if No more than one peak is observed in any interval of the frequency grid then
        if The spacing between two consecutive peaks is greater than a threshold (e.g. 5) then
            if The spread of the peak values for all targets is below a certain threshold then
                Tick the current frequency band
            end if
        end if
    end if
end for
Use any of the frequency bands ticked
```

explain by the higher frequencies covered. To present our results we follow two approaches.

In the first approach, for every realisation, we assess the difference in energy between the sub-echo corresponding to the target in the scene and the other two (e.g. E_1-E_2 and E_1-E_3, when Target 1 is in the scene). Then we average out to get the mean value which we plot in Figs. 7.8(d)-7.8(f). This approach gives us an idea of the margin for the recognition. Our aim with the *optimal* frequency window was to improve the recognition properties for the cases where either Target 1 or 3 are in the scene. Figs. 7.8(d)-7.8(f) confirm that those margins have been significantly improved. In particular, with σ_{std}=0.001 m, the minimum margin increased from 6.1% (E_1-E_2) to 16.7% (E_1-E_3); with σ_{std}=0.005 m, the minimum margin increased from 7.4% (E_1-E_2) to 16.9% (E_1-E_3); with σ_{std}=0.01 m,

the minimum margin increased from 2.7% (E_1-E_2) to 6.4% (E_1-E_2).

Our second approach consists in working out the confusion matrices. To reduce the computational load, we implemented Monte Carlo simulations based on 1000 iterations rather than 5000 as in Section 7.4.1.2. Comparing both cases of *default* and *optimal* windows we see that almost 100% of recognition rate is achieved. However, as σ_{std} increases, the results for the *optimal* case will degrade more strongly. For instance, with σ_{std}=0.01 m, the probability of correct classification of Target 1 is 47.7% in the *optimal* case as opposed to the 63.7% in the *default* case.

7.4.4 Integration of several pulses

7.4.4.1 Noiseless case

A way around the low overall probability of correct classification for the case σ_{std}=0.01 m is to integrate over several echoes. In practice, the use of a sequential procedure to improve the performance (detection, classification) is common in radar. Using the *default* window, we make use of the results from Section 7.4.1.2, where we generated M_{noise}=5000 echoes. We assume that the collection of pulses if made while the targets maintain a high level of correlation. To assess the statistical properties of this approach, we repeat a Monte Carlo approach with the same number of runs, 5000. At every iteration, we pick N_p echoes out of the larger set and we sum their energies. We then base the classification result upon that compound echo. The selection of the N_p echoes is made at random so that throughout the Monte Carlo experiment different sets of echoes are used.

Finally, to smoothen the results further, for every value of N_p that we selected, we repeat our Monte Carlo experiment 50 times and average out the individual probabilities. The mean values for the probability of correct classification and misclassification ensuing this approach for different number of pulses N_p are given in Table 7.3 for each of the three targets.

We observe that integrating 150 pulses ensures an overall probability of correct

Table 7.3: Flattened confusion matrices resulting from the integration of several pulses, with σ_{std}=0.01 m at f_0=1 GHz.

N	Target 1			Target 2			Target 3		
	Pcc_1	$\text{Pmc}_{1,2}$	$\text{Pmc}_{1,3}$	Pcc_2	$\text{Pmc}_{2,1}$	$\text{Pmc}_{2,3}$	Pcc_3	$\text{Pmc}_{3,1}$	$\text{Pmc}_{3,2}$
2	64.0	35.9	0.04	99.1	0.9	0	69.6	6.1	24.2
10	74.4	25.6	0	100	0	0	92.1	0.3	7.6
50	92.0	8.0	0	100	0	0	99.9	0	0.1
100	97.7	2.3	0	100	0	0	100	0	0
150	99.3	0.7	0	100	0	0	100	0	0
200	99.8	0.2	0	100	0	0	100	0	0

classification Pcc=99.8% in our configuration with three targets, σ_{std}=0.01 m and M_{noise}=5000 realisations for each target.

7.4.4.2 With AWGN

When AWGN is superimposed onto the received echoes following the model presented in Fig. 7.1, we expect to maintain reasonable levels of performance since the noise power becomes evenly distributed on the several sub-echoes. In other words, there is no reason that it shall weight more on one sub-echo than any other. We verify our intuition with the very same Monte Carlo simulation for different values of the SNR. To keep the control of the SNR we normalise all echoes prior to adding the noise. Our findings are given in Fig. 7.9 for different values of N_p. We observe that appropriate values for N_p permit to obtain a satisfactory behaviour under low SNR conditions, such as 0 dB or 10 dB.

7.5 Summary

We have proposed and simulated a pulse optimisation technique able to achieve high classification rates in noiseless and noisy conditions. While the pulses rely on the OFDM structure, our optimisation is performed via a genetic algorithm. The merits of this approach are threefold. Firstly the method is flexible since different target models can be plugged. Secondly we can obtain numerous solutions for

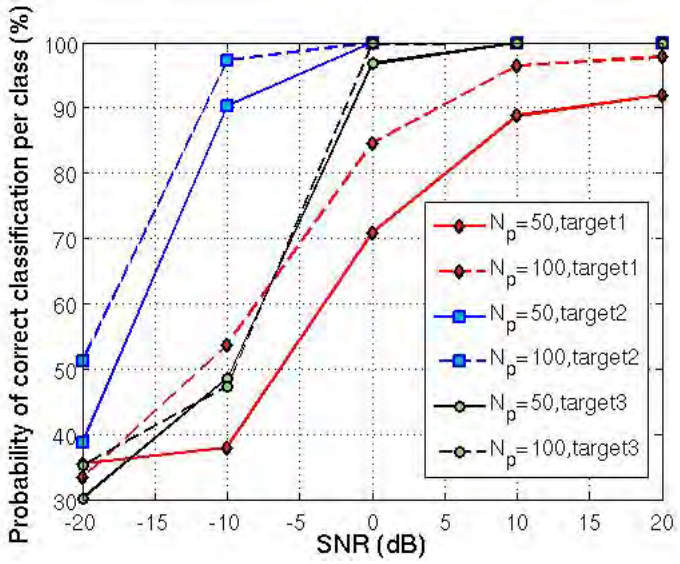

Figure 7.9: Improvement resulting from the integration of several pulses on the probability of correct classification per target class for different values of SNR.

different choices of the tuning parameters. One such example was the *threshold* parameter, which we used to define the dynamic range of the weight vector. Thirdly, we can decide to run the optimisation on the weight vectors only to spare the phase codes for another optimisation of the PMEPR as proposed in Section 5.6.3.3. Furthermore, we tested and validated our technique on a set of three synthetic targets. Each target was composed of several PEC spheres so that an analytical expression for the target reflectivity spectra could be produced. We showed how the bandwidth selection impacts the classification performance and stressed the need to maintain a high correlation level throughout the bandwidth of concern for our target models. Ultimately, our technique is simple. Apart from a matched filter, which we use to localise the start of the received echo, we rely on a basic energy detector to sum the samples of the sub-echoes.

Chapter 8

Conclusions

In this dissertation, we employed OFDM signals as a radar waveform and probed how the overall radar system performance could be improved. Being a wideband signal, the OFDM structure has been known to improve the range resolution along with providing spectral efficiency. Here, we developed methods to process those novel radar waveforms and showed that some communication-inspired techniques were directly applicable to extract radar features. We also proposed several optimisation procedures to improve OFDM as a radar signal and finally established an OFDM phenomenology framework with the intention to improve the classification function of the radar directly on transmission. In the following, we summarise the key contributions of our work and then, discuss some possible directions for future work.

8.1 Key contributions

The scope of our work was threefold.

- After introducing OFDM signals in Chapter 2, in Chapters 3 and 4 we inspected processing methods adapted to the case of a train of OFDM pulses with the point scatterer target model for various waveform concepts.

- In Chapter 5, we explored GA based optimisation algorithms to optimise various aspects of the radar waveform.
- In Chapter 6 and 7, we studied the possibility to use the frequency diversity offered by the OFDM signal to characterise canonical scatterers and classify between several simple targets.

Our key contributions can be summarised as follows.

After analysing the Doppler tolerance of OFDM pulses we demonstrated that the classical processing approach consisting in matched-filtering the echoes in the fast time and then fast Fourier transforming the resulting samples in the slow time was a workable solution. We explained that, in this context, the OFDM pulses shall be designed to offer low autocorrelation sidelobes (PSLR or ISLR) as well as low PMEPR characteristics. We emphasized on the need to have diversity between the pulses to reduce the ambiguities in range and stressed that the ambiguity in Doppler, equal to the PRF, comes as a result of the DFT mechanism and thus could not be avoided in one CPI. We then presented our second processing alternative inspired from the communication demodulation technique used with OFDM signals. We derived our received signal model in matrix forms and characterised the processing in terms of matrix manipulations up to the final range Doppler matrix. We inspected the problem connected to the loss of orthogonality as a consequence of Doppler and derived an analytical expression for the degradation on the range Doppler image. We suggested two mechanisms to retrieve an estimate of the unambiguous radial velocity. While the first mechanism relies on the use of IS for the phase codes of the OFDM pulse, possibly causing high PMEPR, the second applies irrespective of the phase codes as it makes use of the signal after demodulation. Together with the ambiguous Doppler value read from the range Doppler image, this rough estimate of the unambiguous Doppler allows to find an accurate estimate of the unambiguous radial velocity. Because of the demodulation step, the scatterer characteristic function observed on the range Doppler image relies on the Fourier sidelobes only. As such, the OFDM signal requires to be optimised in terms of the single PMEPR. Eventually, we demonstrated that both techniques achieve the same

SNR gain and are thus equivalent in that respect. While the first technique can be applied when there is no prior information on the target, the second method not only requires knowledge of the target position to select the appropriate set of samples but the cell under test must be ISI free. As a result, our first approach is deemed to suit surveillance scenarios while our second approach is deemed to cope with tracking situations.

Similar to the second alternative of the above solutions, matrix formulations were developed to derive the high range resolution profile when the waveform is a train of OFDM pulses where the pulses cover complementary sub-bands of a much larger band. To improve the LPD property of our concept, we proposed to introduce a frequency hopping scheme other than linear and included this aspect into our derivations. Likewise, we then inspected the degradation caused by Doppler in terms of the compression loss at the end of the processing. While the previous exercise inspected the degradation on the range Doppler image, the present analysis was lead on the range profile. Again, the processing gain in the absence of loss was found to be NKM. Next, we presented our concept of frequency hopping based on Costas sequences and showed that this approach, combined with a bank of range migration filters could be used to raise the ambiguity in radial velocity provided that the relative bandwidth was high, though we stressed that this fact was not specific of the OFDM nature of our pulses. We then presented our observations on the correlation sidelobes resulting from the Costas coding and discussed the mitigation of this deterministic effect. We proved by means of simulations that whether the bandwidth of the individual pulses or the total bandwidth is fixed the higher the number of pulses, the lower the level of the correlation sidelobes. Besides, we proposed a solution based on the coherent integration of several batches to improve the contrast between the scatterer and the background. Next, we presented the benefit of our waveform-processing concept via comparisons with typical wideband techniques, namely a train of wideband LFM pulses and a stepped frequency train of unmodulated pulses. Although the drawbacks of the first concept in terms of Doppler resolution and range migration are evident, we explained how the second concept is

similar to ours when the pulses are LFM and thus provide some gain and intermediate range resolution. Lastly, we stressed the merit of our solution in terms of its LPD characteristics, and recalled two facts that still apply: the risk of ISI, and the single PMEPR constraint as a result of the demodulation step in the processing.

The processing concepts explored thus far brought out two observations. The communication inspired processing techniques demodulate the OFDM symbols, hence the sidelobes of the final products are Fourier based and the principal constraint suffered by the OFDM signal becomes the PMEPR. In the context of the classical processing technique, where the received echoes are correlated with the transmitted pulses, the phase codes composing the OFDM signal impact directly the sidelobe level. In that case, the OFDM pulses must be designed to achieve optimal PMEPR and sidelobe levels (e.g. low PSLR). In light of the above comments, we developed GA optimisation based techniques to cope with the single or multiple objectives. We justified the sole use of the complex phase codes (with unit modulus) to serve as parameters, for the sake of saving the frequency diversity, characterised by the real weights attached to each subcarrier, for other purposes. We illustrated this approach via a case study where we optimised sequentially the PMEPR and the detection capability of a particular target. We motivated our choice to rely on GA based methods for the flexibility of the objective functions. In the single PMEPR objective case, we demonstrated how our method equates and even outperforms well-established techniques, like Newman phases, when pulses designed according to realistic scenarios are considered. We also showed how our binary GA based approach could cope with particular alphabets like QPSK, such that existing OFDM systems can be used. Next, we applied the NSGA-II algorithm to our MOO problem and showed that improvements both in terms of PMEPR and PSLR could be achieved as compared to when using random phase codes.

Our next work has been to delve into the concept of phenomenology, which we looked at from a frequency aspect, as opposed to polarisation, which had been

tackled by the pioneers.

From the geometrical theory of diffraction, we observed that many canonical scatterers had well-established frequency responses and proposed to exploit this property to retrieve not only their position or strength but also their type. We suggested a technique based on flat spectrum OFDM pulses and demonstrated the need to have ISI free echoes. Hence, we recommended applying our technique provided that prior knowledge regarding the scatterers' relative position is available. We showed with two examples of a small and extended target how to generate appropriate OFDM pulses. We explained that in the small target case, the pulse had to cover a larger bandwidth to accommodate the short symbol duration when the same number of subcarriers is considered. Then, we presented and illustrated the several steps of our technique before carrying out a performance analysis. We showed how the high relative bandwidth case does outperform the low relative bandwidth case in terms of the overall probability of correct classification for a given SNR value. Lastly, we presented and characterised a method based on the integration of several echoes's spectra to improve the later figure of merit in low SNR conditions.

Finally we inspected the phenomenological approach to improve the classification task. We proposed a concept where most of the classification effort is happening during the waveform design phase as the processing consists in an energy detector. We illustrated our concept with a case study involving three simple targets composed of several perfectly conducting spheres, for which we have exact expressions of the scattered field. We proposed to work in a frequency band where the reflectivity spectra of the three targets are fluctuating according to different patterns. We exploited this fact to build a set of complex masks, one for each target, the goal being that one mask should accentuate the energy scattered by the one target while lessening the energy scattered by the other two targets. Then, we employed a GA based optimisation method to find for each mask the set of weights and phase codes that would maximise the scattered energy. We explained that the probing pulse was built from stacking the three symbols generated in the preceding phase. Next, we tested our concept in a simulation where additional

stochastic features were attributed to the targets to render the uncertainty on the aspect angle. Although the transmission of a single pulse did not permit to achieve a high overall probability of correct classification, we demonstrated the merit of integrating several pulses as values beyond 95% can be obtained despite the presence of AWGN.

8.2 Future work

In this dissertation, a number of methods have been analysed in great details to enhance various aspects of OFDM radar. Further investigation, aimed at demonstrating the practical applicability of those concepts, remains for future research. A list of suggestions for future research is provided hereafter.

- Methods to cope with the issue of ISI for either of our processing techniques, where DFTs are used to tumble in the frequency domain.
- Methods to enhance the performance of the processing in the presence of strong stationary clutter and in particular, methods to raise the ambiguity in Doppler with our frequency domain processing alternative when several echoes from distinct scatterers overlap.
- Methods to cope with migration in range of the received echoes higher than the size of a range cell during the CPI.
- Methods to decrease the correlation sidelobes caused by the selected Costas coding scheme in order to improve the contrast between the scatterer and the background in the high range resolution technique.
- Address GA optimisation when specific positions of the active subcarriers are required.
- Extension of GA based optimisation methods to control the sidelobe level not of a single OFDM pulse, but a train of OFDM pulses.

- Open out to constrained MOO-GA based techniques, for instance to minimise the autocorrelation level with a constraint on the PMEPR of each pulse.
- Optimisation of GA based techniques to speed up the search in single or multiple-objective scenarios.
- Research alternative optimisation strategies, e.g. convex methods, swarm optimisation that can improve the convergence to the best solution in single-objective scenarii possibly including constraints.
- Coding (phase and frequency) methods to optimise the behaviour of two OFDM radar stations used in proximity of each other while minimising the interference level between both signals.
- Hardware implementation of our signal processing techniques using the state-of-the-art processors. The RHINO board at UCT can be used to accommodate OFDM radar signals.
- Account for the components' behaviour (e.g. LNA, RF filter) directly at the waveform design and performance analysis to compare the degradation on the outcome of LFM and OFDM pulses.
- Analysis of the performance degradation due to synchronisation errors, specifically those related to the sampling frequency errors.
- Optimisation of our processing methods to reduce the computational complexity.
- Validate the performance of our proposed techniques with real data.
- Test the capability of our OFDM waveforms to convey information.

Appendix A

Basic frequency conversion steps in an OFDM transceiver

The basic frequency conversion steps of an OFDM transceiver are illustrated through Fig. A.1 to Fig. A.1(a). Fig. A.1(a) depicts the spectrum $S(f)$ of a complex baseband OFDM signal whose bandwidth $B{=}2f_{\max}$ is centred around 0. Assuming that the complex signal is up converted in the digital domain to an intermediate frequency (IF), the spectrum corresponding to the real part of this signal is shown in Fig. A.1(b). The portion in red corresponds the negative frequencies. It is clear that the real part of the spectrum is symmetric around 0 while the imaginary part is anti-symmetric, as expected with real time domain signals.

Assuming that the digital-to-analog conversion stage takes place at IF before the second up conversion to the so-called radio frequency (RF), the real signal transmitted into the channel has a spectrum as shown with the continuous lines in Fig. A.2. If the filter is not perfect, residuals of the dotted portions are also emitted.

In the channel, the real signal is delayed, attenuated by a complex coefficient (with real and imaginary part). We ignore Doppler in our analysis since it does not add to the discussion. In the receiver, the signal is down converted back to

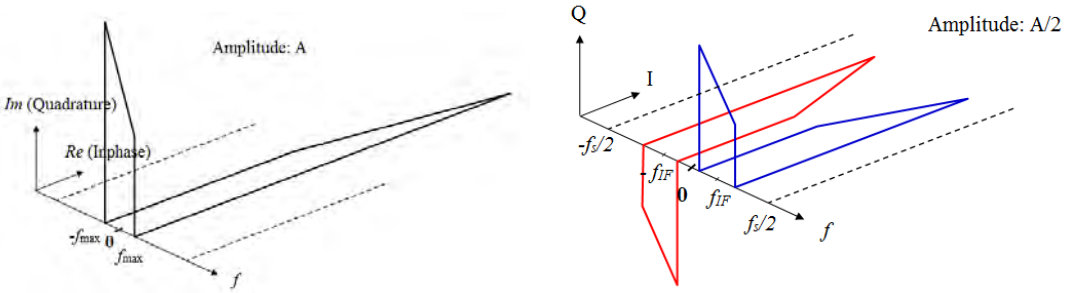

(a) Complex baseband signal spectrum $S(f)$ (b) Real IF signal spectrum $S_{\mathrm{IF}}(f)$

Figure A.1: Spectra of the complex baseband and real IF signals, on transmit, within the non ambiguous window limited by $-f_s/2$ and $f_s/2$, where f_s is the sampling frequency. Taking the real part drops the magnitude of the IF signal by half.

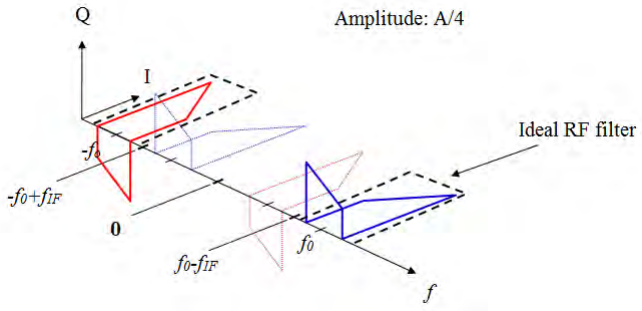

Figure A.2: Real RF band pass signal spectrum $S_{\mathrm{RF}}(f)$, on transmit. The local oscillator used has a frequency $f_0 - f_{\mathrm{IF}}$.

IF. Ideally, the IF filter cancels out the portion of the signal shifted around about twice the carrier frequency on both positive and negative sides, as depicted in Fig. A.3.

After an analog-to-digital conversion stage, the signal undergoes a complex demodulation, which produces two channels, I and Q, as shown in Fig. A.4. While a cosine is used to form the I channel, a sine is used to form the Q channel.

Ultimately, the time domain complex signal is retrieved from summing both time

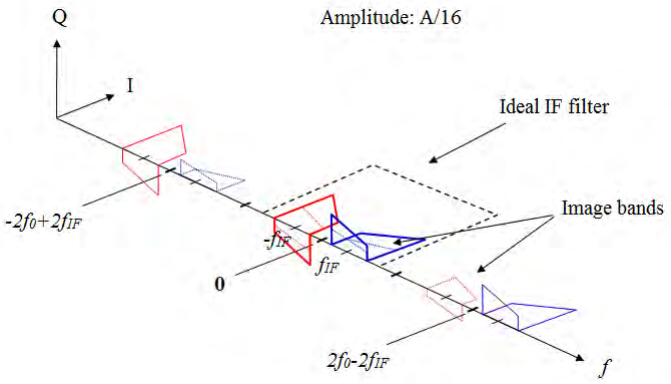

Figure A.3: Real IF signal spectrum $S_{\mathrm{IFrx}}(f)$ on receive.

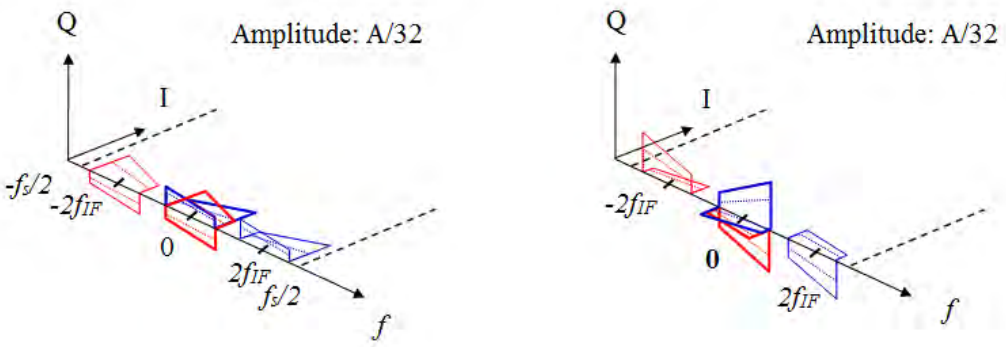

(a) Signal spectrum in the I channel

(b) Signal spectrum in the Q channel

Figure A.4: Spectra of the real signals in both I and Q channels on receive.

domain signals $s_I(t)$ and $s_Q(t)$ as follows:

$$s_{\mathrm{bb}}(t) = s_I(t) - j s_Q(t). \tag{A.1}$$

Fig. A.5 shows the resulting spectrum $S_{\mathrm{BB}}(f)$. The blue part of the signal conforms with the original signal from Fig. A.1(a). Note that through all those steps, we accounted for amplitude decrease that happens at the mixing stage, since multiplication with a cosine (respectively sine), shifts the original spectra to the right and to the left with a loss in magnitude of half.

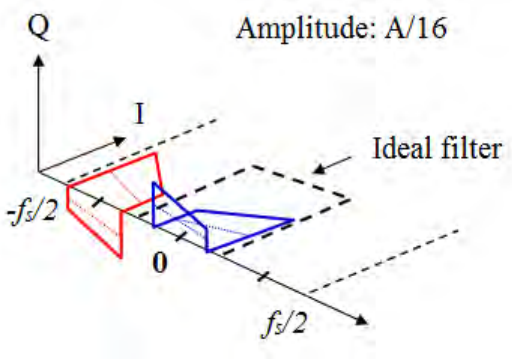

Figure A.5: Complex baseband signal spectrum $S_{\mathrm{BB}}(f)$ on receive.

Hence, one can perfectly model and analyse the effects of the channel by manipulating the analytical OFDM baseband signal.

Appendix B

Expected value of the SNR loss in the HRR profile

The details for the calculation of the expected value of the SNR loss caused by Doppler modulation at the peak of the HRR profile, which was formulated in Eq. 4.38, are given. We first split $\mathbf{B_{k,m,l}}[p]$ into two terms as in Eq. B.1. The first term corresponds to the value retrieved on subcarrier p. The second term describes the interference factor created by the neighbouring subcarriers. For clarity, we drop the scatterer index l.

$$\begin{aligned}\mathbf{B_{k,m}}[p] = w_p a_{p,k,m} \exp(j2\pi p \Delta f \Delta\tau_m) \left(\sum_{n=0}^{N-1} \exp(j2\pi \frac{f_{Dm}}{\Delta f} \frac{n}{N}) \right) \exp(j2\pi \frac{f_{Dm}}{\Delta f} k) \\ + \sum_{\substack{q=0 \\ q\neq p}}^{N-1} w_q a_{q,k,m} \exp(j2\pi q \Delta f \Delta\tau_m) \left(\sum_{n=0}^{N-1} \exp(j2\pi \frac{(q-p)n}{N}) \exp(j2\pi \frac{f_{Dm}}{\Delta f} \frac{n}{N}) \right) \\ \exp(j2\pi \frac{f_{Dm}}{\Delta f} k).\end{aligned} \tag{B.1}$$

After stacking together the vectors $\delta_{\mathbf{k,m}}$ obtained for each symbol k, we form the matrix $\mathbf{\Theta_m}$ and apply the three processing steps as illustrated in Fig. 4.4(b) to create the vector $\tilde{\mathbf{d}}_\mathbf{m}$. Including ς, α_m and κ_m that were left out in $\mathbf{B_{k,m}}[p]$ we

get $\tilde{\mathbf{d}}_\mathbf{m}$ as in Eq. B.2.

$$\begin{aligned}\tilde{\mathbf{d}}_\mathbf{m}[p] = \varsigma\alpha_m\kappa_m \exp(j2\pi p\Delta f\Delta\tau_m)\exp(j\pi\frac{f_{Dm}}{\Delta f}(K-1))\frac{1}{K}\frac{\sin(\pi\frac{f_{Dm}}{\Delta f}K)}{\sin(\pi\frac{f_{Dm}}{\Delta f})}\\ \exp(j\pi\frac{f_{Dm}}{\Delta f}\frac{N-1}{N})\frac{\sin(\pi\frac{f_{Dm}}{\Delta f})}{\sin(\pi\frac{f_{Dm}}{N\Delta f})}\\ +\varsigma\alpha_m\kappa_m\sum_{k=0}^{K-1}\sum_{\substack{q=0\\q\neq p}}^{N-1}\frac{w_q}{Kw_p}a_{q,k,m}a^*_{q,k,m}\exp(j2\pi q\Delta f\Delta\tau_m)\\ \left(\sum_{n=0}^{N-1}\exp(j2\pi\frac{(q-p)n}{N})\exp(j2\pi\frac{f_{Dm}}{\Delta f}\frac{n}{N})\right)\exp(j2\pi\frac{f_{Dm}}{\Delta f}k).\end{aligned} \tag{B.2}$$

We then form the long vector $\breve{\mathbf{d}}$ assuming linear frequency coding rather than Costas, for convenience, as in Eq. B.3.

$$\begin{aligned}\breve{\mathbf{d}}[\xi] = \varsigma\exp(-j2\pi f_0\tau_0)\exp(j2\pi\xi\Delta f\Delta\tau_0)\exp(j2\pi\frac{f_{Dm}}{\Delta f}\Delta\tau_m)\\ \exp(j\pi\frac{f_{Dm}}{\Delta f}(K-1))\frac{1}{K}\frac{\sin(\pi\frac{f_{Dm}}{\Delta f}K)}{\sin(\pi\frac{f_{Dm}}{\Delta f})}\\ \exp(j\pi\frac{f_{Dm}}{\Delta f}\frac{N-1}{N})\frac{\sin(\pi\frac{f_{Dm}}{\Delta f})}{\sin(\pi\frac{f_{Dm}}{N\Delta f})}\\ +\varsigma\exp(-j2\pi f_0\tau_0)\exp(j2\pi\xi\Delta f\Delta\tau_0)\exp(j2\pi\frac{f_{Dm}}{\Delta f}\Delta\tau_m)\\ \sum_{k=0}^{K-1}\sum_{\substack{q=0\\q\neq p}}^{N-1}\frac{w_q}{Kw_p}a_{q,k,m}a^*_{q,k,m}\exp(j2\pi q\Delta f\Delta\tau_m)\\ \left(\sum_{n=0}^{N-1}\exp(j2\pi\frac{(q-p)n}{N})\exp(j2\pi\frac{f_{Dm}}{\Delta f}\frac{n}{N})\right)\exp(j2\pi\frac{f_{Dm}}{\Delta f}k).\end{aligned} \tag{B.3}$$

Next, taking the expected value of $\breve{\mathbf{d}}[\xi]$ we observe in Eq. B.4 that the second term is suppressed as a result of the phase codes.

$$\begin{aligned} E(\breve{\mathbf{d}}[\xi]) = \varsigma \exp(-j2\pi f_0 \tau_0) \exp(j2\pi \xi \Delta f \Delta\tau_0) \exp(j2\pi \frac{f_{Dm}}{\Delta f} \Delta\tau_m) \\ \exp(j\pi \frac{f_{Dm}}{\Delta f}(K-1)) \frac{1}{K} \frac{\sin(\pi \frac{f_{Dm}}{\Delta f} K)}{\sin(\pi \frac{f_{Dm}}{\Delta f})} \\ \exp(j\pi \frac{f_{Dm}}{\Delta f} \frac{N-1}{N}) \frac{\sin(\pi \frac{f_{Dm}}{\Delta f})}{\sin(\pi \frac{f_{Dm}}{N\Delta f})}. \end{aligned} \tag{B.4}$$

We finally retrieve the SNR loss in Eq. B.5.

$$|E(\hat{\mathbf{d}}[\xi])| = \varsigma \frac{1}{K} \frac{\sin(\pi \frac{f_{Dm}}{\Delta f} K)}{\sin(\pi \frac{f_{Dm}}{\Delta f})} \frac{\sin(\pi \frac{f_{Dm}}{\Delta f})}{\sin(\pi \frac{f_{Dm}}{N\Delta f})}. \tag{B.5}$$

If we assume that Doppler will not fluctuate significantly within the set of carrier frequencies, we can make the assumption that f_{Dm}=f_D, where f_D is calculated for the lowest carrier frequency F_0. Like that, we obtain the same result as in Eq. 4.38. This formulation enabled to plot the loss versus the normalised Doppler quite elegantly, as in Fig 4.5.

Bibliography

[1] C. Hülsmeyer, "Verfahren um entfernte metallische gegenstande mittels elektrischer wellen einem beobachter zu melden," 1904. Patent. 1

[2] M. I. Skolnik, "Radar Systems," 2001. 1

[3] M. Skolnik, "Fifty years of radar," *Proceedings of the IEEE*, vol. 73, pp. 182–197, Feb 1985. 1

[4] A. Zyweck and R. E. Bogner, "Radar target classification of commercial aircraft," *Aerospace and Electronic Systems, IEEE Transactions on*, vol. 32, pp. 598–606, April 1996. 2

[5] F. Rice, T. Cooke, and D. Gibbins, "Model based ISAR ship classification," *Digital Signal Processing*, vol. 16, no. 5, pp. 628–637, 2006. 2

[6] G. E. A. Franken, H. Nikookar, and P. van Genderen, "Doppler Tolerance of OFDM-coded Radar Signals," in *Radar Conference, 2006. EuRAD 2006. 3rd European*, pp. 108–111, 2006. 3, 44, 58, 60, 71

[7] S. Hara and R. Prasad, *Multicarrier techniques for 4G mobile communications*. Artech House Publishers, 2003. 3, 30, 37, 89, 120, 176

[8] G. T. Ruck, D. E. Barrick, W. D. Stuart, and C. K. Krichbaum, *Radar cross section handbook*, vol. 1. Plenum Press New York, 1970. 3, 169

[9] C. Sturm and W. Wiesbeck, "Waveform Design and Signal Processing Aspects for Fusion of Wireless Communications and Radar Sensing," *Pro-*

ceedings of the IEEE, vol. 99, no. 7, pp. 1236–1259, 2011. 3, 5, 46, 49, 62, 70

[10] W. Wiesbeck, "The radar of the future," in *Radar Conference (EuRAD), 2013 European*, pp. 137–140, Oct 2013. 4

[11] W. Wiesbeck and L. Sit, "Radar 2020: The future of radar systems," in *Radar, 2014 International Conference on*, Oct 2014. 4

[12] R. Prasad, *OFDM for wireless communications systems*. Artech House Publishers, 2004. 4, 38, 71, 86

[13] N. Levanon, "Multifrequency complementary phase-coded radar signal," *Radar, Sonar and Navigation, IEE Proceedings* -, vol. 147, no. 6, pp. 276–284, 2000. 4, 44, 48

[14] P. Genderen and H. Nikookar, "Radar Network Communication," in *Proc. Communications 2006*, pp. 313–316, June 2006. 5

[15] G. Lellouch and H. Nikookar, "On the capability of a radar network to support communications," in *Communications and Vehicular Technology in the Benelux, 2007 14th IEEE Symposium on*, pp. 1–5. 5

[16] R. Fens, M. Ruggiano, and G. Leus, "Channel characterization using radar for transmission of communication signals," in *Wireless Technology, 2008. EuWiT 2008. European Conference on*, pp. 127–130, IEEE, 2008. 5

[17] P. Tran, "Person localization in adverse complex environment (PLACE) frequency agility in OFDM active radars," Oct. 2006. 5, 44

[18] G. Lellouch, P. Tran, R. Pribic, and P. Van Genderen, "OFDM waveforms for frequency agility and opportunities for Doppler processing in radar," in *Radar Conference, 2008. RADAR '08. IEEE*, pp. 1–6, 2008. 5, 45, 49, 50, 130

[19] G. Lellouch, R. Pribic, and P. Van Genderen, "Wideband OFDM pulse burst and its capabilities for the Doppler processing in radar," in *Radar, 2008 International Conference on*, pp. 531–535, 2008. 5, 45

[20] R. Tigrek, W. de Heij, and P. van Genderen, "Solving Doppler ambiguity by Doppler sensitive pulse compression using multi-carrier waveform," in *Radar Conference, 2008. EuRAD 2008. European*, pp. 72–75, IEEE, 2008. 5

[21] R. Tigrek, W. de Heij, and P. van Genderen, "Multi-carrier radar waveform schemes for range and Doppler processing," in *Radar Conference, 2009 IEEE*, pp. 1–5, IEEE, 2009. 5

[22] P. van Genderen, "Recent advances in waveforms for radar, including those with communication capability," in *Radar Conference, 2009. EuRAD 2009. European*, pp. 318–325, IEEE, 2009. 5, 9

[23] P. van Genderen, "A communication waveform for radar," in *Communications (COMM), 2010 8th International Conference on*, pp. 289–292, IEEE, 2010. 5

[24] E. M. Dominguez, R. Tigrek, M. Ruggiano, G. Lellouch, W. de Heij, D. Bockstal, and P. van Genderen, "Experimental Set Up Demonstrating Combined Use of OFDM for Radar and Communications," *Microwave Journal*, vol. 53, no. 8, pp. 22–36, 2010. 5

[25] C. Sturm, E. Pancera, T. Zwick, and W. Wiesbeck, "A novel approach to OFDM radar processing," in *Radar Conference, 2009 IEEE*, pp. 1–4, IEEE, 2009. 5, 46

[26] C. Sturm, T. Zwick, and W. Wiesbeck, "An OFDM System Concept for Joint Radar and Communications Operations," in *VTC Spring*, 2009. 5

[27] C. Sturm, M. Braun, T. Zwick, and W. Wiesbeck, "A multiple target Doppler estimation algorithm for OFDM based intelligent radar systems," in *Radar Conference (EuRAD), 2010 European*, pp. 73–76, IEEE, 2010. 5, 46

[28] C. Sturm, T. Zwick, W. Wiesbeck, and M. Braun, "Performance verification of symbol-based OFDM radar processing," in *Radar Conference, 2010 IEEE*, pp. 60–63, IEEE, 2010. 5

[29] M. Braun, C. Sturm, A. Niethammer, and F. K. Jondral, "Parametrization of joint OFDM-based radar and communication systems for vehicular applications," in *Personal, Indoor and Mobile Radio Communications, 2009 IEEE 20th International Symposium on*, pp. 3020–3024, IEEE, 2009. 5, 49

[30] M. Braun, C. Sturm, and F. K. Jondral, "Maximum likelihood speed and distance estimation for OFDM radar," in *Radar Conference, 2010 IEEE*, pp. 256–261, IEEE, 2010. 5

[31] N. Levanon and E. Mozeson, "Multicarrier radar signal - pulse train and CW," *Aerospace and Electronic Systems, IEEE Transactions on*, vol. 38, no. 2, pp. 707–720, 2002. 6, 44, 48

[32] M. A. Richards, J. Scheer, and W. A. Holm, *Principles of modern radar: basic principles*. SciTech Pub., 2010. 7, 32, 52, 62, 65, 87, 110, 114, 122, 141, 164, 165

[33] R. Mohseni, A. Sheikhi, and M. M. Shirazi, "A new approach to compress multicarrier phase-coded signals," in *Radar Conference, 2008. RADAR'08. IEEE*, pp. 1–6, IEEE, 2008. 7, 45

[34] K. Huo, B. Deng, Y. Liu, W. Jiang, and J. Mao, "The principle of synthesizing HRRP based on a new OFDM phase-coded stepped-frequency radar signal," in *Signal Processing (ICSP), 2010 IEEE 10th International Conference on*, pp. 1994–1998, 2010. 8, 45, 84, 87, 101, 102

[35] R. Mohseni, A. Sheikhi, and M. M. Shirazi, "Constant envelope OFDM signals for radar applications," in *Radar Conference, 2008. RADAR'08. IEEE*, pp. 1–5, IEEE, 2008. 8

[36] N. Levanon and E. Mozeson, *Radar signals*. Wiley-Interscience, 2004. 8, 44, 52, 53, 55, 58, 102, 111, 119, 125, 127

[37] Y. Paichard, J. C. Castelli, P. Dreuillet, and G. Bobillot, "HYCAM: a RCS measurement and analysis system for time-varying targets," in *Instrumentation and Measurement Technology Conference, 2006. IMTC 2006. Proceedings of the IEEE*, pp. 921–925, IEEE, 2006. 9, 45, 167

[38] S. Sen and A. Nehorai, "Adaptive design of OFDM radar signal with improved wideband ambiguity function," *Signal Processing, IEEE Transactions on*, vol. 58, no. 2, pp. 928–933, 2010. 9, 46, 127

[39] M. R. Bell, "Information theory and radar waveform design," *Information Theory, IEEE Transactions on*, vol. 39, no. 5, pp. 1578–1597, 1993. 9, 138, 139, 166

[40] R. Tigrek, *A processing technique for OFDM-modulated wideband radar signals*. PhD thesis, PhD thesis, TUDelft, 2010. 9, 46

[41] J. R. Guerci, "Optimum matched illumination-reception radar for target classification," Jan. 10 1995. US Patent 5,381,154. 10

[42] D. Garren, M. Osborn, A. Odom, J. S. Goldstein, S. U. Pillai, and J. Guerci, "Enhanced target detection and identification via optimised radar transmission pulse shape," *IEE Proceedings-Radar, Sonar and Navigation*, vol. 148, no. 3, pp. 130–138, 2001. 10, 166

[43] L. C. Potter, D.-M. Chiang, R. Carriere, and M. J. Gerry, "A GTD-based parametric model for radar scattering," *Antennas and Propagation, IEEE Transactions on*, vol. 43, no. 10, pp. 1058–1067, 1995. 18, 147, 148, 149, 160

[44] G. Lellouch and A. K. Mishra, "Multi-carrier Based Radar Signal Optimization Using Genetic Algorithm," in *Proceedings of the Third International Conference on Soft Computing for Problem Solving*, pp. 525–534, Springer, 2014. 20, 64, 79, 92, 126, 137, 177

[45] G. Lellouch, A. Mishra, and M. Inggs, "Impact of the Doppler modulation on the Range and Doppler Processing in OFDM Radar," in *Radar Conference, 2014. RADAR '14. IEEE*, pp. 803–808, 2014. 20, 98, 99, 122

[46] G. Lellouch, A. Mishra, and M. Inggs, "Processing alternatives in OFDM radar," in *Radar Conference (Radar), 2014 International*, pp. 1–6, IEEE, 2014. 20, 114, 122

[47] G. Lellouch, A. K. Mishra, and M. Inggs, "Stepped OFDM radar technique to resolve range and doppler simultaneously," *Aerospace and Electronic Systems, IEEE Transactions on*, vol. 51, no. 2, pp. 937–950, 2015. 20, 123

[48] E. Heras Miguel, "Fiber-based orthogonal frequency division multiplexing transmission systems," 2011. 22

[49] S. Weinstein and P. Ebert, "Data transmission by frequency-division multiplexing using the discrete Fourier transform," *Communication Technology, IEEE Transactions on*, vol. 19, no. 5, pp. 628–634, 1971. 24

[50] S. L. Jansen, I. Morita, T. C. Schenk, N. Takeda, and H. Tanaka, "Coherent optical 25.8-Gb/s OFDM transmission over 4160-km SSMF," *Journal of Lightwave Technology*, vol. 26, no. 1, pp. 6–15, 2008. 25

[51] G. Acosta, "OFDM simulation using matlab," *Report, Smart Antenna*, 2000. 27

[52] X. Yang, Y. Song, T. Owens, J. Cosmas, and T. Itagaki, "Performance analysis of the OFDM scheme in DVB-T," in *Emerging Technologies: Frontiers of Mobile and Wireless Communication, 2004. Proceedings of the IEEE 6th Circuits and Systems Symposium on*, vol. 2, pp. 489–492, IEEE, 2004. 27

[53] J.-J. Van de Beek, M. Sandell, P. O. Borjesson, *et al.*, "ML estimation of time and frequency offset in OFDM systems," *IEEE Transactions on signal processing*, vol. 45, no. 7, pp. 1800–1805, 1997. 39

[54] D. Matic, T. Coenen, F. C. Schoute, and R. Prasad, "OFDM timing synchronisation: Possibilities and limits to the usage of the cyclic prefix for maximum likelihood estimation," in *Vehicular Technology Conference, 1999. VTC 1999-Fall. IEEE VTS 50th*, vol. 2, pp. 668–672, IEEE, 1999. 39

[55] M. Morelli, C. Kuo, and M.-O. Pun, "Synchronization techniques for orthogonal frequency division multiple access (OFDMA): A tutorial review," *PROCEEDINGS-IEEE*, vol. 95, no. 7, p. 1394, 2007. 39

[56] Y. Mostofi and D. C. Cox, "Mathematical analysis of the impact of timing synchronization errors on the performance of an OFDM system," *Communications, IEEE Transactions on*, vol. 54, no. 2, pp. 226–230, 2006. 39

[57] M. García and C. Oberli, "Intercarrier interference in OFDM: a general model for transmissions in mobile environments with imperfect synchronization," *EURASIP Journal on Wireless Communications and Networking*, vol. 2009, p. 36, 2009. 39

[58] W.-S. Hou and B.-S. Chen, "ICI cancellation for OFDM communication systems in time-varying multipath fading channels," *Wireless Communications, IEEE Transactions on*, vol. 4, no. 5, pp. 2100–2110, 2005. 40

[59] T. Keller, L. Piazzo, P. Mandarini, and L. Hanzo, "Orthogonal frequency division multiplex synchronization techniques for frequency-selective fading channels," *Selected Areas in Communications, IEEE Journal on*, vol. 19, no. 6, pp. 999–1008, 2001. 40

[60] A. Laourine, A. Stephenne, and S. Affes, "A new OFDM synchronization symbol for carrier frequency offset estimation," *IEEE signal processing letters*, vol. 14, no. 5, p. 321, 2007. 40

[61] C. Tellambura, "Computation of the continuous-time PAR of an OFDM signal with BPSK subcarriers," *Communications Letters, IEEE*, vol. 5, no. 5, pp. 185–187, 2001. 42, 126

[62] E. Mozeson and N. Levanon, "Multicarrier radar signals with low peak-to-mean envelope power ratio," *Radar, Sonar and Navigation, IEE Proceedings* -, vol. 150, pp. 71–77, Apr 2003. 44

[63] N. N. S. S. R. K. Prasad, V. Shameem, U. Desai, and S. Merchant, "Improvement in target detection performance of pulse coded Doppler radar based on multicarrier modulation with fast Fourier transform (FFT)," *Radar, Sonar and Navigation, IEE Proceedings* -, vol. 151, no. 1, pp. 11–17, 2004. 44

[64] M. Inggs and C. Tong, "Commensal radar using separated reference and surveillance channel configuration," *Electronics letters*, vol. 48, no. 18, pp. 1158–1160, 2012. 44

[65] D. Poullin, "Passive detection using digital broadcasters (DAB, DVB) with COFDM modulation," in *Radar, Sonar and Navigation, IEE Proceedings-*, vol. 152, pp. 143–152, IET, 2005. 44

[66] R. Mohseni, A. Sheikhi, and M. Shirazi, "Compression of Multicarrier Phase-Coded radar signals with low sampling rate," in *Radar, 2008 International Conference on*, pp. 718–721, 2008. 45

[67] M. Sebt, A. Sheikhi, and M. Nayebi, "Orthogonal frequency-division multiplexing radar signal design with optimised ambiguity function and low peak-to-average power ratio," *Radar, Sonar & Navigation, IET*, vol. 3, no. 2, pp. 122–132, 2009. 45

[68] D. Garmatyuk, J. Schuerger, K. Kauffman, and S. Spalding, "Wideband OFDM system for radar and communications," in *Radar Conference, 2009 IEEE*, pp. 1–6, IEEE, 2009. 45

[69] D. Garmatyuk, "Ultrawideband imaging radar based on OFDM: System simulation analysis," in *Defense and Security Symposium*, pp. 621007–621007, International Society for Optics and Photonics, 2006. 45

[70] D. Garmatyuk, J. Schuerger, Y. Morton, K. Binns, M. Durbin, and J. Kimani, "Feasibility study of a multi-carrier dual-use imaging radar and communication system," in *Radar Conference, 2007. EuRAD 2007. European*, pp. 194–197, IEEE, 2007. 45

[71] D. Garmatyuk and J. Schuerger, "Conceptual design of a dual-use radar/communication system based on OFDM," in *Military Communications Conference, 2008. MILCOM 2008. IEEE*, pp. 1–7, IEEE, 2008. 45

[72] Y. Paichard, "Orthogonal multicarrier phased coded signal for netted radar systems," in *Waveform Diversity and Design Conference, 2009 International*, pp. 234–236, 2009. 45

[73] R. Tigrek and P. Van Genderen, "Compensation of range migration for cyclically repetitive Doppler-sensitive waveform (OFDM)," *Aerospace and Electronic Systems, IEEE Transactions on*, vol. 46, no. 4, pp. 2118–2123, 2010. 46

[74] R. Tigrek, W. J. De Heij, and P. Van Genderen, "OFDM signals as the radar waveform to solve doppler ambiguity," *Aerospace and Electronic Systems, IEEE Transactions on*, vol. 48, no. 1, pp. 130–143, 2012. 46

[75] R. Tigrek and W. De Heij, "A method for measuring the radial velocity of a target with a doppler radar," Sept. 29 2010. EP Patent 2,093,589. 46

[76] S. Sen and A. Nehorai, "OFDM MIMO radar with mutual-information waveform design for low-grazing angle tracking," *Signal Processing, IEEE Transactions on*, vol. 58, no. 6, pp. 3152–3162, 2010. 46

[77] S. Sen and A. Nehorai, "Adaptive OFDM radar for target detection in multipath scenarios," *Signal Processing, IEEE Transactions on*, vol. 59, no. 1, pp. 78–90, 2011. 46

[78] S. Sen, G. Tang, and A. Nehorai, "Multiobjective optimization of OFDM radar waveform for target detection," *Signal Processing, IEEE Transactions on*, vol. 59, no. 2, pp. 639–652, 2011. 46, 128

[79] S. Sen and A. Nehorai, "Sparsity-based multi-target tracking using OFDM radar," *Signal Processing, IEEE Transactions on*, vol. 59, no. 4, pp. 1902–1906, 2011. 46

[80] S. Kafshgari and R. Mohseni, "The effect of target fluctuation on the OFDM radar detection performance," in *Telecommunications Forum (TELFOR), 2012 20th*, pp. 827–830, IEEE, 2012. 46

[81] M. Braun, C. Sturm, and F. K. Jondral, "On the single-target accuracy of OFDM radar algorithms," in *Personal Indoor and Mobile Radio Communications (PIMRC), 2011 IEEE 22nd International Symposium on*, pp. 794–798, IEEE, 2011. 49

[82] E. Mozeson and N. Levanon, "MATLAB code for plotting ambiguity functions," *IEEE Transactions on Aerospace and Electronic Systems*, pp. 1064–1068, 2002. 53

[83] G. Lellouch, R. Pribic, and P. Van Genderen, "Frequency agile stepped OFDM waveform for HRR," in *Waveform Diversity and Design Conference, 2009 International*, pp. 90–93, 2009. 84

[84] K. Huo, B. Deng, Y. Liu, W. Jiang, and J. Mao, "High resolution range profile analysis based on multicarrier phase-coded waveforms of OFDM radar," *Systems Engineering and Electronics, Journal of*, vol. 22, no. 3, pp. 421–427, 2011. 84, 101

[85] M. Schikorr, "High range resolution with digital stretch processing," in *Radar Conference, 2008. RADAR'08. IEEE*, pp. 1–6, IEEE, 2008. 85

[86] N. Levanon, "Stepped-frequency pulse-train radar signal," *IEE Proceedings-Radar, Sonar and Navigation*, vol. 149, no. 6, pp. 297–309, 2002. 85, 102, 103, 104, 108, 112, 145

[87] J. P. Costas, "A study of a class of detection waveforms having nearly ideal rangedoppler ambiguity properties," *Proceedings of the IEEE*, vol. 72, no. 8, pp. 996–1009, 1984. 102

[88] M. Inggs, M. Van Zyl, and A. Knight, "A simulation of synthetic range profile radar," in *Communications and Signal Processing, 1992. COMSIG'92., Proceedings of the 1992 South African Symposium on*, pp. 1–16, IEEE, 1992. 108, 112

[89] A. Becker and F. Le Chevalier, "Wideband coherent airborne radar systems: performances for moving target detection," in *Radar, 2001 CIE International Conference on, Proceedings*, pp. 146–149, 2001. 110, 112

[90] D. R. Wehner, "High resolution radar," *Norwood, MA, Artech House, Inc., 1987, 484 p.*, vol. 1, 1987. 111

[91] D. Whitley, "A genetic algorithm tutorial," *Statistics and computing*, vol. 4, no. 2, pp. 65–85, 1994. 119, 129, 130, 131, 177

[92] K. Deb, A. Pratap, S. Agarwal, and T. Meyarivan, "A fast and elitist multiobjective genetic algorithm: NSGA-II," *Evolutionary Computation, IEEE Transactions on*, vol. 6, no. 2, pp. 182–197, 2002. 119, 131

[93] A. K. Sahoo, G. Panda, and P. M. Pradhan, "Generation of pulse compression codes using NSGA-II," in *India Conference (INDICON), 2009 Annual IEEE*, pp. 1–4, IEEE, 2009. 119

[94] A. K. Sahoo and G. Panda, "A multiobjective optimization approach to determine the parameters of stepped frequency pulse train," *Aerospace science and technology*, vol. 24, no. 1, pp. 101–110, 2013. 119

[95] A. E. Jones, T. A. Wilkinson, and S. Barton, "Block coding scheme for reduction of peak to mean envelope power ratio of multicarrier transmission schemes," *Electronics letters*, vol. 30, no. 25, pp. 2098–2099, 1994. 125

[96] L. J. Cimini and N. R. Sollenberger, "Peak-to-average power ratio reduction of an OFDM signal using partial transmit sequences," *Communications Letters, IEEE*, vol. 4, no. 3, pp. 86–88, 2000. 126

[97] C.-L. Wang, S.-J. Ku, and C.-J. Yang, "An Improved Peak-to-Average Power Ratio Estimation Scheme for OFDM Systems," in *Vehicular Technology Conference, 2007. VTC2007-Spring. IEEE 65th*, pp. 2827–2831, April 2007. 126

[98] S. H. Han and J. H. Lee, "An overview of peak-to-average power ratio reduction techniques for multicarrier transmission," *Wireless Communications, IEEE*, vol. 12, no. 2, pp. 56–65, 2005. 128

[99] T. Guo and R. Qiu, "OFDM waveform design compromising spectral nulling, side-lobe suppression and range resolution," in *Radar Conference, 2014 IEEE*, pp. 1424–1429, IEEE, 2014. 128

[100] V. Riché, S. Meric, J.-Y. Baudais, and E. Pottier, "Optimization of OFDM SAR signals for Range ambiguity suppression," in *Radar Conference (EuRAD), 2012 9th European*, pp. 278–281, IEEE, 2012. 128

[101] S. Sen and C. W. Glover, "Frequency adaptability and waveform design for OFDM radar space-time adaptive processing," in *Radar Conference (RADAR), 2012 IEEE*, pp. 0230–0235, IEEE, 2012. 128

[102] S. Sen, "PAPR-constrained Pareto-Optimal waveform design for OFDM-STAP radar," *Geoscience and Remote Sensing, IEEE Transactions on*, vol. 52, no. 6, pp. 3658–3669, 2014. 128

[103] K. Deb and R. B. Agrawal, "Simulated binary crossover for continuous search space," *Complex Systems*, vol. 9, no. 3, pp. 1–15, 1994. 129, 132

[104] R. L. Haupt and S. E. Haupt, *Practical genetic algorithms*. John Wiley & Sons, 2004. 129, 177

[105] C. R. Reeves and J. E. Rowe, *Genetic algorithms: principles and perspectives: a guide to GA theory*, vol. 20. Springer, 2003. 129, 130

[106] A. Seshadri, "A fast elitist multiobjective genetic algorithm: NSGA-II, Matlab Central, file exchange, mathworks," 2007. 131

[107] A. Wilkinson, R. Lord, and M. Inggs, "Stepped-frequency processing by reconstruction of target reflectivity spectrum," in *Communications and Signal Processing, 1998. COMSIG '98. Proceedings of the 1998 South African Symposium on*, pp. 101–104, Sep 1998. 138, 149

[108] F. Gini, *Waveform design and diversity for advanced radar systems*. The Institution of Engineering and Technology, 2012. 140, 165

[109] F. Berizzi, M. Martorella, and M. Bernabo, "A range profiling technique for synthetic wideband radar," *IET Radar, Sonar & Navigation*, vol. 2, no. 5, pp. 334–350, 2008. 145

[110] T. Boulay, J. Lagoutte, A. Mohammad-Djafari, and N. Gac, "A Fuzzy-Logic based non cooperative target recognition," in *Signal Image Technology and Internet Based Systems (SITIS), 2012 Eighth International Conference on*, pp. 410–415, IEEE, 2012. 146

[111] M. Martorella, E. Giusti, L. Demi, Z. Zhou, A. Cacciamano, F. Berizzi, and B. Bates, "Target recognition by means of polarimetric ISAR images," *Aerospace and Electronic Systems, IEEE Transactions on*, vol. 47, no. 1, pp. 225–239, 2011. 146

[112] J. R. Huynen, *Phenomenological theory of radar targets*. PhD thesis, Drukkerij Bronder-Offset NV, 1970. 146, 167

[113] J. R. Huynen, "A revisitation of the phenomenological approach with applications to radar target decomposition," tech. rep., DTIC Document, 1982. 146

[114] L. C. Potter and R. L. Moses, "Attributed scattering centers for SAR ATR," *Image processing, IEEE Transactions on*, vol. 6, no. 1, pp. 79–91, 1997. 147

[115] Y. Akyildiz and R. L. Moses, "Scattering center model for SAR imagery," in *Remote Sensing*, pp. 76–85, International Society for Optics and Photonics, 1999. 147

[116] J. B. Keller, "Geometrical theory of diffraction," *JOSA*, vol. 52, no. 2, pp. 116–130, 1962. 147

[117] R. G. Kouyoumjian and P. H. Pathak, "A uniform geometrical theory of diffraction for an edge in a perfectly conducting surface," *Proceedings of the IEEE*, vol. 62, no. 11, pp. 1448–1461, 1974. 147

[118] M. Plonus, R. Williams, and S. Wang, "Radar cross section of curved plates using geometrical and physical diffraction techniques," *IEEE Transactions on Antennas and Propagation*, vol. 26, pp. 488–493, 1978. 147

[119] P. H. Pathak, "Techniques for high-frequency problems," in *Antenna Handbook*, pp. 195–311, Springer, 1988. 147

[120] C. A. Balanis, *Advanced engineering electromagnetics*, vol. 20. Wiley New York, 1989. 147

[121] E. Kennaugh and D. Moffatt, "Transient and impulse response approximations," *Proceedings of the IEEE*, vol. 53, no. 8, pp. 893–901, 1965. 148

[122] A. K. Mishra and B. Mulgrew, "Automatic target recognition," *Encyclopedia of Aerospace Engineering*, 2010. 158, 183

[123] P. Swerling, "Probability of detection for fluctuating targets," *Information Theory, IRE Transactions on*, vol. 6, no. 2, pp. 269–308, 1960. 164

[124] N. A. Goodman, P. R. Venkata, and M. A. Neifeld, "Adaptive waveform design and sequential hypothesis testing for target recognition with active sensors," *IEEE Journal of Selected Topics in Signal Processing*, vol. 1, no. 1, p. 105, 2007. 165, 167

[125] S. Haykin, "Cognitive radar: a way of the future," *Signal Processing Magazine, IEEE*, vol. 23, no. 1, pp. 30–40, 2006. 165

[126] S. U. Pillai, D. Youla, H. Oh, and J. R. Guerci, "Optimum transmit-receiver design in the presence of signal-dependent interference and channel noise," in *Signals, Systems, and Computers, 1999. Conference Record of the Thirty-Third Asilomar Conference on*, vol. 2, pp. 870–875, IEEE, 1999. 166

[127] S. Kay, "Optimal signal design for detection of Gaussian point targets in stationary Gaussian clutter/reverberation," *Selected Topics in Signal Processing, IEEE Journal of*, vol. 1, no. 1, pp. 31–41, 2007. 166

[128] R. A. Romero, J. Bae, and N. A. Goodman, "Theory and application of SNR and mutual information matched illumination waveforms," *Aerospace and Electronic Systems, IEEE Transactions on*, vol. 47, no. 2, pp. 912–927, 2011. 166

[129] F. Yin, C. Debes, and A. M. Zoubir, "Parametric waveform design for improved target detection," in *European Signal Processing Conference (EUSIPCO)*, 2011. 166

[130] J. R. Guerci and S. U. Pillai, "Theory and application of optimum transmit-receive radar," in *Radar Conference, 2000. The Record of the IEEE 2000 International*, pp. 705–710, IEEE, 2000. 166

[131] D. A. Garren, M. K. Osborn, A. C. Odom, J. S. Goldstein, S. U. Pillai, and J. R. Guerci, "Optimal transmission pulse shape for detection and identification with uncertain target aspect," in *Radar Conference, 2001. Proceedings of the 2001 IEEE*, pp. 123–128, IEEE, 2001. 167

[132] R. Romero and N. Goodman, "Waveform design in signal-dependent interference and application to target recognition with multiple transmissions," *IET radar, sonar & navigation*, vol. 3, no. 4, pp. 328–340, 2009. 167

[133] Y. Wei, H. Meng, Y. Liu, and X. Wang, "Radar phase-coded waveform design for extended target recognition under detection constraints," in *Radar Conference (RADAR), 2011 IEEE*, pp. 1074–1079, IEEE, 2011. 167

[134] A. Balleri, H. Griffiths, K. Woodbridge, C. Baker, and M. Holderied, "Bat-pollinated plants: feature extraction for target recognition in the natural world," in *Radar Conference - Surveillance for a Safer World, 2009. RADAR. International*, pp. 1–5, Oct 2009. 167

[135] C. J. Baker, M. Inggs, and A. K. Mishra, "Waveform processing-domain diversity and ATR," in *19th European Signal Processing Conference (EUSIPCO 2011)*, pp. 431–435, 2011. 169